Author:
Almutairi, Tahani S D

Title:
Theoretical and experimental investigation of n-type doped diamond

THEORETICAL AND EXPERIMENTAL INVESTIGATION OF N-TYPE DOPED DIAMOND

TAHANI SAAD ALMUTAIRI

UNIVERSITY OF BRISTOL

FACULTY OF SCIENCE

SCHOOL OF CHEMISTRY

A dissertation submitted to the University of Bristol in accordance with the requirements for the award of the degree of Doctor of Philosophy in the Faculty of Science, School of Chemistry

December 2020

Word count 36,433

Abstract

It has long been thought that co-doping in semiconductor materials is the best way to overcome the strains induced by large dopants. We report a theoretical and experimental study of different co-doping systems to study n-type semi conductivity in diamond.

Theoretically, individual, and multi-substitutional point defects in diamond, composed of Mg, N, V and P, were studied using spin-polarised hybrid density functional theory and a supercell approach. A range of hybrid functionals, including HSE06, B3LYP, PBE0, PBEsol0 and PBE0-13 were used to calculate the formation, binding, and ionisation energies, in order to explore the solubility and stability of each point defect. The equilibrium geometry and the magnetic and electronic structures were analysed and presented in detail. Based on electronic structure analysis and the empirical marker method, an Mg atom coordinated by three N atoms was predicted to produce a shallower donor in diamond than P. In particular, the ionization potentials calculated for the P and for the MgN_3 complex with B3LYP and 512 supercells are 0.68 eV and 0.26 eV from the CBM, respectively. Different formation baths from pre-existing defects, such as vacancy and 2NV, were investigated. IR spectroscopic simulations were explored using B3LYP with the MgN_2 defect, and the main features were analysed and compared with those of the 2NV defect to determine the main IR peaks.

In addition to the Mg-N system, the effects of bonding one N atom to a P in adjacent substitutional sites were theoretically explored. The defect introduces a unique reconstruction where one of C atoms coordinated to the N atom involved in the elongated C-N bond and creates a new bond with the P atom. The IR spectra of PN defects were investigated with different supercell sizes and found to contain two sharp peaks at the edges of the spectrum, one at high frequency 1,379 cm^{-1} and the second appears at the end range, 234 cm^{-1}, as obtained with the largest supercell (216).

Experimentally, different approaches were examined to introduce the Mg and N dopants into diamond, guided by the results of the DFT calculations. The two main methods studied were: encapsulating the Mg inside nitrogen-doped diamond films during hot filament CVD, and ion implantation with different Mg and N doses followed by annealing up to 1,200°C to monitor the diffusion of the dopants. The morphology and quality of the films were studied by SEM and Raman spectroscopy, while the dopant concentrations and diffusion upon annealing were studied using SIMS. The Mg mass signal was detected by SIMS as an isolated,

narrow, unique peak in the encapsulated samples and shown to be unaffected by the annealing, whereas the N tended to present with high concentrations in the near-surface region of the Mg layer. No diffusion was observed with ion-implanted samples; the Mg concentrations were ~2×10^{19} cm^{-3} and showed similar distributions after annealing at 1,200°C. The immobility of the Mg can be explained by the Mg binding to radiation-induced defects or to N ions implanted along with the Mg.

Acknowledgements

First and foremost, I wish to express my gratitude to my advisor, Professor Paul May, for welcoming me into his group and allowing me to conduct my PhD project; he has spent time on my development, especially in academic writing. I am thankful to Professor Neil Allen for allowing me to perform the theoretical part of this thesis and showing me the wonderful world of defects, which has inspired me in many different ways to explore my project deeply. I greatly appreciate the efforts of Dr James Smith, who was always the first person to provide a demonstration and help in the lab. I also wish to acknowledge Dr Sergio Coneieros, who provided me with the basis for performing my calculations with CRYSTAL. I must also thank Dr Peter Heard for his assistance in the interference analysis centre and his useful discussions during SIMS measurements. I also wish to extend my thanks to Gael Gobaille-Shaw in the electrochemistry lab for his helpful assistance. I would also like to thank all the diamond members I worked with, past and present, and all of my friends who were with me on this journey. I am grateful to the Saudi Arabian Cultural Bureau in the UK (UKSACB) for funding this project and the efforts to make my life comfortable in the UK.

I am also deeply indebted to my parents, Halla Almutairi and Saad Almutairi (who left this world in June 2019), for their continued support, unconditional love, and encouragement to achieve the best. I wish to express my deep gratitude to my husband Essa and my entire, fabulous, small family. Thank you all for your patience with my unpredictable workload; you are a source of unlimited happiness in this life, and without you, I could not have completed this endeavour.

Declaration

I declare that the work in this dissertation was carried out in accordance with the requirements of the University's Regulations and Code of Practice for Research Degree Programmes and that it has not been submitted for any other academic award. Except where indicated by specific reference in the text, the work is the candidate's own work. Work done in collaboration with, or with the assistance of others, is indicated as such. Any views expressed in the dissertation are those of the author and in no way reflect those of the University of Bristol.

SIGNED: …… DATE: …….....

TABLE OF CONTENT

LIST OF FIGURES

LIST OF TABLES

LIST OF ABBRIVATIONS

ACRC	Advanced Computing Research Centre
BFGS	Broyden-Fletcher-Goldfarb-Shanno (BFGS)
BSSE	Basis Set Superposition Error
CASTEP	Cambridge Serial Total Energy Package
CBM	Conduction band minimum
CIRA	Cold Implantation Rapid Annealing
CPHF	Coupled Perturbed Hartree-Fock/Kohn-Sham
CVD	Chemical Vapour Deposition
DCO	Defective Crystalline Orbitals
DFT	Density functional theory
DOS	Density of State
EMM	Empirical Marker Method
FBZ	First Brillouin Zone
FWHM	Full width half maximum
GGA	Generalised Gradient Approximation
GTO	Gaussian-type orbital
HF	Hartree-Fock
HFCVD	Hot Filament Chemical Vapour Deposition
HOCO	Highest Occupied Crystalline Orbital
HPHT	High-pressure, high temperature
I	Self-Interstitial
KS	Kohn-Sham
LDA	Local density approximation
LODDI	Low-Damage Drive-In
LUCO	Lowest unoccupied crystalline orbital
MFCS	Mass Flow Controllers
MPCVD	Microwave Plasma Chemical Vapor Deposition
MPI	Message Passing Interface
MS-SIMS	Magnetic-Sector Secondary Ion Mass Spectrometry
NDD	Nitrogen-doped diamond
PBE	Perdew-Burke-Ernzerhof
PCD	Poly Crystalline Diamond
PDOS	Projected density of states
PW	Plane-wave
QCM	Quartz Crystal Microbalance
RHF	Restricted Hartree-Fock
SCD	Single crystal diamond
SCF	Self-Consistent Field
SEM	Scanning electron microscopy
TRIM	TRansport of Ions in Matter
TZVP	Triple-Zeta Valence With Polarisation
UHF	Unrestricted Hartree-Fock
UNCD	Ultra nanocrystalline diamond
V	Vacancy
VBM	Valence band Maximum
XC	Exchange-Correlation Energy

CHAPTER 1

INTRODUCTION

CHAPTER 1 – INTRODUCTION

1.1 Historical Overview

Graphite and diamond are allotropes of crystalline carbon, in which the carbon atoms bond covalently to form a different structure. Graphite found its application earlier; it was synthesised in the 19th century, whereas diamond was not successfully synthesised until the middle of the 20th century. Most of the scientific understanding of diamond arose following thermodynamic calculations on carbon phase equilibrium stability, which improved the approach to synthesis methods in this period.[1]

In the 20th century, there was a growing interest in diamond synthesis, mainly in the United States (US), Sweden and the Soviet Union. In 1955, the General Electric Company in the US reported the first successful attempt to synthesise diamonds from graphite.[2,3] The graphite was placed into a huge hydraulic press under high-pressure (7–10 GPa) and high-temperature (1,700–2,000 K) conditions. Some references referred to Halvard Liander and Erik Lundblad at the Swedish firm Allmänna Svenska Eliktriska Aktiebolaget (ASEA) as the first achievement in this context[2]; however, their announcement of the result was delayed until 1984.[4]

In the 1960s, new efforts suggested the deposition of carbon onto a diamond substrate to act as a seed crystal, using a condition where the diamond unstable. This method, known as chemical vapour deposition, and was developed by Eversole (Union Carbide Corporation) and both Angus et al. (Case Western Reserve University) and Cleveland and Deryagin et al. (Physical Chemistry Institute) in Moscow.[2,5–7] These efforts continued through the 1970s, and more knowledge of the diamond growth mechanism emerged. An important breakthrough in this period was the finding that diamond film could be deposited continuously, and mostly free from graphite, in the existence of a super equilibrium concentration of hydrogen.[8,9] The role of atomic hydrogen on the growth rate was evident via inhibited graphite nucleation. In the 1980s, the contribution of the National Institute for Research in Inorganic Materials (NIRIM) in Japan significantly improved the deposition conditions using hot-filaments[10,11] and microwaves.[10,12] At the time, the NIRIM papers described the work so precisely that it helped other researchers reproduce its work. Later, in the 1990s, research on thin-film diamonds widely increased across the world and garnered more interest from scientific communities, which led to the establishment of the CVD diamond field.[13]

1.2 Diamond Properties

The increasing interest in diamonds stems from their outstanding physical, mechanical and chemical properties.[14–17] The strong covalent C-C bonding in a diamond's structure results in a high atomic density (1.77×10^{23} cm^{-3}), high melting point (4500 K) and high bond energy, which all give extremely high chemical stability, even in harsh chemical conditions. The thermal conductivity of a diamond crystal (~25 W/ cm.K) is the highest compared with any other known solids with low thermal expansion coefficient (1×10^{-6} K^{-1}) at room temperature; therefore, it can be used as a heat sink in many applications. Diamond's unique structure makes it the hardest known material (10 on the Mohs scale of mineral hardness), which made it the first candidate in mechanical applications, such as cutting and abrasion.

Diamond is a transparent material over a wide wavelength range, starting from the deep UV to the far-infrared, and this feature opens a new window for a synthetic diamond in optical instruments. The electrical resistivity of a diamond is very high, 10^{14}–10^{16} Ω-cm, and it is classed as a wide band-gap semiconductor, with an indirect bandgap of 5.5 eV at 300 K, and hole and electron mobility (3800 cm^2 V^{-1} s^{-1}) and (4500 cm^2 V^{-1} s^{-1}), respectively. The highest value of breakdown field of the diamond (10^7 V/cm) make it able to insulate very high voltages through very thin diamond material. In contrast, a resistivity as low as 0.1 Ω can be achieved using boron-doped diamond, and superconductivity behaviour of heavily boron-doped diamond was demonstrated at 4 K.[18] Thus, diamond has many advantages over other, semiconductors, such as Si, GaAs, GaN and SiC.

1.3 Diamond Synthesis

To successfully synthesise diamonds in laboratories, scientists focused on understanding the formation of diamonds in nature over the past decades. The energetic barrier between diamond and the most stable form of carbon, graphite, made the interconversion between the two phases impossible under normal conditions (room temperature and atmospheric pressure). There is no simple mechanism to transform between the two carbon forms. At high-pressure and high-temperature, and given sufficient time, carbon atoms arranged into a diamond structure, which is the minimum energy state at these extreme conditions. When returned to room temperature and pressure, however, diamond is considered

to be at a metastable state, it is not thermodynamically stable compared to graphite, but it is trapped in the high energy state.

Different techniques have been employed for diamond growth, namely high-pressure, high-temperature (HPHT)[19–21] and chemical vapour deposition (CVD).[8,22] The former is an attempt to mimic the natural conditions that occurred deep in the earth, where diamonds are created, and the latter is a technique performed at low pressure. As the energy cost to produce diamonds is crucial in manufacturing applications, CVD has become one of the most important processes in diamond production today. The possibility of growing polycrystalline diamond films on various substrates materials, such as diamonds, metals and semiconductors, with deposition areas up to several hundred square centimetres [23,24], expands the application of CVD diamonds compared to those produced through HPHT.

1.3.1 Chemical Vapour Deposition (CVD)

The CVD technique is a result of participating in different engineering and scientific disciplines, such as chemistry, plasma physics, kinetics, and thermodynamics. CVD is a technique that chemically decomposes the gas precursors on the surface of solid material, called a substrate, to produce a variety of deposit forms, such as single-crystal, polycrystalline, Nano-crystalline, ultra-Nano-crystalline and amorphous forms, depending on the deposition conditions.

There are a variety of CVD techniques that differ in their details; however, they all share the main principle. The gas sources that are utilised must have at least one gas, for a diamond, this is usually methane, containing carbon atoms. Adding an excess of hydrogen gas to methane is essential for preventing the formation of a sp^2 carbon graphite configuration instead of sp^3 tetrahedral diamond configuration. To ensure the formation of diamond, the temperature of the substrate must be high enough (> 700 °C) and the methane dilution in hydrogen usually has a mixed ratio of 1% vol. A power supply is used to produce an activation region (hot-filament or electric discharge) to dissociate the gas molecules into active species (i.e., free radicals and atoms) that undergo several chemical reactions before diffusing to the substrate surface, then adsorbing or reacting with the available active site. The subsequent reaction process between the dangling bonds in the diamond surface and the gas phase leads to the abstraction of H and the addition of C radicals in the surface, thereby propagating the diamond crystals.[25]

The most popular CVD method to synthesise diamond is hot-filament CVD (HFCVD).[26] In the 1980s, the first successful diamond chemical deposition experiments through thermal activation were carried out by Matsumoto et al.[10,11] To synthesise polycrystalline diamond films with reasonable quality, HFCVD is considered to be the practical and affordable choice with a good deposition rate of 1–10 μm/h [25], based on the conditions of growth and the chamber size. However, the technique suffers from problems that restrict its application to some extent. For instance, there is a limit of gases that can be used with HFCVD because of the sensitivity of the filaments to oxidation; usually, the deposited film contains some unavoidable contamination from metallic filament atoms.

In an HFCVD reactor Figure 1.1, the process conditions are determined by the filament length and diameter, and type, e.g., tantalum, rhenium, and tungsten, as well as by temperature, pressure and gas mixture. The substrate temperature also considers an important factor in film quality optimisation. The distance between the filament and the substrate helps in directing the reactive free radicals that are released from the gas mixture to the substrate surface, thus continuing film deposition.

Besides the HFCVD reactor, there are microwave plasma CVD (MWCVD) reactors that use microwave power to produce a discharge to activate the gases' mixture instead of the thermal combustion used in HFCVD. The microwaves generator (usually works at frequency of 2.45 GHz and powers up to 5 kW) used to produce a plasma ball from the gas phase, which adjusted above the substrate. Additional to the microwave power, other parameters, as with HF, gas phase, pressure, substrate temperature can affect the depositions. MW reactors provide higher growth rate governed by the high power utilized within and high-quality diamond compared with HF. The components of the HFCVD and the most common type of MW reactors, NIRIM-type and ASTEX-type, are shown in Figure 1.1.

1.3.3 Substrates

The choice of substrate is a critical parameter in achieving a film with high quality. Diamond can grow on another diamond substrate without nucleation problems and with minimum defects; this process is called homoepitaxy. Even though the diamond surface provides the best growth potential, it is costly to apply on a large scale in the industry. Matsumoto et al. achieved heteroepitaxial growth for the first time by depositing diamond onto a Si substrate.[10] This achievement gained researchers' attention and motivation to provide a large substrate area. Various substrates have been investigated in the literature, for example,

titanium[27], silicon nitride[28], chromium nitride[29], $SrTiO_3$[30] and tungsten.[31]Among these substrates, silicon is most commonly used, as there is a little mismatch in the lattice parameters between diamond and silicon, and they both have a cubic crystal structure.

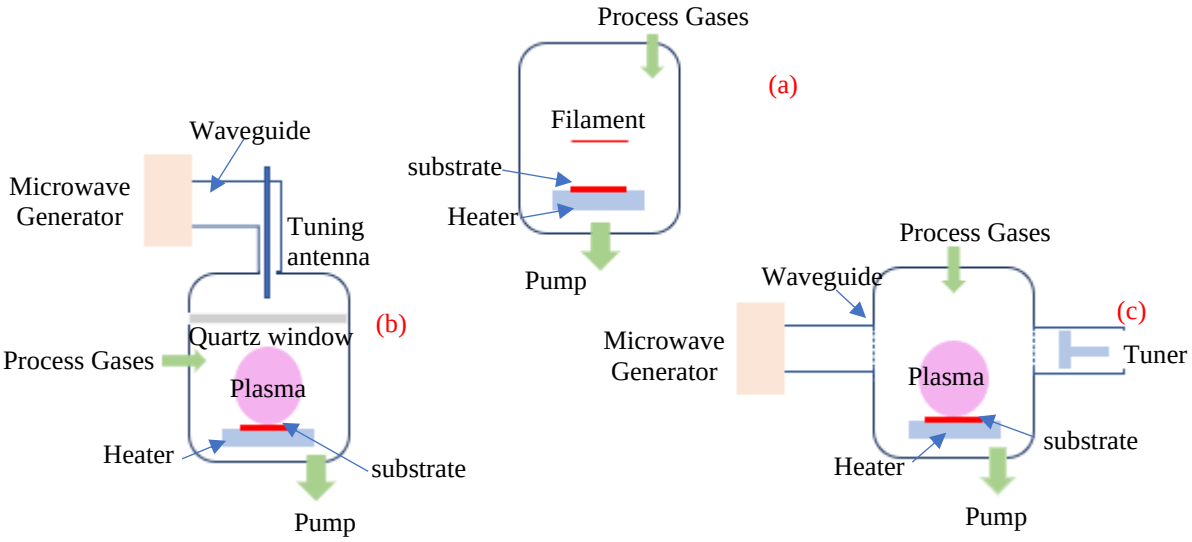

Figure 1-1 Schematic diagrams of HFCVD reactor (a) and MWCVD apparatus, ASTEX-type (b) and NIRIM-type (c), represented by [25].

The substrate types determine the heterogeneous reactions at the substrate surface. Under specific conditions, a suitable substrate must be able to absorb the activated chemical species from the gas mixture and increase the film deposition rate. The lattice mismatch between the substrates and diamond to grow diamond nuclei is one of the most important factors that must be avoided when choosing the substrate.[28] The thermal expansion coefficient must be close to that of a diamond, so that the developing strain is decreased as much as possible during growth. It is generally assumed that the nucleation on non-diamond substrates occurs on an interfacial carbide layer generated from the chemical interactions between activated carbon and the substrate surface.[32]

1.3.4 Effect of Substrate Surface Conditions

Nucleation is important in CVD diamond deposition and growing a diamond film on an untreated foreign substrate usually results in low nucleation densities of approximately 10^2–10^3 nuclei/cm^2. Various pre-treatment processes can enhance nucleation up to 10^{11} nuclei/cm^2. Methods such as scratching by abrasives, seeding with diamond particles, bias enhancement,

carburisation, chemical treatment and substrate coating [33–35] have been tested to enable the control of nucleation density. The most common methods are discussed below.

1.3.4.1 Manual Abrading

In this process, the substrate was polished with other substrates containing small diamond particles with sizes in the range of 0.25 µm, followed by washing with acetone or alcohol. The nucleation enhancement by this process was first reported in 1987.[36] The abrading created scratches and grooves on the Si substrate surface contain some nanoscale diamond particles. These seeds enhanced the nucleation density compared with untreated Si by providing a nucleation site for sp^3 diamond growth. Besides diamonds, abrasive materials, such as carbides, borides, oxides, silicides, and nitrides have been tested but were less efficient compared with diamond grits. The reason behind the enhancement of nucleation density by the abrasion method is attributed to the embedded seeding crystals, as well as the creation of dangling bonds at sharp edges which can rapidly carburise and provide nucleation sites.[35]

1.3.4.2 Sonication Abrading

Ultrasonic vibration is one of the most important pre-treatment processes to overcome the limitation of the manual abrading process and to create a homogeneous powder suspension. This process involves submerging the substrate in an abrasive suspension that contains diamond powder and uses ultrasound to disturb this suspension and force the diamond particles to be trapped in the scratches on the surface of the substrate. Since these particles will leave the suspension to polish the substrate, the concentration of the suspension plays an important role in determining the density of the diamond seeds. After employing this method, the substrate surface contains uniformly dispersed defects, and this results in an increase in nucleation density up to 10^{11} nuclei/cm^2.[37–40]A technique known as the novel nucleation procedure (NNP) was developed to enhance the efficiency of the ultrasonic nucleation process.[41]In this method, a substrate enters the CVD reactor for 30 minutes with conditions similar to those of diamond growth; then it is removed, and ultrasonic seeding is performed with an abrasive suspension containing diamond particles.

1.3.4.3 Bias-Enhanced Nucleation

The bias-enhanced nucleation (BEN) method was broadly used to reduce substrate damage, and it has been considered the efficient method in increasing the nucleation density. Applying a negative bias on a conductive substrate in an MW CVD reactor leads to positive

ions from the gas mixture (i.e., CH_x^+ (x = 1 to 5), C, H^+ and H^+) to bombard the surface of the substrate with high energy. This causes a subsurface carbon layer to form, which becomes supersaturated and then begins to precipitate out of the surface as diamond nuclei. These nuclei are all aligned with the Si substrate, so when they coalesce, there is a greater chance of a single crystal film being formed. The applied voltage and the bias time were found to control the nucleation density.[32,35,42]

1.4 Doping

Many properties of semiconductor materials (mechanical, electronic, magnetic and optical) can be significantly modified by introducing a point defect. Diamond offers extraordinary properties as a semiconductor, and doping seems to be a viable method of solving the problem associated with the fabrication of diamond-based electronic devices in order to exploit those properties. The dopants are believed to play a significant role in reducing the energy barrier to conduction and controlling the mobility of the carriers and the resistivity of the film. Due to the high density of the diamond lattice, doping is typically limited to a small number of elements. The atoms that are deficient in electrons in the valence band (compared to carbon atoms) create an acceptor level above the valence band. This results in holes in the valence band that carry the positive charge across the lattice; such dopants are called p-type. In contrast, atoms incorporated with extra electrons in the valence band (compared to carbon) will affect the energy-band structure of the diamond in another way: the extra electrons will create a new donor level below the conduction band of the diamond and therefore decrease the energy barrier to conduction. These dopants are known as n-type.

1.4.1 p-Type Doping

Boron-doped diamonds are found naturally as IIb-types and B is considered the ideal p-type impurity in a diamond as its covalent radius (0.87 Å) is close to that of carbon (0.67 Å). Introducing substitutional boron in the diamond gives an acceptor level of about 0.37 eV above the valence band (Figure 1-2). Boron-doped diamond films can be deposited via CVD methods by adding a gas source containing boron, such as trimethyl borane or diborane into a hot- filament or microwave reactor. Many studies reported the deposition of boron-doped diamond films with different concentrations (up to 10^{21} cm^{-3}), quality and mobility.[43–48] Ion-implantation has also been used with boron by utilising various annealing schemes.[49,50]

Typically, at a high level of boron doping, a reduction in mobility is predicted as a result of the formation of a boron cluster in the diamond lattice.[51]

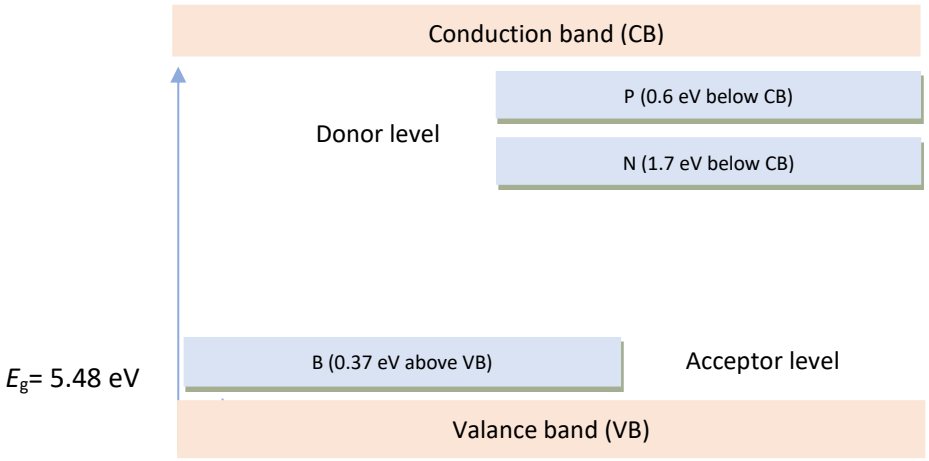

Figure 1-2 Energy diagram of some dopant states, such as phosphorus, boron and nitrogen in the bandgap of the diamond.

1.4.2 n-Type Doping

The driving force in diamond thin-film technology research is finding a suitable n-type diamond to produce an essential part of the p-n junction in electronic devices. Although n-type doping can be found naturally with nitrogen, the resulting deep level of the substitutional N prevents N-doped diamonds from finding an application as a standard n-type dopant in room-temperature devices.[52–55] Theoretical studies have proposed some other impurities to be potentially shallow donors, such as phosphorus in substitutional sites[56–58] analogous to phosphorus-doped n-type Si, and lithium in tetrahedral interstitial sites.[59–61] However, attempts using a variety of experimental methods have not yet produced successful n-type conductivities that meet the demands of diamond-based electronic applications.[57,59–66] The research to find an active n-type dopant is still ongoing, and many methods, such as ion implantation, diffusion, CVD growth and theoretical calculations, were investigated.

1.5 Doping Methods

1.5.1 In-diffusion

Besides *in-situ* doping during chemical vapour deposition using a gas source as a dopant, implantation and ion diffusion are commonly employed in the electronics production for the insertion of dopants into semiconductors to achieve the intended modifications in optical and electric properties. Diffusion causes less damage compared with ion implantation;

therefore, further annealing is not necessary. However, dopants with larger atomic radii are believed to be very difficult to diffuse in diamond, if not impossible. A few results on experimental diffusion were reported with elements such as Li, H, O, B and N.[67–73] Li attracted special interest as it, in theory, is expected to be a shallow donor in interstitial sites.[52,59–61,74,75] No diffusion was observed when Li was implanted into natural diamond crystals; in contrast, Li implanted into a polycrystalline diamond showed diffusivity into the diamond film with annealing up to 1400 °C for 1h[69], suggesting the diffusion mechanism was via the grain-boundaries. The diffusion of Li into natural diamond was also obtained from a layer of Li containing an external source, such as Li_2CO_3[71], Li_3N[76] and Li_2O[77], placed on the diamonds surface.[72,78] The low diffusion coefficients of Li calculated from the in-diffusion method, 10^{-15} cm^2 s^{-1} [76,72], showed general low solubility of Li in the diamond.

1.5.2 Ion Implantation

The high atomic density of the diamond lattice makes thermal diffusion of impurities very slow and not suitable for many dopants. The method of choice for doping the tightly bonded diamond crystal lattice is still ion implantation, especially with impurities with an atomic mass greater than carbon. This method can be used with almost all dopants and offers the best control of impurity depth distribution and levels. The independent size or solubility of the non-equilibrium ion implantation method gives the chance to force any possible dopant atom in the diamond.[79] However, the interaction between the diamond atoms and the high-energy ions can induce defects or amorphisation once the damage level exceeds a critical density[80,81] ~1×10^{22} vacancy cm^{-3} [82,83], independent of implantation ions and their energy. This is always accompanied by bond breakage and the formation of defects in the lattice that may minimise the real chemical effects of the dopant. Such defects may participate in creating a defect-related energy level within the diamond bandgap, giving rise to donor or acceptor states, or it may contribute to the formation of dopant defect clusters, which can passivate the dopant.

Knowledge about the primary interaction processes in this technique can be facilitated for a successful technological application. The recrystallisation of the lattice after thermal annealing observed with Si and Ge became more complex for diamonds because of its metastability with graphite. In an unirradiated sample, the diamond phase deformation can be prevented by controlling any annealing temperature to be lower than the ‘graphitisation’ threshold using sp^3 to sp^2 bond conversion.[84–87] This threshold is determined by different factors, including the annealing temperature, annealing environment (high vacuum, oxygen),

pressure and diamond type (single crystal, poly or nanocrystalline diamond). The radiation-induced defects can decrease the temperature threshold at which the phase transition can occur; therefore, most of the ion implantation features can be lost with the damage induced by radiation that cannot be removed entirely by post-implantation annealing methods. Also, it was found that this damage depends on a critical dose of ions, at which point the diamond structure transforms from crystalline to amorphous carbon.[80,88]

Based on the assumption that the defects induced by implantation are primarily comprised of vacancies and interstitial atoms and the fact that the generated damage in the diamond lattice is determined by the interactions between them[84], two ion implantation schemes have been used that are cold implantation rapid annealing (CIRA)[89,16] and low-damage drive-in (LODDI).[90,15] The procedures showed a very efficient when used with B ion implantation. CIRA is usually performed at low temperatures (using liquid nitrogen), at which the diffusion of the radiated defects is prevented, e.g., vacancies and self-interstitial, followed by a rapid thermal anneal (RTA). The cold-implanted substrate is rapidly heated to a temperature where the self-interstitials and implanted ions can be merged with vacancies and reduce residual damage. Thus, RTA prevents interstitial atoms from diffusion out of the implanted layer.

In the LODDI scheme, a vacancy-containing layer is produced by appropriate ion implantation /annealing schemes, such as He^{+} ions and the CIRA method. Then, the ions are implanted into a nearby layer such that they can merge with the vacancy-containing layer by diffusion.[91] The CIRA method developed for boron-doped diamonds was found to be an appropriate method for doping diamonds with nitrogen, showing that nearly 50% of the implanted N is located in substitutional sites after annealing.[92] However, this scheme did not show the same success with a large dopant like P ions. This was attributed to the large radiation damage induced by the P ions, which was approximately four times greater than that created by B ions. The vacancies diffused to the substitutional P ion, which caused relaxation and lowered the donor level. With low doses (nearly $8.875 \times l0^{9}$ cm^{-3}) of P ions implanted into diamond using CIRA implantation scheme followed by consecutive RTA to 500, 1200 and 1600 °C, the conductivity began to decrease gradually until disappearing after 1600 °C.[93]

1.7 Computational Chemistry

Computational chemistry is an effective integration of theoretical chemistry concepts into a computer program to solve chemical problems and predict a range of substance properties. Most codes used the Density-Functional Theory (DFT); the basic principle of which is that all the complicated electron paired correlations and motions in a many-body system are included in the total electron density. The theoretical foundations of DFT had been established by Hohenberg, Kohn, and Sham in 1964–1965[94,95], and became common for calculations since the 1970s. However, these foundations were not thought precise enough until the 1990s, when the model exchange and correlation interactions were improved through developed the approximations. Today, DFT computational codes, such as CASTEP and CRYSTAL, are used in practical modes to explore chemical structures and their energetic, magnetic, electronic and spectroscopic properties. The cost associated with modelling, time, disk space and memory, depending on the system being explored and the chosen parameters.

1.8 Theoretical background

1.8.1 The Many-Body Problem

To obtain all the information about a given system, it is necessary first to acquire the quantum mechanical wave equation. This can be done by solving the time-independent, nonrelativistic, Schrödinger equation, as follows:

$$\hat{H}\psi = E\psi \qquad 1\text{-}1$$

$$\hat{H}\,\psi_i\,(x_1, x_2, \ldots, x_N, R_1, R_2, \ldots, R_M) = E_i\,\psi_i\,(x_1, x_2, \ldots, x_N, R_1, R_2, \ldots, R_M), \quad (1\text{-}2) \qquad 1\text{-}2$$

In this equation ψ and $\hat{H}$ refer to the many-electron wave function and the Hamiltonian, respectively, and E the energy of the system containing of M nuclei and N electrons.

$$\widehat{H} = \frac{1}{2}\sum_{i=1}^{N}\nabla_i^2 - \frac{1}{2}\sum_{A}^{M}\frac{1}{M_A}\nabla_A^2 - \sum_{i=1}^{N}\sum_{A=1}^{M}\frac{Z_A}{r_{iA}} + \sum_{i=1}^{N}\sum_{j>i}^{N}\frac{1}{r_{ij}} + \sum_{A=1}^{M}\sum_{B>A}^{M}\frac{Z_A Z_B}{R_{AB}}. \quad 1\text{-}3$$

This equation assumes that no magnetic fields or external electrostatic fields are present, so the interaction between the particles is restricted only to the Coulomb interactions. Here, *i* and *j* are electrons, A and B are nucleus, *R* is the nuclei position, and *Z* is the charge on the nucleus. This equation can be divided into four parts: the first two parts are associated with the electron's "kinetic energy" and their nuclei, whereas the second part expresses the electrons and nuclei interaction; the third part expresses the electron-electron interactions, and the fourth represents nuclei-nuclei interactions. The Laplacian operator ∇_q^2 also described as the summation of differential operatives of Cartesian coordinates.

$$\nabla_q^2 = \frac{\partial^2}{\partial x_q^2} + \frac{\partial^2}{\partial y_q^2} + \frac{\partial^2}{\partial z_q^2}. \quad 1\text{-}4$$

Depend on the Born-Oppenheimer approximation, the nuclei are 10^3–10^5 times more massive than electrons; consequently, their "kinetic energy" contribution to the system energy can be considered zero, along with the constant potential energy generated as a result of repulsions between nuclei that can be neglected in equation (1-3) and rewritten as follows:

$$\widehat{H} = -\frac{1}{2}\sum_{i=1}^{N}\nabla_i^2 - \sum_{i=1}^{N}\sum_{A=1}^{M}\frac{Z_A}{r_{iA}} + \sum_{i=1}^{N}\sum_{j>i}^{N}\frac{1}{r_{ij}} = \widehat{\mathrm{T}} + \widehat{\mathrm{V}}_{Ne} + \widehat{\mathrm{V}}_{ee}. \quad 1\text{-}5$$

In the many-body problem, solving the Schrödinger equation consider impossible and very computationally costly due to two reasons: (i) the system contains many-electron wave functions that have 3*N* degrees of freedom, and (ii) the correlation of the electron-electron Coulomb interactions resulting from electronic motions. Incorporating the effects of this correlation hinders the treatment of the system as *N* single-body problems, and this, in turn, is a complicated mathematical task. Thus, approximations are needed to reformulate the Schrödinger equation for it to be solved numerically.

1.8.2 Hartree-Fock Methods

The Hartree-Fock (HF) method is the simplest approximation to solve the many-body Hamiltonian problem for electrons moving under a potential determined by other electrons and nucleus in the system to drive the ground energy. HF use an anti-symmetrised product (known as a Slater determinant, Φ_{SD}) of *N*-one-electron wave functions $\chi_i(\vec{x}_i)$ to approximate the *N*-electron wave function

$$\Phi_{SD} = \frac{1}{\sqrt{N_i}} \det\left(\{x_1(\vec{x}_1),\ x_2(\vec{x}_2), \ldots\ldots\ldots, x_N(\vec{x}_N)\}\right). \qquad 1\text{-}6$$

The spin orbitals $x(\vec{x})$ also known as one-electron functions consist of one spin function (either α(s) or β(s), equivalent to 'spin-up' and 'spin-down') and a spatial orbital $\phi(\vec{r})$.

$$x(\vec{x}) = \phi(\vec{r})\ \sigma(s) \qquad \sigma = \alpha, \beta \qquad 1\text{-}7$$

The spin orbitals are the only term that can vary in a Slater determinant to minimize the energy and attain the ground-state. Deriving the probability values of the Hamiltonian operator with a Slater element can provide the HF energy.

$$E_{HF} = \sum_{1}^{N} (i\,|\hat{h}|\,i) + \frac{1}{2}\sum_{i}^{N}\sum_{j}^{N} (ii|\frac{1}{r_{ij}}|jj) - (ij|\frac{1}{r_{ij}}|ji) \qquad 1\text{-}8$$

The first term $(i|\hat{h}|i)$ expresses the kinetic-energy contribution and the electron-ion potential, respectively, as follows:

$$(i|\hat{h}|i) = \int x^*(\vec{x}) \left\{ -\frac{1}{2}\nabla^2 - \sum_{1}^{N} \frac{z_A}{r_{1A}} \right\} x_i(\overrightarrow{x_1}) d\overrightarrow{x_1} \qquad 1\text{-}9$$

Regarding the last two terms, $(ii|jj)$ and $(ij|ji)$, the first represents the Coulomb integrals (Hartree term), which expresses the electrostatic potential generated from the electrons (N) charge distribution, counting an unphysical self-interaction of electrons. The second represents the integrals of the exchange that come from the Pauli principle (on electrons with the same spin**)** and the supposed Slater determinant form of the wave function.

Equation (1-8) show that the HF energy is a functional of the x_i. So, by introducing the physical interpretation of the orbital energies term (the Lagrangian multipliers, ε_i), one can be defined as the best spin orbitals that obtain the lowest E_{HF} value. This represents the Hartree-Fock equation as follows:

$$\hat{f}x_i = x_i\varepsilon_i \, , i = 1, 2, \dots, N. \qquad 1\text{-}10$$

The Fock operator $\hat{f}$ as a representation of one-electron operator as:

$$\hat{f}_i = -\frac{1}{2}\nabla^2 - \sum_{A}^{M}\frac{z_A}{r_{iA}} + V_{HF}(i). \qquad 1\text{-}11$$

The first and second parts represent the kinetic energy and the potential arising from the electron-nucleus interaction, respectively. Last part, $V_{HF}(i)$ refers to the average potential that an *i*-th electron encounters due to the other N-1 electrons that exist in the system (this term known as Hartree-Fock potential). The technique used to solve equation (1-10) is called the self-consistent field (SCF) method. It begins with a 'guessed' orbital's set, then solves the HF equation to generate a new orbital's set to use in the subsequent iteration. The iteration is continued until the input orbitals differ from the output by less than a pre-set threshold.

The Hartree-Fock approximation is perfect for a computer since it is easily written as an algorithm and matches with the conventional picture of a single-electron structure. For example, the distribution of the many-electrons is determined by the total of one-electron distribution. However, the E_{HF} is essentially always larger than the real energy of the system, E_0, and such difference is known as the correlation energy, which results from the repulsion of the electrons. In the Hartree-Fock scheme, only the average electrostatic interaction is counted; therefore, the electrons often close together, leading to an increase on electron-electron repulsion and E_{HF}.

Neglecting the correlation between electrons led to a poor picture of the electronic structure. Therefore, the Hartree-Fock theory is unsatisfactorily in reaching accurate quantitative predictions for many systems, although it can make qualitatively correct predictions in some materials. The development of techniques that define accurate correlations are considered an active study arena in quantum chemistry.

1.8.3 Density Functional Theory

The significant approach in quantum molecular dynamics simulations is DFT. This theory shows the exact representation of a many-body wave function problem through the density, which is a function of space and time[96–98]. In other words, it reformulates the energy of a system as a function of the electron density $\rho(\vec{r})$ to achieve a solution to the Schrödinger equation. Unlike the Hartree-Fock theory, which uses the many-body wave function directly, the atomic electron-density ground state is adopted in DFT as the fundamental property. Using DFT significantly improves the calculations and becomes very common in different disciplines, especially, in the solid-state physics. The many-body electronic wave function is a function of three spatial variables (Cartesian coordinates *x*, *y* and *z*), and one spin variable for each of the *N* electrons in the system. In comparison, the electron density is only a function of the three spatial variables.

1.8.3.1 Hohenberg-Kohn Theorem

The Hohenberg-Kohn theorem deals with a system of electrons that move under the influence of an external potential $V_{\text{ext}}(\vec{r}_1)$, which is in the theorem a unique functional of $\rho(\vec{r})$ in the ground state. Hence, all the properties of the system can obtain from the ground state electron density only. This theorem separates the energy into three individual components;(i) the potential energy arising from the attractions between nucleus and electrons $E_{\text{ne}}[\rho_0]$, which depends on the real system, (ii) kinetic energy, $T[\rho_0]$, and (iii) the electron-electron interaction, $E_{\text{ee}}[\rho]$.

$$E_0[\rho_0] = E_{\text{ne}}[\rho_0] + T[\rho_0] + E_{\text{ee}}[\rho_0]. \qquad 1\text{-}12$$

The last two terms in the above equation are independent of Z_A, the charges of the nuclei, *N*, the number of electrons, and R_A the position of the nuclei in space. The Hohenberg-Kohn functional $F_{\text{HK}}[\rho_0]$ is a universal function that is entirely independent of the system under study.

$$F_{\text{HK}}[\rho_0] = T[\rho_0] + E_{\text{ee}}[\rho_0]. \qquad 1\text{-}13$$

Hence, if the universal functional $F_{\text{HK}}[\rho_0]$ is known the exact total energy and ground-state electron density can be calculated. However, the Hohenberg-Kohn theorem just proven the known theorems that stated that ‘in principle’ the ground state energy and the ground state

density are related, without providing any direction regarding how the function should be constructed to deliver the ground-state energy.

1.8.3.2 Kohn and Sham Approach

After the contribution by Hohenberg and Kohn to find the ground state, Kohn and Sham (1965) proposed a method for how the $F_{\mathrm{HK}}[\rho_0]$ can be solved. They suggested calculating the main portion of the "kinetic energy" to a high level of accuracy for an artificial system 'a non-interacting reference system' with a set of orbitals. The concept of Kohn and Sham was that if the determination of the "kinetic energy" through an explicit functional was not approached, the focus should be on correctly computing as much of the real kinetic energy as possible, and then approximately dealing with the remainder. Starting from Hohenberg and Kohn's approach, the the $E_{\mathrm{ee}}[\rho_0]$ term in the universal functional $F[\rho]$ can be divided to two parts: the classical coulomb interaction $J[\rho(\vec{\mathrm{r}})]$ and the non-classical portion $E_{\mathrm{ncl}}[\rho(\vec{\mathrm{r}})$ that cause by exchange and correlation and self-interaction correction effects so that $F[\rho]$ can represent as follows:

$$F[\rho(\vec{\mathrm{r}})] = T[\rho(\vec{\mathrm{r}})] + J[\rho(\vec{\mathrm{r}})] + E_{\mathrm{ncl}}[\rho(\vec{\mathrm{r}})]. \qquad 1\text{-}14$$

The main problem in the above expression is that $J[\rho(\vec{\mathrm{r}})]$, the classical Coulomb interaction, is the only known term; the other two parts are unknown. To realise how Kohn and Sham dealt with this situation, recall the Hartree-Fock scheme where the *N* spin orbitals constructed the wave function (a single Slater determinant Φ_{SD}), so the HF approximation was the real wave function of *N*-electrons. Thus, Φ_{SD} represented the exact wave function of an untrue system consisting of non-interacting *N*-electrons. This system has no electron interactions via Coulomb repulsion, and the electrons move in an effective potential V_{HF}. Therefore, the Hamiltonian of this unreal system, which has a potential $V_{\mathrm{S}}(\vec{\mathrm{r}}_1)$ to distinguish this from $V_{\mathrm{HF,}}$ represented as

$$\hat{\mathrm{H}}_{\mathrm{S}} = -\frac{1}{2}\sum_{i}^{N}\nabla_i^2 + \sum_{i}^{N} V_{\mathrm{S}}(\vec{\mathrm{r}}_1) \qquad 1\text{-}15$$

To emphasise that these new terms are not the same as in the HF method, we will use φ instead of the spin-orbital, χ. This gives an equation similar to equations (1–10) and (1–11), represented as follows:

$$\hat{f}^{KS}\varphi_i = \varphi_i\varepsilon_i, \qquad 1\text{-}16$$

Where $\hat{f}^{KS}$ is an effective one-electron operator, represented as

$$\hat{f}^{KS} = -\frac{1}{2}\nabla^2 + V_S(\vec{r}). \qquad 1\text{-}17$$

Kohn and Sham proposed finding the universal functional $F[\rho]$ through calculating the exact kinetic energy of the reference system (T_S) that has zero interaction "non-real", in the same way as the interacted system (T) "real", using the same density. Because $T_S \neq T$, the universal functional can separate as following,

$$F[\rho(\vec{r})] = T_S[\rho(\vec{r})] + J[\rho(\vec{r})] + E_{XC}[\rho(\vec{r})]. \qquad 1\text{-}18$$

$J[\rho(\vec{r})]$ Is the classical Coulomb interaction (electrostatic energy of a charge distribution with itself). The last term is so-called exchange-correlation energy that contains everything that cannot be found exactly: it includes the effects of self-interaction correction, exchange and correlation, and a part related to kinetic energy.

$$E_{XC}[\rho] = (T[\rho] - T_S[\rho]) + (E_{ee}[\rho] - J[\rho]) = T_C[\rho] + E_{ncl}[\rho]. \qquad 1\text{-}19$$

The remaining portion of the real kinetic energy $T_C[\rho]$ is simply added to the non-classical electrostatic contributions due to exchange and correlation effects and self-interaction correction $E_{ncl}[\rho]$ to obtain the exchange-correlation energy$E_{XC}[\rho]$.

$$\left(-\frac{1}{2}\nabla^2 + \left[\frac{\rho(\vec{r}_2)}{r_{12}}d\vec{r}_2 + V_{XC}(\vec{r}_1) - \sum_A^M \frac{Z_A}{r_{1A}}\right]\right)\varphi_i = \left(-\frac{1}{2}\nabla^2 + V_{eff}(\vec{r}_1)\right)\varphi_i = \varepsilon_i\varphi_i. \qquad 1\text{-}20$$

$V_{XC}(\vec{r}_1)$ is the potential due to the exchange-correlation energy, E_{XC}. Thus, V_{eff} depends on the density, which in turn, depends on the orbitals through the Coulomb term. If one compares equation 1–20 with that of the non-interacting reference system, it will be found that

$V_{eff,}$ is equal to V_S in equation 1–17, which includes all the information needed to find the ground-state density and the ground-state energy. As with the Hartree-Fock equation (1–10), the Kohn-Sham one-electron equation (1–20) must also solve iteratively to minimise this energy expression.

It is worth mentioning that, in the KS approach, the approximation only serves to find the unknown functionals for the E_{XC} and the V_{XC}. Therefore, the main aim of DFT is finding the best approximations of these two terms. There is a range of XC-functionals that vary in theory level, from simple, such as local density approximation (LDA) and generalised gradient approximation (GGA), to hybrid theory levels.

1.8.4 The Restricted and Unrestricted Method

Pairing the even number of electrons in a system gives rise to doubly occupied orbitals and the system is called a closed-shell system, such as methane. However, not all systems with an even number of electrons have only doubly occupied orbitals. To clarify this point, recall the one-electron function (equation 1-7), known as spin-orbital $x(\vec{x})$:

$$x^{\uparrow}(\vec{x}) = \phi(\vec{r})\,\alpha\,(s) \qquad 1\text{-}21$$

And

$$x^{\downarrow}(\vec{x}) = \phi(\vec{r})\,\beta\,(s) \qquad 1\text{-}22$$

These two equations consist of different spin orbitals, $x(\vec{x})$, two spin functions α(s), β(s), and the same spatial orbital $\phi(\vec{r})$, known as the Restricted Hartree-Fock (RHF) method. This solution cannot describe a system with unpaired electrons (with an odd number of electrons), such as free radicals, or a system in which not all the electrons occupy pairwise (open-shell situations with an even number of electrons). For instance, when treating homolytic bond breaking with RHF, an H_2 molecule can only be dissociated to ions and not to two H atoms [96]. To solve this issue, it is allowed to differ spatial part, which provides the Unrestricted Hartree-Fock (UHF) method, as follows:

$$x^{\uparrow}(\vec{x}) = \phi^{\uparrow}(\vec{r})\,\alpha\,(s) \qquad 1\text{-}23$$

And

$$x^{\downarrow}(\vec{x}) = \phi^{\downarrow}(\vec{r})\,\beta\,(s) \qquad 1\text{-}24$$

In the UHF method, the α and β orbitals have different energies due to the differences in their spatial characteristics, as the α and β orbitals experience different potentials, HF_V^{α} and HF_V^{β}. In an analogy to the UHF approach, in KS, the unrestricted form of the functionals is commonly used which depend on the densities of α and β spins. Using the unrestricted spin functionals for the exchange and correlation can define a lot of critical point in the physics of the open-shell system compare with the restricted form.

1.8.5 Local Density Approximation (LDA)

The LDA model is based on the concept of a homogenous electron gas system, where all the electrons exist on a positive background charge. Hence, the system is electrically neutral, and $N/V = \rho$ gives a finite value, where the N and V are the number of electrons and the volume of the gas, respectively; N and V can have infinite values. Therefore, the ρ reaches a constant value at any point in the system. The uniform electron gas was chosen in DFT because the functional form of the exchange and correlation energy of this system is known to have very high accuracy. This model assumes that E_{XC} can be expressed in the following simple form:

$$E_{XC}^{LDA}[\rho] = \int \rho(\vec{r})\varepsilon_{XC}\big(\rho(\vec{r})\big)d\vec{r} \qquad 1\text{-}25$$

And

$$\varepsilon_{XC}\big(\rho(\vec{r})\big) = \varepsilon_X\big(\rho(\vec{r})\big) + \varepsilon_C\big(\rho(\vec{r})\big) \qquad 1\text{-}26$$

Here, ε_{XC} is the exchange-correlation energy per particle of a homogeneous electron gas of density $\rho(\vec{r})$ which consists of exchange $\varepsilon_X\big(\rho(\vec{r})\big)$ and correlation contributions $\varepsilon_C\big(\rho(\vec{r})\big)$. The $\varepsilon_X\big(\rho(\vec{r})\big)$ term is derived by Bloch [99] as follows:

$$\varepsilon_X\big(\rho(\vec{r})\big) = -\frac{3}{4}\sqrt[3]{\frac{3\rho(\vec{r})}{\pi}}. \qquad 1\text{-}27$$

The part $\varepsilon_C\big(\rho(\vec{r})\big)$ needs to be approximated, and many studies have introduced expressions for ε_C using complicated interpolation methods.

The approximate functionals typically add extra flexibility by representing an unrestricted form. In such form, instead of the electron density$\rho(\vec{r})$, there are $\rho_\alpha(\vec{r})$ and $\rho_\beta(\vec{r})$,

and $\rho_\alpha(\vec{r}) + \rho_\beta(\vec{r}) = \rho(\vec{r})$. Thus, equations 1–25 have two variables instead of one, giving what is known as a local spin-density approximation (LSD), as shown below.

$$E_{XC}^{LSD}[\rho_\alpha, \rho_\beta] = \int \rho(\vec{r})\varepsilon_{XC}\,(\rho_\alpha(\vec{r}), \rho_\beta(\vec{r}))d\vec{r}. \qquad 1\text{-}28$$

1.8.6 The Generalised Gradient Approximation (GGA)

The fundamental of the generalised gradient approximation (GGA) for the non-homogeneity of the actual electron density is enhances the density with details about the gradient of the charge density $\nabla\rho(\vec{r})$ without relying only on that delivered from the density at a specific point. This gives the GGA as follows:

$$E_{XC}^{GGA}[\rho_\alpha, \rho_\beta] = \int f(\rho_\alpha, \rho_\beta, \nabla_\alpha, \nabla_\beta)d\vec{r}. \qquad 1\text{-}29$$

As with the LDA, the GGA is usually divided into two contributions: exchange, E_X^{GGA}, and correlation, E_C^{GGA}. The approximations for the two terms are obtained separately. Examples of functionals correlated to this approach include the exchange functional, as suggested by Perdew, Burke, and Wang in 1996 (PW91)[100,101]; Perdew, Burke, and Ernzerhof in 1996 (PBE)[102]; and Yang and Parr in 1988 (LYP).[103]

1.8.7 Hybrid Functionals

Most of the calculations concluded that, in most cases, the effect of the exchange contribution was significantly larger than the corresponding correlation one (in absolute numbers). Because the exchange energy can be computed exactly, it is suggested that the approximation only be made on the portion unknown in the HF approach (the electron correlation).

$$E_{XC} = E_X^{exact} + E_C^{KS}. \qquad 1\text{-}30$$

This expression was developed further to obtain a better approximation through different approaches. For instance, inserting the LDA exchange-correlation functional in equation (1-30) gives what is known as a half-and-half (H&H) combination as presented by Becke (1993).[104–106]

$$E_{\mathrm{XC}}^{\mathrm{H\&H}} = \frac{1}{2}\left(E_{\mathrm{X}}^{\mathrm{exact}} + E_{\mathrm{X}}^{\mathrm{LDA}}\right) + \frac{1}{2}E_{\mathrm{C}}^{\mathrm{LDA}}. \qquad 1\text{-}31$$

Becke expanded this equation through the introduction of three constant parameters fitted against selected experimental thermochemical data, giving the following equation:

$$E_{\mathrm{XC}}^{\mathrm{B3}} = E_{\mathrm{XC}}^{\mathrm{LSD}} + a\left(E_{\mathrm{XC}}^{\lambda=0} - E_{\mathrm{X}}^{\mathrm{LSD}}\right) + bE_{\mathrm{X}}^{\mathrm{B}} + cE_{\mathrm{C}}^{\mathrm{PW91}}. \qquad 1\text{-}32$$

Here, *a*, *b*, and *c* are 0.20, 0.72, and 0.81, respectively. Introducing these three parameters in equation (1-31) leads to a good performance. Currently, the most common hybrid functional is B3LYP [96,107] (Becke, 3-parameter, Lee-Yang-Parr), where the PW91 correlation functional is replaced by the LYP functional and *a*, *b* and *c* are as above values.

$$E_{\mathrm{XC}}^{\mathrm{B3LYP}} = (1-a)E_{\mathrm{X}}^{\mathrm{LSD}} + aE_{\mathrm{XC}}^{\lambda=0} + bE_{\mathrm{X}}^{\mathrm{B88}} + cE_{\mathrm{C}}^{\mathrm{LYP}} + (1-c)E_{\mathrm{C}}^{\mathrm{LSD}} \qquad 1\text{-}33$$

1.8.8 Bloch's theorem

The correlated issue of the electrons within a solid is not the only problem in the calculations. The infinite number of valence electrons that contribute to bonding in a typical solid makes electronic structure calculations a complex problem. To simplify this problem to find the ground-state density, the periodicity of the unit cell in crystalline solids is considered. Each unit cell has the same ground-state electronic structure with the same charge distribution; therefore, the potential is periodic.

Bloch's theorem is the formalism for dealing with a periodic potential that states that the wave function of each electron has the form of a plane wave times a function with the periodicity of the lattice unit.

$$\psi_{nK}(r) = e^{ik.r}u_{nK}(r). \qquad 1\text{-}34$$

Here, $u_{nK}(r+R) = u_{nK}(r)$ is a function that has the periodicity of the potential, and the *n* is the n-*th* state associated with the wave vector *k*. *R* is a vector connecting the same point at two unit cells: *r* is the point within one unit cell, and *r* + *R* is the equivalent point within

another unit cell.[108], Therefore, Bloch's Theorem replaces the infinite number of electrons by only those in the unit cell using a pre-determined a finite number of *k*-points.

1.8.9 Basis set

The basis set define as a set of functions utilized to represent the electronic orbitals of the system to enable the calculation on a computer numerically. Two types of basis sets have been introduced within HF and DFT methods: plane-wave basis sets (PW), adopting a linear combination of plane waves, or a linear combination of local atomic orbitals (LCAO).

In the LCAO approach, a set of basic functions (η) linearly expand the Kohn-Sham orbitals. It is very important to choose the set of η such that the linear combination gives an approximation of the exact Kohn-Sham orbitals accurately. The almost universally chosen for η is the Cartesian Gaussian-type-orbitals, GTO which has the general form:

$$\eta^{\mathrm{GTO}}(x, y, z) = N x^{l} y^{m} z^{n} \exp\left[-\alpha r^{2}\right], \qquad 1\text{-}35$$

Where *N* is a normalisation constant, *x*, *y*, and *z* are Cartesian coordinates of the local atom centred, *r* is the radial distance to the atomic centre, and *l*, *m*, and *n* are positive integers that express the angular momentum of the orbital. The width of the orbital is controlled by α (large α gives tight function, small α gives diffuse function).

The smallest possible basis set is known as the minimal basis set, and it comprises one basis function constructed for each atomic orbital in the atom, including the unoccupied one. For example, carbon has five orbitals (1s, 2s, $2p_x$, $2p_y$, and $2p_z$), with one unoccupied ($2p_z$). The STO-3G basis is an example of the minimal basis set and is typically unable to provide highly precise results. To increase the performance of the basis set and achieve more flexibility in the representation of the atomic orbitals, it is necessary to add an extra basis function beside the lowest number required to describe each atom. Double zeta (DZ) basis sets apply a double-basis function onto a minimum basis set. For example, carbon atoms express ten functions. Similarly, there are also the triple zeta (TZ) and quadruple zeta (QZ) basis sets. Alternatively, a variation of the DZ set can be used in which the 1s orbital is represented by only a single function (one basis function per core atomic orbital) because a 1s orbital has a core electron that is less affected by the chemical environment. In this case, a carbon atom is expressed by nine functions and, this basis set is known as ‘double-zeta in the valence’ or ‘split-valence double zeta’, e.g., 6–31G. However, increasing the number of basic functions per atomic orbital

does not result in a good quality basis set. More flexibility is usually achieved by adding a high-angular-momentum basis function to enable polarisation, such as d functions for C atoms. These ‘polarisation functions’ enable each atom to form chemical bonds in any direction, e.g., 6–21G* and Triple-Zeta Valence with Polarization (TZVP).

The critical parameter in the plane-wave basis sets is the electronic “kinetic energy” cut-off. This parameter affects the quality of the calculations and the associated computational cost. High-value cut-off energy is required to increase the number of plane waves to describe the electronic wave functions precisely. The cut-off energy should be adjusted such that the convergence of the total energy become within the expected tolerance.

There is a range of computer programs that use either GTO or PW basis sets. GTO basis sets are commonly used in molecular simulations. They are embedded within a variety of codes, such as GAMESS-UK[109], GAMESS[110], Gaussian03[111], and TURBOMOLE[112], whereas, PW is more common in solid-state calculations with programs such as ABINIT[113], CASTEP[114], CPMD[115], and VASP.[116]

1.8.10 Pseudopotentials

Using a plane-wave basis set usually associated with an unpractical computational cost due to including all-electrons, core and valence, in the calculation, together with the full Coulombic potential of the nuclei. Therefore, using plane-wave basis sets are often combined with a pseudopotential or 'effective core potential'. The ‘pseudopotential’ attempts to express the potential arising from the nucleus and the core electrons, which do not contribute to bonding. In carbon, for example, the pseudopotential describes the nucleus and the 1s electrons. This partition of the electrons between valence and core states is possible because the valence electrons determine most physical properties of solids. In contrast, the core electrons are nearly independent of the environment.

1.9 Thesis Outline & Objectives

Despite various attempts to obtain useful n-type doping in diamonds to expand the range of diamond-based electronic devices, few studies go beyond the usual thinking of simple N defect and attempt to report co-doping of 2 or more dopants as a possible solution. Due to the high N content in diamond, utilising it effectively in co-doping system may be a strategy to activate the N defects.

In this thesis, various computational and experimental techniques will be used to study co-doping systems consist of Mg and N closely and a range of related defects. In the following chapters, we present in detail the experimental and theoretical methods used in the study, followed by the modelling of these point defects in diamond that are related to the project. We shall compare these results with those reported recently in the literature. The single Mg point defect and its multi-atom complex with N to form n-type MgN_3 point defect will be simulated with arrange of functionals, and the energy, charge, magnetic and electronic properties of the defect calculated. The ionisation energy investigation will allow the properties of the MgN_3 defect to be compared with the well-known n-type doped diamond; P. Different formation pathways will be explored to create a MgN_3 defect structure in a diamond. The calculations of IR spectroscopic features of two-point defects, MgN_2 and VN_2, will involve determining the main fingerprints that facilitate identifying these defects in experimental data. This is followed by a study of different experimental approaches to attempt to synthesise the MgN_3 defect in diamond, using a range of techniques to characterise the samples, in order to explore dopant incorporation and diffusion upon thermal annealing. Finally, the calculations will be enlarged to investigate the IR spectroscopic spectrum of a co-doping system consisting of a P and N pair in substitutional sites. Such a system is predicted experimentally and theoretically to passivate the n-type character of P-doped diamond.

1.10 References

1. Prokhorov, A. M. & Stefan, V. A. *Diamond Science and Technology, Vol. 1*. (Stefan University Press, 2002).
2. Angus, J. C. Diamond synthesis by chemical vapor deposition: The early years. *Diam. Relat. Mater.* **49**, 77–86 (2014).
3. Bundy, F., Hall, H., Strong, H. & Wentorf, R. Man-made diamonds. *Nature* **176**, 51–55 (1955).
4. Davies, G. *Diamond*. (CRC press, 1984).
5. Eversole, W. Canadian Patent 628,567, 1961. *US Patents* **3**, 187 (1962).
6. Derjaguin, B. V. *et al.* Filamentary diamond crystals. *J. Cryst. Growth* **2**, 380–384 (1968).

7. Angus, J. C., Will, H. A. & Stanko, W. S. Growth of diamond seed crystals by vapor deposition. *J. Appl. Phys.* **39**, 2915–2922 (1968).

8. Spitsyn, B. V., Bouilov, L. L. & Derjaguin, B. V. Vapor growth of diamond on diamond and other surfaces. *J. Cryst. Growth* **52**, 219–226 (1981).

9. Fedoseev, D. V., Uspenskaya, K. S., Varnin, V. P. & Vnukov, S. P. Effect of hydrogen on diamond growth from a gaseous phase. *Bull. Acad. Sci. USSR Div. Chem. Sci.* **27**, 1088–1091 (1978).

10. Matsumoto, S., Sato, Y., Tsutsumi, M. & Setaka, N. Growth of diamond particles from methane-hydrogen gas. *J. Mater. Sci.* **17**, 3106–3112 (1982).

11. Matsumoto, S., Sato, Y., Kamo, M. & Setaka, N. Vapor Deposition of Diamond Particles from Methane. *Jpn. J. Appl. Phys.* **21**, L183–L185 (1982).

12. Kamo, M., Sato, Y. & Setaka, N. Gas phase synthesis of diamond in microwave plasma. *Nippon Kagaku Kaishi* **10**, 1642–1647 (1984).

13. Spear, K. E. & Dismukes, J. P. *Synthetic Diamond: Emerging CVD Science and Technology*. (John Wiley & Sons, 1994).

14. Field, J. E. *The properties of natural and synthetic diamond*. (Academic Press, 1992).

15. Neves, A. & Nazar, M. *Properties, Growth and Applications of Diamond*. (IET, 2001).

16. Dresselhaus, M. S. & Kalish, R. *Ion implantation in diamond, graphite and related materials*. (Springer Science & Business Media, 2013).

17. Pan, L. S. & Kania, D. R. *Diamond: Electronic Properties and Applications*. (Springer Science & Business Media, 2013).

18. Ekimov, E. *et al.* Superconductivity in diamond. *Nature* **428**, 542–545 (2004).

19. Bundy, F. P., Bovenkerk, H. P., Strong, H. M. & Wentorf, R. H. Diamond-graphite equilibrium line from growth and graphitization of diamond. *J. Chem. Phys.* **35**, 383–391 (1961).

20. Bundy, F. P. Direct conversion of graphite to diamond in static pressure apparatus. *J. Chem. Phys.* **38**, 631–643 (1963).

21. Busch, J. V, Dismukes, J. P., Nallicheri, N. V & Walton, K. R. Economic assessment of

HPHT diamond synthesis technology. in *Materials Science Monographs* 623–633 (Elsevier, 1991).

22. Kamo, M., Sato, Y., Matsumoto, S. & Setaka, N. Diamond synthesis from gas phase in microwave plasma. *J. Cryst. Growth* **62**, 642–644 (1983).

23. Mokuno, Y. *et al.* High rate homoepitaxial growth of diamond by microwave plasma CVD with nitrogen addition. *Diam. Relat. Mater.* **15**, 455–459 (2006).

24. Yan, C. S., Vohra, Y. K., Mao, H. K. & Hemley, R. J. Very high growth rate chemical vapor deposition of single-crystal diamond. *Proc. Natl. Acad. Sci. U. S. A.* **99**, 12523–12525 (2002).

25. May, P. W. Diamond thin films: a 21st-century material. *Philos. Trans. R. Soc. London* **358**, 473–95 (2000).

26. Klages, C. P. & Schäfer, L. *Hot-Filament Deposition of Diamond*. *Low-Pressure Synthetic Diamond* (Springer, 1998).

27. Peng, X. L. & Clyne, T. W. Formation and adhesion of hot filament CVD diamond films on titanium substrates. *Thin Solid Films* **293**, 261–269 (1997).

28. Buchkremer-Hermanns, H., Ren, H., Utsch, J. & Weiss, H. Optimization of MW-PACVD diamond deposition parameters for high nucleation density and growth rate on Si3N4 substrate. *Diam. Relat. Mater.* **6**, 411–416 (1997).

29. Buijnsters, J. G., Van Bouwelen, F. M., Schermer, J. J., Van Enckevort, W. J. P. & Ter Meulen, J. J. Chemical vapour deposition of diamond on nitrided chromium using an oxyacetylene flame. *Diam. Relat. Mater.* **9**, 341–345 (2000).

30. Golding, B., Bednarski-Meinke, C. & Dai, Z. Diamond heteroepitaxy: Pattern formation and mechanisms. *Diam. Relat. Mater.* **13**, 545–551 (2004).

31. Whitfield, M. D., Savage, J. A. & Jackman, R. B. Nucleation and growth of diamond films on single crystal and polycrystalline tungsten substrates. *Diam. Relat. Mater.* **9**, 262–268 (2000).

32. Liu, H. & Dandy, D. S. Studies on nucleation process in diamond CVD: An overview of recent developments. *Diam. Relat. Mater.* **4**, 1173–1188 (1995).

33. Mallika, K. & Komanduri, R. Low pressure microwave plasma assisted chemical vapor

deposition (MPCVD) of diamond coatings on silicon nitride cutting tools. *Thin Solid Films* **396**, 146–166 (2001).

34. Degutis, G. *et al.* CVD diamond growth from nanodiamond seeds buried under a thin chromium layer. *Diam. Relat. Mater.* **64**, 163–168 (2016).

35. Das, D. & Singh, R. N. A review of nucleation, growth and low temperature synthesis of diamond thin films. *Int. Mater. Rev.* **52**, 29–64 (2007).

36. Mitsuda, Y., Kojima, Y., Yoshida, T. & Akashi, K. The growth of diamond in microwave plasma under low pressure. *J. Mater. Sci.* **22**, 1557–1562 (1987).

37. Mendes De Barros, R. C. *et al.* Dispersion liquid properties for efficient seeding in CVD diamond nucleation enhancement. *Diam. Relat. Mater.* **5**, 1323–1332 (1996).

38. Ralchenko, V. *et al.* Nanodiamond Seeding for Nucleation and Growth of CVD Diamond Films. in *Synthesis, Properties and Applications of Ultrananocrystalline Diamond* 109–124 (2005).

39. Hao, T. & Shi, C. Study on enhancement of diamond nucleation on fused silica substrate by ultrasonic pretreatment. *Diam. Relat. Mater.* **13**, 465–472 (2004).

40. Lee, S. T., Lin, Z. & Jiang, X. CVD diamond films: nucleation and growth. *Mater. Sci. Eng. R Reports* **25**, 123–154 (1999).

41. Rotter, S. Z. & Madaleno, J. C. Diamond CVD by a combined plasma pretreatment and seeding procedure. *Chem. Vap. Depos.* **15**, 209–216 (2009).

42. Yugo, S., Kanai, T., Kimura, T. & Muto, T. Generation of diamond nuclei by electric field in plasma chemical vapor deposition. *Appl. Phys. Lett.* **58**, 1036–1038 (1991).

43. Mortet, V. *et al.* Characterization of boron doped diamond epilayers grown in a NIRIM type reactor. *Diam. Relat. Mater.* **17**, 1330–1334 (2008).

44. Nishimura, K., Das, K. & Glass, J. T. Material and electrical characterization of polycrystalline boron-doped diamond films grown by microwave plasma chemical vapor deposition. *J. Appl. Phys.* **69**, 3142–3148 (1991).

45. Lagrange, J. P., Deneuville, A. & Gheeraert, E. Activation energy in low compensated homoepitaxial boron-doped diamond films. *Diam. Relat. Mater.* **7**, 1390–1393 (1998).

46. Visser, E. P. *et al.* Electrical conduction in homoepitaxial, boron-doped diamond films.

J. Phys. Condens. Matter **4**, 7365–7376 (1992).

47. Malta, D. M., Von Windheim, J. A., Wynands, H. A. & Fox, B. A. Comparison of the electrical properties of simultaneously deposited homoepitaxial and polycrystalline diamond films. *J. Appl. Phys.* **77**, 1536–1545 (1995).

48. Lagrange, J. P., Deneuville, A. & Gheeraert, E. Large range of boron doping with low compensation ratio for homoepitaxial diamond films. *Carbon.* **37**, 807–810 (1999).

49. Kalish, R. *Ion implantation in diamond; damage, annealing and doping*. (The Physics of Diamond (A. Paoletti and A. Tucciarone, eds.), 1997).

50. Kalish, R. Doping of diamond. *Carbon.*. **37**, 781–785 (1999).

51. Bourgeois, E., Bustarret, E., Achatz, P., Omnès, F. & Blase, X. Impurity dimers in superconducting B-doped diamond: Experiment and first-principles calculations. *Phys. Rev. B - Condens. Matter Mater. Phys.* **74**, 1–8 (2006).

52. Kajihara, S. A., Antonelli, A., Bernholc, J. & Car, R. Nitrogen and potential n-type dopants in diamond. *Phys. Rev. Lett.* **66**, 2010–2013 (1991).

53. Ferrari, A. M., Salustro, S., Gentile, F. S., Mackrodt, W. C. & Dovesi, R. Substitutional nitrogen atom in diamond. A quantum mechanical investigation of the electronic and spectroscopic properties. *Carbon.*. **134**, 354–365 (2018).

54. Lombardi, E. B., Mainwood, A., Osuch, K. & Reynhardt, E. C. Computational models of the single substitutional nitrogen atom in diamond. *J. Phys. Condens. Matter* **15**, 3135–3149 (2003).

55. Rohrer, E., Graeff, C. F. O., Janssen, R., Nebel, C. E. & Stutzmann, M. Nitrogen-related dopant and defect states in CVD diamond. *Phys. Rev. B* **54**, 90 (1996).

56. Wang, L. G. & Zunger, A. Phosphorus and sulphur doping of diamond. *Phys. Rev. B - Condens. Matter Mater. Phys.* **66**, 1–4 (2002).

57. Miyazaki, T. & Yamasaki, S. Ab initio energetics of phosphorus related complex defects in synthetic diamond. *Phys. B Condens. Matter* **376**–**377**, 304–306 (2006).

58. Goss, J. P., Briddon, P. R., Jones, R. & Sque, S. Donor and acceptor states in diamond. *Diam. Relat. Mater.* **13**, 684–690 (2004).

59. Goss, J. P. & Briddon, P. R. Theoretical study of Li and Na as n -type dopants for

diamond. *Phys. Rev. B - Condens. Matter Mater. Phys.* **75**, 1–9 (2007).

60. Lombardi, E. B., Mainwood, A. & Osuch, K. Ab initio study of lithium and sodium in diamond. *Phys. Rev. B - Condens. Matter Mater. Phys.* **76**, 1–8 (2007).

61. Lombardi, E. B. & Mainwood, A. A first principles study of lithium, sodium and aluminum in diamond. *Diam. Relat. Mater.* **17**, 1349–1352 (2008).

62. Jones, R., Lowther, J. E. & Goss, J. Limitations to n-type doping in diamond: The phosphorus-vacancy complex. *Appl. Phys. Lett.* **69**, 2489–2491 (1996).

63. Kalish, R. The search for donors in diamond. *Diam. Relat. Mater.* **10**, 1749–1755 (2001).

64. Katagiri, M., Isoya, J., Koizumi, S. & Kanda, H. Lightly phosphorus-doped homoepitaxial diamond films grown by chemical vapor deposition. *Appl. Phys. Lett.* **85**, 6365–6367 (2004).

65. Koizumi, S., Teraji, T. & Kanda, H. Phosphorus-doped chemical vapor deposition of diamond. *Diam. Relat. Mater.* **9**, 935–940 (2000).

66. Hofsäss, H. *et al.* Lattice sites of ion implanted Li in indium antimonide. *Nucl. Inst. Methods Phys. Res. B* **85**, 468–473 (1994).

67. Popovici, G., Sung, T., Khasawinah, S., Prelas, M. A. & Wilson, R. G. Forced diffusion of impurities in natural diamond and polycrystalline diamond films. *J. Appl. Phys.* **77**, 5625–5629 (1995).

68. Popovici, G. *et al.* Properties of diffused diamond films with n-type conductivity. *Diam. Relat. Mater.* **4**, 877–881 (1995).

69. Cytermann, C., Brener, R. & Kalish, R. Search for diffusion of Li implants in natural and polycrystalline CVD diamond. *Diam. Relat. Mater.* **3**, 677–680 (1994).

70. Othman, M. Z., May, P. W., Fox, N. A. & Heard, P. J. Incorporation of lithium and nitrogen into CVD diamond thin films. *Diam. Relat. Mater.* **44**, 1–7 (2014).

71. Popovici, G., Wilson, R. G., Sung, T., Prelas, M. A. & Khasawinah, S. Diffusion of boron, lithium, oxygen, hydrogen, and nitrogen in type IIa natural diamond. *J. Appl. Phys.* **77**, 5103–5106 (1995).

72. Uzan-Saguy, C. *et al.* Diffusion of lithium in diamond. *Phys. Status Solidi Appl. Res.* **193**, 508–516 (2002).

73. Okumura, K., Mort, J. & Machonkin, M. Lithium doping and photoemission of diamond thin films. *Appl. Phys. Lett.* **57**, 1907–1909 (1990).

74. Bernholc, J., Kajihara, S. A., Wang, C., Antonelli, A. & Davis, R. F. Theory of native defects, doping and diffusion in diamond and silicon carbide. *Mater. Sci. Eng. B* **11**, 265–272 (1992).

75. Anderson, A. B. & Mehandru, S. P. N-type dopants and conduction-band electrons in diamond: Cluster molecular-orbital theory. *Phys. Rev. B* **48**, 4423–4427 (1993).

76. Halliwell, S. C., May, P. W., Fox, N. A. & Othman, M. Z. Investigations of the co-doping of boron and lithium into CVD diamond thin films. *Diam. Relat. Mater.* **76**, 115–122 (2017).

77. J. te Nijenhuis, G.Z. Cao, P.C.H.J Smits, W.J.P. van Enckevort, L.J. Giling, P.F.A Alkemade, M. Nesladek, Z. R. Incorporation of lithium in single crystal diamond: diffusion profiles and optical and electrical properties. *Diam. Relat. Mater.* **6**, 1726–1732 (1997).

78. Shaanan, M. & Kalish, R. Simulation of SIMS measurements of light element profiles in diamond. *Nucl. Instruments Methods Phys. Res. Sect. B Beam Interact. with Mater. Atoms* **171**, 332–341 (2000).

79. Kalish, R. Ion beam modification of diamond. *Diam. Relat. Mater.* **2**, 621–633 (1993).

80. Prawer, S., Uzan-Saguy, C., Braunstein, G. & Kalish, R. Can n-type doping of diamond be achieved by Li or Na ion implantation? *Appl. Phys. Lett.* **63**, 2502–2504 (1993).

81. Kalish, R. & Prawer, S. Graphitization of diamond by ion impact: Fundamentals and applications. *Nucl. Inst. Methods Phys. Res. B* **106**, 492–499 (1995).

82. Orwa, J. O., Nugent, K. W., Jamieson, D. N. & Prawer, S. Raman investigation of damage caused by deep ion implantation in diamond. *Phys. Rev. B - Condens. Matter Mater. Phys.* **62**, 5461–5472 (2000).

83. Uzan-Saguy, C. *et al.* Damage threshold for ion-beam induced graphitization of diamond. *Appl. Phys. Lett.* **67**, 1194 (1995).

84. Prins, J. F. Ion implantation of diamond for electronic applications. *Semicond. Sci. Technol.* **14**, S27 (2003).

85. Nebel, C. E. *et al.* Structure and properties of high-temperature annealed CVD diamond. *Diam. Relat. Mater.* **12**, 1873–1876 (2003).

86. Nistor, L. *et al.* Formation of Amorphous Carbon and Graphite in CVD Diamond upon Annealing: A HREM, EELS, Raman and Optical Study. *Phys. Status Solidi Appl. Res.* **186**, 207–214 (2001).

87. Wang, J. B. & Yang, G. W. Phase transformation between diamond and graphite in preparation of diamonds by pulsed-laser induced liquid-solid interface reaction. *J. Phys. Condens. Matter* **11**, 7089–7094 (1999).

88. Prawer, S., Hoffman, A. & Kalish, R. Ion beam induced conductivity in chemically vapor deposited diamond films. *Appl. Phys. Lett.* **57**, 2187–2189 (1990).

89. Fontaine, F., Uzan-Saguy, C., Philosoph, B. & Kalish, R. Boron implantation / in situ annealing procedure for optimal p -type properties of diamond. *Appl. Phys. Lett.* **68**, 2264–2266 (1996).

90. Prins, J. F. Doping of diamond by the diffusion of interstitial atoms into layers containing a low density of vacancies. *Diam. Relat. Mater.* **7**, 545–549 (1998).

91. Prins, J. F. Ion implantation and diamond: some recent results on growth and doping. *Thin Solid Films* **212**, 11–18 (1992).

92. Kalish, R. *et al.* Nitrogen doping of diamond by ion implantation. *Diam. Relat. Mater.* **6**, 516–520 (1997).

93. Johan F.Prins. Ion-implanted n-type diamond: electrical evidence. *Diam. Relat. Mater.* **4**, 580–585 (1995).

94. Hohenberg, P. & Kohn, W. Inhomogeneous electron gas. *Phys. Rev.* **136**, B864 (1964).

95. Kohn, W. & Sham, L. J. No Title. *Phys. Rev.* **140**, A1133 (1965).

96. Stanton, J. F. *A Chemist's Guide to Density Functional Theory*. *Journal of the American Chemical Society* **123**, (2001).

97. Sholl, D. & Steckel, J. A. *Density Functional Theory: A Practical Introduction*. (John Wiley & Sons, 2011).

98. Tsuneda, T. *Density Functional Theory in Quantum Chemistry*. (Springer Science & Business Media, 2014).

99. Dirac, P. A. M. Note on Exchange Phenomena in the Thomas Atom. *Math. Proc. Cambridge Philos. Soc.* **26**, 376–385 (1930).

100. Perdew, J. P. *et al.* Atoms, molecules, solids, and surfaces: Applications of the generalized gradient approximation for exchange and correlation. *Phys. Rev. B* **48**, 4978 (1993).

101. Perdew, J. P., Burke, K. & Wang, Y. Generalized gradient approximation for the exchange-correlation hole of a many-electron system. *Phys. Rev. B* **54**, 16533 (1996).

102. Perdew, J. P., Burke, K. & Ernzerhof, M. Generalized gradient approximation made simple. *Phys. Rev. Lett.* **77**, 3865 (1996).

103. Lee, Chengteh and Yang, Weitao and Parr, R. G. Development of the Colle-Salvetti correlation-energy formula into a functional of the electron density. *Phys. Rev. B* **37**, 785 (1988).

104. A.D. Becke. Becke's three parameter hybrid method using the LYP correlation functional. *J. Chem. Phys.* **98**, 5648–5652 (1993).

105. Becke, A. D. Density-functional exchange-energy approximation with correct asymptotic behavior. *Phys. Rev. A* **38**, 3098 (1988).

106. Lee, C and Yang, W and Parr, R. Density-functional exchange-energy approximation with correct asymptotic behaviour. *Phys. Rev. B* **37**, 785–789 (1988).

107. Stephens, P. J., Devlin, F. J., Chabalowski, C. F. & Frisch, M. J. Ab Initio calculation of vibrational absorption and circular dichroism spectra using density functional force fields. *J. Phys. Chem.* **98**, 11623–11627 (1994).

108. O'Reilly, E. *Quantum Theory of Solids*. (CRC press, 2003).

109. Guest, M. F. *et al.* The GAMESS-UK electronic structure package: Algorithms, developments and applications. *Mol. Phys.* **103**, 719–747 (2005).

110. Schmidt, M. W. *et al.* General atomic and molecular electronic structure system. *J. Comput. Chem.* **14**, 1347–1363 (1993).

111. Frisch, M. J. *et al.* Gaussian 03; Gaussian, Inc. *Wallingford. CT* **6492**, (2004).

112. Ahlrichs, R., Bär, M., Häser, M., Horn, H. & Kölmel, C. Electronic structure calculations on workstation computers: The program system turbomole. *Chem. Phys.*

Lett. **162**, 165–169 (1989).

113. Johannesen, E., Hvingel, C., Aschan, M. & Bogstad, B. Survey based estimation of consumption: spatial and seasonal aspects of cod predation on shrimp. *NAFA SCR Document* **07/80**, 17 (2007).

114. Segall, M. D. *et al.* First-principles simulation: Ideas, illustrations and the CASTEP code. *J. Phys. Condens. Matter* **14**, 2717–2744 (2002).

115. Andreoni, W. & Curioni, A. New advances in chemistry and materials science with CPMD and parallel computing. *Parallel Comput.* **26**, 819–842 (2000).

116. Kresse, G. & Furthmüller, J. Efficiency of ab-initio total energy calculations for metals and semiconductors using a plane-wave basis set. *Comput. Mater. Sci.* **6**, 15–50 (1996).

CHAPTER 2

EXPERIMENTAL TECHNIQUES AND METHODS

CHAPTER 2 – EXPERIMENTAL TECHNIQUES AND METHODS

2.1 Introduction

This chapter describes the experimental techniques used to prepare and characterise the samples in the present study. The theories behind these techniques and the practices that describe how they are used are discussed in detail.

2.2 Materials Preparation

2.2.1 Hot Filament Chemical Vapour Deposition (HFCVD)

A custom-built hot filament reactor (Figure 2.1, 2.2) was used to grow the diamond.[1] The reactor consisted of a gas system, a vacuum chamber, and pressure and heater controllers. The setup procedure began by cutting a tantalum filament with 0.25-mm diameter (Advent Research Material Ltd) into three equal pieces of approximately 10 cm each. Tantalum wires were used due to their relatively low cost compared to other filament types, e.g., rhenium, and they were replaced with each new growth. Three identical filaments were threaded in parallel between two parallel, hollow, stainless-steel filament holders (c). Then, the wires were each (a) attached to a spring (b) at one of the filament holders (c), and at the other holder, they were held by a screw-clamp (d). In this way, the springs accommodated the filaments' expansion during growth and kept the filaments rigid and straight. The three springs were enclosed in a small stainless-steel tube to protect them from the reactive gases inside the chamber, as well as acting as heat shields to prevent the springs from losing their elasticity. The filament wires were connected electrically in parallel, and then to electrical feedthrough on the lid of the reactor. DC power supply were used to heate the filaments by passing 25 A through them, which required a voltage of ~10 V.

The sample stage was positioned ~3 mm under the constructed filaments. The stage was made from three layers: a thin Mo upper plate, an Ni/Cr wire coil electrically insulated with ceramic beads, and a thick stainless-steel baseplate (e, f and g, respectively). The Mo plate protected the Ni/Cr coil from the harsh environment inside the chamber and helped to diffuse the heat from the heated Ni/Cr wire uniformly across the plate. The size of the Mo plate had space for only two substrates at the same time, each with dimensions of 10×10 mm (h). The Ni/Cr resistance wires were connected to electrical feedthrough on the chamber lid and were

heated by passing a current of 4 A from a DC power supply through them. This heat was then transferred to the Mo plate and from there into the substrate.

.

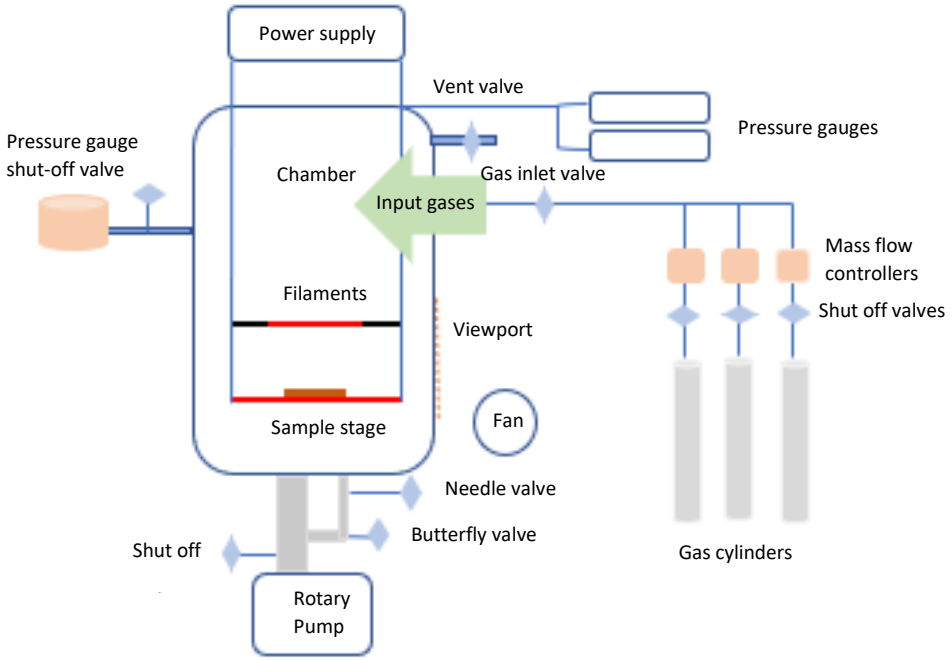

Figure 2-1 Schematic diagram of the component's hot filament CVD reactor.

After setting up the filaments and placing the prepared substrate on the Mo plate, the flange that holds both the sample stage and the filament was carefully inserted into the stainless-steel chamber, which was closed tightly by three bolts. The chamber was attached to a rotary pump (Leybold Vacuum GMBH, D10E) by thick and thin pipes in parallel to control the pressure inside the chamber. For fast, efficient pump-down, pumping occurred through the thick pipes, which had high gas conductance. But for accurate process pressure control, the thick pipe was closed off, and pumping occurred only via the thin pipe, which could be further throttled by closing a manual needle valve. For pump-down, the air inlet valve used to vent the chamber was tightly closed, while the valves connected to the thick and thin pipes and the needle valve under the chamber were all opened for maximum pumping rate. The time required to attain the base pressure of 10^{-2} torr depended on the period for which the chamber had been left open and varied from 30 min to 2 h. There were two pressure gauges attached to a side-arm on the chamber, and which were protected from pressure jumps when pumping down from atmosphere or venting via a shut-off isolation valve. The first pressure gauge was a Pirani which was used for measuring pressures in the range 1 mtorr-1 torr, *i.e.* for base-pressure

readings and leak checking. The second was a Baratron (capacitance manometer) that operated from 1-100 torr and was used to monitor the process pressure.

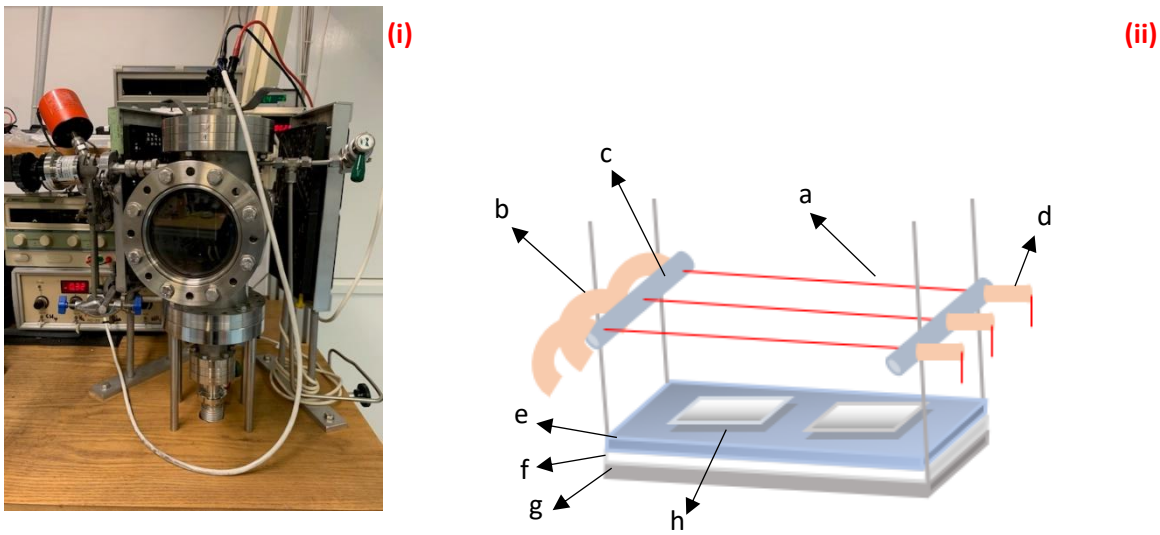

Figure 2-2 A photograph of the hot filament CVD reactor home-built at Bristol University (i), and a diagram of sample stage parts (ii).

When the base pressure was attained, the substrate heater was turned on, and the DC current was adjusted to 4 A and left for approximately 45 minutes to heat the substrate. This was crucial to outgas any water vapour and desorb any oxygen-containing adsorbates that may have entered the chamber when it was open to the atmosphere. If this was not done, or the heating time reduced to <30 mins, the filaments would react with any residual oxygen in the chamber and break – usually within a few seconds of turning them on. The fans were turned on to cool the chamber surface from the outside.

The flow rate of each gas was set and monitored by individual mass flow controllers (MFCs) (Tylan, FC260 for CH_3, H_2 and MKS for NH_3). These MFCs automatically controlled the flow of each gas during growth (in standard cubic cm, per minute (sccm)). Then, the valves attached to each gas cylinder were opened to start the flow. The gas cylinders (CH_4 gas (99.99%) and H_2 gas (99.99%), Air Liquide, Ltd) with regulators were stored in cabinets and were linked to the reactor using stainless-steel pipes. The NH_3 gas came in a lecture bottle, (Sigma-Aldrich, 10% diluted in hydrogen).

After opening the gases, the pumping valve attached to the thick pipe was closed, and pumping was achieved via the thin pipe. The exhaust gases were diluted 1000 times with air before being expelled from the building. The pressure inside the chamber was adjusted to 20 torr by manually closing the needle valve. Finally, growth was initiated by gradually turning

on the filament power supply to 25 A. This caused the three filaments to glow dazzling white-hot, so a dark plastic screen was needed to cover the viewport. Because the process gas mixture contained methane, the hot Ta filaments gradually carburised (converted into TaC) over a few hours. This process changed the electrical resistance of the filaments, and so the current had to be manually adjusted back to 25 A every 30 mins or so throughout the deposition run. After about 3 h of growth, the filaments had almost completely converted to TaC and become brittle and fragile. This was why new filaments were required for each new deposition run.

After finishing the deposition, the shut-down process was started by turning off the mass flow controllers for CH_4 and NH_3 gases and closing the gas source valves, leaving only the hydrogen gas running for H-termination purposes for five minutes. The filament power supply was gradually decreased to 0 A, and then switched off, and the substrate heater power supplies were also switched off. The H_2 gas mass flow controller was the switched off and the source gas valve closed. The needle valve and pump-down valves were opened to pump the chamber back to base pressure for thirty minutes, allowing time for the chamber contents to cool down. The venting starts by closing all the pumping valves, the needle valve, the mfc isolation valves, and the pressure gauge valve. The vent valve is opened gradually allowing air to enter the chamber, bringing it up to atmospheric pressure over about 1-2 min. The lid was then unbolted, and the sample holder removed from the chamber. After removing the sample from the substrate stage, the holder is inserted back into the chamber to start the pumping-down process as described above.

Since it is well acknowledged that different growth conditions will greatly affect the diamond film, optimising and benchmarking these conditions is of importance before any doping experiments can begin. Figure 2.3 shows the Raman and SEM measurements of a pure diamond grown on two types of substrates – silicon (Si) and polycrystalline diamond (PCD) – under the previous adjusted conditions and by flowing 200 standard cubic cm per minute (sccm) of H_2 and 2 sccm of CH_3 (0.81% CH_4/H_2) gases. The narrow single Raman peak demonstrates the resulting good microcrystalline diamond quality at 1,332 cm^{-1}, which is characteristic of the extended C sp^3 structure in diamond. [2]

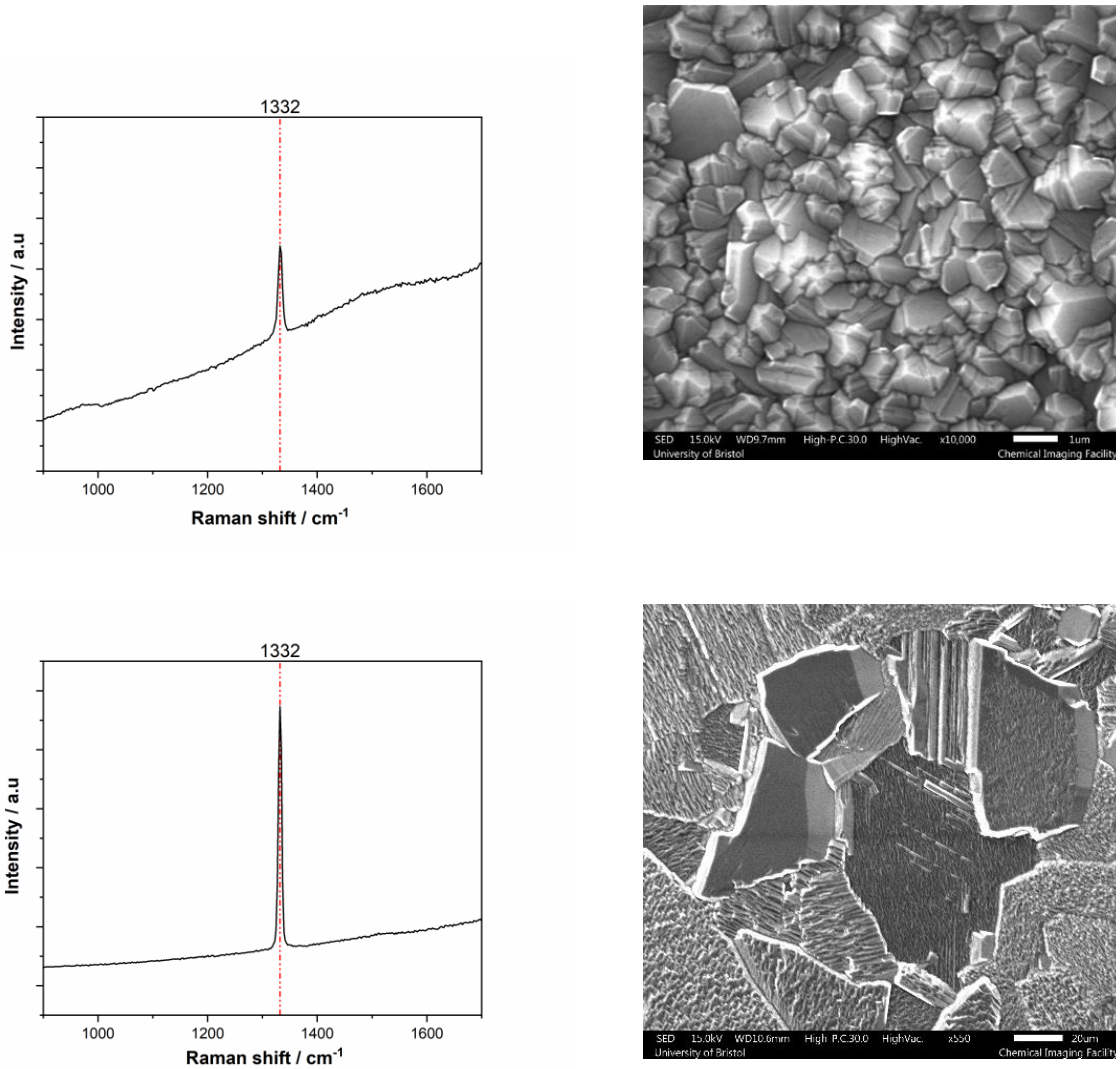

Figure 2-3 In the top panel, the Raman spectra taken with 520-nm wavelength excitation and an SEM image of undoped diamond film grown on a silicon substrate (Si). The lower panel refers to the corresponding data for a film grown on a polycrystalline diamond substrate (PCD)

2.2.2 Ion Implantation

Ion implantation is a low-temperature high-vacuum method. It uses ions of one element for implantation into a sample through electrostatic acceleration, leading to changes in their properties. The energy of the ions can be lost through interaction primarily with the electrons in the substrate, which slow down the ions, causing what is known as an "Electronic stopping" or the conversion to a "Nuclear stopping" as a result of the interaction directly with the nuclei of the substrate. [3]

In the case of high ion energy, the overall energy transferred to electrons will be very low - insufficient to displace any carbon atoms from their lattice sites. This is because the high

velocity of ions gives a short time for interaction with the atom electrons. Implantation occurs only with nuclear stopping process and is more efficient at a low ion energy, ~ tens of keV. The implanted ion eventually loses all its "kinetic energy" in collisions, and remains inside the substrate, either in an interstitial or substitutional site. If the "kinetic energy" transferred to a lattice atom overcomes its displacement energy, this will displace an atom from its lattice site, which, in turn, may have high "kinetic energy" and cause further displacements throw interact with other crystal atoms.[6] If the number of knock-on atoms is large, a region might experience an unstable situation. A so-called displacement spike can occur, which can relax to form a nonhomogeneous distributed amorphous region, occurring around the paths of knock-out atoms.

The systematic diagram of a typical ion implantation set-up is shown in Figure 2.4. It has an ion source to produce the ions that are transported through the vacuum system into the accelerator section. The mass separation occurs by the movement of the obtained ion via a magnetic filter assembly combined with exit path 'slits', permitting only the desired charge-to-mass ratio ions to continue down the path. The size of the ion beam can be modified by beam scanning and wafer motion using a deflection arrangement to ensure a uniform distribution of ions over the sample surface. The target chamber is connected to a Faraday cup that measures the integrated current of the passaged ion beam.

All the implanted samples in this study were implanted in implantation facilities at Surrey University at room temperature by Dr Luke Antwis. Their ion implanter (Danfysik 1090 model) consists of four main parts, source chamber, analysing magnet, acceleration tube and target chamber.[5] The role of the source chamber maintains a plasma necessary to extract the desired ions. In this chamber, a thermionic reaction extracts the electrons from a tungsten filament which are accelerated onto the source containing the atoms needed to be ionised. The desired ions are directed towards the end of the source chamber by a negative potential (15-40 kV). The mass selection of ions occurs before the acceleration, which is needed to decrease the size of the analysing magnet. The extracted beam contains varieties of ions varying in the mass-to-charge ratio; therefore, an analysing magnet is used to filter out the unwanted ions by adjusting the magnetic field to a value that affects the desired ions and drives them around a 90° corner. The ions are accelerated to the desired velocity utilising an electric field. The tubes enclosing the beam may acquire a 7° offset before reaching the substrate chamber. The accelerated ions then strike the substrate and implant to a depth defined by the velocity and angle of the beam. Parameters such as substrate temperature, angle and rotation can all be

modified. Ion energies of less than 10 keV can be attained by a deceleration lens, which is also mounted in the target chamber with a potential deceleration range of 100 eV to 30 keV.

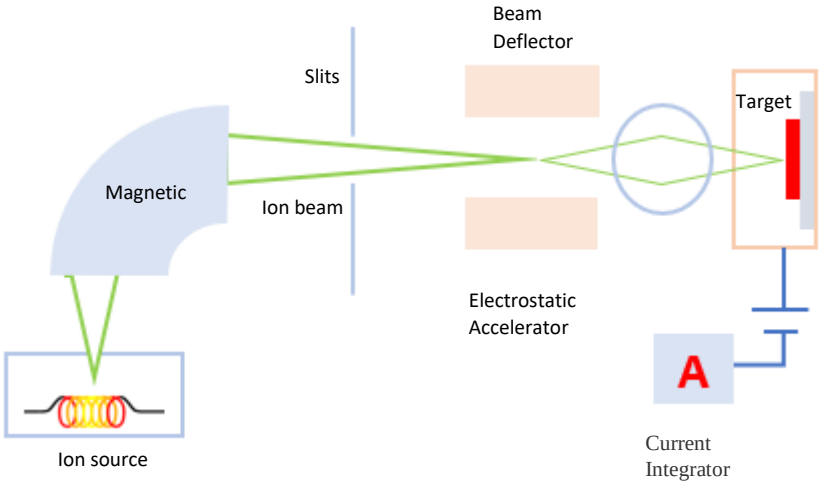

Figure 2-4 Systematic diagram of the main ion-implantation components.

2.2.3 Acid Cleaning, Aqua Regia and O-Termination

To clean a diamond surface from contaminated metals, a standard acid cleaning procedure was performed. A solution of 6.5 g KNO_3 and 100 mL H_2SO_4 (95-97%) was poured into a small, round-bottomed flask and positioned in a refluxing system in a fume hood for ~3 h. The adjusted time was increased depending on the sample conditions, or if any remaining contamination could be seen by the eye or under an optical microscope. The samples were then rinsed carefully with deionised water and dried with Ar gas ready to be stored for the next experiment.

An aqua regia solution was specifically used to remove the metal contacts (Ti/Au) from the surface, as this was more efficient compared with standard acid cleaning. The mixture was prepared by adding 5 mL of HNO_3 (>90%) to15 mL of HCl (35%) (1:3), which was then refluxed with the sample for 3–6 h in a fume hood. The mixture was used only once, as its potency degraded with use.

The acid cleaning procedures were also a method of creating an O-terminated diamond surface. This could also be generated using an oxygen plasma in a converted Edwards S150A sputter coater. The sample was placed in the chamber between two electrodes separated by ~1 cm. The first electrode was the grounded stainless-steel stage which supported the sample

while the upper electrode was powered. The system was pumped down to ~10^{-2} torr before opening the oxygen gas (99.9%) flow by adjusting the mass flow controller to 10 sccm. The a.c. High Tension (HT) controller was turned for 5 seconds to strike a plasma between the two electrodes. After this time, the power was switched off, and the system was pumped back to base pressure, before being vented and the now O-terminated sample removed.

2.2.4 Hydrogen termination

The hydrogen termination was performed using the MWCVD-ASTEX type reactor at a frequency of 2.45 GHz and power up to 1.5 kW. The chamber has a cooling system that utilizes the flowing water on the walls to protect the magnetron from the reflected power. The termination was started by placing the sample on a tungsten disc isolated from the water-cooled baseplate in the chamber bottom by 9 mInch Mo wire to control temperature. Once the system was pumped down to the base pressure, less than 4×10^{-2} torr, the hydrogen gas was opened with flow rate 300 sccm to ignite the plasma at 110 torr and 1250 W, which gives the plasma temperature of about 850 °C, for about 2 mins to remove any previous termination from the sample surface. The parameters were then decreased to 45 torr and 750–800 W, ~ 500 °C, for an extra 2 mins. The power is switched off while the hydrogen is left to flow for an extra 2 mins to allow the hydrogen termination before close the gas inlet valve and pumping the system to the base pressure.

2.2.5 Evaporator

Evaporation is a popular method used to deposit a thin-layer film in a vacuum that permits direct interaction between the vapour materials and the target substance. In this technique, the diamond film is mounted on the substrate stage, and a tungsten filament or boat (source holder), which is used as a resistant heater, is constructed. The metals to be evaporated, e.g., gold and titanium wires, were held tightly on two separate sets of tungsten filaments that were shielded by a bridge to prevent cross-contamination. The system was then allowed to pump down to 10^{-6} torr and was heated to 200 °C by the sample heater power supply (home-built) for 1 h to outgas any adsorbates. The sample heater power supply has a Eurotherm controller that monitors the temperature via a thermocouple. When the temperature is too low, it closes a switch that supplies AC mains power to the bulbs that heat the stage. Electrical current (up to 50A) was passed through the tungsten filament causing it, and the Ti or Au wire wrapped around it, to heat up to temperatures above the melting point of the two metal, but below that of tungsten. Each metal was evaporated in turn, Ti then gold, to form separate layers on the

substrate surface. This was done by slowly increasing the power to the tungsten filament while monitoring the film thickness using a quartz crystal microbalance (QCM). The process took more time to evaporate the titanium compared with gold due to the difference in their melting points. The deposited film thickness measured using the QCM was ~50 nm for Ti and ~100 nm for Au.

2.2.6 Tube Furnace

A tube furnace is an electric heating method that was used in this study to anneal diamond samples with working temperatures up to 1200 °C. The tube furnace has a cylindrical hollow enveloped by heating coils that are located inside a heat insulating casing. A quartz tube sits centrally in the cavity and is attached to Ar gas line and gas flow meters. This tube was flushed with Ar three times to prevent an unwanted etching effect of the quartz by any residual oxygen. The temperature was measured using a thermocouple, while a digital temperature controller enabled programmable segments, such as ramping, timing and heating.

The sample to be annealed was placed inside a small quartz vial which was evacuated to a pressure of $< 10^{-2}$ torr and then sealed under vacuum in the Physics workshops (Figure 2.5 (i)). This vial was placed inside the long quartz tube and positioned centrally within the furnace (Figure 2.5 (ii)). A typical annealing sequence involved 20 ^{o}C / minute. Once the annealing cycle was completed, the sample was left to cool down overnight.

Figure.2-5 A photograph of the evacuated samples in a quartz tube manufactured in the glass workshop (i), and a photograph of the Tube furnace used in this study (ii).

2.3 Characterisation Techniques

2.3.1 Raman Spectroscopy

Laser Raman spectroscopy is one of the most important and well-established methods for characterising materials. It is a non-destructive and widely used method for characterising the bonding type in diamond films. The characteristic first-order Raman spectrum of a single-crystal diamond at 1,332 cm^{-1} (FWHM 5–10 cm^{-1}), allows the diamond structure to be distinguished from other carbon materials, such as graphite (the G peak 1520–1580 cm^{-1}) or the disordered graphite (the D peak 1345 cm^{-1}), and to determine the diamond purity. [6–8] Other information about the stress development in the polycrystalline diamond films can be studied from the peak widths. This simple diamond fingerprint makes Raman spectroscopy a useful technique to study the diamond purity and crystalline perfection as a function of deposition conditions.

In Raman spectroscopy (Figure 2.6), a set of mirrors is used to direct and focus a laser beam, through a microscope onto the sample. The laser light interacts with the sample, and the reflected laser light, plus the Raman-shifted light returns along the same pathway. However, the Raman-shifted light is filtered out from the reflected laser light by a blocking lens and is focused and then dispersed via a grating onto a detector. Raman spectra are produced by plotting the scattered light intensity against the Raman-shift wavenumber – the reciprocal of wavelength – in cm^{-1} units.

The Raman effect occurs when the photons of the incident laser beam interact with a sample, causing low-energy frequency modes, such as rotational and vibrational electronic states, and this places the sample at a higher energy level. This excited state typically lasts a short time before it relaxes back and re-radiates the photons as scattered light (Figure 2.7). The inelastic scatterings of the incoming photons can occur with either higher energy (anti-Stokes scattering) or lower energy (Stokes scattering), compared with the income photon energy. The difference in the resulting energy depends on what lattice vibrations (phonons) are possible inside the sample. Since anti-Stokes Raman is less intense than the Stokes scattering, it is rarely used in Raman spectroscopy. A large fraction of photons is scattered as elastic photons – known as Rayleigh scattering – where the emitting and incoming photons have the same energy. Therefore, a dual filter is used to isolate the stokes scatterings from Rayleigh scatterings.

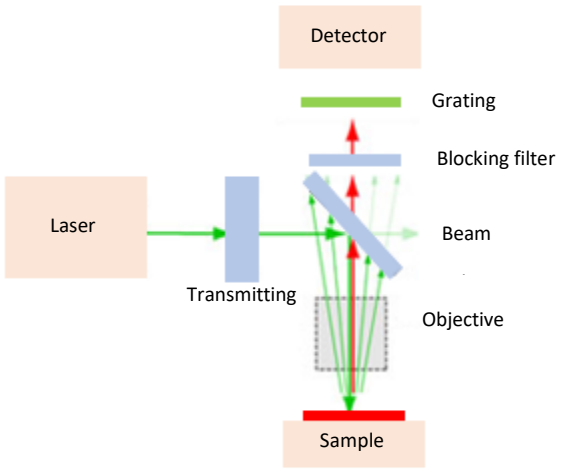

Figure 2-6 A schematic diagram of a Raman spectrometer

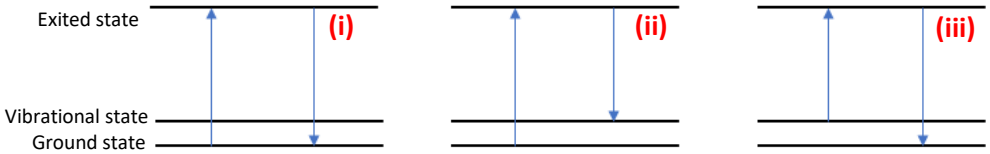

Figure 2-7 Excitation diagram for Rayleigh scattering (i), Stokes shift (i), and anti-Stokes shift (iii)

The sensitivity to the CVD diamond film components is largely dependent on the chosen laser wavelength since the sp^2 and sp^3 resonant enhancement depends on the excitation wavelength. Diamond and non-diamond components are sensitive to UV and NIR, respectively. Therefore, studying microcrystalline films might be accomplished by using variable wavelengths.

2.3.2 Scanning Electron Microscopy (SEM)

Scanning electron microscopy (SEM) is a magnification technique that provides important details about the sample, involving morphology, chemical composition, and orientation.

The principles of this technique involve the use of accelerating electrons between the cathode and anode in a column to scan a surface (Figure 2.8). [9] The system is typically operated in high vacuum. The electrons are emitted from field-emission or thermionic electron guns, accelerated by voltages of up to 50 kV, focused into a beam using pairs of deflector lenses. When the incident beam strikes the sample, the electrons transfer their “kinetic energy” to the sample, to ~1 μm in depth from the surface, causing a series of further electron scattering events. The cascade of secondary electrons and reflected primary electrons are scattered and

collected by a detector, which builds up an image of the sample surface morphology. SEMs can have a magnification of up to 500,000 times.

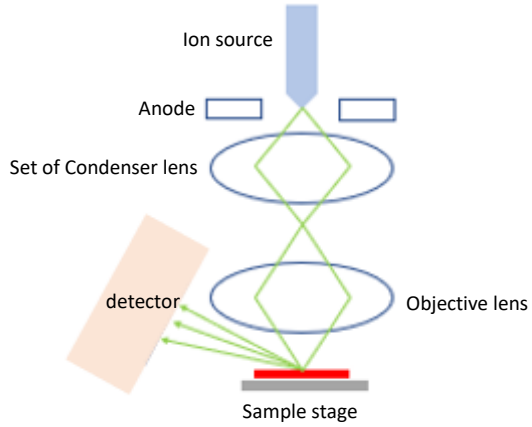

Figure 2-8 The basic components of a secondary electron microscope.

2.3.3 Magnetic-Sector Secondary Ion Mass Spectrometry (MS-SIMS)

Secondary ion mass spectrometry (SIMS) is a technique that is broadly utilized for the qualitative analysis of the components in solid materials.[10] A schematic diagram of this technique is shown in Figure 2.9. It is performed in ultra-high vacuum ($<10^{-6}$ torr) by focusing and accelerating a primary ion beam (Cs^+, O_2^+, O, Ar^+ or Ga^+) onto the sample, with varying energies (usually several keV); in the present study, Ga^+ was used.

The primary ions strike the sample surface with an oblique incidence angle, causing a series of collisions, and knocks them free of their lattice position, some of which are emitted from the surface. The ejected species may be positive or negative secondary ions, molecules or atoms, with kinetic energies varying between 0 and several 100 eV, depending on the primary ion energy. These fragments provide useful information about the contents of the sample under analysis. The ejected ions separation process is based on their mass-to-charge (m/z) ratios using a magnetic field, and then detected and plotted as a mass spectrum. To prevent electric charge build-up on the sample surface, it must be discharged by connecting it to ground. This requires the sample to be electrically conductive, or to be coated with a thin film of gold or silver.

The capability of the SIMS for quantitative analyses is based on the compositions and chemistry of the sample surface, such as the ionisation potential or electron affinity of the secondary ions, and on the variability of the emitted ions from each surface. These variations mean that the absolute magnitude of any SIMS signal depends on the sample type and the machine used. Thus, quantitative analysis requires the use of standard calibration samples for

each species being measured, which are fabricated in advance using ion implantation of the known dose of the species. In this study, the University of Surrey prepared for us polycrystalline diamond calibration samples supplied from Element Six, implanted with a known concentration of either Mg (Mg^+ implanted at 10^{12}, 10^{14} and 10^{15} cm^{-2} at 100 keV) or N (N^+ implanted at 5×10^{14} and 5×10^{12} cm^{-2} at 120 keV). The calibration was performed at Interface Analysis Centre (IAC) in the School of Physics by Dr Peter Heard, using a gallium ion beam at 25 keV energy. Nitrogen and magnesium signals were detected in SIMS as CN^- and Mg^+ in the negative and positive mode, respectively. Some interpretations from other secondary ions that were ejected from the sample were corrected to make the SIMS data more reliable. In the negative mode of the SIMS depth profile, both $CN^-$and $C_2H_2^-$ have the same mass/charge ratio (26); therefore, there is the probability of the $C_2H_2^-$ signal contributing to the CN^-signal. To solve this problem, the concentration of $C_2H_2^-$was measured using an undoped diamond film to be ~1.1×10^{19} cm^{-3}, which was taken as the detection limit for CN^- and hence of N. Similarly, in the positive mode of the SIMS depth profile, $Mg^+$and C_2^+ have the same mass/charge ratio (24). Therefore, the $C_2^+ : C^+$ ratio was calculated for an undoped diamond sample and then subtracted from the $Mg^+ : C^+$ ratio in all Mg-doped samples. From the calibration report, the calibration factor for N and Mg were calculated as:

N concentration [N] = 3.4×10^{20} × (CN^-/C^- ratio).

Mg concentration [Mg] = 2.3×10^{20} × (Mg^+/C^+ ratio – (0.16-0.18). cm^{-3}

2.3.4 Van der Pauw Sheet Resistance Measurements

The resistivity of the semiconductor samples usually measured by The Van der Pauw method. It utilises a four-point probe located around the corner of the sample that provides an average resistivity value. In this technique, a set of currents are allowed to flow along with the adjacent contact points while the voltage on the other side of the adjacent points is measured. In this way, the sheet resistance is determined from the gradient of the current-voltage (*I-V*) plot using Ohm's law.

$$R_{21,34} = V_{34} / I_{21} \qquad 2\text{-}1$$

In this equation, (I_{21}) a known applied DC current (6221, Keithley, UK), is injected into contact 2 and readout of contact 1 (in A), and (V_{34}) is the voltage between contact 3 and 4 (in V) measured using a nano voltmeter (2182A, Keithley, UK).

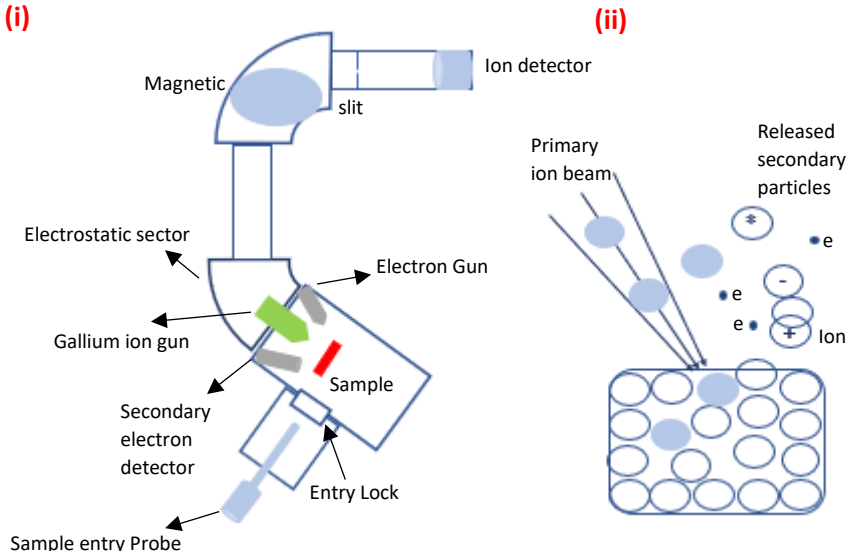

Figure 2-9: (i) The main components of a magnetic sector SIMS analysis instrument home-built at Bristol University. (ii) Schematic diagram of the interaction of gallium ions (primary beam) with the sample and the different species released, which include: electrons, positive ions, negative ions and neutrals, represented by .[11]

Through repeating this measurement with another three configurations, $R_{12,43}$, $R_{43,12}$, $R_{34,21}$, the average value, R_A, can then be calculated using equation (2.2).

$$R_A = \frac{R_{21,34} + R_{12,43} + R_{43,12} + R_{34,21}}{4} \qquad 2\text{-}2$$

The same measurement is performed with the other four configurations ($R_{32,41}$, $R_{23,14}$, $R_{14,23}$, $R_{41,32}$) to obtain R_B according to the following equation.

$$R_B = \frac{R_{32,41} + R_{23,14} + R_{14,23} + R_{41,32}}{4} \qquad 2\text{-}3$$

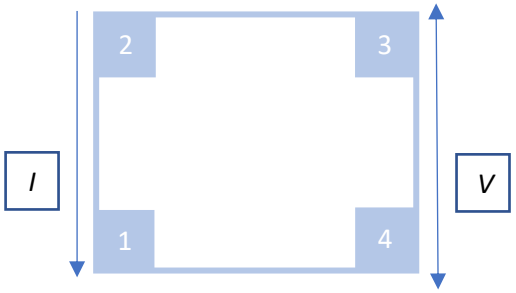

Figure 2-10: Schematic configuration used to measure the characteristic resistance, $R_{21,34}$, using the Van der Pauw method.

The sheet resistance, R_S, can then be calculated (using MATLAB) from the two previous resistances, R_A, R_B, applying the Van der Pauw equation, as follows:

$$\exp(-\pi R_A/R_S) + \exp(-\pi R_B/R_S) = 1 \qquad 2\text{-}4$$

$$\sim Rs = \frac{\pi}{\ln 2}\left[\frac{R_A + R_B}{2}\right] \qquad 2\text{-}5$$

In this study, a standard sample of lightly boron-doped diamond grown on a silicon substrate prepared by hot filament CVD was first used to determine the accuracy and reliability of the van der Pauw set-up. Square-shaped layers of Ti 50 nm /100 nm Au contact pads were evaporated through a quartz mask (designed by Enterprise Q Ltd, Figure 2.10 (i)) onto the four corners of the sample, then heated to ~ 400 ^{o}C to achieve better adhesion on the surface. The sample was then held between the four copper arms soldered on the measurement stage (Figure 2.10 (ii)) of the vdP rig, then placed inside a small aluminium box that was used as a Faraday shield to prevent any electrical noise. The resistances obtained for the standard sample, which were in the range of 457.9–458.9 MΩ with a small error ±0.9 MΩ collected from four different measurements, indicated that the current Van der Pauw resistance set-up could measure a high resistance up to 500 MΩ with good accuracy.

(i) 

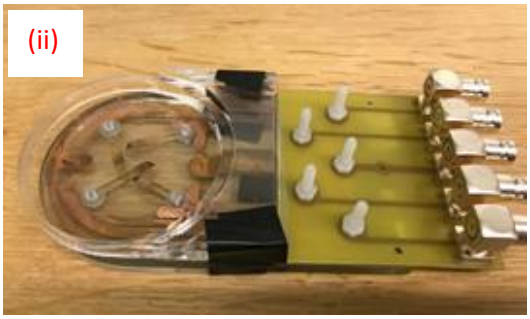

Figure 2-11 Photographs of (i) the base and cover of the quartz mask used to make the contacts and (ii) the four-point probe sample stage.

2.4 Computer Codes

2.4.1 CASTEP

The Cambridge Serial Total Energy Package (CASTEP) code was developed specifically for solid-state materials science to perform *ab initio* calculations. It uses the density functional theory plane-wave pseudopotential method, which allows the ground-state energy calculations and the prediction of various properties of materials from first-principal quantum mechanics. The electronic properties of crystalline solids, molecules, amorphous materials, and surfaces can be simulated. Typical applications of CASTEP, including surface chemistry, geometry optimisation, the density of states, band structure, transition states, phonon dispersion and other applications, can be found on the CASTEP website. [12]

The input files consist of two files: .cell and .param. The former contains details of the unit cell of the system under study, including lattice parameters (required), atomic positions (required), *k*-points (optional), symmetry (optional) and pseudopotentials (optional). The latter contains directions regarding the chosen task to be calculated for the system provided in the .cell file (i.e. tasks include single-point energy, geometry optimisation, the density of states, band structure, phonons and NMR). The output file .castep is printed out during the calculation: the header (version number, references) and summary of the parameters used, the cell used and the results of the calculations.

The crystal structure must first be defined ('built') in a separate program (i.e., DLV or CRYSTAL); then, the atom positions, lattice parameters and symmetry operations are placed in three different blocks in the .cell file. In the .param file, the type of task and theory level, functionals, cut-off energy, spin-polarised, number of unpaired electrons, SCF control parameters and more, can be defined with specific keywords.

The small set of *ab initio* calculations in Chapter 4 were performed with spin-polarised DFT as implemented in the CASTEP code.[12] To decrease the number of plane-wave basis sets, an ultra-soft pseudopotential was chosen in the present study with 600 eV cut-off energy of the plane waves. PW91, PBE-parameterised forms of the generalised gradient approximation (GGA), were used to describe the exchange-correlation energy. To simulate one atomic defect or dopant at a reasonable concentration (corresponding to 3.5×10^{20} cm^{-3} in the diamond), required a supercell size of 512-atoms, with 2×2×2 as *k*-points values to sample the reciprocal space. The Broyden-Fletcher-Goldfarb-Shanno (BFGS) method in the geometric optimisation

was used to minimise the forces on the atoms. In the self-consistent field (SCF) calculation, the Pulay mixing scheme was used in the density-mixing procedure. The accuracy of the total energy was controlled by geometry energy tolerance and electron force tolerance, which were set to 0.1×10^{-6} eV/atom and 0.5×10^{-3} eV/Å, respectively. The lattice parameters; C-C bond lengths; bandgap for the undefective diamond from the PW91 and PBE functional were 3.73 and 3.71 Å; 1.547 and 1.546 Å; 4.2 eV, respectively.

2.4.2 CRYSTAL

The code is used to calculate the ground-state energy and electronic wave function to determine a variety of materials properties. A range of systems can be calculated with this code: zero dimensions (i.e., molecules), one dimension (i.e., polymers), two dimensions (i.e., slabs), and three dimensions (i.e., crystals). The code has a high level of flexibility to construct the desired structure using specific keywords. ATOMSUBS, ATOMINS, ATOMREMO and ATOMDISP are examples of keywords used to create a point defect in crystal. There are different keywords available for each type of calculation (i.e., symmetry, crystal size and spin). Different options of functionals can be used in the calculations, including Hartree-Fock (restricted (RHF) for close shell and unrestricted (UHF) for open-shell systems) or Kohn-Sham (DFT/ spin polarised/ SPIN). The code has only one file for the input information, unlike CASTEP, consisting of three blocks: geometry, basis sets and functional (default: RHF) and SCF control parameters, see CRYSTAL user manual [13] for more specific information. Chapter 3 has more details regarding the parameters used in this study, including the functional type, basis sets, energy tolerance, symmetry, and spin control.

2.5 Blue Crystal

Most of the calculations were run on Blue Crystal Phase 4, which is a cluster in the Advanced Computing Research Centre (ACRC) at Bristol University. To reduce the computational time, the ACRC enabled the parallel message passing interface (MPI). Phase 4 is mainly suitable for large parallel jobs as each of the 525 computing nodes has two 14 core and 128 Gb of RAM. Also, there are 17 additional high-memory nodes, each of which has 512 Gb of RAM. Computational ‘jobs’ were submitted to different partitions (i.e., a set of nodes each one has 28 processors), including the cpu_test, veryshort, cpu, and hmem, through the study based on the estimated time and resources needed for each job. The calculations were run from ‘scratch space’ (with a quota of 512 Gb). The requested resources were based on the supercell size,

basis sets, dopants and the symmetry point group. Most of the jobs that included geometry optimisation of 128 and 216 supercells required 4 nodes containing 112 processors on a cpu partition and finished within 72 h as wall-time. The unfinished jobs were re-submitted starting from the end of the previous run to save the resources with a new estimation for the wall-time. For example, in geometry optimisation, to continue a calculation we used either the RESTART keyword in CRYSTAL with the OPTINFO.DAT file which has the information from previous runs or the CONTINUATION (default) keyword in CASTEP with the CHECK file. The high memory partition (hmem) was needed only when simulating the MgN_3 complex in a 512 supercell using CRYSTAL and the other 512 cells that released the symmetry.

2.6 Reference

1. May, P. W. Diamond thin films: a 21st-century material. *Philos. Trans. R. Soc. London* **358**, 473–95 (2000).
2. Hetherington, A. V., Wort, C. J. H. & Southworth, P. Crystalline Perfection of Chemical Vapor Deposited Diamond Films. *J. Mater. Res.* **5**, 1591–1594 (1990).
3. Dresselhaus, M. S. & Kalish, R. *Ion implantation in diamond, graphite and related materials*. (Springer Science & Business Media, 2013).
4. Clark, C. D., Kemmey, P. J. & Mitchell, E. W. J. Optical and electrical effects of radiation damage in diamond. *Discuss. Faraday Soc.* **31**, 96–106 (1961).
5. Smith, A. The formation of Ultra-shallow p-type Junctions using Vacancy Engineering. (University of Surrey, 2006).
6. Mehl, M. J. & Pickett, W. E. Zone-Center Raman Active Modes In Cubic And Hexagonal Diamond. In Raman Scattering, Luminescence and Spectroscopic Instrumentation in Technology. *Int. Soc. Opt. Photonics* **1055**, 181–184 (1989).
7. Prawer, S. & Nemanich, R. J. Raman spectroscopy of diamond and doped diamond. *Philos. Trans. R. Soc. A Math. Phys. Eng. Sci.* **362**, 2537–2565 (2004).
8. Filik, J. Raman spectroscopy : A simple, non-destructive way to characterise diamond and diamond-like materials. *Spectrosc. Eur.* **17**, 10–16 (2005).
9. Khursheed, A. *Scanning electron microscope optics and spectrometers*. (World

scientific, 2011).

10. Williams, P. Secondary ion mass spectrometry. *Annu. Rev. Mater. Sci.* **15**, 517–548 (1985).

11. Heard, P. J., Feeney, K. A., Allen, G. C. & Shewry, P. R. Determination of the elemental composition of mature wheat grain using a modified secondary ion mass spectrometer (SIMS). *Plant J.* **30**, 237–245 (2002).

12. Clark, S. J. *et al.* First principles methods using CASTEP. **220**, 567–570 (2005).

13. Saunders, V. R. *et al.* CRYSTAL User Manual. (2003).

CHAPTER 3

THEORETICAL REVIEW OF VACANCY, C- CENTRE, AND PHOSPHORUS IN DIAMOND

CHAPTER 3 – THEORETICAL REVIEW OF VACANCY, C-CENTRE, AND PHOSPHORUS DEFECTS IN DIAMOND

3.1. Introduction

This chapter covers the most well-known point defects in diamonds: vacancy, C-centre, and phosphorus. A set of calculations were performed to calculate the energy, geometry, and electronic structure of these defects. The aim of this chapter was tested the computational parameters and explore the necessary keywords used to control and direct the calculations. The results were compared to the previous calculations in this context to validate our models. These will be used in chapters 4 and 7 to calculate the formation, binding, and ionisation energies of multi complexes impurities consisting of one or more of these defects.

3.1.1. Vacancy

A vacancy (V) defect can be generated in the diamond by electron irradiation with energies between 300 and 400 keV at room temperature[1]. The ground state of the neutral V is singlet 'diamagnetic'[2], due to couple the four electrons in the defect site. It readily diffuses through the diamond lattice with an activation energy of 2.3 ± 0.3 eV[2] forming complexes with other defects.

Many theoretical studies have adopted the 'defect-molecule' approach to investigate different point defects in diamond.[3] The principle of this model is that there will be only a small distortion of the lattice around a tetrahedral defect because it involves all the carbon atoms (excluding the V neighbours) in covalent bonds, such that the distribution of the vacancy electrons is only influenced by the dominant tetrahedral electric field of the neighbouring atoms. Thus, the model treats the vacancy region as if it were a molecule, and this greatly simplifies the calculations (Figure 3.1).

The electrons in the defect region can also be understood through Jahn–Teller theorem, which states that any point defect or symmetric molecule with degenerate energy levels will distort to elevate the degeneracy and lower its energy.[4,5] From Coulson and Kearsley's work, the orbitals formed by the 4 dangling bonds split into a non-degenerate a_1 and a triply degenerate t_2. The vacancy with T_d symmetry in its singlet ground state ($a_1(\uparrow\downarrow)$, t_2 ($\uparrow\downarrow$:0:0), is unstable and undergoes Jahn–Teller distortion.

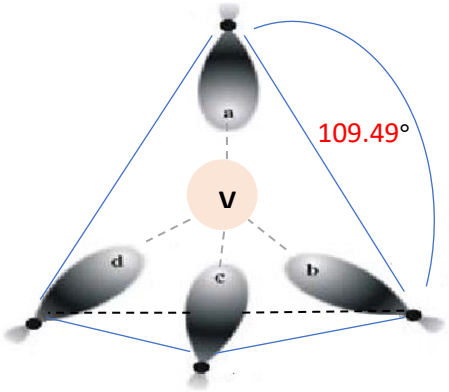

Figure 3-1 Orbitals of the C atoms that are the first-nearest neighbours to a vacancy in diamond with tetrahedral symmetry.

In Local Density Approximation (LDA) calculations the 4 neighbouring C atoms relax away from the vacancy producing a D_{2d} distortion which lowers the energy by approximately 0.36 eV, leading to a split of the $t_2(\uparrow\downarrow:0:0)$ into fully occupied $b_2(\uparrow\downarrow)$ and unoccupied $e(0:0)$ states. [6] Later calculations with GGA and the PBE exchange functional [7] found a metastable state involving a different electronic structure which was higher in energy than the D_{2d} by approximately 0.24 eV. In this singlet, the doubly degenerate e level was lower in energy than the b_2 level. However, when this calculation was repeated using the HSE06 functional, the total energy decreased such that this structure became the ground state.[7] Since this singlet distortion is unstable from the Jahn-Teller point of view, their calculation only considered the triplet state $a_1(\uparrow\downarrow)$, $e(\uparrow:\uparrow) + b_2(0)$, which was higher in energy by 0.18 eV compared to another singlet that split $e(\uparrow:\downarrow)$ into $b_1(\uparrow) + b_2(\downarrow)$ with C_{2v} symmetry. The singlet (C_{2v}) has been considered the ground state in recent calculations with the CRYSTAL code that examined the V electronic structure with different states corresponding to C_{2v} $a_1(\uparrow\downarrow) + b_1(\uparrow) + b_2(\downarrow)$, C_{3v} $a_1(\uparrow\downarrow) + e(\uparrow:\uparrow)$, and T_d ($a_1(\uparrow)$, $t_2(\uparrow:\uparrow:\uparrow)$) symmetries and using different hybrid functionals. [8]

3.1.2. The C–centre

Nitrogen is the most common defect in diamond and assumes many different forms characterised by the nature of each defect. Depending on its nitrogen content, a diamond can be classified into Ia (which contains aggregate N) or Ib (containing the simplest nitrogen defect, also called the C-centre, which consists of an isolated one nitrogen atom at a substitutional site). The most common forms of N aggregates are A-centres (pairs of N atoms in nearest-neighbour positions) and B-centres (vacancies surrounded by four N atoms). The C-centres are typically rare in natural diamond but are a common defect in HPHT diamonds. At high

geological temperatures and pressures, or in extreme laboratory conditions, multiple N atoms form various aggregates; this type of diamond is classified as type Ia.

The C-centre has a distinct infrared spectrum with a sharp vibrational mode at 1135 cm^{-1}. [4] The energy level of this defect produces a very deep donor with ionisation energy at 1.7 eV [9] and at 2.3[10]-2.4 eV[11] below the conduction band. Another threshold observed by photoconductivity spectroscopy at 4.5 eV in HPHT crystals which has been attributed to the hole excitation from the unoccupied defect level [10]. The absence of this 4.5 eV threshold in the CVD polycrystalline diamond is explained by the existence of structural defects within crystallites behaving as efficient hole traps.

Experimentally, it is well known that the C-centre has C_{3v} symmetry in which there is a dangling bond that points along the [111] direction. Various theoretical explanations have been suggested to investigate this C_{3v} distortion. The deep state of this defect is predicted to originate from an antibonding combination between the dangling bond orbital on one of the C atoms bonded to N and the lone-pair orbital on N. The simplest description of this defect is that the four N sp^3 hybrid orbitals are divided into three singly occupied states that form bonds with three of the neighbouring carbons, and one doubly occupied by the nitrogen lone-pair electrons. This results in a partially occupied antibonding orbital on one of the C neighbours [144]. This description can also be interpreted by crystal field theory [145], in which the N sp^3 valence hybrid orbitals in T_d symmetry form a non-degenerate a_1 orbital and a triply degenerate t_2. Because the N atom is surrounded by four C atoms that also have sp^3 hybrid orbitals, the three N-C bonding orbitals have lower energy and merge with valence orbitals (the same as for the other C-C bonds). One electron in the a_1 state in the gap has higher energy resulting from the combination between the orbitals of the lone pair on N and the dangling-bond orbital. Under distortion, the symmetry reduces from T_d to C_{3v}, which splits the t_2 level into a doublet e level and a partially occupied antibonding orbital a_1.

Theoretically, many studies have investigated this defect. Some of them modelled this defect with C_{3v} symmetry and others found distortion to T_d, depending on the computational conditions and the defect position at the starting point of the calculations. [12–17]

3.1.3 Phosphorus

Among all of the experimental trials for a doped diamond with different n-type dopants, phosphorus is considered the only atom that behaves as a shallow n-type dopant.[18] Different substances, such as tertiary butyl phosphine (TBP: $C_4H_{11}P$), trimethyl phosphine (TMP: $P(CH_3)_3$), and phosphine gas (PH_3), were used as the precursor for the phosphorus atom in

CVD diamond technology.[18–22] The NIRIM group achieved the first report of successful n-type doping in 1997.[23] They grew CVD diamond films with microwave plasma-assisted CVD using PH_3 as a source of phosphorus on (111) diamond substrates. The n-type conductivity was proven using Hall-effect measurements and with an activation energy of about 0.6 eV below the conduction band. [19]

Theoretically, studies on this defect in its substitutional site showed a significant outward distortion of the neighbouring carbon atoms and a low solubility. [24,25] The phosphorus can keep the tetrahedral symmetry of the perfect lattice [27,26], or it can be distorted to cause a different symmetry subgroup.[29] According to the Jahn–Teller theorem, this distortion gives rise to non-degenerate orbitals. It can potentially lower the total energy of the system, as shown with vacancy and C-centre. The C_{3v} symmetry was found to have the lowest energy in most of the previous studies[24–28], whereas the distortion of the tetragonal symmetry was shown in other studies as the ground state.[29,30] However, in general, the reported difference in energies between the two C_{3v} and D_{2d} symmetries was very small (~30 meV[29] and 10 meV[26] using the same supercell size, 216-atoms).

3.2 Computational parameters

All of the spin-polarised spin-polarized calculations were performed with a range of hybrid functionals HSE06[31], B3LYP [32], and PBE0 [33], PBE0-13 [34] (a revised version of the PBE0 functional with 33.33% of HF exchange), and PBEsol0 [35,36] as implemented in the CRYSTAL17 code [37], which affords an accurate description of the electronic spin localisation compared with simpler formulations of the density functional theory, such as LDA and GGA. Full optimization for lattice parameters and atomic positions were performed in all the calculations using FULLOPTG keyword. The 64, 216 and 512, and 128 supercells were created by expanding the conventional and primitive cells, respectively. The truncation criteria of the Coulomb and series of exchange infinite were determined by five thresholds technique that were changed to 8 (T1–T4) and 16 (T5 = T1 × 2), the defaults were 6 and 12, respectively. The threshold energy in the procedure of the self-consistent field (SCF) was predetermined in the optimisation and frequency calculations to be 10^{-8} and 10^{-10} hartree, respectively. If the energy change (absolute value) from one cycle to cycle is less than the predetermined value, the SCF cycle stop, and the system converge. The default is 10^{-6} hartree.

A choice of basis sets is available in the CRYSTAL library, for carbon: 6-21G* [38,39], and triple-zeta valence with polarisation (TZVP) were used which resulted in values for the C- C bond length, equilibrium lattice parameter, energy per atom, and indirect band gap of pure diamond that are summarised in Table 3.1. For nitrogen and phosphorus, only one basis set (TZVP)[40] was used. Reciprocal space was sampled using Γ-centred regular Pack−Monkhorst [41,42], identified in CRYSTAL by a shrinking factor of 24 for primitive cell and 4 for the supercells up to 512-atoms. This corresponds to 8 *k*-points with 128-atoms and 10 with other cubic supercells, in the irreducible part of the first Brillouin zone (FBZ) when the T_d symmetry of the pure diamond lattice is preserved, and 13 when the symmetry is lowered to C_{3v}. To simulate the vacancy defect, we use the "ghost" atom approach that represents the vacancy as a 'ghost atom' by removing the shell electron and nuclear charge, while keeping the basis set. We also repeated the calculations of 2NV in the next chapter with a 6-21G* basis set of C using the ATOMREMO keyword that removed the atom completely to create a vacancy instead of GHOST. No differences were found in the results in terms of geometry, charge, spin distribution or energy.

In the CRYSTAL code, the symmetry exploitation was used to decrease the number of SCF calculations because residual symmetry was only used for the calculation, such that the calculations were only performed on the irreducible atoms of each point group. In all the defects studied here, the calculations were performed with and without the symmetry constraint to precisely find the ground state energy, including the largest supercell, 512. After convergence under specific symmetry, the calculations were rerun without constraint to see any property that did not converge. In the frequencies calculations, the system was fixed at a stationary point on the potential-energy surface, which demanded optimizing the geometry in a previous step.

The calculation of IR intensities In this study was through the Berry-phase approach[43, 44], which is only suitable for an insulating system. This scheme was recently used with a range of defects in diamond, including the A-centre and pairs of B-B and N-B defects[45], and in another work[46] with VN_3H, I_{2N} and VH_4.

Table 3.1 Summary of the values for the C-C bond length, lattice parameter a_0 (in Å), energy per atom *E* (in hartree) and indirect band gap (BG) of the pure diamond (in eV) calculated with different computational parameters. SC refer to supercell size.

6-21G*	SC	HSE06	B3LYP	PBE0	PBE0sol0	PBE0-13	HF	SC	HSE06 TZVP
C-C	2	1.546	1.556	1.546	1.541	1.542	1.547	2	1.535
	64	1.546	1.556	1.546	1.541	1.542	1.547	64	1.535
	128	1.546	1.556	1.546	1.541	1.542	1.547	128	1.535
	216	1.546	1.556	1.546	-	-	-	216	1.535
	512	-	1.556	-	-	-	-		-
a_0	2	3.5709	3.5941	3.5702	3.5597	3.5621	3.5732	2	3.5447
	64	3.5707	3.5939	3.5702	3.5597	3.5621	3.5732	64	3.5448
	128	3.5707	3.5939	3.5702	3.5597	3.5621	3.5732	128	3.5448
	216	3.5710	3.5941	3.5702	-	-	-	216	3.5448
	512	-	3.5941	-	-	-	-	-	-
E	2	38.0543	38.0671	38.0549	37.9477	38.0574	37.8573	2	38.0837
	64	38.0543	38.0671	38.0549	37.9477	38.0574	37.8573	64	38.0837
	128	38.0543	38.0671	38.0549	37.9477	38.0574	37.8573	128	38.0837
	216	38.0543	38.0671	38.0549	-	-	-	216	38.0837
	512	-	38.0671	-	-	-	-	-	-
BG DOS	2	5.148	5.716	5.797	5.727	6.432	12.158	2	5.388
	64	5.148	5.716	5.797	5.727	6.432	12.158	64	5.388
	128	5.148	5.716	5.797	5.727	6.432	12.158	128	5.388
	216	5.147	5.716	5.797	-	-	-	216	5.388
	512	-	5.715	-	-	-	-	-	-

3.3. Results and discussion

3.3.1 Vacancy

3.3.1.1 Energy, geometry, charge and spin distribution

As anticipated in the introduction, different spin states for the vacancy defect have been predicted in the literature. There are three open-shell solutions for the vacancy: (a) all electrons have spin-up (quintet), (b) three up and one down (triplet), and (c) two up and two down (singlet). These were investigated in detail at different computational levels (Table 3.2).

Table 3.2 Show Mulliken atomic charges (q); the spin momentum (μ) (all in e); equilibrium distances between opposite carbon atoms of the next four carbon atoms to the V (e.g. $C_{A\alpha}$–$C_{B\alpha}$ and $C_{C\beta}$–$C_{D\beta}$ interatomic distances in the singlet state, Figure 3.2) (R) (in Å); the energies of the cell (E) (in hartree); the relative energy to that of the S_z = 0 state R_e. (in eV). All the calculations were performed with 128-atom supercells.

Functionals / basis set of C			S_z = 2 (T_d)		S_z = 1 (C_{3v})			S_z = 0 (C_{2v})		
			V	$4C_\alpha$	V	$3C_\alpha$	C_β	V	$2C_\alpha$	$2C_\beta$
HSE06	(6-21G*)	q	-0.056	0.057	0.071	0.05	-0.129	0.038	0.049	-0.007
		μ	0.131	0.874	0.015	0.747	-0.399	0.011	0.703	-0.705
		R	-	2.803	-	2.745	2.663	-	2.738	2.735
		E	-4832.58854			-4832.63850			-4832.64266	
		R_e	1.472			0.113			0	
HSE06	(TZVP)	q	- 0.127	0.074	-0.136	0.059	0.115	-0.132	0.074	0.075
		μ	0.163	0.881	0.040	0.754	-0.417	0.000	0.706	-0.707
		R	-	2.785	-	2.728	2.644	-	2.722	2.722
		E	-4836.31639			-4836.36630			-4836.37103	
		R_e	1.486			0.128			0	
B3LYP	(6-21G*)	q	- 0.066	0.042	-0.079	0.027	0.060	-0.079	0.037	0.035
		μ	0.116	0.857	0.020	0.731	-0.403	-0.001	0.677	-0.676
		R	-	2.831	-	2.775	2.696	-	2.769	2.769
		E	-4834.23454			-4834.28215			-4834.28679	
		R_e	1. 421			0.126			0	
PBE0	(6-21G*)	q	-0.055	0.057	-0.074	0.041	0.072	-0.073	0.051	0.048
		μ	0.135	0.878	0.022	0.756	-0.439	-0.000	0.706	-0.705
		R		2.804		2.746	2.661		2.740	2.740
		E	-4832.67201			-4832.71964			-4832.72444	
		R_e	1.426			0.130			0	

The three spin states were generated using the following CRYSTAL keywords: SPINLOCK that controls the spin density per cell, and ATOMSPIN that puts a specific spin [(1) (spin up, α) or (-1) (spin down, β)] on specific atoms alongside MODISYMM to lower the symmetry to the corresponding spin setting. The relative energies of the three spin states are consistent with previously reported values[8] in which the singlet was lower in energy than the triplet and quintet states by 0.1 and 1.4 eV, respectively.

Comparing the relaxed position of the four neighbour atoms to their positions in the perfect diamond (*i.e.*, the distance between C_A–C_B and C_C–C_D in the perfect diamond 2.5 Å (see Figure 3.2)) revealed them to be outwardly relaxed in all spin states. This relaxation was the greatest in S_z = 2 (~2.8 Å, 11%) and was lower in the other two spin states with almost symmetrical relaxation in S_z = 0 (~2.7 Å, 7%). The charge in the defect region (the vacancy and itis neighbouring atoms) was negligibly small with 6-21G*. At the same time, with TZVP there was a small but also negligible accumulation of charge of ~ 0.1e. The spin density as

indicated by a Mulliken population analysis was essentially localised at the four C atoms in the defect region with nearly equal values for the α (spin-up) and β (spin down) cases in the singlet state. The β spin density is lower by approximately 0.3*e* in the triplet state.

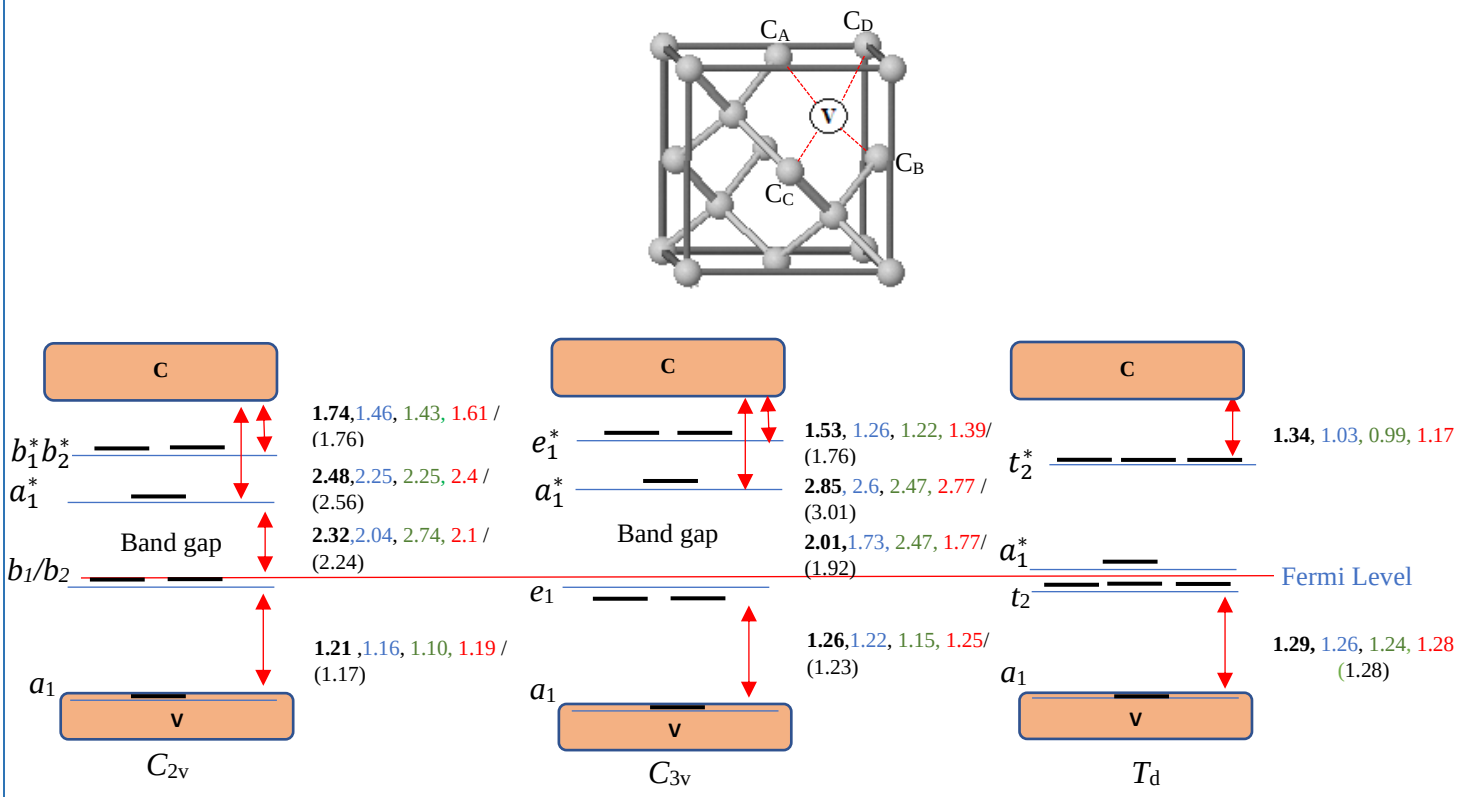

Figure 3-2 Show the states of different spin configuration and symmetry (C_{2v}, C_{3v}, T_d) of a neutral vacancy defect in diamond. All energies level were calculated at the Γ point, and the LUCO of the host lattice was taken at the X point. The energies in bold, blue, and green refer to B3LYP, HSE06, and PBE0 calculations, respectively, with 6-21G* basis sets, whereas the red refers to HSE06 with TZVP basis sets. The value between the brackets was taken from reference [8] for comparison. The symbols *e*, a_1, and t_2 indicate the irreducible representations of the symmetry levels. The horizontal red lines indicate the Fermi level.

3.3.1.2 Electronic structure

The band structures simulated with B3LYP with 6-21G* basis sets for the different spin states are shown in Figure 3.3 alongside those for pure diamond. Continuous and dotted lines respectively represent the energy levels relating to the α and β electrons. In T_d symmetry, the singly occupied non-degenerate a_1 level merges with the highest level of valence band (easy to distinguish at the Γ point), while the half-occupied t_2 overlaps with the empty a_1 level, giving a conducting state with HSE06 and B3LYP.

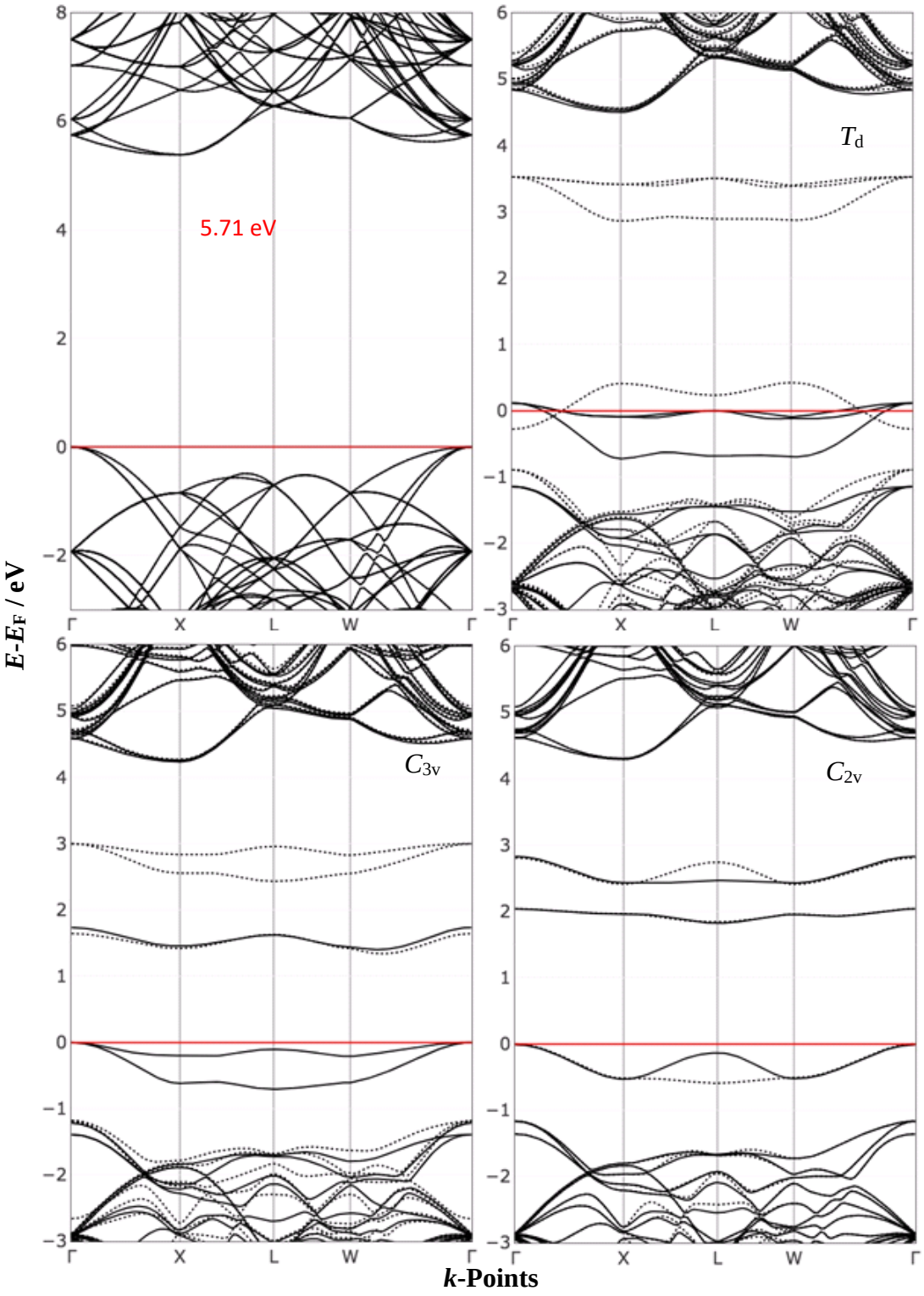

Figure 3-3 Band structure of perfect diamond compared with V defects with different symmetries. All calculations were computed with B3LYP/6-21G* and 128-atom supercells. The energies are presented relative to the Fermi energy. The red line refers to Fermi level, and the continuous and dashed black lines refer to the (spin up) and (spin down) energy levels, respectively.

However, using PBE0 this same calculation gave an insulating state which might be due to the difference in the exact exchange percentage (20% in B3YLP and 25% in PBE0) or simply as a result of the difference in the band gap. The large shift between the α and β levels resulted from the fact that all the α levels were occupied while β was empty. In C_{3v}, the a_1 level was fully occupied (and therefore too difficult to distinguish in the band), whereas the half-occupied e_1 level is immediately below the Fermi level. In the gap, there are also two empty states: (antibonding) a_1 above the Fermi level and e_1 below the bottom of the conduction states. In C_{2v}, a_1 is full occupied (similar to the situation for C_{3v} and $b_1(\uparrow) + b_2(\downarrow)$ located below the Fermi level. All the levels are summarised in Figure 2.3 and the energies differences compared with the previous calculation.[8]

3.3.2 C-centre defect

3.3.2.1 Geometry, charge, spin distribution and formation energy

Figure 3.4 shows the geometry of the optimised neutral C-centre in the 128 supercells and the electronic charge and spin distribution resulting from a Mulliken analysis.

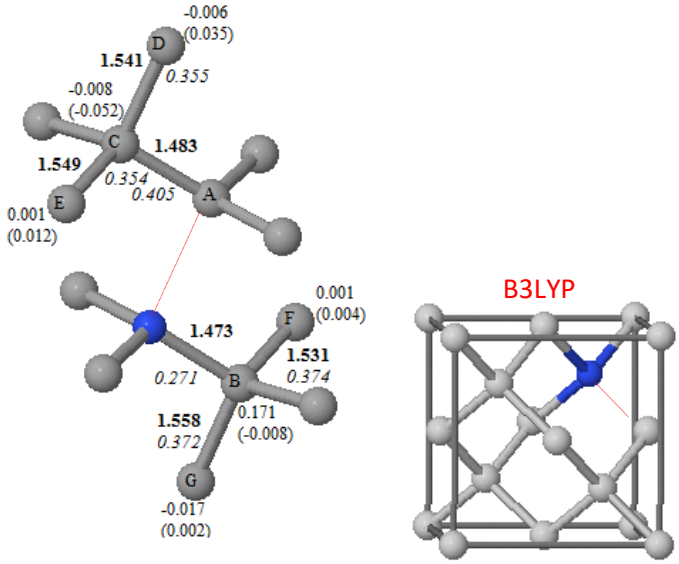

Figure 3-4 Interatomic distances (in Å) (**bold**), spin momentum (between brackets), Mulliken charges, bond overlap population (*italics*) (all in e) for irreducible C atoms in the first, second and third shell of the N points defects (with C_{3v}). Grey and blue indicate C and N atoms, respectively. All data refer to the C/6-21G* and N/TZVP basis sets, B3LYP and the 128-atom supercells.

In the present calculation, offsetting the nitrogen atom at the beginning of the calculation[47,27,48] by only 0.08 Å along the [111] direction was enough to ensure convergence to the known ground state with C_{3v} symmetry (one C-C distance (~2.0 Å) and three shortened bonds (~1.48 Å)), no distortion to T_d was obtained, even with symmetry release (Table 3.3). This leads to one unique carbon atom (C_A), and three symmetrically identical carbons (C_B) as nearest neighbours to the N defect. The C-C_A-C angle increases from 109.47° to ~116° and C-N-C_B angle to 115° (Figure 3.4). The perturbation in the lattice decays rapidly as the compression on the C_A-C, and N-C_B bonds (1.47-1.48 Å) are ~1.53 - 1.56 Å in the second shell of neighbours of the N atom, close to the value for C-C bonds in a perfect diamond lattice (Table 3.1).

Table 3.3 Show spin momentum (μ); Mulliken atomic charges (*q*) (both in *e*) at the defect site (N) and on the four nearest carbon atoms around the defect (C_A and $3C_B$); equilibrium distances (*R*) (in Å) of the first neighbours from the N; overlap bond populations (*b*) (in *e*) of the bond between N atoms and the first neighbours; the bond length (C-C) and overlap bond population (*italic*) in pure diamond (in Å and *e*, respectively), for comparison. All data refer to 128-atom supercells calculations.

Functionals /basis set of C			**(C_{3v})**			**C-C**
			N	CA	3CB	
HSE06	(6-21G*)	*q*	-0.332	0.056	0.171	1.546 *0.359*
		μ	0.168	0.759	-0.008	
		R		2.038	1.473	
		b		-0.089	0.271	
HSE06	(TZVP)	*q*	-0.661	0.061	0.281	1.535 *0.329*
		μ	0.175	0.763	-0.007	
		R		2.018	1.467	
		b		-0.110	0.215	
B3LYP	(6-21G*)	*q*	-0.296	0.045	0.158	1.556 *0.348*
		μ	0.170	0.750	-0.008	
		R		2.062	1.483	
		b		-0.074	0.262	
PBE0	(6-21G*)	*q*	-0.334	0.057	0.170	1.546 *0.358*
		μ	0.168	0.766	-0.008	
		R		2.039	1.473	
		b		-0.091	0.268	
PBEsol0	(6-21G*)	*q*	-0.404	0.068	0.183	1.541 *0.360*
		μ	0.175	0.743	-0.008	
		R		2.027	1.468	
		b		-0.090	0.274	
PBE0-13	(6-21G*)	*q*	-0.344	0.056	0.175	1.542 *0.362*
		μ	0.163	0.794	-0.009	
		R		2.038	1.469	
		b		-0.100	0.267	

In this C_{3v} geometry, the unique C atom (C_A) involved in the broken bond acquires a small positive charge of ~ 0.07 *e*. In comparison, the other three equivalent C_B atoms have charge ~ 0.26 *e*, which together compensate for the negative charge on the N atom. The charge on the second-neighbour carbons is almost neutral. The localisation of spin on the C_A atom (0.75 *e*) and the N atom (0.17 *e*) is confirmed by the spin moments (μ), which is consistent with the literature due to the repulsion between the lone pair on the N atom and the electron in the dangling bond on the C_A atom. Values of spin density up to several shells of neighbour atoms from the defect site were only 0.03–0.004 *e* (with alternating sign). The antibonding interaction between the N and C_A atom was also confirmed by the negative value of the N-C_A bond population of approximately -0.07 *e*. The value of the N-C_B population bond (+ 0.26 *e*) is positive and approximate to the conforming value in pure diamond (+0.34 *e*).

3.3.2.2 Electronic structure

The band structures of the C-centre in diamond computed with B3LYP functional and four different supercell size are reported in Figure 3.5. Two bands appear in the gap: one occupied band (spin-up) is deeply localised in the gap while another unoccupied band (spin down) is situated below the conduction band; the major contribution to both comes from the C atom in the long N-C bond (C_A in Figure 3.4). The band gap in the α and β DOS are shown in Table 3.4 together with the band gap in a pure diamond. The values vary with the functional and basis set used, affected by the band gap of a pure diamond as reported before.[49] The α band is varies less with supercell size from 64 to 128-atoms and show a small increase of 0.2 eV in the 216 and 512- atoms. The calculated density of states, shown in Figure 3.6 for α and β spin, confirm that most of the contributions of the defect states come from C_A while only ~20% for α and ~10% for β were from the N atom, again in agreement with earlier work.[49]

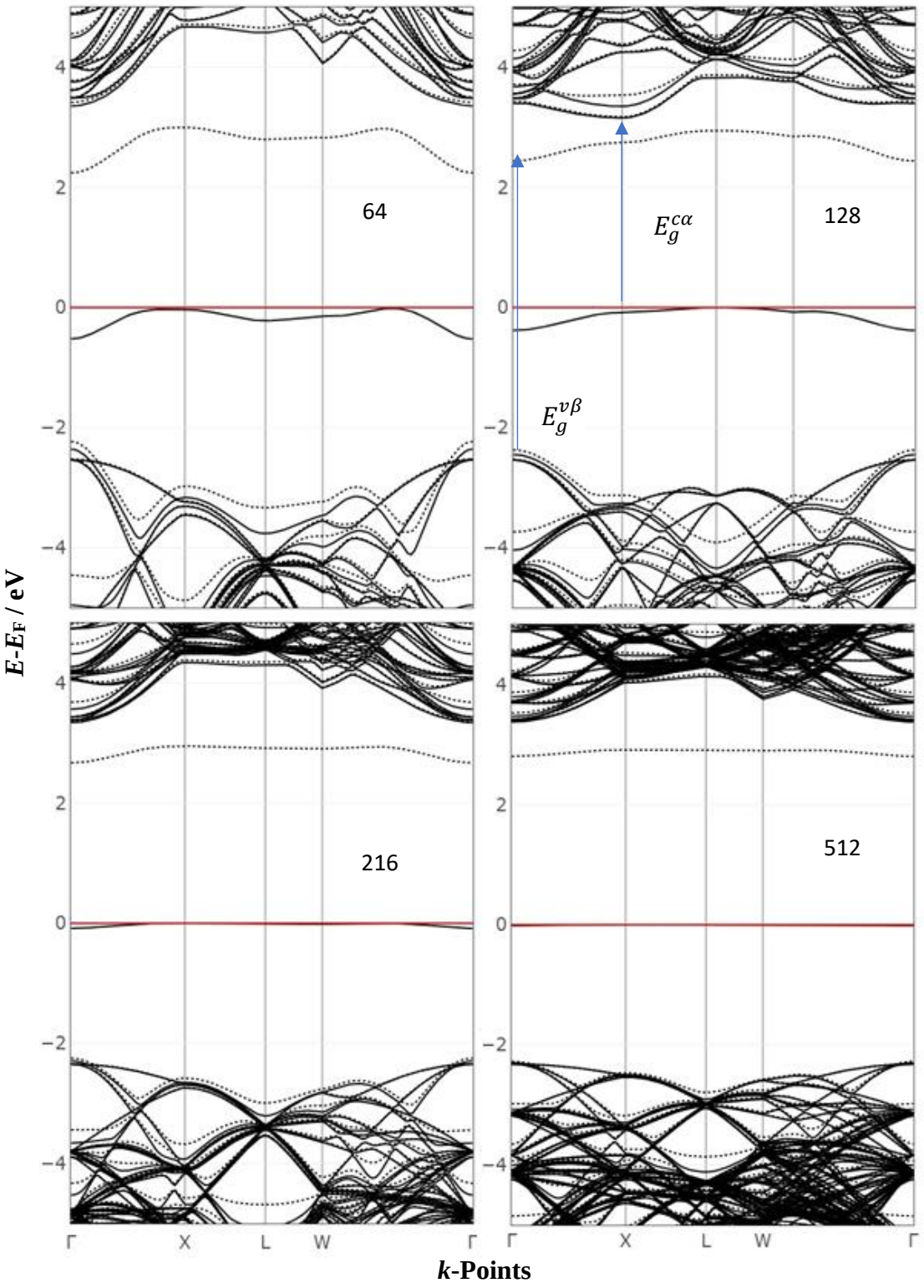

Figure 3-5 Band structures of the N defect in a substitutional site with C_{3v} symmetry and four supercell sizes: 64, 128, 216 and 512. All calculations were performed with B3LYP and the C/6-21G* and N/TZVP basis set. The energies are presented relative to the Fermi energy. The red line refers to Fermi level, and the continuous and dashed black lines refer to the (spin up) and (spin down) energy levels, respectively.

Table 3.4 Shows band gaps calculated with different functionals and a basis set of C, with $E_g^{c\alpha}$, $E_g^{v\beta}$ as indicated in Figure 3-5. E_g^{pure} is the corresponding band gap in pure diamond. All energies are in eV. SC refers to supercell size.

SC	Functionals /basis set of C		$E_g^{c\alpha}$	$E_g^{v\beta}$	E_g^{pure}	Reference [49]		
						$E_g^{c\alpha}$	$E_g^{v\beta}$	E_g^{pure}
64	HSE06	(6-21G*)	2.603	4.092	5.15	2.46	4.23	5.17
128			2.603	4.429				
216			2.829	4.507				
128		TZVP	2.694	4.599	5.38			
64	B3LYP	(6-21G*)	3.153	4.476	5.71	3.01	4.59	5.56
128			3.157	4.813		3.02	4.95	5.73
216			3.338	4.919		3.15	5.04	5.73
512			3.376	5.080		3.22	5.22	5.76
64	PBE0	(6-21G*)	3.327	4.726	5.79	3.19	4.86	5.80
128			3.325	5.069				
216			3.546	5.152				
64	PBEsol0	(6-21G*)	3.198	4.645	5.72			
128			3.198	4.990				
64	PBE0-13	(6-21G*)	4.056	5.383	6.43			
128			4.054	5.738				

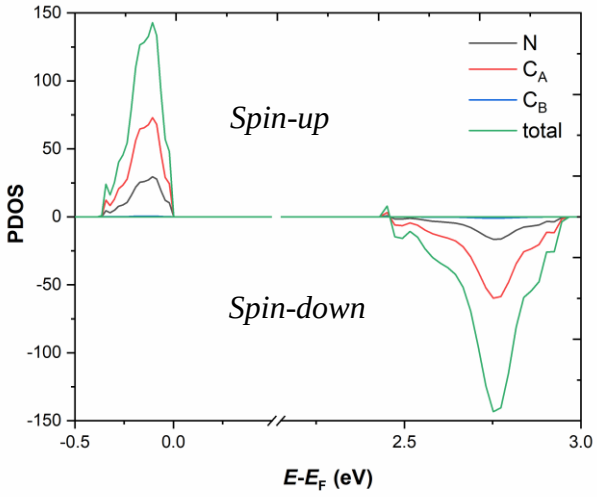

Figure 3-6 Projected DOS values of the C-centre bands that appear in the band gap calculated with 128-atom supercells, B3LYP, and C/6-21G* and N/TZVP basis sets. Atoms C_A and C_B are as indicated in Figure 3.4.

3.3.2.3 Infrared spectrum

In pure diamond, the Raman spectra are very simple and characterises by a single peak at 1332 cm^{-1}. The computed counterpart with HSE06, PBE0, PBEsol0, PBE0-13 and B3LYP were at 1362.24, 1368.11, 1376.87, 1394.14 and 1331.58 cm^{-1}, respectively (using the 6-21G* basis set and primitive cell).

In these sections, we aim to explore the IR spectra for the C-centre and compare the results from the previous calculations with those using the CRYSTAL code. The 64-atom supercell size was adopted here to decrease the computational cost associated with this calculation. B3LYP with 6-21G* were chosen due to the resulting Raman frequency value being closest to the experimental one at 1332 cm^{-1}.

The IR spectra of the C-centre defect are shown in Figure 3.7 and comprise five intense peaks; their frequencies are summarised in Table 3.5 and compared with their corresponding values in reference.[49] Table 3.5 indicates that, despite the different methods used in this calculation with open shell system, only minor shifts (approximately 1–6 cm^{-1}) were observed in the frequencies, and the overall shape of the spectrum was almost maintained. The most intense peak localised at 1132 cm^{-1} was in good agreement with the previous calculations and experimental results.[50] The spectrum of N^{15} in a single substitutional lattice site shows a shift of approximately 6 cm^{-1} for the most intense peak at 1132 cm^{-1} as previously experimentally observed. [51]

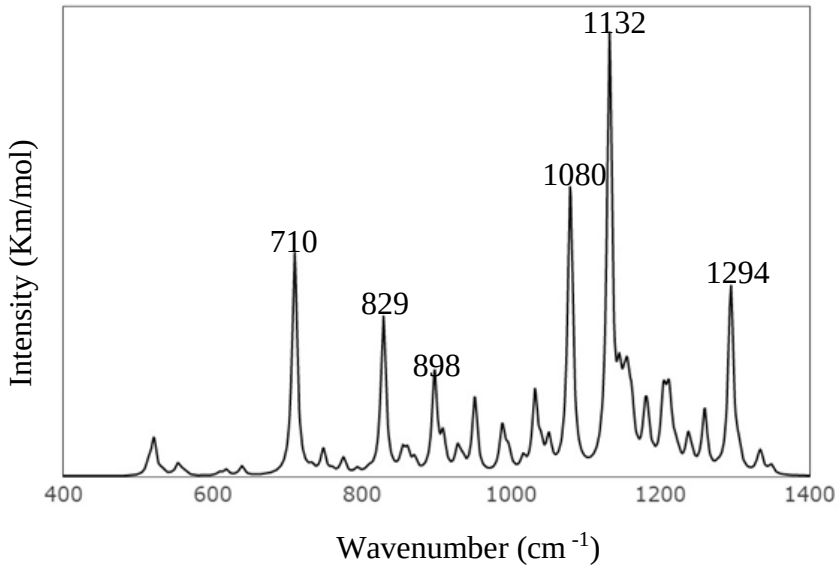

Figure 3-7 B3LYP (6-21G*)-simulated IR spectra for the C-centre defect obtained with a 64-atom supercell.

Table 3.5 B3LYP (6-21G*) wavenumbers (in cm^{-1}) as obtained from the 64-supercell size for the C-centre compared with reference.[49] The isotopic wave numbers of N^{15} and their shifts (all in cm^{-1}).

$\bar{\nu}$ (cm^{-1})	$\bar{\nu}$ (cm^{-1}) [49]	Isotopic N^{15} $\bar{\nu}$ (cm^{-1})	Isotopic Shift of N^{15} (cm^{-1})
1294	1287	1294	0
1132	1130	1126	6
1080	1074	1076	4
898	897	896	2
828	831	826	2
710	712	705	5

3.3.3 Phosphorus

3.3.3.1 Energy, geometry, charge and spin distribution

The system of the phosphorus in its substitutional site is an open-shell solution: one electron is donated by the P atom to the diamond lattice. From the brief review in the introduction, there are mainly two possible symmetries for P in substitutional sites: C_{3v} and D_{2d}. These configurations can only be obtained by either moving the P atom from the original position in the T_d along [111] direction (as with the C-centre) by 0.08 Å that directly breaks the symmetry into C_{3v} (six symmetry operations) or, it can be obtained by displacing their first neighbours in directions that preserve the D_{2d} symmetry (eight symmetry operations).

To investigate the relative energy between the two configurations, we performed the calculations using different supercell sizes and hybrid functionals to make a comprehensive comparison. Both structures (C_{3v} and D_{2d}) retained their symmetry after repeated the calculation with release the symmetry, indicating both structures are stable. Figure 3.8 shows the resulting geometry as calculated using B3LYP. It is worth noticing that the D_{2d} structure was very sensitive to the relative angles between the first neighbours at the beginning of the calculations, as indicated in Figure 3.8. The difference in energy between the two geometries was very small < 0.1 eV in all the calculations, with C_{3v} having the lower energy (Table 3.6). Performing the calculation with a 512 supercell and B3LYP gave a very small value in the energy difference, 0.003 eV.

The geometric data obtained from all the functionals, bond populations, charges, and spin distributions are listed in Table 3.7. The defect causes elongation of all the bonds around P by ~ 0.2 Å relative to pure bonds, with high bond population in all the bonds (~0.23 *e*), except

the long bond in the C_{3v} structure. The former showed a drop in bond population by about one order of magnitude compared to the other three bonds, but it was still positive compared to the corresponding one in the C-centre. This indicated that the bonding interaction induced by overlapping the orbitals of the defect with the host atoms was due to the size of the P atom. Mulliken analysis showed that a P atom acquired a positive charge of ~ +0.8 *e*, all the neighbouring C atoms gain a charge of ~ -0.16 *e*. This was expected from the difference in electronegativity between the two atoms. In both geometries, the net spin per cell was one electron. The significant point appeared with a high-spin density on the P atom in both geometries (~ 0.4 *e*). The neighbouring C atoms showed almost zero spin density in D_{2d}. In contrast, in C_{3v} the carbon atom involved in the elongated bond showed a small apparent spin density (~ 0.08 *e*) compared to the other three C atoms (~ 0.01 *e*).

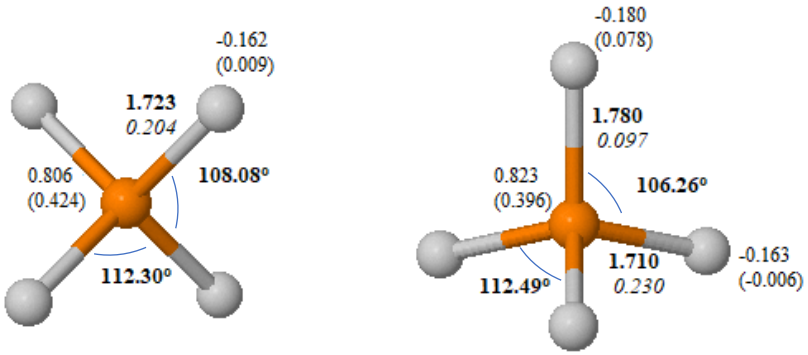

Figure 3-8 Show bond distances (in Å); angle (both **bold**); spin momentum (between brackets); Mulliken charges; bond overlap population (*italics*) (all in *e*) for the first neighbours of the P points defects (with C_{3v} on the right and D_{2d} on the left). Grey and orange indicate C and P atoms, respectively. The two configurations were calculated with the C/6- 21G* and P/TZVP basis sets, and B3LYP and 128-atom supercells.

3.3.3.2 Electronic structure

In this section, we will provide only the analysis for the C_{3v} electronic configuration. Figure 3.9 shows the band structures of the P defect in a substitutional site in its C_{3v} symmetry with four supercell sizes: 64, 128, 216 and 512. These were compared to those for pure diamond calculated using B3LYP.

Table 3.6 Energies (in hartree) of P in the substitutional site with the two symmetry C_{3v} and D_{2d}. E_R is the relative energy (in eV). E_g^C is the band gaps along α and β states, as indicated in band structure plots. All calculations were performed with C/6-21G* and P/TZVP basis sets, with arrange of supercell (SC) sizes.

Functionals	Basis set of C	C_{3v}	D_{2d}	E_R	SC	E_g / C_{3v}		E_{pure}^C
						$E_g^{\alpha C}$	$E_g^{\beta v}$	
HSE06	6-21G*	-2738.39468	-2738.39229	0.065	64	metallic	4.772	5.15
		-5173.86904	-5173.86818	0.023	128	metallic	4.907	
		-8522.64896	-8522.64758	0.037	216	0.093	5.033	
HSE06	TZVP	-5177.59216	-5177.59097	0.032	128	0.057	5.150	5.38
B3LYP	6-21G*	-2739.27458	-2739.27179	0.075	64	0.245	5.333	5.71
		-5175.57125	-5175.56851	0.074	128	0.472	5.489	
		-8525.48491	-8525.48359	0.035	216	0.553	5.579	
		-1979.33741	-1979.33731	0.003	512	0.680	5.635	
PBE0	6-21G*	-2738.43417	-2738.43138	0.075	64	0.470	5.422	5.79
		-5173.94965	-5173.94676	0.078	128	0.678	5.577	
		-8522.78929	-8522.78790	0.037	216	0.778	5.688	
PBE0-13	6-21G*	-2738.58956	-2738.58651	0.082	64	1.013	6.049	6.43
		-5174.25906	-5174.25631	0.074	128	1.193	6.212	
PBEsol0	6-21G*	-2731.27667	-2731.27447	0.059	64	0.356	5.346	5.72
		-5159.93203	-5159.92962	0.065	128	0.581	5.499	

Table 3.7 Show spin momentum (μ); Mulliken atomic charges (*q*); (both in *e*); equilibrium distances of the first neighbours from the P (*R*) (in Å); the overlap bond population of the bond between P atoms and the first neighbours (*b*) (in *e*). All data refer to 128-atom supercells calculations.

Functionals		C_{3v}			D_{2d}	
		P	3C	C	P	4C
HSE06	*q*	0.806	-0.159	-0.171	0.821	-0.162
	μ	0.333	-0.013	0.055	0.289	-0.000
	R		1.705	1.749		1.714
	b		0.259	0.128		0.245
B3LYP	*q*	0.823	-0.163	-0.180	0.806	-0.162
	μ	0.396	-0.006	0.078	0.424	0.009
	R		1.710	1.780		1.723
	b		0.230	0.097		0.204
PBE0	*q*	0.764	-0.155	-0.170	0.744	-0.152
	μ	0.433	-0.012	0.080	0.465	0.002
	R		1.703	1.773		1.716
	b		0.217	0.089		0.195
PBE0-13	*q*	0.775	-0.159	-0.177	0.747	-0.155
	μ	0.482	-0.010	0.089	0.527	0.002
	R		1.700	1.777		1.713
	b		0.191	0.091		0.181
PBEsol0	*q*	0.709	-0.143	-0.158	0.688	-0.141
	μ	0.400	-0.009	0.078	0.438	0.006
	R		1.700	1.764		1.712
	b		0.231	0.086		0.199

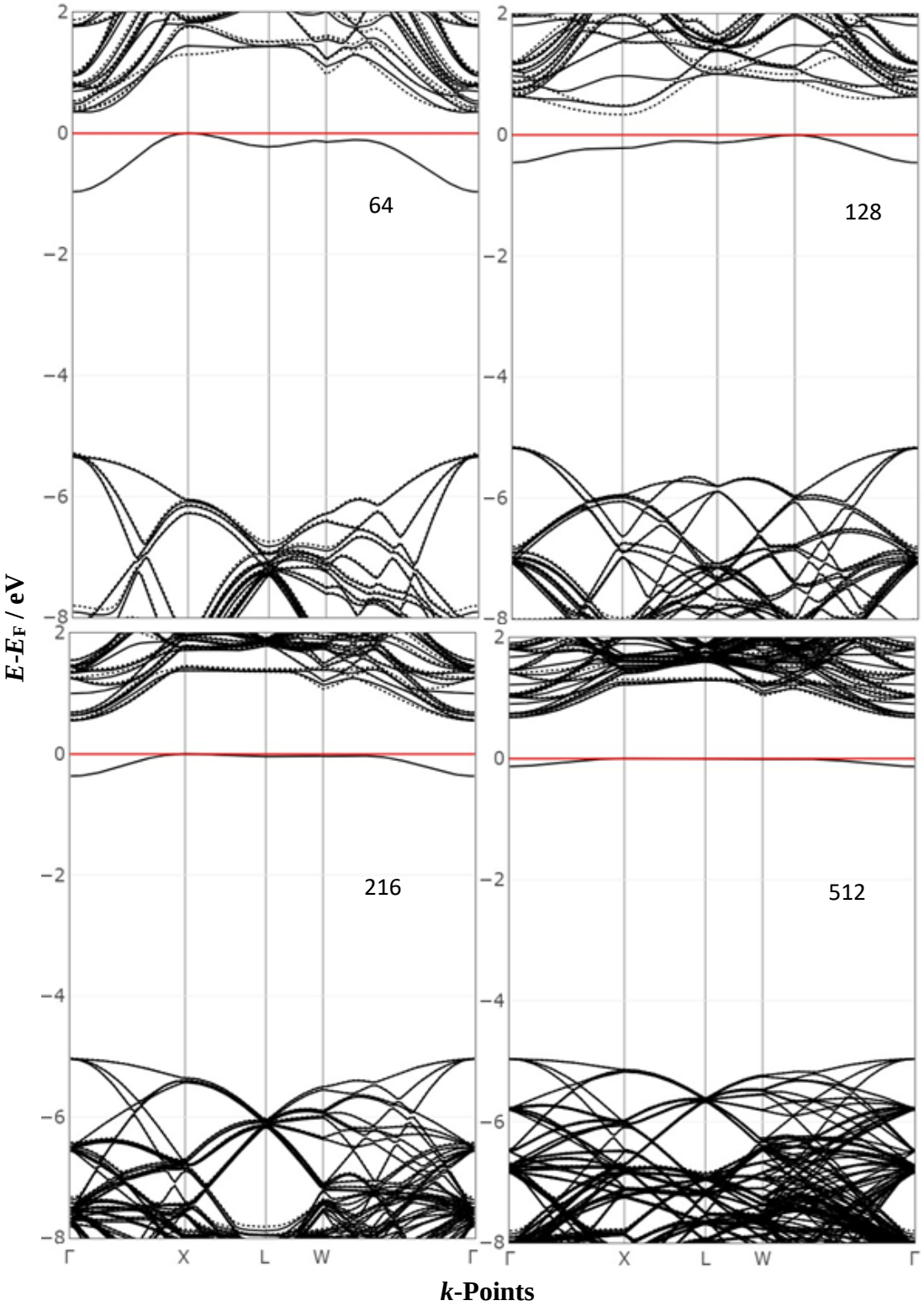

Figure 3-9 Band structure comparing four defective supercells containing P in a substitutional site, 64, 128, 216 and 512. All calculations were computed using C/6-21G* and P/TZVP basis sets, and the B3LYP. The energies are presented relative to the Fermi energy. The red line refers to Fermi level, and the continuous and dashed black lines refer to the (spin up) and (spin down) energy levels, respectively. The corresponding symmetry is C_{3v}.

The non-degenerate state occupied by the donor electron is a shallower level compared to the corresponding N level (Table 3.4). The resulting indirect band gap between this level and the bottom of the conduction band was (0.1-1.2 eV) affected by the band gap of pure diamond, as seen previously with the C-centre. The empty β state associated with the defective donor level overlapped with the conduction band minimum, which made it difficult to distinguish in the band gap, approximately 5-6 eV above the valence band. This created an indirect band gap. The orbital overlap for a given internuclear distance was large with P compared to that with N, due to the larger atomic size of P, which resulted in the formation of a shallower level. The energy dispersion of the impurity levels shows an obvious reduction with an increase in the supercell size. The band gaps increased by about 0.1 eV with increasing supercell sizes, which indicate defect-defect interaction. The contribution of the P atom in the donor band is the higher, ~32%, and ~7% come from the C atom involves in the long P-C bond (C_A), and ~2% come from the other three equivalents C atoms (C_B) (Figure 3-10).

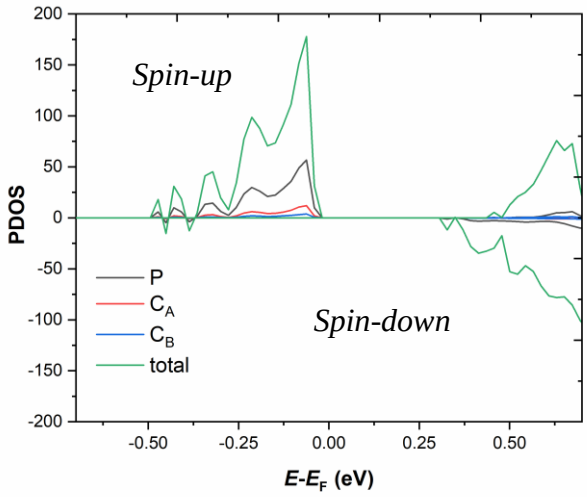

Figure 3-10 Projected DOS of the P_{sub} donor band appears in the band gap calculated with 128-atom supercell, B3LYP, and C/6-21G* and P/TZVP basis sets. C_A the carbon atom involves in the long P-C bond and C_B the other three equivalents nearest-neighbour C atoms.

3.4 Conclusion

In this work, a series of hybrid DFT functionals were used to explore the vacancy, C-centre and phosphorus in substitutional site point defects. The geometric, energetic electronic and vibrational features of these defects demonstrated a good agreement with the previous

calculations. The vacancy centre in its spin states— singlet, triplet, and quintuplet— was characterised. The polarised singlet spin state became the ground state. It was more stable than the triplet state, but only by ~0.1 eV. The electronic configurations evaluated from the band structure were analysed in detail.

In the C-centre, the local geometry with C_{3v} symmetry exhibited three shortened bonds of ~1.47 Å and one elongated bond along the C_3 axis. The spin density was highly localised on the carbon atom that was involved in the broken bond. The non-binding nature between the N lone pair and one of the carbon atoms led to a deep-donor state occupied by one α electron that appeared in approximately the middle of the gap, and another unoccupied β state located below the conduction band. The vibrational frequency of the C-centre showed a sharp peak at 1132 cm^{-1}. It was associated with an isotopic shift (N^{14}-N^{15}) of approximately 6 cm^{-1} to a lower frequency, in a good agreement with a previously reported value of 1130 cm^{-1}.[49]

Turning to the P defect, we mainly explored the relative energies between the two symmetries C_{3v} and D_{2d} that have been extensively investigated in the literature. In all the calculations, the C_{3v} was lower in energy by less than 0.1 eV. The structures corresponding to each symmetry were reported in detail. This defect led to a shallow level compared to the C- centre, occupied by a donor electron, and which appeared below the conduction band. The associated unoccupied acceptor state merged with the conduction band and gave a wide gap of ~ 5 eV from the highest level of their valence band. The band gaps along with the majority and minority spin state were affected by defect concentration and increased with the supercell size, as noticed with the C-centre. All of the energies computed in this chapter are to be used in Chapters 4 and 7 to calculate the formation, binding, and ionisation energies of complexes.

3.5 References

1. Steeds, J. W. *et al.* Creation and mobility of self-interstitials in diamond by use of a transmission electron microscope and their subsequent study by photoluminescence microscopy. *Diam. Relat. Mater.* **8**, 94–100 (1999).
2. Davies, G., Lawson, S. C., Collins, T., Mainwood, A. & Sharp, J. Vacancy-related centers in diamond. *Phys. Rev.* **46**, 157–170 (1992).
3. Coulson, C. A. & Kearsley, M. J. Colour centres in irradiated diamonds. **241**, 433–454 (1957).
4. Walker, J. Optical absorption and luminescence in diamond. *Reports Prog. Phys.* **42**,

1605–1659 (1979).

5. Jahn, H. A. & Teller, E. Stability of Polyatomic Molecules in Degenerate Electronic States I—Orbital Degeneracy. *Proc. R. Soc.* **161**, 220–235 (1937).
6. Breuer, S. J. & Briddon, P. R. Ab initio investigation of the native defects in diamond and self-diffusion. *Phys. Rev. B* **51**, 6984–6994 (1995).
7. Deák, P., Aradi, B., Kaviani, M., Frauenheim, T. & Gali, A. Formation of NV centers in diamond: A theoretical study based on calculated transitions and migration of nitrogen and vacancy related defects. *Phys. Rev. B - Condens. Matter Mater. Phys.* **89**, 1–12 (2014).
8. Zelferino, A. *et al.* The electronic states of the neutral vacancy in diamond: a quantum mechanical approach. *Theor. Chem. Acc.* **135**, 1–11 (2016).
9. Farrer, R. G. On the substitutional nitrogen donor in diamond. *Solid State Commun.* **7**, 685–688 (1969).
10. Iakoubovskii, K. & Adriaenssens, G. J. Optical transitions at the substitutional nitrogen centre in diamond. *J. Phys. Condens. Matter* **12**, (2000).
11. Dyer, H. B., Raal, F. A., Du Preez, L. & Loubser, J. H. N. Optical absorption features associated with paramagnetic nitrogen in diamond. *Philos. Mag.* **11**, 763–774 (1965).
12. Messmer, R. P. & Watkins, G. D. Molecular-orbital treatment for deep levels in semiconductors: Substitutional nitrogen and the lattice vacancy in diamond. *Phys. Rev. B* **7**, 2568–2590 (1973).
13. Jones, R. & Goss, J. P. Theory of aggregation of nitrogen in diamond. *EMIS Datareviews Ser.* **26**, 127–129 (2002).
14. Lombardi, E. B., Mainwood, A., Osuch, K. & Reynhardt, E. C. Computational models of the single substitutional nitrogen atom in diamond. *J. Phys. Condens. Matter* **15**, 3135–3149 (2003).
15. Kajihara, S. A., Antonelli, A., Bernholc, J. & Car, R. Nitrogen and potential n-type dopants in diamond. *Phys. Rev. Lett.* **66**, 2010–2013 (1991).
16. Hang, D. B. Electronic Band Structure of N and P Dopants in Diamond. *Bull. Korean Chem. Soc.* **19**, 628–634 (1998).
17. Anderson, A. B. & Kostadinov, L. N. P and N compensation in diamond molecular orbital theory. *J. Appl. Phys.* **81**, 264–267 (1997).
18. Kociniewski, T. *et al.* N-type CVD diamond doped with phosphorus using the MOCVD technology for dopant incorporation. *Phys. Status Solidi Appl. Mater. Sci.* **203**, 3136–3141 (2006).

19. Koizumi, S., Teraji, T. & Kanda, H. Phosphorus-doped chemical vapor deposition of diamond. *Diam. Relat. Mater.* **9**, 935–940 (2000).
20. Kato, H., Futako, W., Yamasaki, S. & Okushi, H. Growth of phosphorus-doped diamond using tertiarybutylphosphine and trimethylphosphine as dopant gases. *Diam. Relat. Mater.* **14**, 340–343 (2005).
21. Chen, C. F., Lo, S. F. & Chen, S. H. The synthesis and characterization of phosphorus-doped diamond films using trimethyl-phosphite as a dopping source. *Diam. Relat. Mater.* **5**, 766–770 (1996).
22. Cao, G. Z., Giling, L. J. & Alkemade, P. F. A. Growth of phosphorus and nitrogen co-doped diamond films. *Diam. Relat. Mater.* **4**, 775–779 (1995).
23. Koizumi, S. Growth and characterization of phosphorus doped n-type diamond thin films. *Phys. Status Solidi Appl. Res.* **172**, 71–78 (1999).
24. Goss, J. P., Briddon, P. R., Jones, R. & Sque, S. Donor and acceptor states in diamond. *Diam. Relat. Mater.* **13**, 684–690 (2004).
25. Wang, L. G. & Zunger, A. Phosphorus and sulphur doping of diamond. *Phys. Rev. B - Condens. Matter Mater. Phys.* **66**, 1–4 (2002).
26. Eyre, R. J., Goss, J. P., Briddon, P. R. & Hagon, J. P. Theory of Jahn-Teller distortions of the P donor in diamond. *J. Phys. Condens. Matter* **17**, 5831–5837 (2005).
27. Sque, S. J., Jones, R., Goss, J. P. & Briddon, P. R. Shallow Donors in Diamond: Chalcogens, Pnictogens, and their Hydrogen Complexes. *Phys. Rev. Lett.* **92**, 4 (2004).
28. Nishimatsu, T., Katayama-Yoshida, H. & Orita, N. Ab initio study of donor-hydrogen complexes for low-resistivity n-type diamond semiconductor. *Japanese J. Appl. Physics, Part 1 Regul. Pap. Short Notes Rev. Pap.* **41**, 1952–1962 (2002).
29. Butorac, B. & Mainwood, A. Symmetry of the phosphorus donor in diamond from first principles. *Phys. Rev. B - Condens. Matter Mater. Phys.* **78**, 1–8 (2008).
30. Orita, N., Nishimatsu, T. & Katayama-Yoshida, H. Ab initio study for site symmetry of phosphorus-doped diamond. *Japanese J. Appl. Physics, Part 1 Regul. Pap. Short Notes Rev. Pap.* **46**, 315–317 (2007).
31. Krukau, A. V., Vydrov, O. A., Izmaylov, A. F. & Scuseria, G. E. Influence of the exchange screening parameter on the performance of screened hybrid functionals. *J. Chem. Phys.* **125**, 0–5 (2006).
32. Becke, A. D. Density-functional thermochemistry. I. The effect of the exchange-only gradient correction. *J. Chem. Phys* **3**, 2155–2160 (1992).
33. Adamo, C. & Barone, V. Toward chemical accuracy in the computation of NMR

shieldings: The PBE0 model. *Chem. Phys. Lett.* **298**, 113–119 (1998).

34. Guido, C. A., Brémond, E., Adamo, C. & Cortona, P. Communication: One third: A new recipe for the PBE0 paradigm. *J. Chem. Phys.* **138**, 0–4 (2013).
35. Perdew, J. P. *et al.* Generalized gradient approximation for solids and their surfaces. 2–5 (2007). doi:10.1103/PhysRevLett.100.136406
36. Perdew, J. P. *et al.* Restoring the density-gradient expansion for exchange in solids and surfaces. *Phys. Rev. Lett.* **100**, 1–4 (2008).
37. Dovesi, R. *et al.* C RYSTAL 14 : A Program for the Ab Initio Investigation of Crystalline Solids. *Int. J. Quantum Chem.* **114**, 1287–1317 (2014).
38. Catti, M., Pavese, A., Dovesi, R. & Saunders, V. R. Static lattice and electron properties of MgCO3 (magnesite) calculated by ab initio periodic Hartree-Fock method. *Phys. Rev. B* **47**, 9189 (1993).
39. Dovesi, R., Causa', M., Orlando, R., Roetti, C. & Saunders, V. R. Ab initio approach to molecular crystals: A periodic Hartree-Fock study of crystalline urea. *J. Chem. Phys.* **92**, 7402–7411 (1990).
40. Peintinger, M. F., Oliveira, D. V. & Bredow, T. Consistent Gaussian Basis Sets of Triple-Zeta Valence with Polarization Quality for Solid-State Calculations. **813**, 451–459 (2013).
41. Monkhorst, H. J. & Pack, J. D. Special points for Brillouin-zone integrations. *Phys. Rev. B* **13**, 5188–5192 (1976).
42. Pisani, C., Dovesi, R. & Roetti, C. *Hartree-Fock Ab Initio Treatment of Crystalline Systems*. (Springer Berlin Heidelberg, 2012).
43. Saunders, V. R. *et al.* CRYSTAL User Manual. (2003).
44. F. Pascale, C.M. Zicovich-Wilson, F. Lopez, B. Civalleri, R. Orlando, R. D. The Calculation of the Vibrational Frequencies of Crystalline Compounds and Its Implementation in the CRYSTAL Code. *J. Comput. Chem.* **25**, 888–897 (2004).
45. Salustro, S. *et al.* Substitutional boron and nitrogen pairs in diamond. A quantum mechanical vibrational analysis. *Carbon N. Y.* **146**, 709–716 (2019).
46. Pascale, F. *et al.* The Infrared spectrum of very large (periodic) systems: global versus fragment strategies—the case of three defects in diamond. *Theor. Chem. Acc.* **137**, 1–7 (2018).
47. Briddon, P. R. & Jones, R. Theory of impurities in diamond. *Phys. B Phys. Condens. Matter* **185**, 179–189 (1993).
48. Bernholc, J., Kajihara, S. A., Wang, C., Antonelli, A. & Davis, R. F. Theory of native

defects, doping and diffusion in diamond and silicon carbide. *Mater. Sci. Eng. B* **11**, 265–272 (1992).

49. Ferrari, A. M., Salustro, S., Gentile, F. S., Mackrodt, W. C. & Dovesi, R. Substitutional nitrogen atom in diamond. A quantum mechanical investigation of the electronic and spectroscopic properties. *Carbon N. Y.* **134**, 354–365 (2018).
50. Collins, A. T. & Woods, G. S. An anomaly in the infrared absorption spectrum of synthetic diamond. *Philos. Mag. B Phys. Condens. Matter; Stat. Mech. Electron. Opt. Magn. Prop.* **46**, 77–83 (1982).
51. Collins, A. T., Stanley, M. & Woods, G. S. Nitrogen isotope effects in synthetic diamonds. *J. Phys. D. Appl. Phys.* **20**, 969–974 (1987).

CHAPTER 4

ELECTRONIC AND MAGNETIC STRUCTURE OF SUBSTITUTIONAL Mg AND N IN DIAMOND: SPIN POLARIZED, HYBRID DFT

CHAPTER 4 – ELECTRONIC AND MAGNETIC STRUCTURE OF SUBSTITUTIONAL Mg AND N IN DIAMOND; SPIN-POLARIZED, HYBRID DFT

4.1 Introduction

Although it has been proven that the n-type diamond semiconductor can be obtained with phosphorus doping, the resulting ionisation energy (0.6 eV) and mobility (~23–28 $cm^2/V\ s$) [1–4] are still inadequate for practical application. Theoretical studies have revealed that this is partly because the effects of the many phosphorus atoms incorporated in the diamond lattice are compensated by acceptor states. For instance, a phosphorus-vacancy[5] complex was found theoretically to produce an acceptor state at E_c - 4.5 eV (below the conduction band minimum). [6] PH complex was also predicted to be stable, with H being in the antibonding site, producing a deep level at E_c -2.86 eV.[7]

A number of single dopants have been proposed theoretically to be a potential donor in diamond (Table 4.1). One of these candidates is the substitutional arsenic [8,9] with an ionisation energy of ~ E_c -0.3-0.4 eV[8], producing a level shallower than phosphorus by ~0.1 eV. [9] However, the formation energy of this defect is very high (~ 10.4 eV) [9], which prevents its incorporation in diamond with a detectable donor level. [10] Lithium and sodium at the tetrahedral interstitial site has also been predicted to be a donor for diamond [11,12], but with the limitation that same dopants occupy the substitutional site and then behave as a deep acceptor, which, in the case of Na, is more energetically favourable, as the formation energy of Na_{sub} is 2.87 eV[12] lower than that of the interstitial site. Even though Li prefers both sites, it has been predicted to be mobile under elevated temperatures in CVD conditions and cluster spontaneously at neighbouring tetrahedral interstitial sites.[13,14] One calculation suggests one interstitial lithium atom induces C–C bond breaking by introducing an extra band below the conduction band minimum. [15] This leads to the deactivation of any donor level produced by an isolated interstitial. The transition state for the diffusion of Li between two tetrahedral interstitial sites is located at a hexagonal interstitial site, and the energy barrier is calculated to be around 1.1[15], 0.85[11,16], 1.09[15] and 1.3 eV[17,14], significantly lower than that for Na_i diffusion (3.5 e)[14] and in line with the highest value found experimentally for Li diffusion from a solid source, which is 0.9 ± 0.3 eV[19] and 0.26 eV.[18] Such a low barrier explains the observed reduction of conductivity measured for an Li- implanted diamond after heating at 600 ^oC[20], which is attributed to the passivation of Li interstitial donors by another complex.[19,18]

Sulfur was also among the elements that attracted a special interest in the doping of diamond. Sakaguchi et al. reported that a doped diamond with sulfur using hydrogen sulphide (H_2S) as a source shows conductivity with electron mobilities at about 597 cm^2/Vs at room temperature and an activation energy of 0.38 eV obtained in a range of 250–550 K.[21,22] However, their samples were shown later by Kalish et al.[23] to be unintentionally contaminated by boron. The n-type conduction of a sulfur-doped diamond using CVD was observed in another study, with an estimated activation energy at 0.5–0.75 eV above 600 K.[24] The boron concentration in these samples was below the detection limit, and sulfur concentration was ~ 3×10^{16} cm^{-3}. The sulfur also implanted in diamonds with a concentration up to 10^{20} cm^{-3}.[25] The samples show an increase in the activation energy, from 0.19–0.33 eV in a temperature range below 700 K to 1.9 eV at above 900 K, which attributed to activating the nitrogen-related defects (100 ppm). The higher activation energy is in line with most theoretical calculations predicting that the sulfur will behave as a deep double-donor in diamonds with an activation energy at 1.4[8], 1.53[26], 1.63 [27,28] and 1.2[29] eV below the conduction band. The sulphur in the substitutional site undergoes a Jahn–Teller distortion, reducing the symmetry from T_d to C_{3v}, which leads to a split of the partially occupied (two electrons) t_2 orbital (E_c-0.8 eV) to a_1 fully occupied (Ec-1.63 eV) and empty e orbitals.[28] Such distortions may not have been considered in the calculations that predicted S being shallower than P. [30,31]

Co-doping, i.e., forming a donor-acceptor-donor complex, to control the valence electrons is another possible route to produce n-type doped diamond. Different theoretical approaches have led to the proposal of various candidates, such as LiN_4, BeN_3, BN_2, AlN_2, BS, HS, 2NH and Si_4N.[26,28,30,32–36] The calculated ionisation energies of these clusters are the same or higher than that of single substitutional P, except for LiN_4.

The main difficulty with co-doping two light elements, such as Li and N, into a diamond is the low activation energy, which, in turn, leads to the formation of various electrically inactive complexes during exposure to heat. Experimental studies have provided evidence that nitrogen can also diffuse through diamond-forming complexes, such as the A-centre and the B-centre[189]. In these cases, there are two possible diffusion mechanisms: trapping of the substitutional nitrogen by a thermally produced mobile vacancy (V) or a self-interstitial (I) (carbon in an interstitial site).[38, 39] Both V and I formation energies in diamond have been predicted to be very large: about 7–6[40,41,17,16,42] and 12 eV[43,44], respectively. It is assumed that there is an internal source of vacancies or interstitials formed, for instance, by electron irradiation[45] or by a catalyst used in the HPHT process.[46–48] The migration barriers of V and I

were calculated to be 2.4 eV[49], 2.3±0.3 eV[44] and 1.6 [38] eV, respectively. However, it is expected from the previous calculations that N can diffuse via the formation of the N_i complex (N_i, nitrogen trapped by self-interstitial) with a low migration barrier of ~ 1.8 eV[38,39,50] compared to a direct exchange of the nitrogen with a neighbouring carbon atom[51] that has been predicted to have much higher activation energy (6.3 eV)[49], (8 eV).[52,39]

In this study, we explore a new co-doping system—nitrogen with magnesium for n- type doping—with which we aim to avoid the inactive complex observed previously in the N-Li[70] system. The stability of the multi-complex of Mg and N in diamond is predicted based on the stability of the corresponding N_xV complexes (X = 1-4), where the N atoms tend to diffuse to the vacancy to terminate the dangling bonds upon annealing. Replacing the vacancy with an Mg atom that has two dangling bonds is presumed to play a similar role as a vacancy. We have studied the geometric, magnetic and electronic properties of individual point defects, including Mg, and multi-complex defects, including MgN_2, 2NV and MgN_3 in diamond using a supercell approach. The formation, binding and ionisation energies were calculated for the systems using different methods to predict the solubility, stabilities of the dopants and the possible formation path.

4.2 Computational Setup

For details on the CRYSTAL code, and discussion of the parameters used, please see Chapter 3.

4.3 Results and discussion

The following section is separated into two parts: the first part presents a description for the geometry, the electronic structure and the formation energy of an Mg defect. The second part presents the same analysis for the MgN_3 multi-complex point defect.

4.3.1 Single-substituted Mg atom

4.3.1.1 Charge, Geometry and spin densities

Different structural models of spin states corresponding to different point symmetries of the substitutional Mg defect in a diamond were considered (Figure 4.1 a,b).

Table 4.1 Summary of the ionisation energies calculated by different studies for various candidates to achieve n-type doping in a diamond.

Single dopant		**Co-doping**	
Atom	Ionization energy (eV)	**Complex**	Ionization energy (eV)
Li_i	0.1 shallower than P_{sub} [13]	Si_4N	E_c - 0.09 [36]
	E_c -0.1 [11,16]		0.1 below P_{sub} donor level [9]
	E_c -0.35 [15]	LiN_4	E_c - 0.48, 0.27±0.06 [34]
	E_c -0.4 [54]	BeN_3	E_c - 0.78, 0.62 [34]
	E_c -0.63[14]	N-N-B	E_v +1.43 [33]
			N_{sub} E_v +3.36
Na_i	E_c -0.3 [11,16]	N-B-N	E_c –1.17 [27]
	E_c -0.63 [14]		E_c – ~1.6-1.30 [55]
	E_v+3.6 [13]		E_c –1.30, 1.19 [34]
S	E_c -0.77 [56]	$S–H^c_{ab}$	E_c -0.61 [7]
	E_c -1.1 [7]	$S–H_{ab}$	E_c -1.0 [8]
	E_c -1.2 [29]	$S–H_{ab}$	E_c -1.07 [27,57]
	E_c -1.53[26]	SB	E_c -1.49[26]
	E_c -1.4 [8]	SBS	E_c -0.50 [29]
	E_c -1.63 [27,28]	SB	E_c -0.55 [30]
		SBS	E_c -0.50
			P_{sub} E_c -0.59
			S_{sub} E_c -0.30
Se	E_c -1.2 [8]	$Se–H^c_{ab}$	E_c -0.9 [8]
Te	E_c -1.4 [8]	$Te–H^c_{ab}$	E_c -0.4 (64) [8]
			E_c -0.7 (216)
As	E_c -0.3 eV (64) [8]	N-Al-N	E_c – ~0.6-0.75 [55]
	E_c -0.4 eV (216)	N-Al-N	E_v +3.73 [33]
			N_{sub} E_v +3.36
Sb	E_c -0.2 eV (64) [8]	N-Al-N	E_c -0.4 [35]
	E_c -0.3 eV (216)	N-Ga-N	E_c – ~0.6-0.7 [55]
		N-In-N	E_c – ~0.6 [55]
		$N-H_{bc}-N$	E_v + 4.42 [33]
			N_{sub} E_v +3.36
		$B-H_{2bc}$	E_c −1.84−2.88 [7]

(i); interstitial site
$S–H^c_{ab}$; the H in anti-bonding site behind the C atom that bonded to S
$S–H_{ab}$, ; the H in anti-bonding site behind the S atom
H_{bc}; the H in bond centre site

A closed-shell system of Mg, in which α and β electrons must occupy the same defective crystalline orbitals, showed higher energy by ~ 0.6–0.8 eV compared with all the open-shell calculations. In the open-shell solutions, the α and β electrons are permitted to occupy different defective crystalline orbitals (DCO), which for the Mg supercell, results in two spin states: the singlet $S_z = 0$ and triplet $S_z = 1$ (Figure 4.1). Full optimisation of the basis atom positions and lattice parameter following the substitution of a single carbon by a magnesium atom with $S_z = 1$, two α spin electrons, maintains the symmetry of the pure diamond T_d (24 symmetry operations). Mg in the substitutional site also has another structure, with C_{2v} symmetry and $S_z = 0$ found with the two supercells (64 and 128). This configuration was generated using ATOMSPIN with MODISYMM keywords to break the symmetry to the corresponding spin setting, as performed with the vacancy defect in Chapter 3. Release the symmetry with both spin setting maintains the structure and energy, indicating that both spin configurations are stable in diamond.

The relative energy of the two spin states is almost independent of the supercell sizes and the basis sets but does vary with the functionals used in the calculation. The triplet state becomes lower in energy than the singlet by ~ 0.1 eV with the HSE06, but this difference was reduced and reversed with the PBE0 and PBEsol0 to be ~ 0.03 eV, and with B3LYP the difference became of the order of 10^{-3} eV.

From Table 4.2, it appears that the computational conditions (i.e. choice of basis-set) change the values of the local perturbation of the lattice, i.e. bond lengths, charge and spin distribution slightly but preserve the overall trend. The outward relaxation associated with substitution of carbon with Mg atom leading to an increase in the C-C bond lengths from 1.546 and 1.535 Å in pure diamond with (6-21G*) and (TZVP) basis sets, respectively, to be about 1.85 Å in Mg-C bond, giving an increase of about 16-17%. The C-C bonds in which one of the C atoms (labelled by A and B in Figure 4.1) bonded to Mg showed a compression that resulted in a length of ~ 1.5 Å. A small change in the other C-C bonds was observed beyond the defect region (i.e. the bonds become ~1.54–1.56 Å). The calculated Mg-C Mulliken bond populations (*b*) were less than those for C-C in the host lattice (0.36 *e*) by about two orders of magnitude. However, the positive value of *b* indicates a bonding interaction. The charge distribution on the four nearest-neighbour carbon atoms shows a strong polarisation in Mg-C bonds as a result of the charge transfer from Mg to C due to the difference in the electronegativities. From the Mulliken atomic net charges, all the C atoms around the Mg gain a charge of ~ -0.3 *e*, and the

Mg consequently loses charge by ~ 1.2 *e*, while the charge on the second-neighbour carbons was very small (less than ~ 0.01 *e*).

Table 4.2 Show spin momentum (μ); Mulliken atomic charges (*q*) (both in *e*) at defect sites and on the four carbon atoms around the defect (C_α and C_β); equilibrium bond distances of the first neighbours from the Mg (*R*) (in Å); overlap bond populations of the bond between Mg atoms and the first neighbours (*b*) (in *e*); the energy (*E*)(in hartree); the energies relative to that of compared to S_z = 1 (T_d) (E_R) (in eV). SC refers to supercell size. See Appendix for other functionals.

Functional	**SC**	**Basis set**		**S_z = 1 (T_d)**		**S_z = 0 (C_{2v})**		
				Mg	$4C_\alpha$	Mg	$2C_\alpha$	$2C_\beta$
HSE06	64	(Mg / 6-311G(d)) (C / 6-21G*)	*q*	1.020	-0.249	1.011	-0.247	-0.247
			μ	0.033	0.397	0.000	0.400	- 0.401
			R		1.863		1.862	1.862
			b		0.145		0.145	0.145
			E	-2597.0097			-2597.0059	
			E_R	0			0.10	
		(Mg / TZVP) (C / 6-21G*)	*q*	1.243	-0.314	1.236	-0.312	-0.312
			μ	0.093	0.388	0.000	0.390	-0.391
			R		1.860		1.857	1.858
			b		0.100		0.101	0.101
			E	-2597.0022			-2596.9984	
			E_R	0			0.10	
HSE06	128	(Mg / 6-311G(d)) (C / 6-21G*)	*q*	1.029	-0.251	1.022	-0.248	-0.248
			μ	0.032	0.396	0.000	0.399	-0.399
			R		1.855		1.853	1.853
			b		0.144		0.144	0.144
			E	-5032.4793			-5032.4754	
			E_R	0			0.10	
		(Mg / TZVP) (C / 6-21G*)	*q*	1.246	-0.315	1.239	-0.313	-0.313
			μ	0.093	0.387	0.000	0.389	-0.389
			R		1.852		1.849	1.850
			b		0.098		0.100	0.100
			E	-5032.4721			-5032.4682	
			E_R	0			0.10	
HSE06	128	(Mg / 311G(d)) (C / TZVP)	*q*	0.882	-0.286	0.875	-0.284	-0.284
			μ	0.038	0.402	0.00	0.408	- 0.408
			R		1.846		1.844	1.844
			b		0.149		0.149	0.149
			E	-5036.2004			-5036.1966	
			E_R	0			0.10	
		(Mg / TZVP) (C / TZVP)	*q*	1.299	-0.388	1.294	-0.385	-0.385
			μ	0.098	0.393	0.000	0.399	-0.399
			R		1.843		1.841	1.841
			b		0.078		0.078	0.078
			E	-5036.1971			-5036.1934	
			E_R	0			0.10	

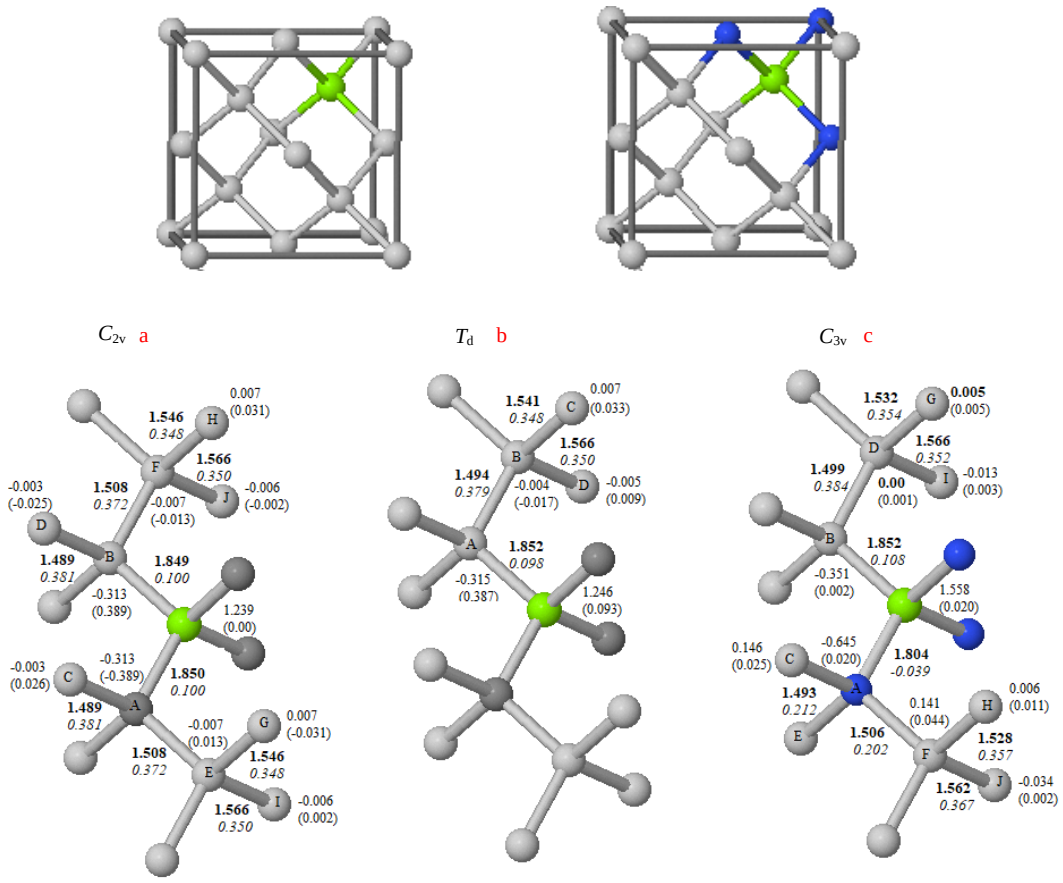

Figure 4-1 Top graphs show Mg (left) and MgN_3 complex (right) in the conventional cubic diamond cell. Below graphs show bond distances (in Å, bold), bond overlap populations (*italic*), spin momentum (in brackets), Mulliken charges, (all in *e*) for irreducible C atoms in the first, second and third shell of the Mg in T_d (a) and C_{2v} (b) symmetries and MgN_3 (c). Grey, green and blue indicate C, Mg and N atoms, respectively. All data refer to calculations using the HSE06 functional, C/6-21G* and Mg, N/TZVP basis sets and 128-atoms supercells.

The most noticeable difference between the two symmetries is the spin density. The localisation of electrons on the four carbon atoms around the defect is confirmed by the spin moments. In T_d, the localisation of electrons is equal on the four carbon atoms around the Mg with α spin. In C_{2v}, two of the neighbours are α, two β and overall $S_z = 0$. The Mg atom has a small spin moment, less than 0.1 *e* in T_d symmetry and zero value with C_{2v}. The spin density propagated across the C atoms dampened variation (sign alternation) smoothly with negligible values on the rest of the carbon neighbours.

4.3.1.2 Electronic structure

Figure 4.2 shows the band structure of a single Mg-substitutional defect calculated using the B3LYP functional, with the three resulting symmetries being compared with that of pure

diamond. Despite the small difference in energy between the singlet $S_z = 0$ and the triplet ground state $S_z = 1$, the spin state has a significant impact on their electronic structures.

In the $S_z = 1$ state with T_d symmetry, the six electrons in the defect region produced a fully occupied totally symmetric a_1 (↑↓) state merged with the valence band of the host lattice (which makes it difficult to distinguish), along with a triply degenerate (t_2) deep level with configuration (↑:↑:↑) localised close to the HOCO (highest occupied crystalline orbital), $E_g^{v\alpha}$ ~ 1.1 eV at the Γ point. This resulted in an indirect band-gap between the LUCO (lowest unoccupied crystalline orbital) and this level along the majority spin channel, $E_g^{c\alpha}$ ~ 5 eV. Another t_2 band partially occupied by one electron with configuration (↓:0:0) appears in the middle of the gap, with an indirect band-gap along the minority spin channel, $E_g^{c\beta}$ ~ 3.5 eV and separated from the HOCO by $E_g^{v\beta}$ ~ 2.3 eV at Γ. This is close to the energy calculated previously by the formation energy method [58] (2.25 eV) and measured by fluorescence spectroscopy (ZPL, 557.4 nm).[59] An electron can be excited from the valence band to this empty level giving the p-type semiconductor character of Mg defect.

The band gaps between defect states are slightly affected by the computational conditions, as indicated in Table 4.3. A dramatic difference in the band structure is seen in the $S_z = 0$ state, where the acceptor character disappears. The t_2 electronic level splits to form three states ($a_1b_1b_2$), with no noticeable shift between α and β states. The b_1 and b_2 states lie below the fully occupied totally symmetric a_1 state and about 0.9 eV from the HOCO at Γ. The empty of b_1/b_2 states appear in the gap, ~ 3 eV below the LUCO, that result in a small band-gap ~ 0.5 eV between the bonding a_1 and the antibonding b_1/b_2 (indirect gap). The defect concentrations affect the positions of the electronic levels in the gaps which vary with supercell size indicating some interaction between defects.

To gain a better understanding of the electron distribution, it was useful to examine the orbitals involved in the linear combination in the defect region by the atom-projected densities of states (PDOS) of the minority and majority spins, as shown in Figure 4.3. Orbitals of the carbon atoms around the defect make the most contribution (~ 50-60 %) to the density of both the majority and minority spins with a smaller contribution from Mg orbitals (~ 3-9%).

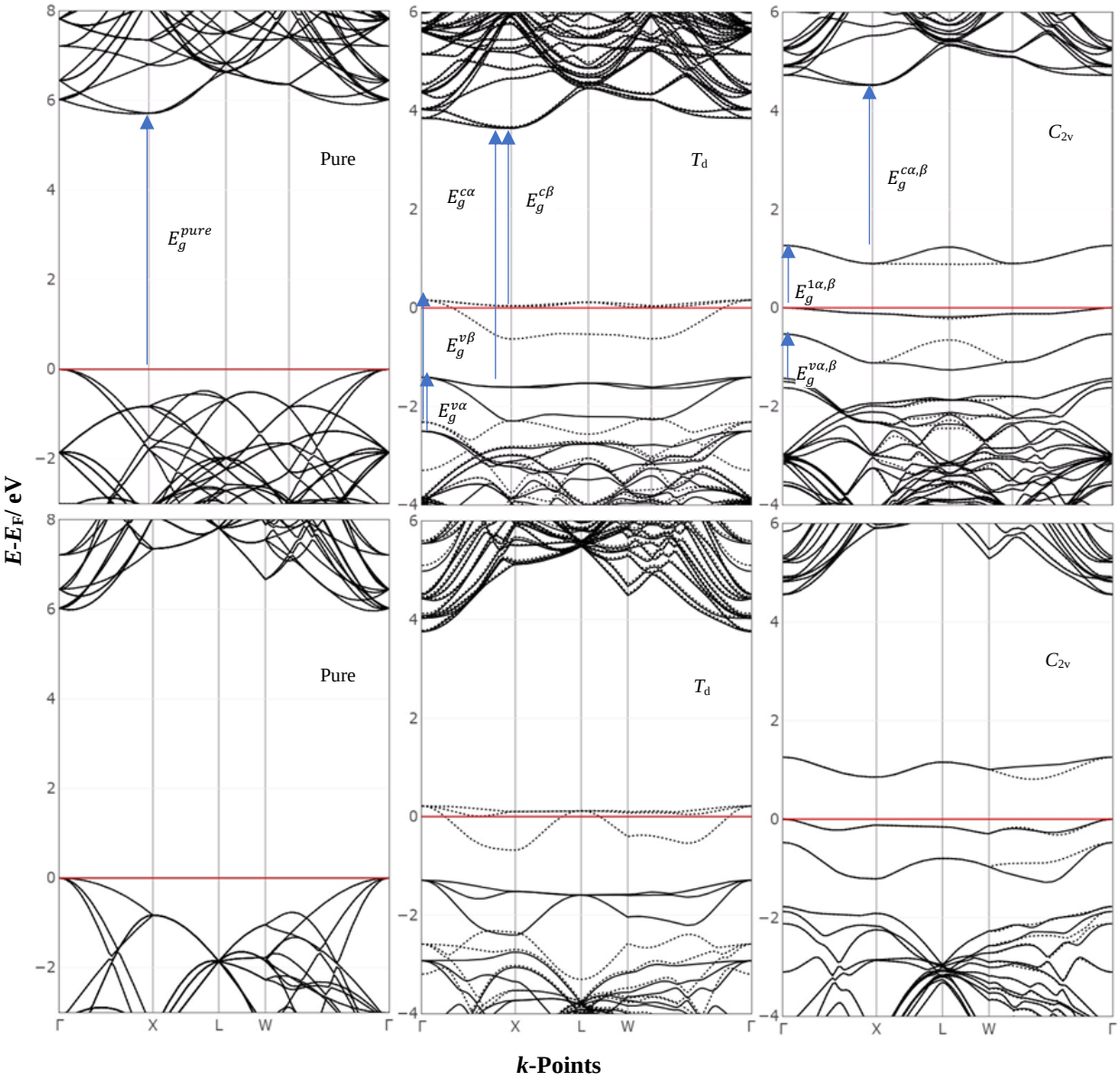

Figure 4-2 Band structure of pure diamond compared with those from an Mg defect in substitutional sites with $S_z = 1$ and $S_z = 0$. The top three panels refer to 128-atom supercells and the lower refer to 64-atom supercells. All calculations were computed with the B3LYP and C/6-21G* and Mg/TZVP basis sets. The energies are presented relative to the Fermi energy. The red line refers to Fermi level, and the continuous and dashed black lines refer to the (spin up) and (spin down) energy levels, respectively.

Table 4.3.Shows Mg defect energy gaps $E_g^{\alpha}, E_g^{\beta}$ as indicated in the dispersion curves (Figure 4.2). The calculated band gaps of pure diamond E_g^{pure} are also listed for comparison. The data were calculated using different basis sets and functionals for the corresponding symmetry and spin. All gaps are in eV and calculated at Γ points. The LUCO of the host lattice was taken at *x* point. SC and BS refer to supercell size and basis sets, respectively.

functional	SC	BS on C	BS on Mg	Sym	S_z	$E_g^{v\alpha}$	$E_g^{v\beta}$	$E_g^{c\alpha}$	$E_g^{c\beta}$	$E_g^{1\alpha}$	$E_g^{1\beta}$	E_g^{pure}
HSE06	64	(6-21G*)	(TZVP)	T_d	1	1.695	2.646	4.370	3.094			5.15
				C_{2v}	0	1.357	1.357	2.930	2.933	0.919	0.916	
			(6-311G(d))	T_d	1	1.693	2.658	4.362	3.069			
				C_{2v}	0	1.353	1.354	2.904	2.907	0.933	0.929	
HSE06	128	6-21G*	TZVP	T_d	1	1.127	2.294	4.492	3.145			5.15
				C_{2v}	0	0.940	0.941	3.006	3.009	0.923	0.921	
			6-311G(d)	T_d	1	1.128	2.311	4.485	3.123			
				C_{2v}	0	0.941	0.941	2.983	2.983	0.936	0.934	
HSE06	128	TZVP	TZVP	T_d	1	1.155	2.387	4.687	3.286			5.38
				C_{2v}	0	0.977	0.977	3.143	3.146	0.952	0.949	
			6-311G(d)	T_d	1	1.157	2.398	4.680	3.272			
				C_{2v}	0	0.979	0.980	3.129	3.131	0.956	0.954	
B3LYP	64	6-21G*	TZVP	T_d	1	1.635	2.805	4.927	3.448			5.71
				C_{2v}	0	1.298	1.298	3.169	3.168	1.258	1.258	
B3LYP	128	6-21G*	TZVP	T_d	1	1.093	2.475	5.055	3.501			5.71
				C_{2v}	0	0.901	0.901	3.250	3.250	1.267	1.267	
B3LYP	128	6-21G*	6-311G(d)	T_d	1	1.095	2.492	5.047	3.480			5.71
				C_{2v}	0	0.902	0.902	3.229	3.229	1.279	1.279	
PBE0	64	6-21G*	TZVP	T_d	1	1.713	3.054	5.050	3.342			5.79
				C_{2v}	0	1.309	1.306	2.999	2.999	1.493	1.493	
PBE0	128	6-21G*	TZVP	T_d	1	1.117	2.695	5.185	3.398			5.79
				C_{2v}	0	0.880	0.880	3.077	3.077	1.509	1.509	
PBE0	128	6-21G*	6-311G(d)	T_d	1	1.118	2.716	5.178	3.371			5.79
				C_{2v}	0	0.881	0.881	3.051	3.051	1.525	1.525	
PBEsol0	64	6-21G*	TZVP	T_d	1	1.732	3.035	4.969	3.308			5.72
				C_{2v}	0	1.340	1.339	2.965	2.965	1.471	1.472	

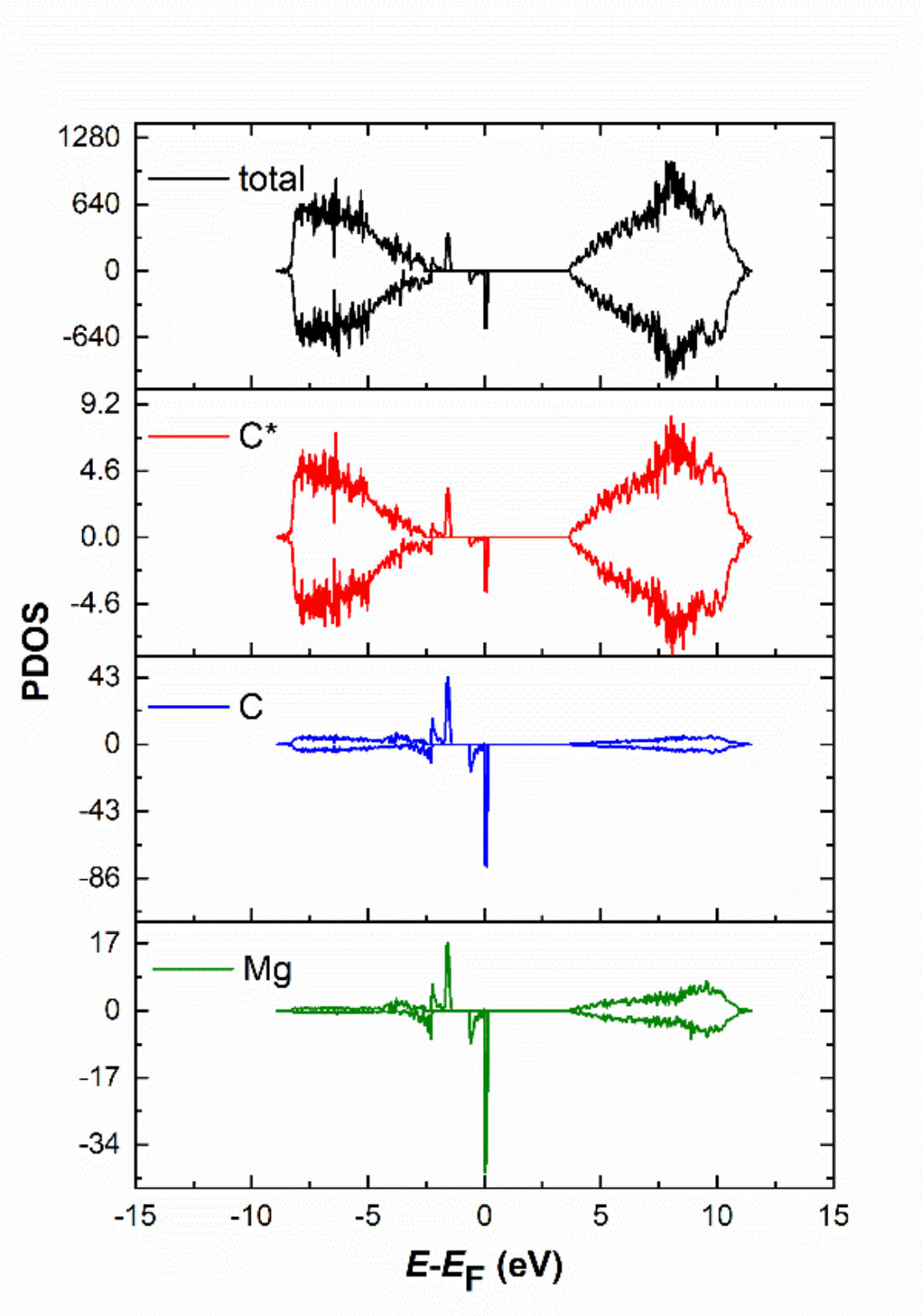

Figure 4-3 Projected DOSs of the Mg defect in a 128-atoms supercell calculated using B3LYP functional and (6-21G*) and TZVP basis sets for C and Mg, respectively. The spin state is S_z=1. 'C' is the C atom bonded directly to Mg and 'C*' is the next-nearest neighbouring C atom.

4.3.1.3 Formation energy

The formation energies of the neutral substitutional Mg atom were calculated from a perfect supercell (equation 4-1) and from a diamond supercell containing one vacancy defect (equation 4-2), (Table 4.4), as follows.

$$\Delta E_f^1 = E_{tot}^{Mg} - E_{tot}^{Perf} - \sum n_i\ \mu_i \qquad 4\text{-}1$$

$$\Delta E_f^2 = E_{tot}^{Mg} - E_{tot}^{V} - \sum n_i\ \mu_i \qquad 4\text{-}2$$

where E_{tot}^{Perf}, E_{tot}^{Mg} and E_{tot}^{V} are the total energies calculated for the pure, defective, and pre-existing one vacancy diamond supercells, respectively, and μ_i is the chemical potential of the n_i atom. In the chosen reference state of C, this is the energy per atom of the bulk diamond, while for Mg it is the calculated energy per atom in the most stable solid form of Mg (hexagonal closest packed, hcp). The E_f^1 of Mg calculated from a perfect diamond cell is high compared with the defect formation energy of common dopants for diamond (N, B), but almost the same magnitude of that of self-interstitials.[43,44] Incorporation of the Mg dopant in a pre-existing vacancy in the diamond lattice, rather than the substitution, shows a large decrease in the formation energy from ~11-12 eV to ~ 5 eV. Consider recalculate the E_f^2 taken the chemical potential of Mg from free atom resulted in a further drop in formation energy E_f^3 to be ~ 3eV. Thus, it is highly unlikely that this individual defect will be formed under the thermodynamic conditions, although there remains the kinetic as the available solution to introduce this dopant in the diamond lattice. Ion implantation provides a good method of doping bulk diamond with Mg. In a recent study[59], the fluorescence spectrum showed that a ~12% yield of Mg centres was obtained by implanting diamond with Mg ions followed by annealing at 1600° C for four hours.

The vacancy formation energies calculated here using the HSE06, B3YLP and PBE0 are about 6.10, 6.73 and 7.04 eV, respectively, with that for the singlet state (S_z = 0) in a good agreement with a previous study [139]. We reproduce their result, with S_z = 0 being lower in energy than S_z = 1 (C_{3v}) and S_z = 2 (T_d) by 0.1 eV and 1.4 eV, respectively, which is in agreement with HSE06 calculation, 7.14 eV.[50] In PBE and PW91, the formation energy of a vacancy is about 6.40 and 6.44 eV, respectively, which is also in agreement with previous calculations using GGA 6.07 eV [40] 7.2 eV [41], 6.77[17] and 7.2 eV[16]. All the calculated formation energies in Table 4.4 are found to be almost consistent, with only small differences (2.5%), (0.1 - 0.3 eV) depending on the computational method (codes, functional, basis set).

Table 4.4. The formation energy of a Mg defect from bulk diamond $\boldsymbol{E_f^1}$, from a vacancy-containing diamond taken the chemical potential of Mg from solid form $\boldsymbol{E_f^2}$ or isolated atom $\boldsymbol{E_f^3}$. The formation energy of a neutral vacancy $\boldsymbol{E_f^V}$. All energies are in eV and obtained with various functionals. SC refer to supercell size.

SC	functional	basis set		$\boldsymbol{E_f^1}$	$\boldsymbol{E_f^2}$	$\boldsymbol{E_f^3}$	$\boldsymbol{E_f^V}$
		C	Mg				
128	HSE06	(6-21G*)	(TZVP)	11.974	4.993	2.531	6.980
			(6-311G(d))	11.771	4.791	3.399	
		(TZVP)	(TZVP)	12.161	5.085	2.622	
			(6-311G(d)	12.071	4.995	3.603	7.075
128	B3LYP	(6-21G*)	(TZVP)	11.388	4.657	2.784	
			(6-311G(d))	11.183	4.451	3.787	6.731
128	PBE0	(6-21G*)	(TZVP)	12.163	5.119	2.584	
			(6-311G(d))	11.960	4.917	3.545	7.040
500	PBE			10.880	4.540		6.398
	PW91			10.990	4.530		6.346

4.3.2 MgN_3 Cluster

4.3.2.1 Charge, Geometry and spin densities

The geometry for the fully relaxed MgN_3 complex with a spin configuration S_z = ½ per cell are shown in Figure 4.1c. The structure shows the C_{3v} symmetry determined by the complex. Lowering the symmetry or releasing it result on no noticeable change in the energy, geometry or electronic structure. As shown in Figure 4.1c, all the atoms around the Mg move away, increasing the length of Mg-C and Mg-N bonds by about 19.6% and 16.4%, respectively, from the values in the unrelaxed host lattice when all bonds are equal to that of a C-C bond. Comparing the Mg-C bonds in Figure 4.1b with those in Figure 4.1c showed no change in Mg- C (1.85 Å), whereas Mg-N was reduced by 0.05 Å. The perturbation in the structure rapidly decays, such that the C-C bonds became ~1.5 Å in the first shell, 1.53–1.56 Å in the second shell, and by the third shell, the lattice perturbation was barely noticeable. The Mulliken charges show a distribution of the charge over a long range; a charge of about 0.01–0.04 *e* was gained per C atom, extending from the inner to the outer shell. The Mg-C and Mg-N bonds were strongly polarised. The charge on Mg was ~1.5 *e*; on the N and C bonded to Mg, it was

about ~ -0.6 *e* and ~ -0.3 *e*, respectively. The first three nearest C neighbours of N had a charge of 0.14 *e*, which compensated for the negative charge on N, while those that bonded to the C atom in the MgN_3C complex typically remained neutral. The negative value of the bond population of Mg-N compared to that of Mg-C indicated an antibonding character for this interaction.

4.3.2.2 Electronic Structure

The band structures of perfect bulk diamond and the MgN_3 multi-complex calculated with B3LYP and the three supercell sizes (128, 216 and 512) are shown in Figure 4.4. From periodic supercell calculations, we found that the MgN_3 complex produced a nondegenerate, singly occupied band. This band joined with the bottom of the conduction band with the HSE06 and B3LYP, which caused the systems to become conductive, except for 512– supercell/B3LYP, which had a slightly more apparent indirect gap of about 0.259 eV. The latter value obtained with largest supercell was significantly lower by ~ 0.4 eV than that computed at the same level of theory for the P defect, 0.680 eV[1,2] (Chapter 3). In the PBE0 calculation, there was a small indirect band gap of 0.127 eV with 128 supercells, and it increased to 0.225 eV with 216 supercells. The small differences in the computed band gaps were probably due to the donor level being marginally affected by the band gap of the pure diamond, as seen before with the C-centre[60], and as a result of the obvious decrease in the dispersion of the impurity bands with the increase in cell size.

Another unoccupied band associated with the MgN_3 cluster merged with the conduction band ~ 4–5 eV from the highest levels of the valence band at the Γ point. There was also an apparent full-occupied band (about 0.75 eV from the HOCO at the Γ point), which had higher energy compared to the valence electrons. Most of the contribution in this band came from the C bonded directly to Mg (as illustrated in the PDOS in Figure 4.5) due to the negative charge on this atom compared with the other C atoms.

In addition to the analysis of the defect levels obtained through the electronic structure calculations, we also included an empirical marker method (EMM) to find the thermodynamic transition levels.[6-8,61]This method calculates the electron ionisation energy of a defective system relative to that of a known reference state, as illustrated in equation 4-3.

$$X^{(0/+)} = R^{(0/+)} + \{[E(X^0) - E(X^+)] - [E(R^0) - E(R^+)]\} \qquad 4\text{-}3$$

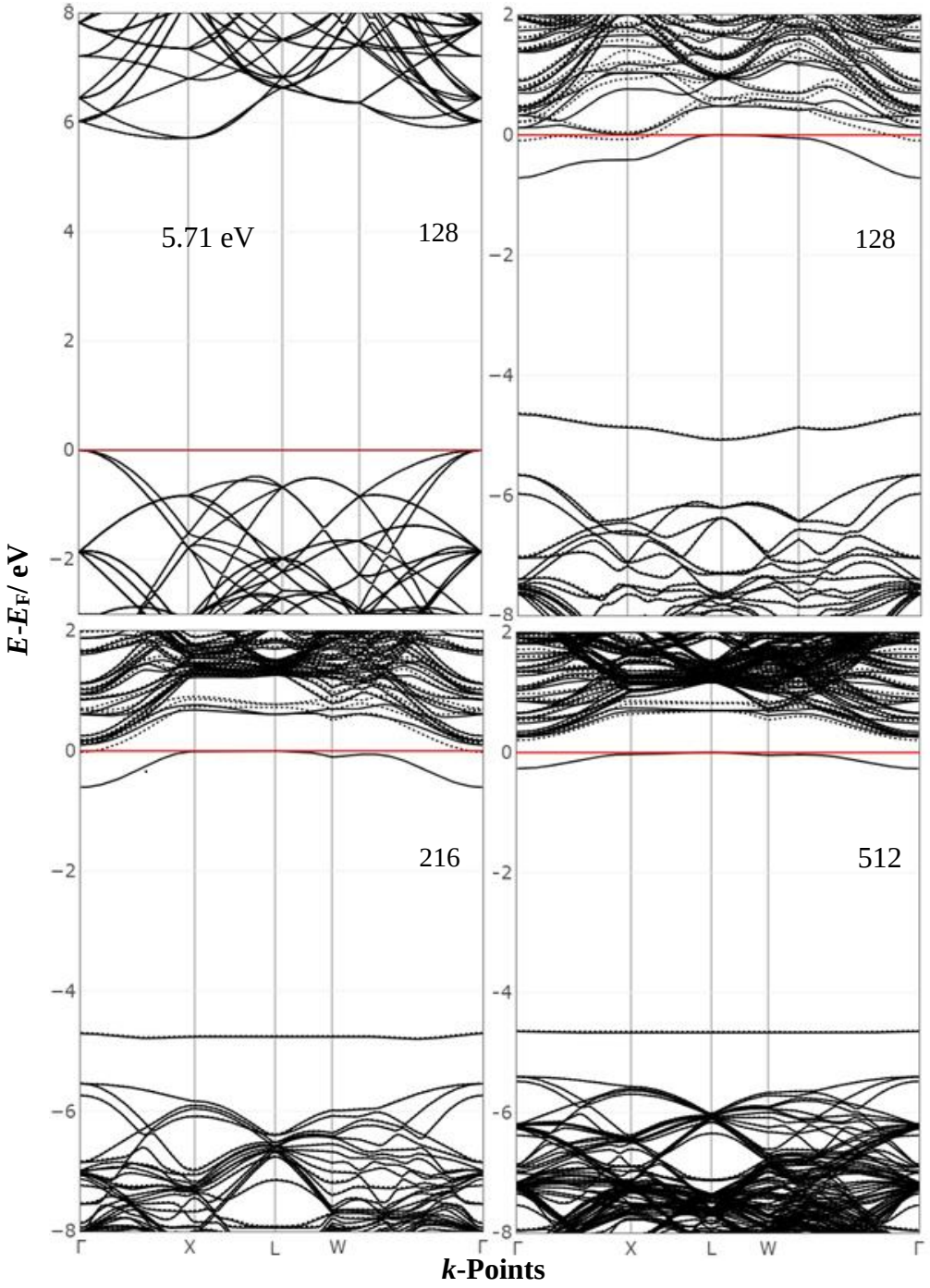

Figure 4-4 Band structure of perfect diamond compared with a corresponding MgN_3 defect in a substitutional site with C_{3v} symmetry. The top panel refers to128-atom supercells, and the lower refers to 216 and 512-atom supercells. All calculations were computed with B3LYP and C/6-21G* and Mg, N/TZVP basis sets. The energies are presented relative to the Fermi energy. The red line refers to Fermi level, and the continuous and dashed black lines refer to the (spin up) and (spin down) energy levels, respectively.

Here, $X^{(0/+)}$ is the ionisation energies of a system with an X defect and $R^{(0/+)}$ is the corresponding value of reference, while $E(X)$ and $E(X^+)$ are the total energies of the system in

a neutral and charged state, respectively. The calculations were performed with different hybrid functionals and supercell sizes (Table 4.5). The ground energy of P and N point defects were computed as described in chapter 3. The charged defects were generated by removing one electron from the cell, which gives rise to closed-shell systems. Additionally, we also include two GGA functionals as implanted in CASTEP and adopting two approaches: (i) relaxed volume, in which the lattice parameter and fractional coordinates are optimised, and (ii) fixed volume, in which the lattice parameter of the supercell is fixed to its theoretical value calculated with each functional (a = 3.71 PBE and a = 3.73 with PW91).[9] All dopants with GGA were offset from their original equilibrium positions in pure diamond to ensure the global minimum was reached.

The ionisation energy of the C-centre and MgN_3 complex were calculated taken the reference state $R^{(0/+)}$ as the experimental ionisation energy of the phosphorus, which is E_C- 0.6 eV. The results are summarised in Table 4.5 and show a good agreement with previous experimental and theoretical studies with C-centre (see chapter 3). This we predict the MgN_3 complex exhibits a shallow donor level with ionisation energy between 0.32 and 0.51 eV below the conduction band. The ionisation energy of MgN_3 calculated from EMM/B3LYP/512 (- 0.374 eV) close to that found from the electronic structure analysis using the same level of theory and cell size (- 0.259 eV), with a difference of about 0.1 eV. In all the presented calculations, the MgN_3 complex was shallower than P, providing a potentially attractive method to produce an n-type doped diamond.

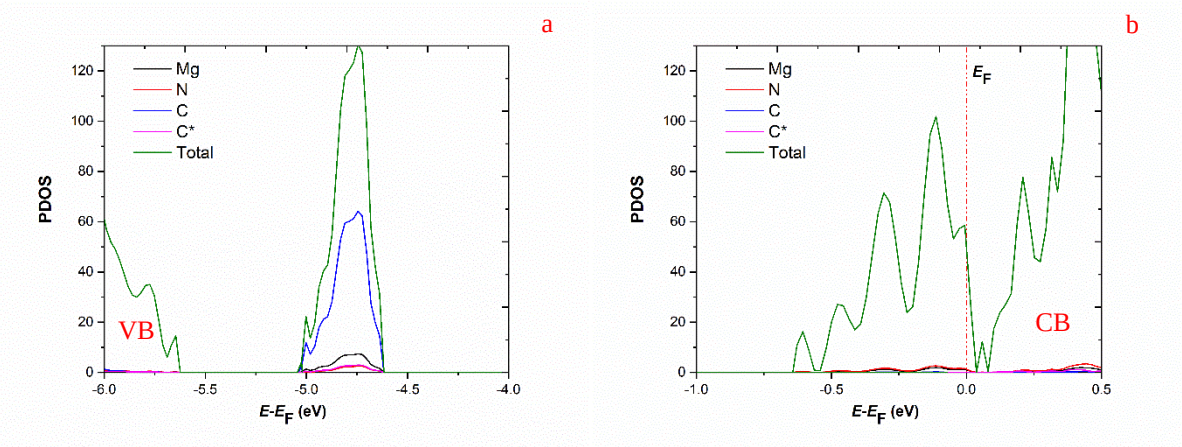

Figure 4-5 Projected B3LYP DOSs of the extra band that appears at the top of the valence band (a) and the donor band (b) of an MgN_3 complex in diamond using C/6-21G* and Mg/TZVP basis sets. 'C' is the C atom bonded directly to Mg, while 'C*' is the C atom located in the next nearest neighbour position to the Mg atom. The C* contribution is lying over the N density line in (a).

Table 4.5 Ionisation energy for different substitutional defects in diamond, calculated with the EMM and different functionals. SC refers to supercell size.

Defects	SC	Neutral Energy $E(x^0)$/Hartree	Charge Energy $E(x^+)$/Hartree	Difference Energy $(E(x^o) - E(x^+))/eV$	Ionisation energy E_c/ eV
			(6-21G*/ C) B3LYP		
P		-5175.5712	-5176.2517	18.517	Ref
N	128	-4889.1307	-4889.7545	16.974	-2.143
MgN_3		-5084.2344	-5084.9185	18.615	-0.502
P		-8525.4849	-8526.1625	18.438	Ref
N	216	-8239.0450	-8239.6652	16.876	-2.162
MgN_3		-8434.1491	-8434.8337	18.628	-0.410
P		-19793.3741	-19794.0484	18.348	Ref
N	512	-19506.9352	-19507.5505	16.743	-2.205
MgN_3		-19702.0385	-19702.7211	18.574	-0.374
			(6-21G*/ C) HSE06		
P		-5173.8690	-5174.5456	18.411	Ref
N	128	-4887.4658	-4888.0959	17.145	-1.866
MgN_3		-5082.4791	-5083.1596	18.517	-0.494
P		-8522.6489	-8523.3238	18.364	Ref
N	216	-8236.2474	-8236.8734	17.034	-1.930
MgN_3		-8431.2608	-8431.9426	18.552	-0.412
			(TZVP/ C) HSE06		
P		-5177.5921	-5178.2786	18.680	Ref
N	128	-4891.1932	-4891.8327	17.401	-1.879
MgN_3		-5086.1026	-5086.7921	18.762	-0.518
			(6-21G*/ C) PBE0		
P		-5173.9496	-5174.6308	18.536	Ref
N	128	-4887.5498	-4888.1799	17.145	-1.991
MgN_3		-5082.5557	-5083.2437	18.721	-0.415
P		-8522.7892	-8523.4672	18.449	Ref
N	216	-8236.3898	-8237.0159	17.037	-2.012
MgN_3		-8431.3968	-8432.0850	18.726	-0.323
			PW91/ eV (Fixed Volume)		
P		-80877.2035	-80891.6960	14.4925	Ref
N	512	-80937.0851	-80950.5528	13.4677	-1.6248
MgN_3		-82702.4967	-82717.0858	14.5891	-0.5034
			PW91/ eV (Relaxed Volume)		
P		-80877.2528	-80891.7039	14.4510	Ref
N	512	-80937.0993	-80950.5612	13.4619	-1.5891
MgN_3		-82702.5703	-82717.1039	14.5336	-0.5174
			PBE0/ eV (Fixed Volume)		
P		-80769.6474	-80784.1805	14.5331	Ref
N	512	-80829.5918	-80843.1241	13.5323	-1.6008
MgN_3		-82593.7247	-82608.3591	14.6344	-0.4987
			PBE0/ eV (Relaxed Volume)		
P		-80769.6823	-80784.1818	14.4995	Ref
N	512	-80829.6006	-80843.1392	13.5386	-1.5609
MgN_3		-82593.7812	-82608.3675	14.5863	-0.5132

4.3.2.3 Formation and binding energy of MgN_3

Based on the calculation in section (4.3.1.3), the incorporation of a single neutral Mg in undoped diamond lattice is very insoluble and a big challenge due to the increased atomic radius of Mg compared with that of C. The equilibrium concentration of Mg in a diamond can be related to the formation of energy by

$$[\mathrm{Mg}] \sim N_o \exp(-E_f / kT) \qquad 4\text{-}4$$

where N_o is the defect site per unit volume, T and k are temperature and the Boltzmann constant, respectively. To the best of our knowledge, there have been no experimental attempts with CVD diamond to introduce Mg, even though this element is used frequently to dope GaN.[63,64] In order to explore the solubility of Mg in the doped-diamond crystal, which contains a vacancy and nitrogen complex, we computed the formation energies of MgN_3 with a two-step mechanism. First, we used a pre-existing 2NV defect in diamond to form the initial complex MgN_2; then, an N atom was added to MgN_2 to form MgN_3, as follows:

$$VN_2 + Mg \rightarrow MgN_2 \qquad \boldsymbol{E_f^1} \qquad 4\text{-}5$$

$$MgN_2 + \frac{1}{2}N_2 \rightarrow MgN_3 \qquad \boldsymbol{E_f^2} \qquad 4\text{-}6$$

Using Equation 4-1, the formation energies were computed, adopting different approaches. In the first method (Table 4.6 A), the chemical potential for C was taken, plus that for Mg as used previously with the $\boldsymbol{E_f^1}$ of Mg defect, and that for N from the energy per atom of highly stable form taken by N_2. In the second method (Table 4.6 B), the energy per atom was computed for isolated carbon, magnesium and nitrogen atoms. To correct the basis set superposition error (BSSE) of isolated atoms, we surrounded them with three shells of neighbouring 'ghost' atoms (basis set functions without electrons or protons), positioned as in the diamond structure.[65,66] In the last method (Table 4.6 C), the chemical potential of N was taken such that the formation energy of the C-centre is zero[38,67]to ensure the consistently high solubility of N in the diamond. The calculated formation energies of N_{sub} in A were in good agreement with the 3.96 eV reported with HSE06[50], the 3.2 eV reported with GGA[9] and that reported recently with hybrid functionals[60] using the first two methods (A and B). In Table 4.6

C, we also included the formation energies of the 2NV defect to be compared with those reported by Jones et al. (-2.2 eV) [38], using the same method, which was also in good agreement.

The 2NV defect consists of a vacancy surrounded by two nitrogen atoms and two carbons with dangling bonds. It is created by the diffusion of a mobile vacancy to form an NV complex that, in turn, can migrate with a barrier energy of ~ 4.9 eV[50, 39] (~1500 ^{o}C) to be trapped by another nitrogen in diamond[190]. This diffusion mechanism mainly depends on the presence of vacancies or self-interstitials in the lattice, which explains why radiation damage increases nitrogen aggregation.[47,48] This defect suffers from charge deficiency, and it is more energetically favourable to terminate the two dangling carbon bonds with the two electrons coming from the valence band of Mg. As shown in Tables 4A, B and C, the formation energies of $\boldsymbol{E_f^1}$ show positive values with an endo thermic nature, but are significantly lower than that calculated from the direct substitution of Mg atom by C. The barrier estimated to diffuse the N in the V-assistance mechanism into a 4.8 eV (the jump of N from a substitutional site into a next-neighbour V) was higher than ~ 1.8 eV, which was predicted via the formation of N_i (N_i, nitrogen trapped by self-interstitial).[39,50] Thus, any annulling temperature followed by implanting the Mg into the N-doped diamond must be enough to overcome the N diffusion barrier. In method C, the $\boldsymbol{E_f^{MgN3}}$ and support the hypothesis of increasing the Mg solubility in excess of N, which can be attained using the CVD technique.

The most significant findings are the high stability of MgN_2 and MgN_3 complexes in a diamond, as estimated from the binding energy (E_b), which is defined by

$$\Delta E_b = E_{f(X)}^{Def} + E_{f(A)}^{Def} - E_{f(XA)}^{Def} \qquad 4\text{-}7$$

where $E_{f(X)}^{Def}$ and $E_{f(A)}^{Def}$ are the E_f of the isolated defects X and A, and $E_{f(XA)}^{Def}$ is the E_f of the dopant complex of both X and A atoms. It is worth noting that the binding energy is independent of the chemical potentials used in the calculation. The E_b^1 and E_b^2 of MgN_3 and MgN_2, respectively, are listed in Table 4.4 and indicate that both defects are very stable once they have formed inside the lattice, with the relative stability of $E_b^1 > E_b^2$, which is almost three times the magnitude of that previously reported for a Si_4N complex.[36]

Table 4.6 Formation energies of an MgN_3 complex from pure diamond $\boldsymbol{E_f^{MgN3}}$; formation energy of an MgN_2 complex from a 2NV defect E_f^1; formation energy of MgN_3 from an MgN_2 defect E_f^2; the formation energy of an N defect E_f^N; E_b^1 and E_b^2 are the binding energies of an MgN_3 and MgN_2 complex, respectively. All energies are in eV. SC refers to supercell size (see text about the difference between tables A, B and C).

A		basis set		$\boldsymbol{E_f^{MgN3}}$	$\boldsymbol{E_f^N}$	$\boldsymbol{E_b^1}$	$\boldsymbol{E_f^1}$	$\boldsymbol{E_b^2}$	$\boldsymbol{E_f^2}$
SC	Functional	C	Mg						
128	HSE06	(6-21G*)	(TZVP)	9.931	3.586	12.801	3.559	10.937	1.723
			(6-311G(d))	9.862		12.667	3.473	10.821	1.740
		(TZVP)	(TZVP)	10.483	3.706	12.796	3.758	10.992	1.903
			(6-311G(d))	10.473		12.716	3.739	10.922	1.913
128	B3LYP	(6-21G*)	(TZVP)	10.369	3.809	12.446	3.105	10.889	2.253
			(6-311G(d))	10.276		12.334	3.000	10.788	2.264
128	PBE0	(6-21G*)	(TZVP)	10.126	3.603	12.846	3.525	11.169	1.927
			(6-311G(d))	10.048		12.721	3.436	11.056	1.938
512	PBE		PW	11.04	3.878	11.482	3.754	9.484	1.892
	PW91		PW	11.67	3.838	11.670	3.634	9.711	1.880

B		basis set		$\boldsymbol{E_f^{MgN3}}$	$\boldsymbol{E_f^N}$	$\boldsymbol{E_b^1}$	$\boldsymbol{E_f^1}$	$\boldsymbol{E_b^2}$	$\boldsymbol{E_f^2}$
SC	Functional	C	Mg						
128	HSE06	(6-21G*)	(TZVP)	28.192	7.710	12.801	1.097	10.937	5.847
			(6-311G(d))	29.194		12.667	2.081	10.821	5.864
		(TZVP)	(TZVP)	29.443	8.006	12.799	1.296	10.992	6.202
			(6-311G(d))	30.504		12.720	2.347	10.922	6.211
128	B3LYP	(6-21G*)	(TZVP)	27.282	7.433	12.445	1.232	10.888	5.877
			(6-311G(d))	28.397		12.333	2.336	10.788	5.982
128	PBE0	(6-21G*)	(TZVP)	29.362	8.000	12.846	0.950	11.170	6.324
			(6-311G(d))	30.487		12.723	2.064	11.057	6.335

C		basis set		E_f^{2NV}	E_f^{MgN3}	E_f^N	E_b^1	E_f^1	E_b^2	E_f^2
SC	Functional	C	Mg							
128	HSE06	(6-21G*)	(TZVP)	-2.524	-0.828	0	12.802	3.559	10.939	-1.863
			(6-311G(d))		-0.897		12.668	3.473	10.822	-1.846
		(TZVP)	(TZVP)	-2.591	-0.636	0	12.797	3.758	10.993	-1.803
			(6-311G(d))		-0.645		12.716	3.739	10.923	-1.793
128	B3YLP	(6-21G*)	(TZVP)	-2.606	-1.058	0	12.446	3.104	10.889	-1.556
			(6-311G(d))		-1.151		12.334	3.000	10.789	-1.544
128	PBE0	(6-21G*)	(TZVP)	-2.534	-0.684	0	12.847	3.526	11.171	-1.676
			(6-311G(d))		-0.763		12.723	3.436	11.058	-1.665

4.4 Conclusions

Different properties of the neutral Mg defect in diamond in its singlet and triplet spin states were studied using hybrid functionals with Crystal-17 code. The calculations were also extended to include the multi-complex of Mg and N, up to three atoms. The local structural perturbation by the introduction of the Mg defect to the lattice is restricted to the first and second shell of C atoms surrounding the Mg. The electronic structure of the Mg centre in its singlet and triplet state was analysed in detail. The calculated formation energies of single Mg, N and V point defects agree well with the previous calculations.[38,40–42,58,60] Analysis of the band structure of the MgN_3 multi-complex calculated by hybrid functionals suggests that the MgN_3 defect introduces an n-type level shallower than the P donor level, which is aided by the EMM method.

The calculated formation energy of the MgN_2 defect formed from a 2NV pre-existing defect is a good value from which to engineer MgN_3 defects inside diamond by ion-implantation followed by annulling to induce migration of N defects to the Mg centre. We recommend that, first, the Mg are implanted inside the nitrogen-doped diamond crystal, followed by heating the sample up to 1500^o C to induce diffusion of the N-related defects to Mg and anneal out any implantation damage caused by Mg. The successful implantation scheme with B-doped diamond, such as cold implantation rapid annealing (CIRA) [68,69] or low-damage drive-in (LODDI)[70,71] might be examined with Mg in the presence of an N defect. Temperature control is necessary for this process, which demands a more precise experimental study. We also showed that the Mg introduction in a diamond can be thermodynamically favourable if it is introduced during the CVD process in excess of N, given that the formation energy of N in diamond is zero, which is broadly consistent with the experimental observations.

5.4 References

1. Koizumi, S., Teraji, T. & Kanda, H. Phosphorus-doped chemical vapor deposition of diamond. *Diam. Relat. Mater.* **9**, 935–940 (2000).

2. Katagiri, M., Isoya, J., Koizumi, S. & Kanda, H. Lightly phosphorus-doped homoepitaxial diamond films grown by chemical vapor deposition. *Appl. Phys. Lett.* **85**, 6365–6367 (2004).

3. Koizumi, S., Kamo, M., Sato, Y., Ozaki, H. & Inuzuka, T. Growth and characterization of phosphorous doped {111} homoepitaxial diamond thin films. *Appl. Phys. Lett.* **71**, 1065–1067 (1997).

4. Koizumi, S. Growth and characterization of phosphorus doped n-type diamond thin films. *Phys. Status Solidi Appl. Res.* **172**, 71–78 (1999).

5. Jones, R., Lowther, J. E. & Goss, J. Limitations to n-type doping in diamond: The phosphorus-vacancy complex. *Appl. Phys. Lett.* **69**, 2489–2491 (1996).

6. Goss, J. P., Briddon, P. R., Jones, R. & Sque, S. Donor and acceptor states in diamond. *Diam. Relat. Mater.* **13**, 684–690 (2004).

7. Lombardi, E. B. & Mainwood, A. Interaction of hydrogen with boron , phosphorus , and sulfur in diamond. **205201**, 1–12 (2004).

8. Sque, S. J., Jones, R., Goss, J. P. & Briddon, P. R. Shallow Donors in Diamond: Chalcogens, Pnictogens, and their Hydrogen Complexes. *Phys. Rev. Lett.* **92**, 4 (2004).

9. Goss, J. P., Briddon, P. R. & Eyre, R. J. Donor levels for selected n -type dopants in diamond: A computational study of the effect of supercell size. *Phys. Rev. B - Condens. Matter Mater. Phys.* **74**, 1–7 (2006).

10. Frangieh, G., Pinault, M. A., Barjon, J., Jomard, F. & Chevallier, J. Incorporation of arsenic in diamond grown by chemical vapor deposition. *Phys. Status Solidi Appl. Mater. Sci.* **205**, 2207–2210 (2008).

11. Kajihara, S. A., Antonelli, A., Bernholc, J. & Car, R. Nitrogen and potential n-type dopants in diamond. *Phys. Rev. Lett.* **66**, 2010–2013 (1991).

12. Lombardi, E. B. & Mainwood, A. A first principles study of lithium, sodium and

aluminum in diamond. *Diam. Relat. Mater.* **17**, 1349–1352 (2008).

13. Goss, J. P. & Briddon, P. R. Theoretical study of Li and Na as n -type dopants for diamond. *Phys. Rev. B - Condens. Matter Mater. Phys.* **75**, 1–9 (2007).

14. Lombardi, E. B., Mainwood, A. & Osuch, K. Ab initio study of lithium and sodium in diamond. *Phys. Rev. B - Condens. Matter Mater. Phys.* **76**, 1–8 (2007).

15. Yilmaz, H., Weiner, B. R. & Morell, G. Formation of lithium clusters and their effects on conductivity in diamond: A density functional theory study. *Diam. Relat. Mater.* **16**, 840–844 (2007).

16. Bernholc, J., Kajihara, S. A., Wang, C., Antonelli, A. & Davis, R. F. Theory of native defects, doping and diffusion in diamond and silicon carbide. *Mater. Sci. Eng. B* **11**, 265–272 (1992).

17. Lombardi, E. B. & Mainwood, A. Li and Na in diamond: A comparison of DFT models. *Phys. B Condens. Matter* **401**–**402**, 57–61 (2007).

18. Uzan-Saguy, C. *et al.* Diffusion of lithium in diamond. *Phys. Status Solidi Appl. Res.* **193**, 508–516 (2002).

19. J. te Nijenhuis, G.Z. Cao, P.C.H.J Smits, W.J.P. van Enckevort, L.J. Giling, P.F.A Alkemade, M. Nesladek, Z. R. Incorporation of lithium in single crystal diamond: diffusion profiles and optical and electrical properties. *Diam. Relat. Mater.* **6**, 1726–1732 (1997).

20. Weima, J. A., von Borany, J., Meusinger, K., Horstmann, J. & Fahrner, W. R. A comparative study of the I-V characteristics of diodes fabricated on as-grown and thermochemically polished CVD diamond films. *Diam. Relat. Mater.* **12**, 1307–1314 (2003).

21. Sakaguchi, I. *et al.* Sulfur: A donor dopant for n-type diamond semiconductors. *Phys. Rev. B - Condens. Matter Mater. Phys.* **60**, R2139–R2141 (1999).

22. Nishitani-Gamo, M. *et al.* Sulfur-doped homoepitaxial (001) diamond with n-type semiconductive properties. *Diam. Relat. Mater.* **9**, 941–947 (2000).

23. Kalish, R., Reznik, A., Uzan-Saguy, C. & Cytermann, C. Is sulfur a donor in diamond? *Appl. Phys. Lett.* **76**, 757–759 (2000).

24. Nakazawa, K. *et al.* Cathodoluminescence and hall-effect measurements in sulfur-doped chemical-vapor-deposited diamond. *Appl. Phys. Lett.* **82**, 2074–2076 (2003).

25. Hasegawa, M. *et al.* N-Type Control By Sulfur Ion Implantation in Homoepitaxial Diamond Films Grown By Chemical Vapor Deposition. *Japanese J. Appl. Physics, Part 2 Lett.* **38**, (1999).

26. Albu, T. V, Anderson, A. B. & Angus, J. C. Dopants in Diamond Nanoparticles and Bulk Diamond : Density Functional Study of Substitutional B , N , P , SB , S , PN , O , NN , and Interstitial H Dopants in Diamond Nanoparticles and Bulk Diamond. *J. Electrochem. Soc.* **149**, E143–E147 (2002).

27. Katayama-Yoshida, H., Nishimatsu, T., Yamamoto, T. & Orita, N. Codoping method for the fabrication of low-resistivity wide band-gap semiconductors in p-type GaN, p-type AlN and n-type diamond: Prediction versus experiment. *J. Phys. Condens. Matter* **13**, 8901–8914 (2001).

28. Nishimatsu, T., Katayama-Yoshida, H. & Orita, N. Ab initio study of donor-hydrogen complexes for low-resistivity n-type diamond semiconductor. *Japanese J. Appl. Physics, Part 1 Regul. Pap. Short Notes Rev. Pap.* **41**, 1952–1962 (2002).

29. Miyazaki, T. & Okushi, H. A theoretical study of a sulfur impurity in diamond. *Diam. Relat. Mater.* **10**, 449–452 (2001).

30. Tang, L., Yue, R. & Wang, Y. N-type B-S co-doping and S doping in diamond from first principles. *Carbon N. Y.* **130**, 458–465 (2018).

31. Saada, D., Adler, J. & Kalish, R. Sulfur: A potential donor in diamond. *Appl. Phys. Lett.* **77**, 878–879 (2000).

32. Katayama-Yoshida, H., Nishimatsu, T., Yamamoto, T. & Orita, N. Comparison between the theoretical prediction of codoping and the recent experimental evidences in p-type GaN, Aln, ZnSe, CuInS2 and n-type diamond. *Phys. Status Solidi Basic Res.* **210**, 429–436 (1998).

33. Miyazaki, T., Okushi, H. & Uda, T. Shallow donor state due to nitrogen-hydrogen complex in diamond. *Phys. Rev. Lett.* **88**, 66402/1-66402/4 (2002).

34. Moussa, J. E., Marom, N., Sai, N. & Chelikowsky, J. R. Theoretical design of a shallow donor in diamond by lithium-nitrogen codoping. *Phys. Rev. Lett.* **108**, 1–5 (2012).

35. Yu, B. D., Miyamoto, Y. & Sugino, O. Efficient n-type doping of diamond using surfactant-mediated epitaxial growth. *Appl. Phys. Lett.* **76**, 976–978 (2000).

36. Segev, D. & Wei, S. H. Design of shallow donor levels in diamond by isovalent-donor coupling. *Phys. Rev. Lett.* **91**, 2–5 (2003).

37. Evans, T. & Qi, Z. The Kinetics of the Aggregation of Nitrogen Atoms in Diamond. *Proc. R. Soc. A Math. Phys. Eng. Sci.* **381**, 159–178 (2006).

38. Jones, R., Goss, J. P., Pinto, H. & Palmer, D. W. Diffusion of nitrogen in diamond and the formation of A-centres. *Diam. Relat. Mater.* **53**, 35–39 (2015).

39. Pinto, H. *et al.* On the diffusion of NV defects in diamond. *Phys. Status Solidi Appl. Mater. Sci.* **209**, 1765–1768 (2012).

40. Hyde-Volpe, D., Slepetz, B. & Kertesz, M. The [V-C=C-V] divacancy and the interstitial defect in diamond: Vibrational properties. *J. Phys. Chem. C* **114**, 9563–9567 (2010).

41. Shim, J. & Lee, E. Density-functional calculations of defect formation energies using supercell methods : Defects in diamond. 1–12 (2005). doi:10.1103/PhysRevB.71.035206

42. Zelferino, A. *et al.* The electronic states of the neutral vacancy in diamond: a quantum mechanical approach. *Theor. Chem. Acc.* **135**, 1–11 (2016).

43. Salustro, S. *et al.* Infrared and Raman spectroscopic features of the self-interstitial defect in diamond from exact-exchange hybrid DFT calculations. *Phys. Chem. Chem. Phys.* **18**, 21288–21295 (2016).

44. Davies, G., Lawson, S. C., Collins, T., Mainwood, A. & Sharp, J. Vacancy-related centers in diamond. *Phys. Rev.* **46**, 157–170 (1992).

45. Collins, A. T. Vacancy enhanced aggregation of nitrogen in diamond. *J. Phys. C Solid State Phys.* **13**, 2641–2650 (1980).

46. Kiflawi, I., Kanda, H., Fisher, D. & Lawson, S. C. The aggregation of nitrogen and the formation of A centres in diamonds. *Diam. Relat. Mater.* **6**, 1643–1649 (1997).

47. Isaac Kiflawi, Hisao Kanda, A. M. The effect of nickel and the kinetics of the aggregation of nitrogen in diamond. *Diam. Relat. Mater.* **7**, 327–332 (1998).

48. Nadolinny, V. A. *et al.* Mechanisms of nitrogen aggregation in nickel- and cobalt-containing synthetic diamonds. *Diam. Relat. Mater.* **9**, 883–886 (2000).

49. Mainwood, A. Nitrogen and nitrogen-vacancy complexes and their formation in diamond. *Phys. Rev. B* **49**, 7934–7940 (1994).

50. Deák, P., Aradi, B., Kaviani, M., Frauenheim, T. & Gali, A. Formation of NV centers in diamond: A theoretical study based on calculated transitions and migration of nitrogen and vacancy related defects. *Phys. Rev. B - Condens. Matter Mater. Phys.* **89**, 1–12 (2014).

51. Goss, J. P., Briddon, P. R., Papagiannidis, S. & Jones, R. Interstitial nitrogen and its complexes in diamond. *Phys. Rev. B - Condens. Matter Mater. Phys.* **70**, 1–15 (2004).

52. S., P. Ab initio modelling of defect complexes in semiconductors. (University of Newcastle upon Tyne, 2003).

53. Othman, M. Z., May, P. W., Fox, N. A. & Heard, P. J. Incorporation of lithium and nitrogen into CVD diamond thin films. *Diam. Relat. Mater.* **44**, 1–7 (2014).

54. Anderson, A. B. & Mehandru, S. P. N-type dopants and conduction-band electrons in diamond: Cluster molecular-orbital theory. *Phys. Rev. B* **48**, 4423–4427 (1993).

55. Eyre, R. J., Goss, J. P., Briddon, P. R. & Wardle, M. G. Multi-impurity complexes for n-type diamond: A computational study. *Phys. Status Solidi Appl. Mater. Sci.* **204**, 2971–2977 (2007).

56. Wang, L. G. & Zunger, A. Phosphorus and sulphur doping of diamond. *Phys. Rev. B - Condens. Matter Mater. Phys.* **66**, 1–4 (2002).

57. Nishimatsu, T., Katayama-Yoshida, H. & Orita, N. Theoretical study of hydrogen-related complexes in diamond for low-resistive n-type diamond semiconductor. *Phys. B Condens. Matter* **302**–**303**, 149–154 (2001).

58. Czelej, K., Śpiewak, P. & Kurzydłowski, K. J. Electronic structure of substitutionally doped diamond: Spin-polarized, hybrid density functional theory analysis. *Diam. Relat. Mater.* **75**, 146–151 (2017).

59. Lühmann, T. *et al.* Screening and engineering of colour centres in diamond. *J. Phys. D. Appl. Phys.* **51**, 483002 (2018).

60. Ferrari, A. M., Salustro, S., Gentile, F. S., Mackrodt, W. C. & Dovesi, R. Substitutional nitrogen atom in diamond. A quantum mechanical investigation of the electronic and spectroscopic properties. *Carbon N. Y.* **134**, 354–365 (2018).

61. Goss, J. P. Shaw, M. J. Briddon, P. R. *Marker-Method Calculations for Electrical Levels Using Gaussian-Orbital Topics in Applied Physics Volume 104*. **94**, (2015).

62. Eyre, R. J., Goss, J. P., Briddon, P. R. & Hagon, J. P. Theory of Jahn-Teller distortions of the P donor in diamond. *J. Phys. Condens. Matter* **17**, 5831–5837 (2005).

63. Nakamura, S., Mukai, T., Senoh, M. & Iwasa, N. Thermal annealing effects on P-type Mg-doped GaN films. *Jpn. J. Appl. Phys.* **31**, 139–142 (1992).

64. Chichibu, S. F. *et al.* Large electron capture-cross-section of the major nonradiative recombination centers in Mg-doped GaN epilayers grown on a GaN substrate. *Appl. Phys. Lett.* **112**, 211901 (2018).

65. Salustro, S. *et al.* The A-center defect in diamond: Quantum mechanical characterization through the infrared spectrum. *Phys. Chem. Chem. Phys.* **19**, 14478–14485 (2017).

66. Salustro, S. *et al.* Characterization of the B-Center Defect in Diamond through the Vibrational Spectrum: A Quantum-Mechanical Approach. *J. Phys. Chem. A* **122**, 594–600 (2018).

67. Goss, J. P. *et al.* Theory of hydrogen in diamond. *Phys. Rev. B - Condens. Matter Mater. Phys.* **65**, 1–13 (2002).

68. Fontaine, F., Uzan-Saguy, C., Philosoph, B. & Kalish, R. Boron implantation / in situ annealing procedure for optimal p -type properties of diamond. *Appl. Phys. Lett.* **68**, 2264–2266 (1996).

69. Dresselhaus, M. S. & Kalish, R. *Ion implantation in diamond, graphite and related materials*. (Springer Science & Business Media, 2013).

70. Prins, J. F. Doping of diamond by the diffusion of interstitial atoms into layers containing a low density of vacancies. *Diam. Relat. Mater.* **7**, 545–549 (1998).

71. Neves, A. & Nazar, M. *Properties, Growth and Applications of Diamond*. (IET, 2001).

CHAPTER 5

THEORETICAL STUDY ON 2NV AND MgN_2 DEFECTS IN DIAMOND

CHAPTER 5 –THEORETICAL STUDY ON 2NV AND MgN2 IN DIAMOND

5.1 Introduction

Like other solid materials, the diamond lattice can simultaneously maintain a wide range of defects (impurities, dislocations, vacancies and self-interstitials and grain boundaries). This makes it very difficult to perform any accurate experimental measurements to detect one defect type in the diamond or to assign one measurement to a particular defect. The power of simulation is that the researcher can isolate one defect with a specific concentration in diamond and, in the absence of any other defects, obtain clear insights into this defect. In recent years, many simulated spectra for a range of single-point defects in diamond have been realised A- centre [1], B-centre [2], C-centre [3], self-interstitial [4], vacancy [5], vacancy and self-interstitial [6], BH, NH [7], V_2 [8], VN_3H [9], $VH_{(x,1-4)}$ [10] and VN_xH_y [11] which raise the motivation to investigate other defects possibly synthesised experimentally.

In Chapter 4, we suggested a new combination of nitrogen and magnesium to produce an n-type cluster (MgN_3). Taking advantage of the high binding energy between Mg and N ensures the stability of the Mg-N bond once it is formed inside the lattice. N has a greater electronegativity than C, so locating the Mg atom between two nitrogen atoms in as an MgN_2 defect enhances the Mg solubility in diamond and decreases the formation energy when calculated from the 2NV point defect. This, forming MgN_2 in the lattice is the primary step to form the main MgN_3 complex and consequently to produce n-type semiconducting material.

As the infrared (IR) spectroscopy is considered a good experimental method in the effort to investigate the atomic behaviour of diamond [12–15], in this chapter, we explored the geometry, electronic structure and vibrational frequencies of MgN_2 and 2NV point defects in diamond. The main characteristics of the simulated IR spectra of individual MgN_2 defects were determined and compared these with those of 2NV, which might help detect the MgN_2 defect in a complex spectrum.

5.2 Computational setup

For details on the CRYSTAL code, and discussion of the parameters used, please see Chapter 3.

5.3 Result and discussion

5.3.1 Geometry, charge and spin distribution

For both point defects – MgN_2 and 2NV – the local optimised structure and its charge and spin distribution are reported in Table 5.1, 5.2, respectively, and Figure 5.1. It can be simply described the MgN_2 defect starting from 2NV; an Mg atom occupies the centre instead of the removed C atom in 2NV, leading to saturation of the two dangling bonds. Starting the analysis from the 2NV defect, the two unpair electrons (on the two carbon atoms nearest to the V defect) can couple to generate two possible S_z spin states (i.e., 1 and 0), which can be specified using different optional keywords in CRYSTAL (i.e., SPINLOCK, ATOMSPIN). The repulsion interaction between the unpaired electrons on the two C atom nearest to the vacancy in S_z = 1 slightly affects the C_α-C_α distance, which was approximately 2.7 Å compared to the corresponding value in S_z = 0,2.6 Å. The singlet spin state is slightly more stable than the triplet by 0.2 eV with all the functionals and the basis sets used. This singlet was found to be the ground state with HSE06 in a previous study with stability 0.18 eV compared with the triplet[16], which is in good agreement with our calculation. The strong coupling of electrons on the carbon atoms nearest to the vacancy in 2NV is similar to the coupling of the four electrons in the vacancy defect. In 2NV, this coupling generates C_s symmetry with the singlet and C_{2v} with the triplet.

To explore the charge and spin distribution, Mulliken population analyses were executed. The values of (q) and (μ) per atom calculated with the two configurations confirm the net spin per cell. It is important to notice that in the spin-polarised system, the spin density is mainly localised on the carbon with dangling bonds, and this localisation is greatly affected by the percent of "exact" HF exchange contained in the functional used in the calculations. For example, the localisation is one electron / atom with HF [5], and vary with other hybrid functionals. In the functionals used in this work, such as HSE06, B3LYP or PBE0, the localisation is still high ~ 0.8 *e* but less than one *e*. In the S_z = 0 state, μ on the two carbon atoms is approximately 0.75 *e* with different signs on each atom, whereas when S_z = 1, μ increased to ~ 0.85 *e* with a positive value. N atoms with all the spin states exhibit almost zero μ values. With *q*, the two carbon atoms gain a small charge of approximately 0.05 to 0.06 *e*, while the N atoms gain a higher charge ~ 0.3-0.4 *e* with (6-21G*).

The ground state with the MgN_2 defect has a closed-shell configuration, and there is no spin density per atom or cell. This system has C_{2v} symmetry determine by the dopants, and no change in the geometry was obtained by lowering the symmetry to C_s or even C_1. The geometrical data regarding this defect are reported in Table 5.2. Introducing an Mg atom in a vacant site in a 2NV defect led to elongating the Mg-N and Mg-C bonds by only ~ 0.2 Å and 0.1 Å, respectively, while compression of the 6N-C bonds decreased their length by ~ 0.01 Å. The difference in electronegativity between the Mg atom and it is neighbours affected the charge distribution. The Mg atom lost charge, and consequently, the N and C atoms gained charge. As with the MgN_3 defect, the polarity of 2Mg-N bonds extended to include the 6N-C bonds because all the C atoms in the N-C bonds lost charge by approximately 0.14 to 0.15 *e*. It is worth noting that the N charge is almost doubled in MgN_2 compared with 2NV, which significantly affected the polarity of the N-C bonds. For example, with B3LYP in 2NV, there was -0.344 *e* on the N atoms and +0.169 *e* on the C atoms involved in the N-C bond, which become in MgN_2, -0.619 *e* on N and + 0.150 *e* on C, increasing the mutual electrostatic interaction among N-C bonds. The bond population analyses of Mg-N refer to locating the N lone pairs in an antibonding site (negative value). In contrast, Mg-C has a strong interaction resulting from the Mg to 2C charge transfer. More useful information about the distribution of the bond lengths, charge, spin, and bond population up to the third shell, is provided in Figure 5.1.

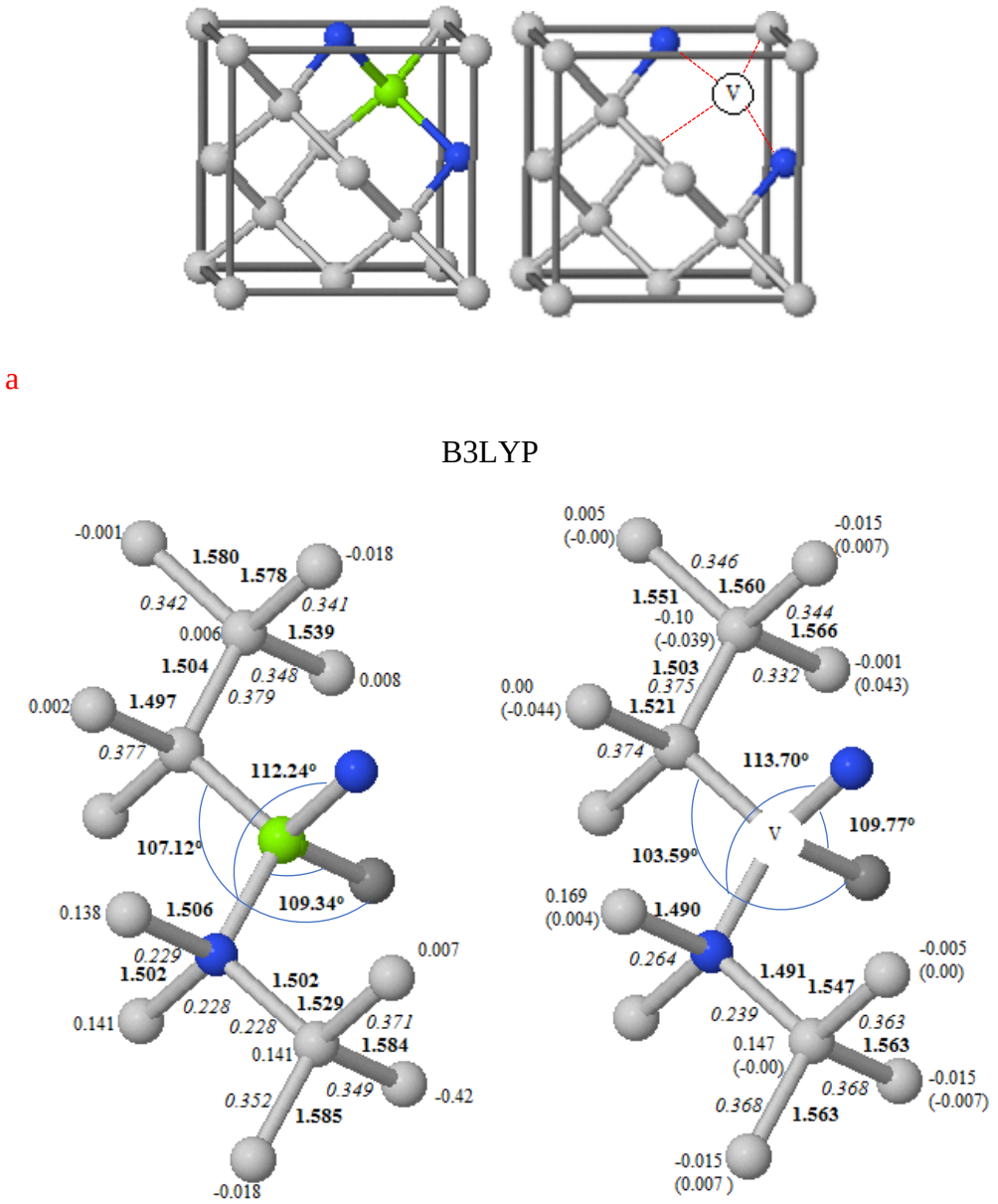

Figure 5-1: Bond length (in Å), angles (in degrees) (both **bold**), spin momentum (between brackets), Mulliken charges, bond overlap population (*italic*) (all in *e*) for irreducible C atoms in the first and the second shell of the (a) MgN_2 and (b) 2NV points defects in their ground state. Grey, green and blue indicate C, Mg and N atoms, respectively. All data were obtained with C/6-21G* and Mg, N/TZVP basis sets, 128-atom supercells and B3LYP functional. Both N atoms in the two-point defect are equivalent by symmetry, and similarly for their nearest neighbours. The C_β nearest neighbours in 2NV are equivalent to C_α nearest neighbours except they have an opposite spin sign. For information at defect site and first nearest neighbours see Table 5.1.

Table 5.1 Show spin momentum (μ); Mulliken atomic charges (*q*) (both in *e*) at the defect region (N_2V) in its two spin states; equilibrium bond distances of the first neighbours (the two C and the two N atoms) from the V (R_1) (in Å); equilibrium bond distances between of the C- C and N-N neighbours to V (R_2) (in Å); the overlap bond populations in the bond between V and the first neighbours (*b*) (in *e*); relative stabilities to $S_z = 0$ (*E*) (in eV). All the calculations were performed with 128-atom supercell and TZVP basis set for N.

Functionals	**basis set of C**		***S*z = 1**			***S*z = 0**			
			V	2N	2C_α	V	2N	C_α	C_β
HSE06	**(6-21G*)**	*q*	0.095	-0.397	0.063	0.090	-0.394	0.063	0.063
		μ	0.008	0.049	0.861	0.000	0.000	0.770	-0.770
		R_1	-	1.629	1.707	-	1.633	1.686	1.686
		b		-0.036	-0.030		-0.035	-0.027	-0.027
		R_2		2.713	2.748		2.733	2.649	
		E		0.217			0		
HSE06	**TZVP**	*q*	-0.091	-0.739	0.052	-0.069	-0.734	0.051	0.051
		μ	0.032	0.040	0.872	0.001	-0.00	0.792	-0.792
		R_1		1.621	1.687		1.625	1.666	1.665
		b		-0.075	-0.054		-0.070	-0.059	-0.059
		R_2		2.689	2.731		2.703	2.637	
		E		0.207			0		
B3LYP	**(6-21G*)**	*q*	-0.065	-0.348	0.053	-0.060	-0.344	0.054	0.054
		μ	0.007	0.050	0.843	0.00	-0.000	0.751	-0.751
		R_1		1.643	1.726		1.647	1.706	1.706
		b		-0.025	-0.023		-0.024	-0.020	-0.020
		R_2		2.744	2.776		2.759	2.681	
		E		0.211			0		
PBE0	**(6-21G*)**	*q*	-0.095	-0.399	0.064	-0.089	-0.396	0.064	0.064
		μ	0.010	0.048	0.867	-0.00	0.00	0.784	-0.784
		R_1		1.629	1.707		1.633	1.685	1.685
		b		-0.036	-0.030		-0.036	-0.027	-0.027
		R_2	2.717	2.748			2.732	2.652	
		E		0.211			0		

Table 5.2 Show Mulliken atomic charges (*q*) (in *e*) at the defect region (MgN_2C_2); equilibrium bond distances of the closest neighbours to the Mg (in Å) (R); overlap bond population (*b*) of the bond between Mg atoms and the closest neighbours (in *e*). All calculations were performed with 128-atom supercells.

Functionals / basis set			Mg	2N	2C
HSE06	C / 6-21G* Mg / 6-311G(d)	*q*	1.229	-0.525	-0.288
		R		1.806	1.834
		b		-0.061	0.230
	C / 6-21G* Mg / TZVP	*q*	1.456	-0.666	-0.355
		R		1.804	1.832
		b		-0.044	0.104
	C / TZVP Mg / 6-311G(d)	*q*	1.081	-0.828	-0.357
		R		1.799	1.823
		b		-0.045	0.214
	C / TZVP Mg / TZVP	*q*	1.478	-0.973	-0.445
		R		1.797	1.822
		b		-0.048	0.073
B3LYP	C / 6-21G* Mg / TZVP	*q*	1.443	-0.619	-0.362
		R		1.811	1.837
		b		-0.033	0.107
	C / 6-21G* Mg / 6-311G(d)	*q*	1.265	-0.486	-0.302
		R		1.813	1.840
		b		-0.059	0.218
PBE0	C / 6-21G* Mg / TZVP	*q*	1.546	-0.665	-0.354
		R		1.804	1.832
		b		-0.045	0.105
	C / 6-21G* Mg / 6-311G(d)	*q*	1.214	-0.523	-0.286
		R		1.806	1.833
		b		-0.072	0.234

5.3.2 Electronic structure

The band structures of the three investigated systems – the two open shells of 2NV and the one closed shell of MgN_2 – alongside the band structures of pure diamond computed with B3LYP are shown in Figure 5.2. In the 2NV system and $S_z = 1$, there is a significant shift from the α and β levels in the gap. The bands appear in the gap correspond to the defective electrons: the bands lowest Fermi level are occupied (spin-up) whereas the highest levels (spin down) are unoccupied. The energy difference between the highest occupied level (α) and the bottom of the conduction band of the host cell is 4.6 eV. In contrast, the energy gap between the top of the valence bands of the host lattice and the lowest-unoccupied level (β) is 2.7 eV.

In the case of 2NV with $S_z = 0$, the α and β levels almost coincide, generating three defect levels in the gap. The first one lies above the valence band by approximately 0.1 eV, corresponding to a level weakly localised on the nitrogen (Figure 5.3) [16], followed by the highest-

occupied states and then the unoccupied states that mostly belong to unsaturated C atoms. The gap between the former states is 2.7 eV, in agreement with previous HSE06 calculations (2.7−2.8 eV).[16] Saturation of the C atoms on 2NV defect that carrying α and β electrons by the two valence electrons of the Mg atom in MgN_2 give rise to two fully occupied bands in the gap and stable structure. The indirect transition between the highest-occupied defect level and the bottom of the conduction band of the host lattice is 3.8 eV. All the values of the gaps in both defects vary slightly with the functionals and basis sets used, as shown in Table 5.3.

Table 5.3 Defect energy gaps $E_g^{c\alpha}, E_g^{c\beta}$ as shown in the band-structure graphs (Figure 5-2) and the gap of pure diamond E_g^{pure} calculated using different basis sets and functionals. All energy gaps are in eV. 128-atom supercells were used. BS refers to the basis set.

Functional	BS of C	BS of Mg	Defects	S_z	$E_g^{c\alpha}$	$E_g^{c\beta}$	E_g^{pure}
HSE06	**(6-21G*)**	**(TZVP)**			3.339		5.15
		(6-311G(d))	MgN_2	-	3.338		
			2NV	1	4.141	2.422	
			2NV	0	2.499	2.493	
HSE06	**TZVP**	**(TZVP)**			3.480		5.38
		(6-311G(d))	MgN_2	-	3.477		
			2NV	1	4.325	2.507	
			2NV	0	2.570	2.563	
B3LYP	**(6-21G*)**	**(TZVP)**			3.870		5.71
		(6-311G(d))	MgN_2	-	3.868		
			2NV	1	4.625	2.73	
			2NV	0	2.758	2.758	
PBE0	**(6-21G*)**	**(TZVP)**			4.037		5.79
		(6-311G(d))	MgN_2	-	4.037		
			2NV	1	4.853	3.077	
			2NV	0	3.195	3.195	

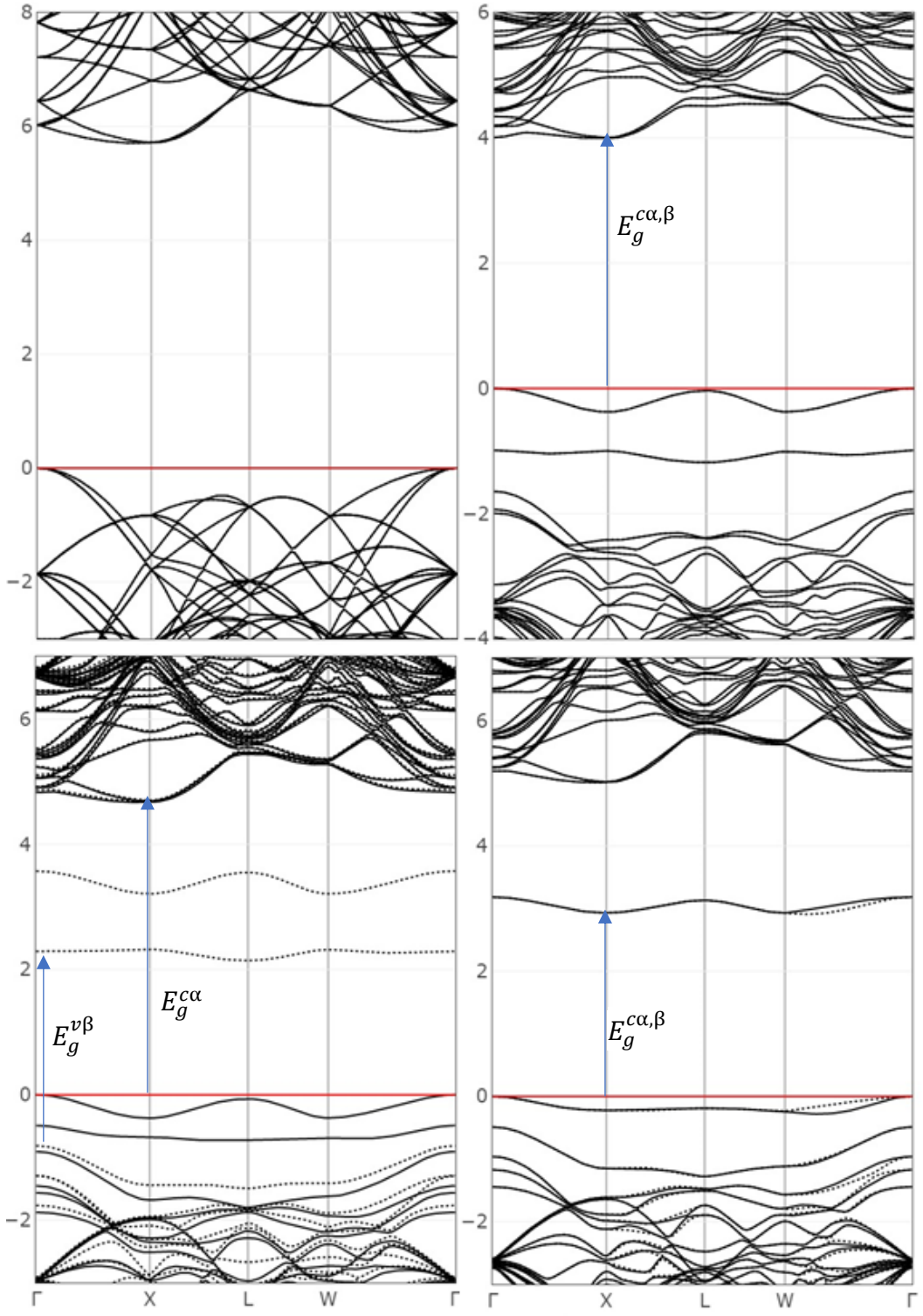

Figure 5-2 Electronic band structure of pure diamond, a closed-shell system of MgN_2 (top panel, left and right, respectively), an unsaturated open-shell 2NV system (bottom panel) with its two spin states, triplet (left) and singlet (right). The energies are presented relative to the Fermi energy. The red line refers to Fermi level, and the continuous and dashed black lines refer to the (spin up) and (spin down) energy levels, respectively. All calculations were performed with the 128-atom supercells, B3LYP and C/6-21G* and Mg, N/TZVP basis sets

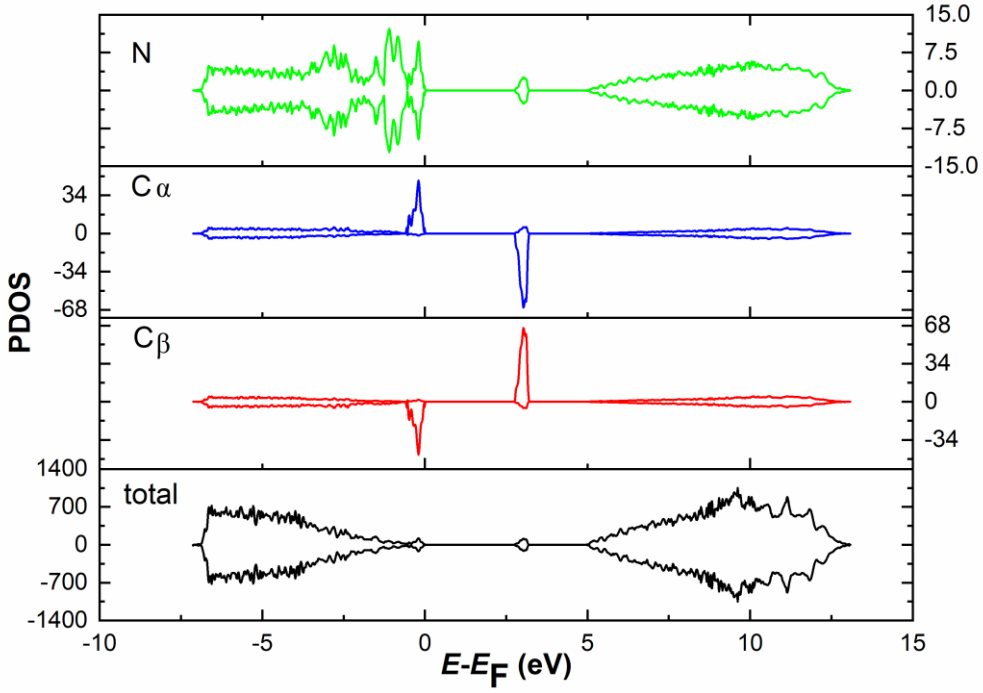

Figure 5-3 Projected DOSs of the 2NV defect performed with 128-atom supercells, B3LYP and C/6-21G* and Mg, N/TZVP basis sets with a ground state of $S_z = 0$, plotted only for a 300 to 500 band range

5.3.3 IR spectroscopy

The simulation can begin with the spectra of pure diamond, which was simpler because there are no peaks; therefore, all the bands obtained from the simulated IR spectra of the MgN_2 and 2NV defect can be allocated explicitly to the simulated defect. However, considering all the characteristics of the IR spectrum to be a "fingerprint" of a defect in a diamond is extremely difficult due to the presence of the same frequencies in several defects. Consequently, to reveal a point defect in a complex spectrum, it is useful to identify the frequencies associated with the significantly localised nuclear vibration modes in the defect area and which have higher intensity in comparison with other peaks.

As seen in chapter 3, the computed Raman peaks in primitive cells using HSE06, PBE0, and B3LYP were at 1,362, 1,368 and 1,331 cm^{-1}, respectively. The best theoretical value 1,331 cm^{-1}, 1 cm^{-1} below the corresponding experimental value, was obtained by B3LYP, therefore, in the following section, the B3LYP functional was used to calculate and analysis the spectrum of the two-point defects. The simulated IR spectra of MgN_2 defect in the range of 300 cm^{-1} to 1,400 cm^{-1} are shown in Figure 5.4; no peaks appear above 1340 cm^{-1}. The normal modes of

the most significant spectral features were interpreted by the ANALYSIS keyword that prints out analysis indicated which mode involve; bending or stretching for each frequency, in addition to visualising the graphical animations that help to track the atomic motions during vibration. The point defect activates modes with a series of frequencies that are located just below the significant Raman value of 1,332 cm^{-1}. There are three prominent absorption groups classified based on their intensities noteworthy in the features of the overall spectra. The spectra are identified by localised, intense peaks at 1,060 cm^{-1} and 1,071 cm^{-1} (~34.5 km mol^{-1}) and by few peaks with lower intense at 1,307, 1,180 and 1,031 cm^{-1} (~16 km mol^{-1}) and 1,235 cm^{-1} (~11 km mol^{-1}). The last group contains peaks below 901 cm^{-1} that have small intensities comparing to those appearing at higher wavenumbers.

Analyses of atomic motions show that the 1,060 cm^{-1} peak involves the stretching mode of the two N-C bonds containing two C-C bonds; one of the carbon atoms is in N-C, and all the bonds are located along the mirror plane crossing the Mg, resulting in asymmetric stretching of the two N-C-C fragments. The 1,071 cm^{-1} peak arises from the stretching of the other four N-C-C clusters in the defect, as does the 1,060 cm^{-1} peak. These two peaks can be considered as significant features of the MgN_2 defect due to the localisation on the defect site and the high intensities relative to the other bands. Comparatively, the 1,180 cm^{-1} peak has weak localisation and shows more collective character as it involves the stretching of the two Mg-C bonds and the bending of the four C-C-C fragments, in which one C is bonded to Mg. Better localisation is shown by the 1,031 cm^{-1} peak that involves the vibration of the N-Mg-N fragment in asymmetric stretching mode.

In the low-intensity region, the peak at 324 cm^{-1} corresponds to the bending mode of Mg with its closest neighbours; it is extremely well localised on the defect. The low intensity of this peak relative to those at 1,060 and 1,071 cm^{-1}, alongside the vibration at low frequency, is due to the involvement of the heavier Mg atom in the mode and the charge distribution on the defect area (Figure 5.1). It appears that the entire bipolarity in the MgN_2 defect is not restricted to the three foreign atoms but extends to involve the two Mg-C bonds and the six C nearest to N. Therefore, the intensity of the vibration mode at 324 cm^{-1} seems to be largely affected by the magnitude of bipolarity more than other modes. Also, Mg-N bonds are strongly dipolar, and any fluctuation in their dipole moment (movement) is associated with opposing action in the two C atoms bonded to Mg.

To confirm the localisation of these modes in the defect region and investigate their correlation to specific elements, the spectra of isotopic substitutions were acquired. In the case of N^{14}, the most stable alternative isotope N^{15} was used. For Mg^{24}, there are two other possible, stable isotopes – Mg^{25} and Mg^{26} – of which the only Mg^{25} was used.

The two most intense peaks at 1,060 and 1,071 cm^{-1} showed a strong isotopic shift to low frequencies with N^{15} by approximately 5 and 4 cm^{-1}, respectively, whereas with Mg^{25} the shift was small: ~ 1 cm^{-1}. The 1,031 cm^{-1} peaks were slightly affected by Mg^{25} with a shift by ~ 2 cm^{-1}, and their intensity was highly diminished by N^{15} giving shift of ~ 4 cm^{-1}. With Mg^{25}, the peak at 324 cm^{-1} shifted by approximately 4 cm^{-1}, confirming the correlation of this peak to Mg.

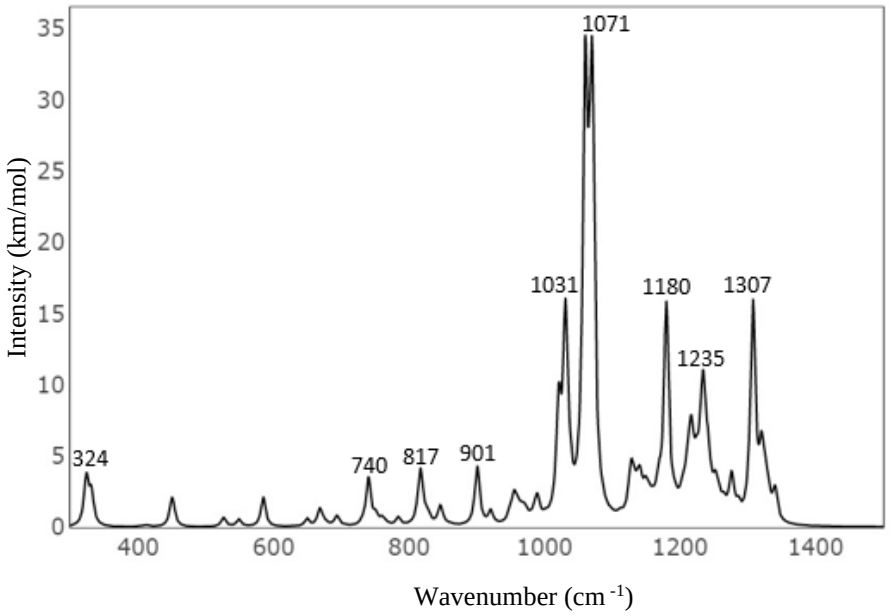

Figure 5-4 Show the IR spectra of the MgN_2 defect in diamond using 128-atom supercell, B3LYP and C/6-21G* and Mg, N/TZVP basis sets. A full width at half-maximum (FWHM) 8 cm^{-1} was used with a Lorentzian function.

In Figure 5.5, a comparison between the IR spectra of MgN_2 and the correspondin spectra of the unsaturated system 2NV is shown. The spectra in the 2NV defect are dense compared with that in MgN_2, which can be expected from neutralising the unsaturated bonds using Mg, which is heavier than the nearest neighbours and the host atoms. The most intense peak in 2NV was contained in the stretching mode of the two C-C bonds where one of the C atoms bonded directly to the unsaturated C and they were all located along the mirror plane and appeared at a higher frequency (1,095 cm^{-1}) compared to the corresponding frequency in

MgN_2. This peak behaved similarly to the 1,060 and 1,071 cm^{-1} peaks in MgN_2 spectra when affected by N^{15} isotopic and shifted to a lower frequency by 4 cm^{-1}, indicating that it is well localised on the defect.

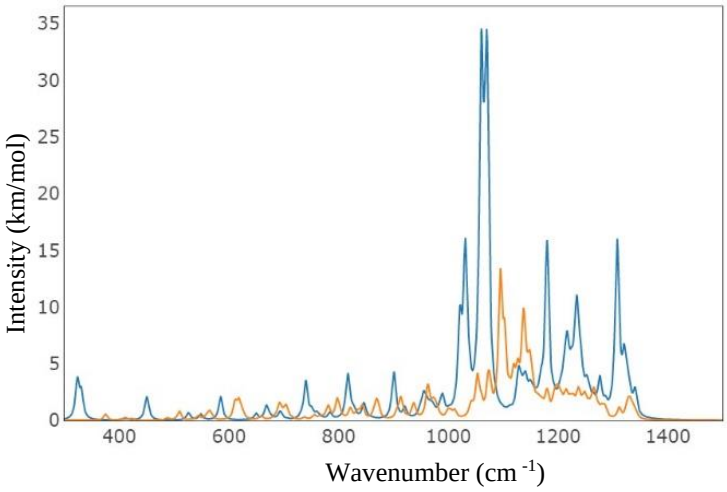

Figure 5-5 A comparison between the IR spectra of the MgN_2 defect (blue line) and 2NV (orange line) computed with the 128-atom supercells, B3LYP, and C/6-21G* and Mg, N/TZVP basis sets. The full width at half-maximum (FWHM) 8 cm^{-1} was used with a Lorentzian function.

Table 5.4 B3LYP (6-21G*) wavenumber shifts (in cm^{-1}) as obtained from the 128-atom supercells for the MgN_2 defect using the wavenumbers from Mg^{25} and N^{15}. All the shifts are in cm^{-1}.

$\bar{\nu}$ (cm^{-1})	Mg^{25} $\bar{\nu}$	Shift	N^{15} $\bar{\nu}$	Shift
1307	1307	0	1307	0
1235	1235	0	1235	0
1180	1180	0	1180	0
1071	1069	1	1066	4
1060	1059	1	1053	5
1031	1029	2	1027	4
901	901	0	901	1
817	817	0	817	0
740	740	0	740	0
324	320	4	323	1

5.4 Conclusion

The geometrical, energetic, electronic, and IR features of two- point defects– 2NV and MgN_2 – in diamond were studied through 128 supercell calculations and using three hybrids functional. The local changes in the geometries, including the spin and the charge distribution, were presented in detail. The open-shell solution of the 2NV defect showed that the singlet state is the ground state of the system, with relative stability being approximately 0.2 eV compared to that of the triplet state. The band structure analysis of the singlet state indicated that the defect created one unoccupied band below the conduction band minimum and other two occupied bands appear in the gap below the fermi level, with the lower one being approximately 0.1 eV from the top of the valence band. The top two bands are very localised in the two carbon atoms contained in the dangling bonds, as confirmed by PDOS analysis.

In comparison, the MgN_2 defect exhibited a closed-shell system with a small local distortion in the lattice compared to that induced by the 2NV defect, (i.e., the distance between the two C atom nearest neighbours to Mg increased by approximately 0.2 Å). The two electrons from the Mg valence bands coupled with the two electrons from the dangling bonds generated two fully occupied bands in the gap. This resulted in an insulating system with a bandgap of approximately 4 eV between the top level and the bottom of the conduction band.

The most significant IR peaks for MgN_2 are the peak at 1,071 with a shoulder at 1,060 cm^{-1} computed with B3LYP. Despite the low intensity of the peak at 324 cm^{-1} relatives to those appearing at higher frequencies, it is potentially measurable for two reasons. First, this peak is strongly localised on the Mg atom as concluded from the isotopic shift, second, it appears in a region that usually has no features in the IR spectra from the best-known defects in diamond (N, B, H) [11,7,10]. Therefore, detection of this peak in a complex spectrum for a sample containing only Mg and N is more likely related to Mg.

5.5 References

1. Salustro, S. *et al.* The A-center defect in diamond: Quantum mechanical characterization through the infrared spectrum. *Phys. Chem. Chem. Phys.* **19**, 14478–14485 (2017).

2. Salustro, S. *et al.* Characterization of the B-Center Defect in Diamond through the Vibrational Spectrum: A Quantum-Mechanical Approach. *J. Phys. Chem. A* **122**, 594–

600 (2018).

3. Ferrari, A. M., Salustro, S., Gentile, F. S., Mackrodt, W. C. & Dovesi, R. Substitutional nitrogen atom in diamond. A quantum mechanical investigation of the electronic and spectroscopic properties. *Carbon N. Y.* **134**, 354–365 (2018).

4. Salustro, S. *et al.* Infrared and Raman spectroscopic features of the self-interstitial defect in diamond from exact-exchange hybrid DFT calculations. *Phys. Chem. Chem. Phys.* **18**, 21288–21295 (2016).

5. Zelferino, A. *et al.* The electronic states of the neutral vacancy in diamond: a quantum mechanical approach. *Theor. Chem. Acc.* **135**, 1–11 (2016).

6. Salustro, S., Nöel, Y., Zicovich-Wilson, C. M., Olivero, P. & Dovesi, R. The v + i defects in diamond: An ab initio investigation of the electronic structure, of the Raman and IR spectra, and of their possible recombination. *J. Chem. Phys.* **145**, (2016).

7. Gentile, F. S. *et al.* Hydrogen, boron and nitrogen atoms in diamond: a quantum mechanical vibrational analysis. *Theor. Chem. Acc.* **137**, 1–10 (2018).

8. Sansone, G. *et al.* Looking for sp2 carbon atoms in diamond: a quantum mechanical study of interacting vacancies. *Theor. Chem. Acc.* **137**, 1–9 (2018).

9. Gentile, F. S. *et al.* The VN3H defect in diamond: A quantum-mechanical characterization. *Phys. Chem. Chem. Phys.* **19**, 22221–22229 (2017).

10. Salustro, S. *et al.* Hydrogen atoms in the diamond vacancy defect. A quantum mechanical vibrational analysis. *Carbon N. Y.* **129**, 349–356 (2018).

11. Salustro, S. *et al.* The characterization of the VNxHy defects in diamond through the infrared vibrational spectrum. A quantum mechanical investigation. *Carbon N. Y.* **132**, 210–219 (2018).

12. Collins, A. T., Stanley, M. & Woods, G. S. Nitrogen isotope effects in synthetic diamonds. *J. Phys. D. Appl. Phys.* **20**, 969–974 (1987).

13. Collins, A. T. & Woods, G. S. An anomaly in the infrared absorption spectrum of synthetic diamond. *Philos. Mag. B Phys. Condens. Matter; Stat. Mech. Electron. Opt. Magn. Prop.* **46**, 77–83 (1982).

14. Davies, G. The A nitrogen aggregate in diamond-its symmetry and possible structure. *J.*

Phys. C Solid State Phys. **9**, L537 (1976).

15. Sutherland, G.B.B.M., Blackwell, D.E. and Simeral, W. G. The problem of the two types of diamond. *Nature* **174**, 901–904 (1954).

16. Deák, P., Aradi, B., Kaviani, M., Frauenheim, T. & Gali, A. Formation of NV centers in diamond: A theoretical study based on calculated transitions and migration of nitrogen and vacancy related defects. *Phys. Rev. B - Condens. Matter Mater. Phys.* **89**, 1–12 (2014).

CHAPTER 6

AN EXPERIMENTAL STUDY ON THE DIFFUSION OF NITROGEN DOPED DIAMOND IN THE PRESENCE OF MAGNESIUM

CHAPTER 6 – AN EXPERIMENTAL STUDY ON THE DIFFUSION OF NITROGEN DOPED DIAMOND IN THE PRESENCE OF MAGNESIUM

6.1 Introduction

Not all the commonly used techniques for doping semiconductors, such as incorporating the dopant during crystal growth (CVD), diffusion or ion implantation, are appropriate to diamond due to the extremely tight binding of its carbon bonds and its metastability with respect to graphite. Thus, attempts to dope diamond by n-type dopants have not yielded convincing electron conductivities. The electrical activity of the residual damage, the difficulty of controlling the mobilities of the dopants upon annealing, and problems related to achieving ohmic contacts on the n-type doped layer, all contribute to electrical behaviour that is difficult to distinguish from the actual chemical effect of the dopants.[1]

Even though the co-doping of diamond by a metal and N atoms to form a complex with shallow n-type character has been theoretically calculated to be viable (see chapter 4), few studies have attempted to explore such a system from the experimental side.[2–7] Nitrogen is readily incorporated into the diamond lattice making it a common element in synthetic and natural diamond. Therefore, the challenge of the low solubilities of larger dopants can be overcome by introducing the chosen co-dopant together with an excess of N, followed by a thermal treatment to activate the dopants.

One of the challenges in using a complex of dopants efficiently seems to be the concentration of these complexes, which is mainly due to the high mobilities of the dopants at elevated temperatures. In order to successfully engineer a co-doping system in diamond, any thermal treatment must be tailored in such way as to prevent the formation of undesired defects. For instance, controlling the thermal treatment for dopants such as Li and N to form LiN_4 is not experimentally practicable due to the low activation energy of diffusion of both dopants, which causes them to form various inactive complexes. Replacing the Li with a larger dopant, i.e., Mg, will hinder the mobility of the metal, at least at the temperature where the N and V become mobile to form VN_x complexes,[8] which helps the formation of MgN_3 at reasonable energies, as shown in chapter 4. We propose a step-by-step formation mechanism based on the following points.

- The vacancy migration barrier, 2.3 eV, is low enough to promote diffusion of vacancies at temperatures ~ 600 ^{o}C which can then either be trapped by N in a substitutional site to form a NV defect [9] or merge with Mg.
- The migration barrier of NV is calculated to be 4.9 eV (~1500 ^{o}C) while the dissociation barrier of NV to N and V is estimated to be 5.8 eV.[10] Therefore, migration is likely to rule out the dissociating mechanism under annealing treatment.
- 2NV is stable and needs a higher temperature (more than 1700 ^{o}C) to dissociate to the A-centre and V.[10]
- From chapter 4, the formation energy of Mg from 2NV is comparatively low ~ < 3.7 eV, which can guarantee formation of MgN_2 under annealing treatment once the 2NV is presented.
- The binding energy of MgN_2 and MgN_3 are very high > 10 eV which ensures stability of these complexes once they formed. The relative stability is MgN_3 > MgN_2 by about ~2 eV.

In this chapter we report a combination of different co-doping techniques to investigate co-doping of diamond with both Mg and N atoms. Monitoring the nitrogen diffusion upon thermal annealing was a primary aim of this study. The small ionization energy of MgN_3 compared with P are a significant motivation to attempt synthesis of an MgN_3 complex in diamond.

The study is divided into two sections depending on the method used to introduce the elements into diamond film: Intermediate layer in CVD diamond or ion implantation. The samples were characterized by different techniques to study the possible effect of the dopants' diffusion on the electrical properties.

6.2 Experiment Details

6.2.1 CVD method

In the CVD method, ammonia (NH_3) gas was used as a source for nitrogen to dope the diamond. The main obstacle was the magnesium source. Amongst the few forms of commercially available Mg compounds, magnesium nitride (Mg_3N_2) was chosen as the source because it is suitable to use as a precursor within the HFCVD reactor; it is also affordable, and non-hazardous. Furthermore, the nitrogen content does not cause issues in co-doping with

nitrogen. The main drawback of magnesium nitride is its sensitivity to water, reacting to form magnesium hydroxide and ammonia. Therefore, Mg_3N_2 was suspended in toluene and introduced into the chamber in a semi-liquid form with argon gas flow to give the system extra time to reach the vacuum state before completely evaporating the solvent.

6.2.2 Preparation procedure

6.2.2.1 Manual abrading of Si substrate

Before seeding, the substrate surface must be cleaned to remove the residual dust. This was done by placing the substrate in an ultrasound bath with acetone or methanol for 5 min, then removing the substrate and allowing it to dry naturally. Manual abrasion of the silicon (Si) substrate with small diamond particles (0.25 µm) was used to enhance diamond nucleation, using a second Si wafer as an abrasion pad, followed by washing with acetone or alcohol in an ultrasound bath for 5 min to remove any excess diamond powder.

6.2.2.2 N-doped diamond (NDD) film

Comprehensive experiments were carried out using ammonia as a source of nitrogen with two types of substrates, silicon (Si) and polycrystalline diamond (PCD), to determine the optimum ammonia ratio that maintains a reasonable microcrystalline diamond growth rate and good quality. The films were grown by flowing 200 standard cubic cm per minute (sccm) of H_2, two sccm of CH_4 (0.81% CH_4/H_2) and different ratios of NH_3. Table 6.1 shows the NH_3 ratios used with each substrate type.

Table 6.1 Gases used for diamond film deposition and the percentage of the gases relative to H_2.

Substrate	Gases	Percentage relative to H_2 atmosphere
Si/PCD	H_2	-
Si/PCD	CH_4	0.81 %
Si	NH_3	0.41-0.58 %
PCD		0.41-1.15 %

6.2.2.3 Encapsulation of magnesium into NDD films

The Mg suspension was prepared in N_2 atmosphere in a glovebox using magnesium nitride (dull-yellow powder, Sigma Aldrich, 99.5% purity) as a source of Mg (~ 0.01 g). Toluene (2.5 ml) was used as a medium to disperse the Mg_3N_2 particles due to their high density

and its low evaporation rates. The combination was placed in an ultrasonic bath for 30 min then used immediately. Mg_3N_2 addition was dropped onto the surface of a pre-prepared NDD film., in 25 µl aliquots, and with a total addition of 200 µl for a substrate of 10 × 10 mm dimensions and 50 µl for a 5 × 5 mm substrate. After each drop, a waiting period of a few seconds occurred to maintain the surface tension of the liquid film and to prevent the droplet from spilling outside the sample surface. After the partial evaporation of the solvent, about ten min, the sample was placed in the HFCVD chamber which was evacuated to its base pressure, and the CVD start-up process initiated using the same standard conditions used previously (chapter 2). This involved first turning on the substrate heater (400°C) for 30 mins followed by turning on the filaments under flowing hydrogen gas for one h. After the Mg_3N_2 dissociation (as seen from the viewport of HF reactor through appears all the shiny surface of the substrate), a thin diamond capping layer was deposited to ensure the encapsulation of the magnesium inside the film. CH_4 and NH_3 gases were introduced into the chamber to start NDD growth.

After deposition, the samples were removed from the CVD reactor. Aiming to enhance the Mg diffusion in diamond and increase the homogeneity, all the dopant samples were placed into a quartz tube, which was evacuated and then sealed in the departmental glass workshop. The tube was then heated up to about 1200 ^{o}C for 2 h in a tube furnace, ramping up at 20 ^{o}C/min, then left to cool down to room temperature overnight to be characterized.

6.2.2.4 Carburization of filaments

The tantalum filaments were carburized for different lengths of time and with different ratios of hydrogen and methane gases to determine the best carburization method that would enable the tantalum filaments to later survive in the pure hydrogen environment. The filaments were carburized for 30 min before introducing Mg_2N_3 by flowing 1.33% of methane in hydrogen gas. The carburization process increased the survival period of the filaments to more than 3 h. Raising the filament temperature gradually (i.e., 5 ^{o}C/min), after turning on the heater source, demonstrated an effective way to avoid thermal shock and filament breakage, which were employed when turning off the filament heater after carburization and prior to commencing the heating.

6.2.3 Ion implantation

For ion implantation studies, all the cut and polished single crystal diamond (SCD) substrates (3.0×3.0×0.3 mm) used in this study were purchased from Diamond Elements Pvt. Ltd. These samples were grown by a “Microwave Plasma Chemical Vapor Deposition” (MPCVD)

method and had very high thermal conductivity. After boiling the samples in a hot KNO_3+H_2SO_4 solution for 3 h then rinsing in deionized water, the samples were sent to the Surrey Ion Beam Centre at the University of Surrey where ion implantation was performed at room temperature. The Mg and N ions were implanted with different energy and doses, as described in Table 6.2, to avoid damage caused by exceeding the critical level and the lattice restructuring into graphite.[11] After implantation, the samples were completely transparent and did not exhibit any evidence of forming black amorphized carbon near the surface.

Samples MgN12 and MgN14 were divided into two groups. The first group was evacuated in quartz tubes to a vacuum of > 10^{-2} mbar (to prevent graphitization) and annealed at 1200 ^{o}C in the tube furnace for 2 h. SIMS depth profile measurements were performed to study the effect of the annealing on the diffusivity of N and Mg. Since SIMS measurements destroy the samples due to etching by the ion beam, no electrical measurements were performed with these samples. After each measurement, we selected a new region on the sample surface upon which to perform the next SIMS measurement.

The second group (including Mg14 sample) selected for electric measurement study was also evacuated in quartz tubes and annealed for 2 h at different temperatures (400, 800, or 1200 ^{o}C) to monitor the graphitization and the electrical resistance of the samples. Different implantation/annealing schemes reported in the literature[12–17] were tested with varied results depending on the implanted ions. Therefore, in this study, we used a common strategy of annealing the samples under different temperatures.

Table 6-6.2 Implantation dose and energy of nitrogen and magnesium ions.

Count	Sample label	Description	Ion	Energy (keV)	Dose (Ions/cm^2)
1	**Mg14**	**Control Sample/ Mg**	Mg	50	1×10^{14}
2	**MgN12**	**Mg + N**	Mg	50	1×10^{14}
			N	40	3×10^{12}
3	**MgN14**	**Mg + N**	Mg	50	1×10^{14}
			N	40	1×10^{14}

6.3 Instruments

6.3.1 Hot filament

A hot-filament reactor was utilized to prepare all the diamond samples in this section. The standard gases that were adjusted during the experiments are listed in Table 6.1. A tantalum filament with 0.25 mm diameter and 99.9% purity was used in all the growth and diffusion processes. Th filaments were separated from the substrate by approximately 3 mm. Two types of substrate were used here: a silicon wafer (P-doped, 1-5 Ω cm^{-1}, one-side polished, 100), which was manually abraded by diamond grit, and a polycrystalline diamond substrate provided by Element Six (bulk and surface resistivity of 10^{12} and 10^{10} Ohm cm respectively). The pressure was adjusted to ~ 20 Torr.

6.3.2 SIMS

All the SIMS depth profiles in this study were achieved using a gallium ion beam at 25 keV energy and an incident angle of ~ 45°. Depth profiles were performed with a beam current of 3.0 nA, measured using a Keithley picoammeter, at a magnification of 3000×. The system operated under high vacuum $<10^{-7}$ mbar (Vacuum Generators model 7035). The control software used was 'Pisces' running under the Windows system.

The only selected ions ($^{24}Mg^{+}$, $^{26}CN^{-}$ and $^{12}C^{+}$) from the mass spectrum were observed during a depth profile as a function of time through ion counting. Positive and negative ions were measured in different set-up experiments. A "gating" technique was used to isolate the sidewalls of the pits formed by the primary ion beam from the off optical axis secondary ions. The off-axis ions contribution gives lower mass resolutions and occur when the primary beam raster sputters a large area rather than the point at which the primary beam interacts the sample. The ratio of the signal from a selected ion to that from carbon was multiplied by a calibration factor estimated from a standard sample previously implanted with known concentrations to determine the concentration of each dopant.

6.3.2 RAMAN

A Renishaw 2000 spectrometer (Renishaw, UK) attached to a microscope was used at room temperature to detect the Raman shift with 514 nm excitation wavelength from an Ar ion laser (green). The recorded spectra gave an insight into the composition of the samples by

measuring the relative intensities of sp^3 diamond signals to sp^2 graphitic signals, which vary with the sample and deposition conditions.[18]

6.3.3 SEM

A JEOL JSM IT300, with thermal emission and a resolution ~100 nm, was utilized to characterize the morphology of all the samples and determine the optimum time needed to grow the capping layers. Different magnification was used depending on the prepared sample with a beam energy of ~ 15 kV and 10-20 mm working distance.

6.3.4 Electrical Resistance

Four contacts were fabricated on the sample surface by depositing 50 nm of Ti capped by 100 nm of the Au to prevent oxidation of the Ti by oxygen in the air.[19] Annealing of the contacts was done in a tube furnace at 400 ˚C to bond Ti and diamond to form a thin layer of TiC at the interface, thus improving adhesion. Annealing at a higher temperature might provide better adhesion, but it can cause a complication during the later removal of the contacts with aqua regia[20,21]; therefore, further annealing at 600 °C was tested only with the implanted samples that were heated at 1,200 °C.

For the PCD samples, the contacts were deposited on the as-grown surface that already had H-termination. These films, after deposition in a hot filament reactor, were cooled down in H_2 to ensure hydrogenation of the surface. The sample that was annealed at 1200°C was re- hydrogenated in a hot filament reactor to replace the lost H-termination expected from the annealing step. The conductivity was compared with that of a sample treated with an oxygen plasma kit (Edwards S150A sputter coater) for 5 min to terminate the surface by oxygen to remove the conductive layer.[4,22–25]

In the implanted samples, to avoid metal evaporation or diffusion, an aqua regia solution was used to remove the contact metals from the surface of the implanted samples before starting the next heating cycle. After acid cleaning or an aqua regia wash for the implanted samples, the surfaces were oxygen terminated. The H-termination of these samples was performed using the MWCVD reactor (done by Michael James). Conductive samples were re-annealed in ambient air at 200, 300 and 400 °C to monitor the sheet resistance thermal stability in air.[26,27] Van der Pauw measurements were taken immediately after cooling the samples to room temperature. Afterwards, the samples were treated with an oxygen plasma kit (Edwards S150A sputter coater) for 5 minutes before checking its resistance.

6.4 Results and Discussion

6.4.1 Deposited nitrogen-doped diamond

6.4.1.1 Surface morphology and Raman intensity

Starting with Si samples, NH_3 gas was introduced into the reactor with specific NH_3/H_2 ratios, 0.41%, 0.46%, 0.52% and 0.58% (from 4100 to 11500 ppm), to deposited N-doped diamond films. Scanning electron microscopy provided a comparative description of morphology, grain sizes and grain boundaries of the as-grown films. Figure 6.1 shows that an increase in the NH_3 ratio significantly affected the sample morphology, which was expected after the NH_3 addition. The crystal shapes transformed from random facets seen in un-doped diamond to nearly fully square smooth faces with some finer polycrystalline material deposited between. This was seen with ratios of 0.41% and 0.46%, without noticeable difference between these ratios. Such enhancement on [100] faces by nitrogen addition had been widely observed before.[28–31] The large square-shaped facets (about 1 µm) started to diminish with ratios of 0.52% and 0.58%, accompanied by an increase in crystals smaller than 0.5 µm that caused deterioration on the film quality with N input,[31] as the films became more nanocrystalline.

The variation of the quality and crystallinity of the as-deposited diamond film is commonly interpreted from the corresponding Raman spectra.[18] Figure 6.4 shows the Raman spectra of the four ratios of NH_3 with a clear diamond peak positioned at ~ 1332 cm^{-1}. The degradation of quality observed with SEM was also confirmed by a sharp increase in the intensity of the G-band at 1,550-1,540 cm^{-1}, introduced by non-diamond carbon phases.[32] There was also an appearance of an impurity band at 1,190 cm^{-1} with 0.52% and 0.58%. This peak was attributed to sp^2 carbon in *trans*-polyacetylene at the grain boundaries and disordered sp^3 bonding[33,34] and is an indicator of the change to nanocrystalline diamond with the increasing concentration of NH_3 in the gas feed. As the increase of NH_3 at ratios above 0.41% did not lead to any further enhancement in the quality of the diamond grown on Si, this ratio was used in the rest of the study.

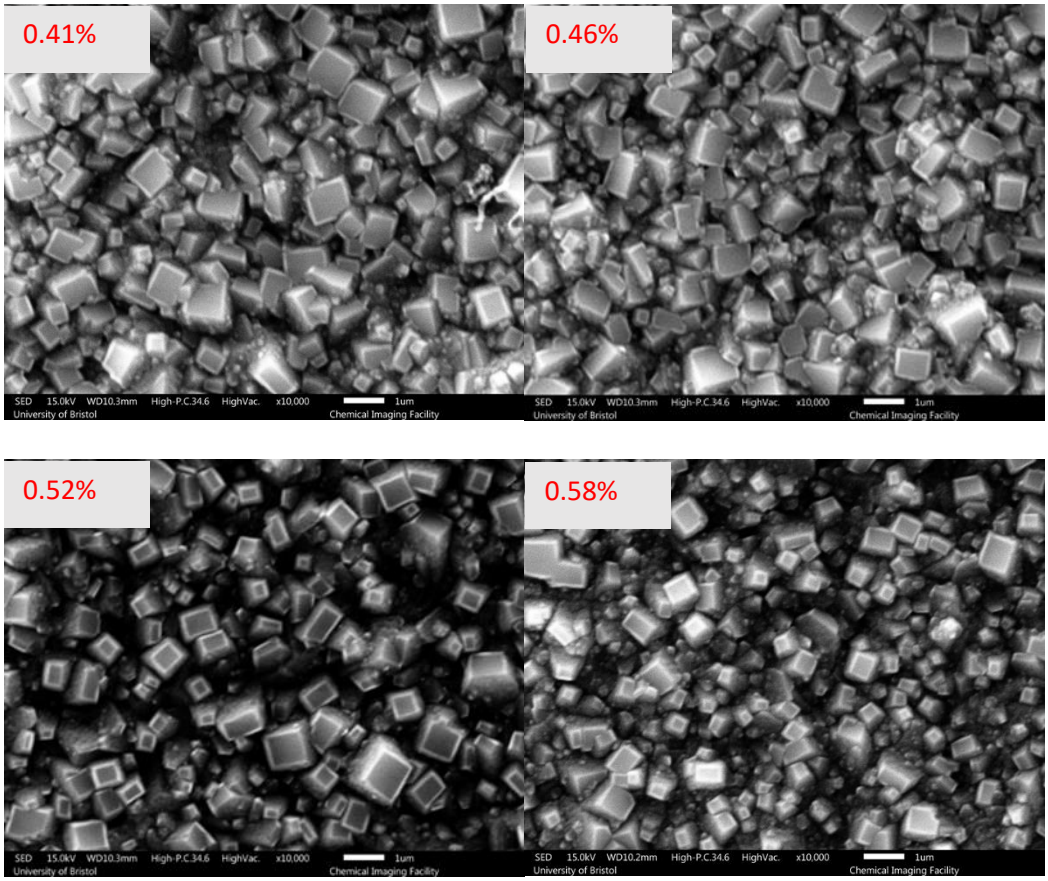

Figure 6-1 SEM micrographs of films grown on silicon substrates (Si). All images share the same magnification, 10,000 × with scale bar equal to 1 µm.

Figure 6.2 shows the morphology of samples grown on the polished side of PCD with 0.41%, 0.58%, 0.86% and 1.15% ratios of NH_3. All samples shared the main morphological characteristics involving randomly orientated domains defined by the polished substrate. The [100] texture induced by NH_3 was observed by increasing the magnification by 8-20 × for 0.41%, as seen in Figure 6.3, with disappearing borders between some square facets not shown in Si. Such overlaps increased with the higher ratios: 0.86% and 1.15%. The main features of PCD films were the relatively large crystal sizes (more than 20 µm), causing a significant reduction in grain-boundary density. The high quality of these films, as seen in the Raman spectra in Figure 6.4, compared with the Si group grown in the same conditions, was expected due to the high density of nucleation sites governed by the homoepitaxial substrate relative to the films grown on a silicon carbide interfacial layer.

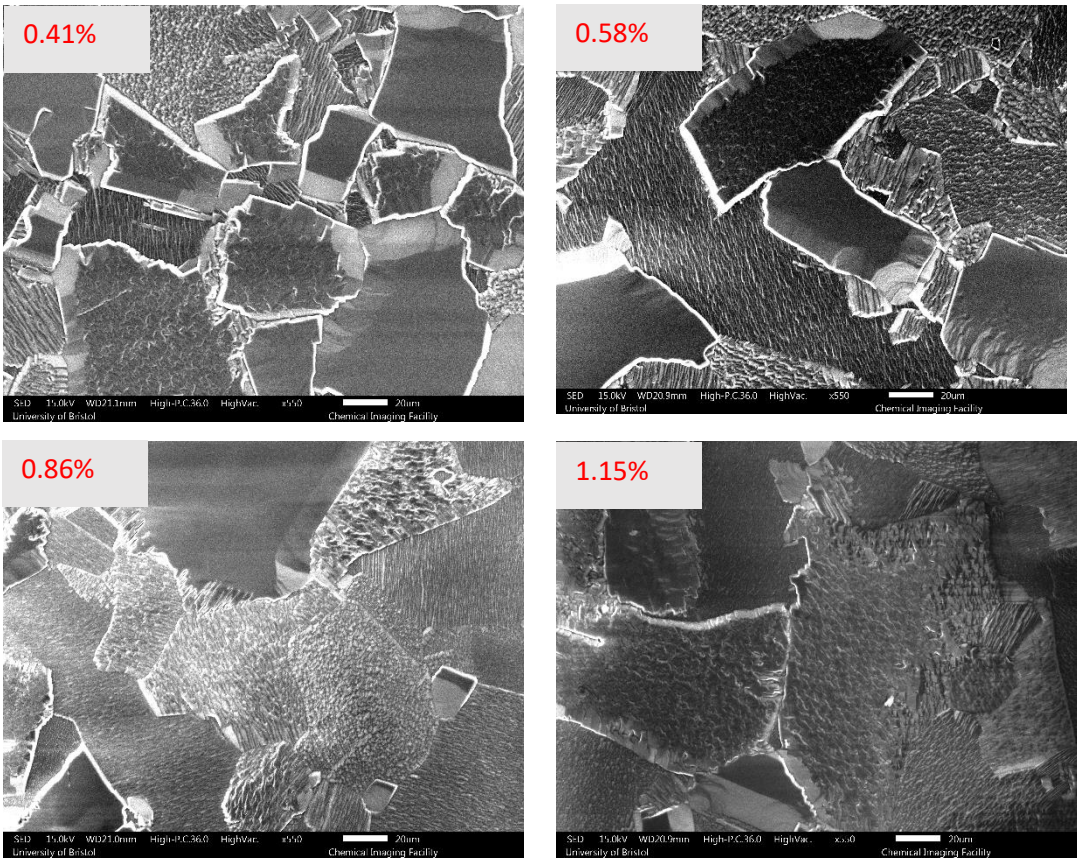

Figure 6-2 SEM micrographs of films grown on polycrystalline diamond substrate (PCD) with different ratios of NH_3. All images share the same magnification, 550 × with scale bar equal to 20 µm.

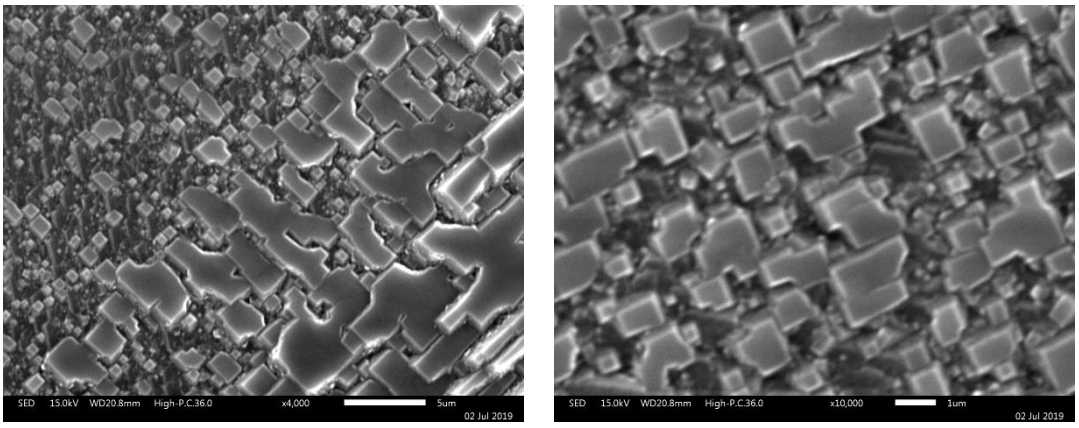

Figure 6-3 SEM micrographs show the 100 texture of films grown on polycrystalline diamond substrate (PCD) with 0.41% ratio of NH_3 with two magnifications, 4,000× and 10,000× with scale bar of 5 µm and 1 µm from left to right.

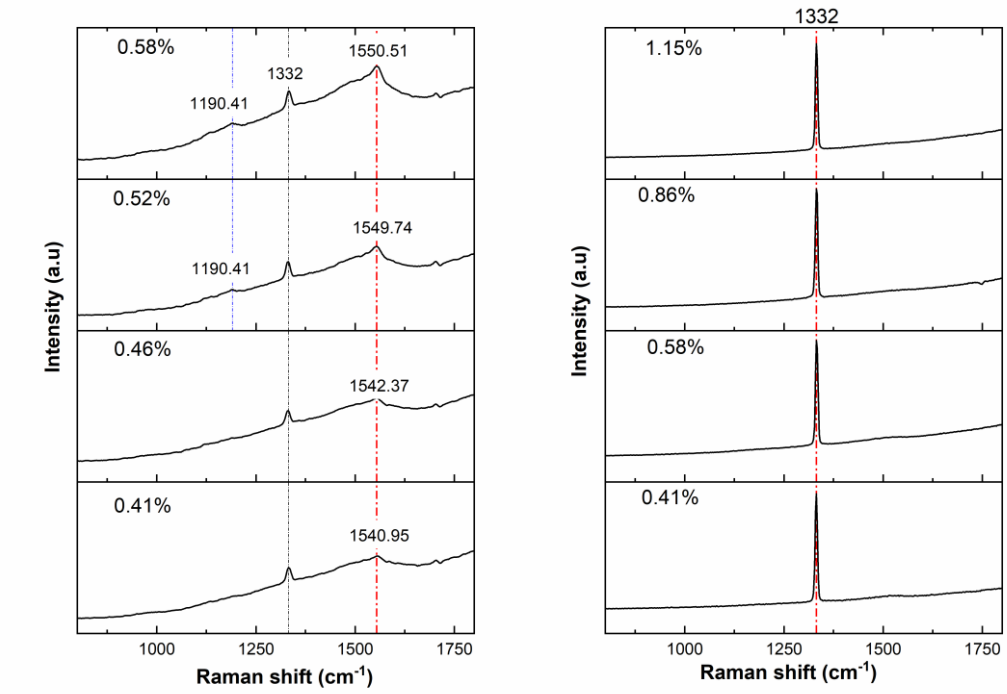

Figure 6-4 Raman spectra using 514 nm excitation wavelength of the two groups of films grown on silicon substrates (left panel) and polycrystalline diamond substrates (right panel). The ratios of NH_3 are indicated.

6.4.1.2 Growth rate and concentration

For the films grown on Si, the sample grown with 0.41% of NH_3 was only characterized with SIMS. The growth rate was calculated from the interface layer that isolate the grown film from the Si, taking the point at which, the Si signal started to increase as an indicator of the start of the substrate. Figure 6.5(a) is an example of identifying the interface layer used in this work. The etching rate used to calculate the depth (in nm) was determined by Dr. Peter Heard from the IAC. The etching time obtained directly from the depth profile might be affected slightly by the morphology and composition of the sample, which can be reflected directly by the accuracy of the depth measurements. We compared the growth rates of a set of six samples grown under the same conditions over 1.5 hours, shown in Figure 6.5(b). The growth rates calculated here were approximately constant over the six samples (0.34-0.39 μm/h) with a small noticeable increment upon N uptake, indicating reasonable consistency of the estimated etch rate. The average N concentration varied between $4\text{-}9\times10^{19}$ atoms cm^{-3} throughout all the prepared samples.

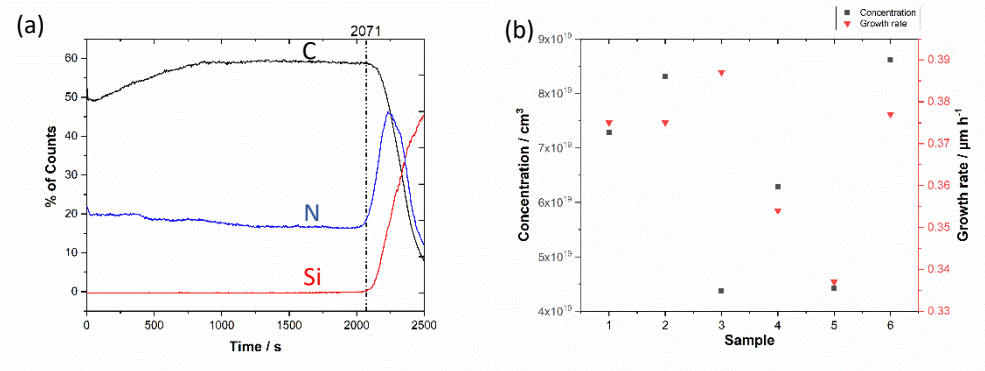

Figure 6-5 (a) an example of a SIMS depth profile obtained from NDD grown on Si with 0.41% of NH_3 for 1.5 h; (b) the concentration and growth rate calculated for a set of six samples grown under the same conditions for 1.5 h.

In PCD films, the depth where the CN^-signal started to drop quickly indicated a switch in how mass 26 was tracked, from $CN^-$to $C_2H_2^-$ signal that typically exists in all diamond films. As Figure 6.6 shows, the growth rate of films grown on PCD over 2 h increased progressively with increasing concentration of NH_3 gas.[32,35–39] The films showed variable ability to uptake the N, with average concentrations in the range of 10^{19}- 10^{20} atoms cm^{-3}. As all the samples showed a high quality of diamond, the 0.86 % film was used to perform the co-doping in the next section.

6.4.2 Encapsulated Mg in N-doped diamond film (NDD).

A growth capping layer covering the Mg deposited on the surface of NDD is an important step for a sensible SIMS measurement. The depth profile gives only the percent of the counts at a specific depth divided by the counts measured on the surface, for each mass monitored, rather than the actual percentage of each element within the film. The problem is that both Mg and C_2 (a common ion when analysing diamond) have mass 24, thus Mg-doped diamond will provide a signal at mass 24 composed of both species. To decompose the signal into its two components, a capping layer of diamond was used because this does not contain Mg and so the intensity of the mass 24 signal due to C_2 can be calibrated. It is worth noting that the signal of mass 24 is always present in diamond, with distribution behaviour over the film similar to that of C signal, mass 12. However, a trade-off was required, the thicker the capping layer, the deeper the doped conducing region became and the less reliable the conductivity measurements. But the capping layer needed to be sufficiently thick to produce a continuous film covering all the Mg layer.

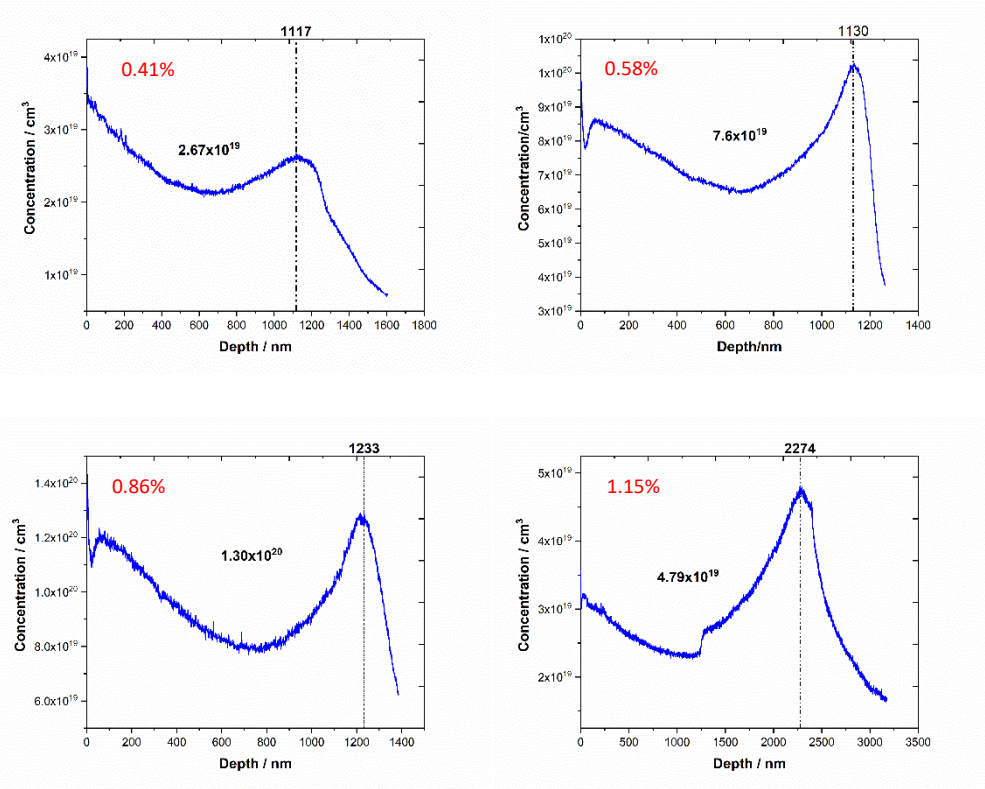

Figure 6-6 The N concentration (cm^{-3}) is shown as a function of depth (nm) calculated from SIMS depth profiles of NDD films grown on PCD over 2 h with different NH_3 ratios.

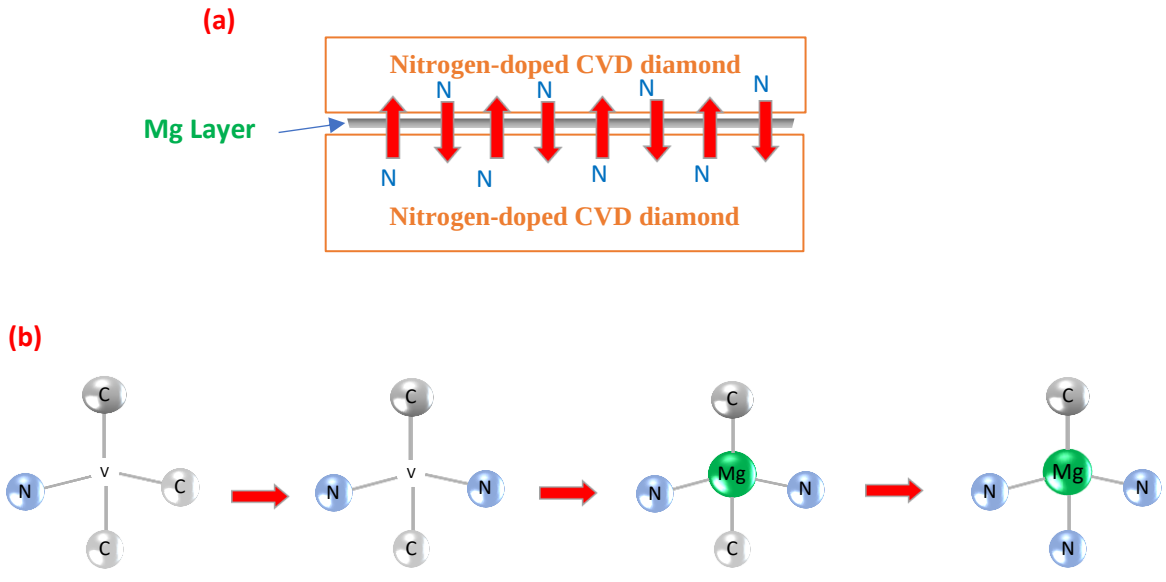

Figure 6-7 (a) A systematic diagram of the layers used in the study to drive the nitrogen diffusion; (b) the proposed formation path presented in chapter 4.

In Si, the small crystals grown with 0.41 % of NH_3 required at least 45-60 min growth to coat all of the surface with a capping layer of diamond, otherwise the film exhibited isolated holes and showed non-continuous growth behaviour (Figure 6.8). It is worth noting that, in addition to the growth time, a non-continuous film can also be a result of the Mg_3N_2 suspension clumping in some regions, which prevented complete decomposition during the heating cycle, as observed through the viewport. The capping layer was only grown after completing the dissociation of the suspension, and the appearance of a shiny substrate surface, which usually did not take more than 1 h. The grown capping layer shared the same square facets as the base film, with noticeable increases in the crystal sizes and a slight change of the smooth surface to an invariably rough texture. This might have been caused by etching of sp^2 C using pure hydrogen while heating up the film, which increased the nucleation sites for the second layer growth.

The capping layer grown with 0.86% of NH_3 on PCD showed complete coverage within 10-15 min of growth, which was almost a quarter of the time needed for those grown on Si, due to the high growth rate of this film ~ 0.15 µm/15 min (Figure 6.6). The morphology did not show any noticeable distinctions, with well-defined large crystals preserving the high quality of the homoepitaxial film.

The effect of the annealing to 1200 ^oC over 2 h on the diffusion of the dopants was studied by SIMS. Figure 6.9 (a) shows the sample that contained three layers of Mg encapsulated in diamond film grown with 0.41% of NH_3 on Si over 2 h where the layers were isolated by a diamond film grown for ~ 45 min. Figure 6.9 (b) shows the calibrated concentration of Mg. Only two layers were well-defined in the film while the third one was undetectable due to the unequal distribution of the Mg over the film surface, which was unavoidable. It is worth noting that the calibrated concentration represented only the Mg in the region where the mass 24 signal was different to the flat signal of C^+, as the rest of the mass 24 signal referred to C_2^+ species. In addition, all the measured samples contained a positive mode signal for mass 40 following the same trend of Mg^+, which is expected to belong to the undissociated MgO^+ species trapped in the film alongside Mg^+ during encapsulation process.

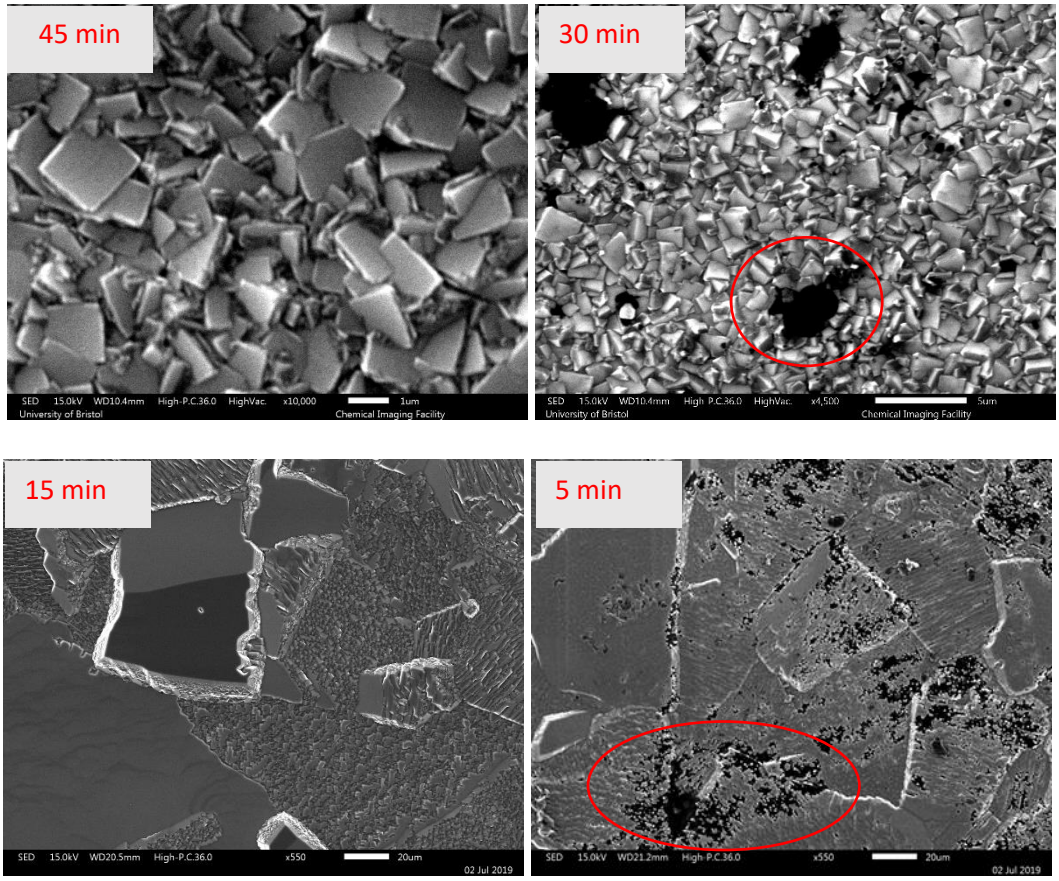

Figure 6-8 SEM micrographs show the coated films of NDD grown on Si with 0.41% ratio of NH_3 (top panel) and polycrystalline diamond substrate (PCD) with 0.86% (lower panels). The growth times are indicated. The red circles refer to incomplete growth regions

Figure 6.9 (a,b) shows the positive spectra taken from two different regions on the film after annealing in a vacuum for 2 h, to provide a comprehensive picture of the dopant's distribution on the film. The two isolated Mg layers appeared in the two regions with maximum concentration varying between 10^{18}-10^{19} cm^{-3} and positioned at ~ 380 and 600 nm from the surface, approximately close to that detected in the sample (before annealing). Meanwhile, the third layer only appears in region 2 with scattered behaviour over ~ 200 nm. The negative mode of CN^-signal taken from the two different regions shows a significant accumulation of N at ~ 500 nm with its maximum concentration varying between regions (10, 4 $\times 10^{20}$ cm^{-3}) associated with a slight reduction in the intensity of C^- at ~ 500 nm. Typically, a small accumulation of nitrogen in the interface between the two NDD films contains Mg usually occurring during growth, causing this variation of the nitrogen distribution near this region.[6] However, sharpening this behaviour upon annealing confirms that the metal plays a role in promoting nitrogen diffusion.

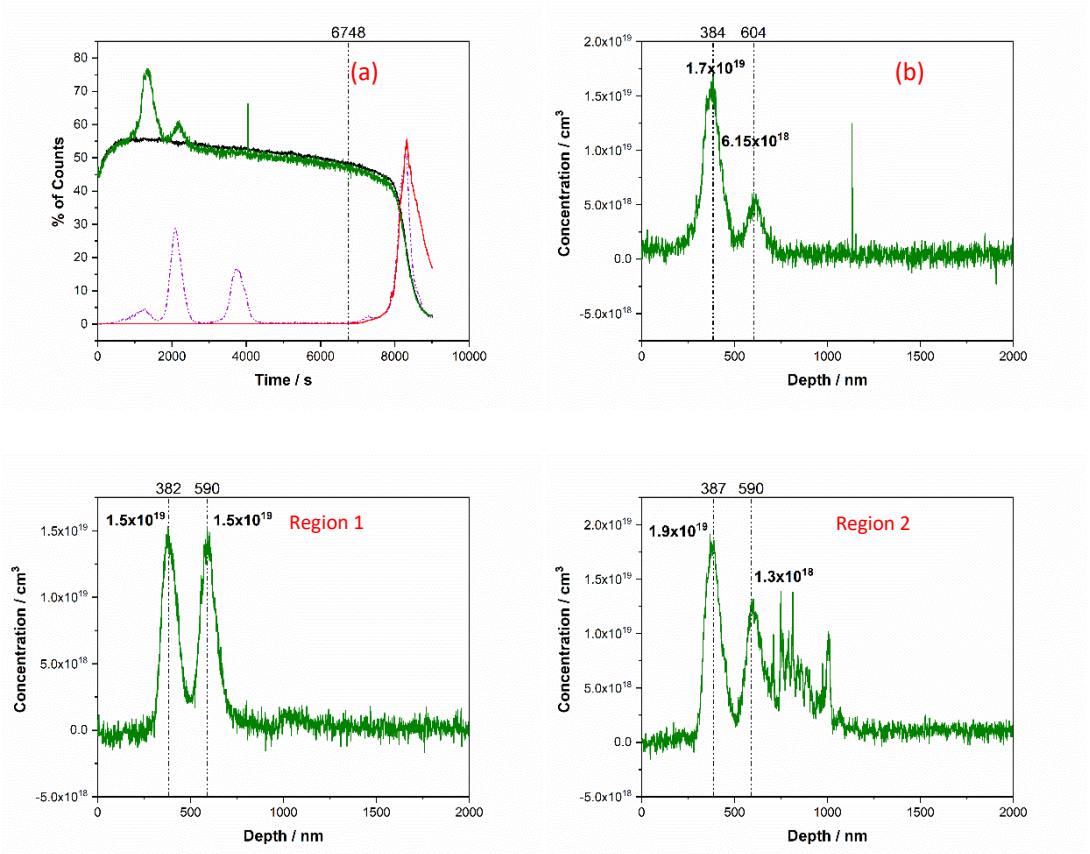

Figure 6-9 Two top panels show SIMS depth profiles as a function of etch time per second (a) and the corresponding calibrated concentration of mass 24 (b) obtained from a sample with three Mg layers encapsulated in an NDD film grown on Si with 0.41% of NH_3 for 2 h (the profile was taken before annealing). The second set of panels show the calibrated concentration of mass 24, taken from two different regions after annealing at 1200 ^oC for 2 h. Black, green, red, and purple refers to 12, 24, 28, and 40 masses, respectively.

According to Figure 6.9, the overlap between $Mg^+$and CN^-signals in the region 380-600 nm depth might improve the solubility of Mg via present the N near the metal upon annealing. There is no direct evidence from SIMS about the Mg solubility in diamond. The Mg^+ signal extended over a very small region ~ 230 nm, which indicates that a large fraction of the Mg remains present as a physical layer distributed between the grain boundaries of the crystal surface (i.e., NDD / NDD interface) and did not necessarily indicate the incorporation ofthe Mg into the diamond matrix, as needed for real chemical doping. The process involving re- implantation of residual Mg on the surface by the probing SIMS beam 'known as recoil implantation' may have also contributed to the appearance of the Mg profile with such narrow distributions.[40,41]

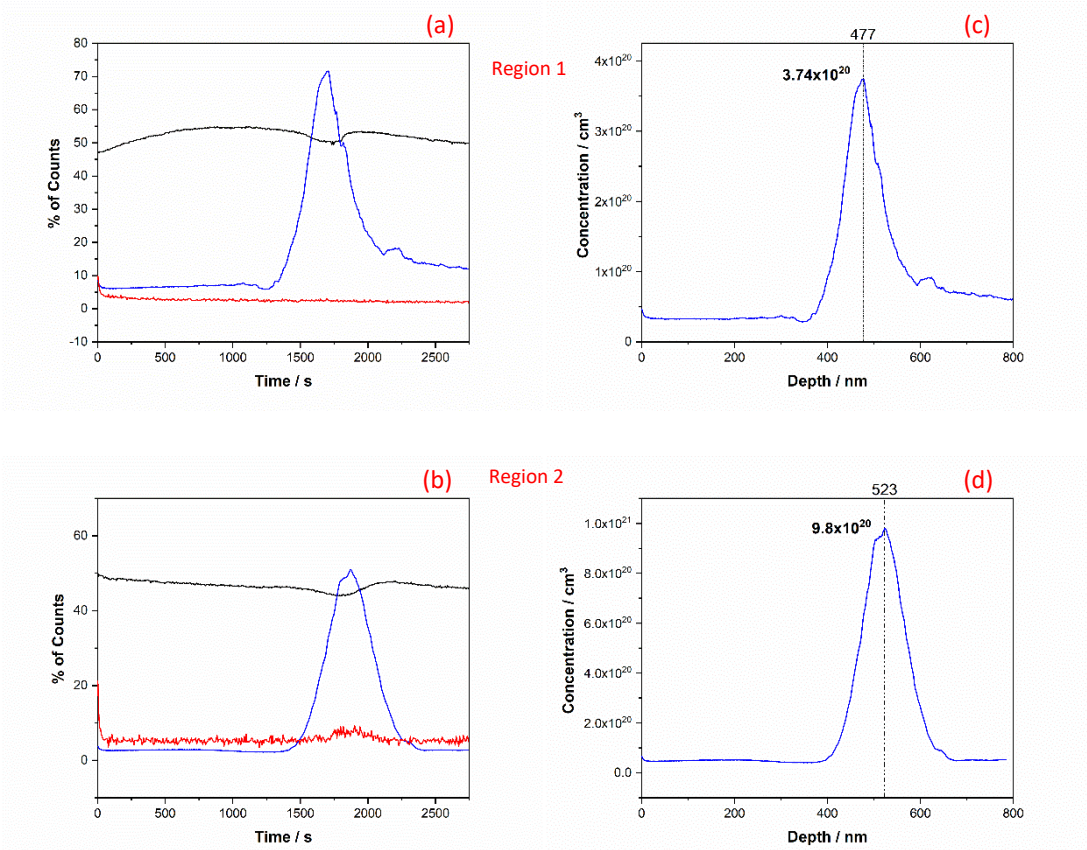

Figure 6-10. The panels a and b show the SIMS depth profile as a function of etch time per second and c and d show the corresponding calibrated concentration of mass 26 taken from the two regions for the same sample annealed at 1200 ^{o}C for 2 h. Black, blue, and red refers to 12, 26, and 28 masses, respectively. The regions were selected randomly, i.e. fresh area for each measurement.

Figure 6.10 shows SIMS measurements of samples annealed in vacuum for 2 h, containing a Mg layer encapsulated in a film grown with 0.86% of NH_3 on PCD over 2 h. The continuous capping layer grown for only 15 min brought the Mg layer closer to the surface at ~ 150-180 nm depth with maximum concentration close to that detected in the samples grown on Si. The accumulation of N on the surface of the Mg layer was also observed, with a maximum concentration being high ~ 10^{20} cm^{-3} at a depth ~ 70 nm, then starting to drop down to ~ 300 nm, then decreasing slowly, reaching the detection limit of N of 1.1×10^{19} cm^{-3}.

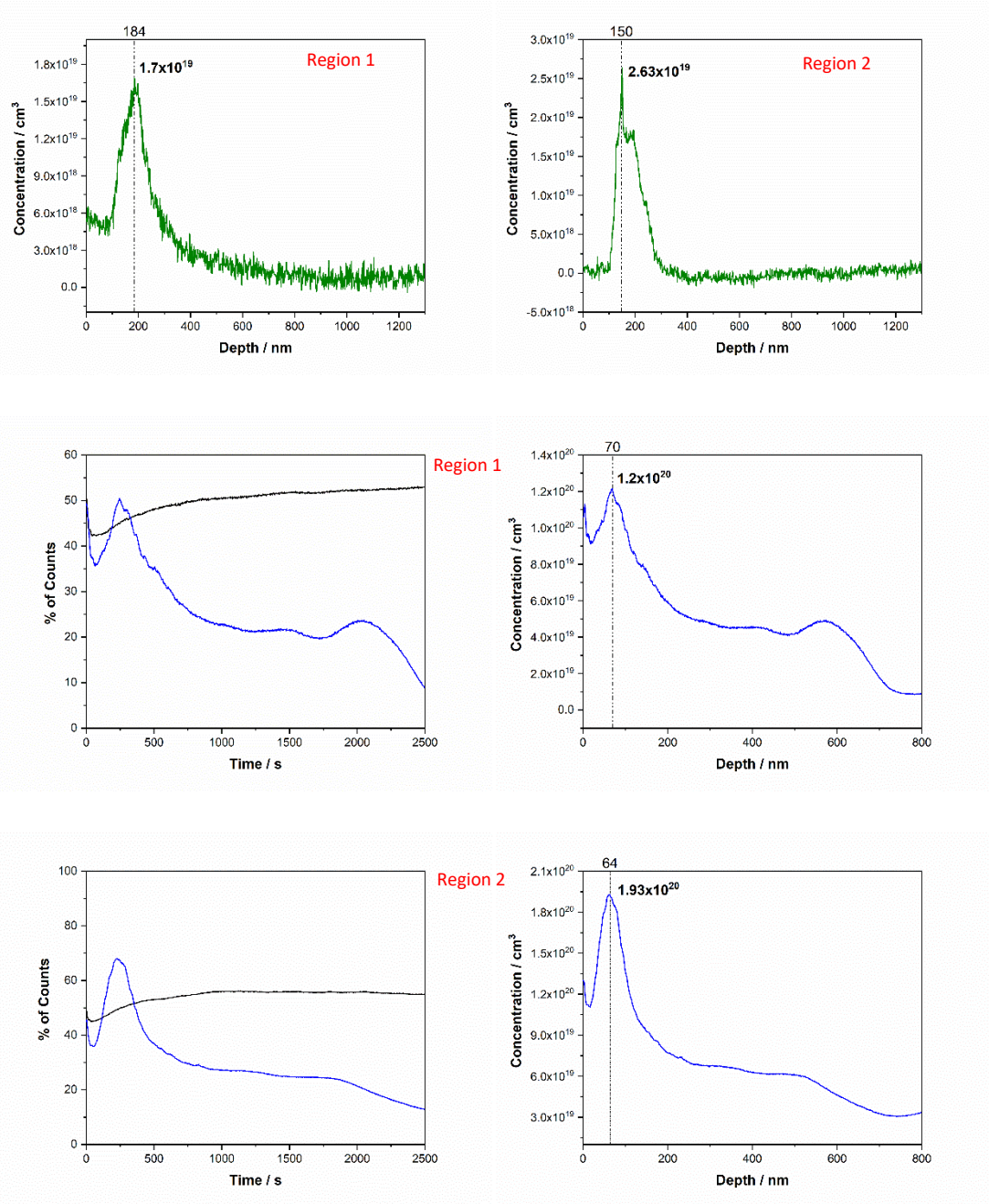

Figure 6-11 The top panels show the SIMS calibrated concentration of mass 24 as a function on depth where a sample has one Mg layer encapsulated in the base of NDD film grown on PCD with 0.86% of NH_3 for 2 h, taken from two different regions. The second and third panels show the SIMS depth profile as a function of etch time per second and the corresponding calibrated concentration of mass 26, taken from the two regions. The sample was annealed at 1200 ^{o}C for 2 h. Black, blue, and green lines refer to 12, 26, and 24 masses, respectively

.

Since the SIMS and SEM measurements destroy the samples by burning the surface due to the high energy of electrons/ions, the etching process, and gold coating, all the conductivity measurements were conducted with new sets of samples grown on symmetrical substrates with 10×10 mm dimensions. Despite the presence of a region where the Mg and N depth profiles overlap, which is also close to the surface and contains excess N, no electrical conduction measurements were obtained for Mg-N co-doping films. The voltage-current behaviour of the sample was typically non-linear (random points) and the resistance hopped unreliably to an average value with inconsistent changes in the measured resistance. The hysteresis between each measurement indicated that this result most likely resulted from the sample reaching high resistance that was difficult to measure with the van der Pauw technique. This can be attributed to the non-homogeneous distribution and low density of any activated acceptor-donor complexes. Annealing the sample to temperatures higher than 1200 ^{o}C may be beneficial to activate NV diffusion, ~5 eV [9,10,42] (~1500^{o}C) and might also activate the Mg atoms to accommodate the substitutional site. In recent studies with ion implantation of (Mg)[16], (As, P) [17] and B[23], annealing up to 1600 ^{o}C for 4 h,1700 ^{o}C for 30 min, and at 1400 ^{o}C, respectively, were employed to activate the dopants and successfully incorporate a fraction of the implanted ions in the substitutional site.

6.4.3 Ion implantation

The effect of annealing on the defects formed from the kinetic interaction between the implanted ions and diamond lattice can involve a complex process, i.e., a single defect can form a complex defect, and then it can be dissociated to a simpler form. In order to explore these consequences, SIMS depth profiles were acquired (Figure 6.11) for MgN12 and MgN14 before and after the annealing in a vacuum for 2 h. Before annealing, the Mg^{+} signal was distributed closer to the surface and extended up to ~ 350 nm with a maximum concentration of ~ 2×10^{19} / cm^{3} at a depth of less than 200 nm. After annealing, no significant diffusion was detected for both samples apart from a small difference ~10 nm in the measured depth of the maximum concentration detected, which might be due to the small fluctuation in the etching current ~3 nA used in SIMS. The absence of Mg diffusion in diamond might be due to Mg atoms captured by ion-implantation-induced defects, which create a very stable immobile complex,[43–45] or to Mg atoms bonded with N atoms that implanted with Mg, taking into account the high calculated binding energy of Mg-N bonds (chapter 4). In addition, the annealing temperature of 1200 ^{o}C was insufficient to overcome the activation energy needed for Mg diffusion, but enough to enhance the N diffusion based on the predicted mechanism via the

formation of N_i (N_i, nitrogen trapped by self-interstitial), with a barrier of ~ 1.8 eV.[10] The CN^- signals were less than the detection limit of N for both samples; therefore, no SIMS data were presented for the N distribution. In a previous implantation study[46] of a total dose of 2.8×10^{14} cm^{-2} of N ions implanted on single crystal, the calculated concentration was about 4×10^{18} cm^{-3}, much lower than our detection limit.

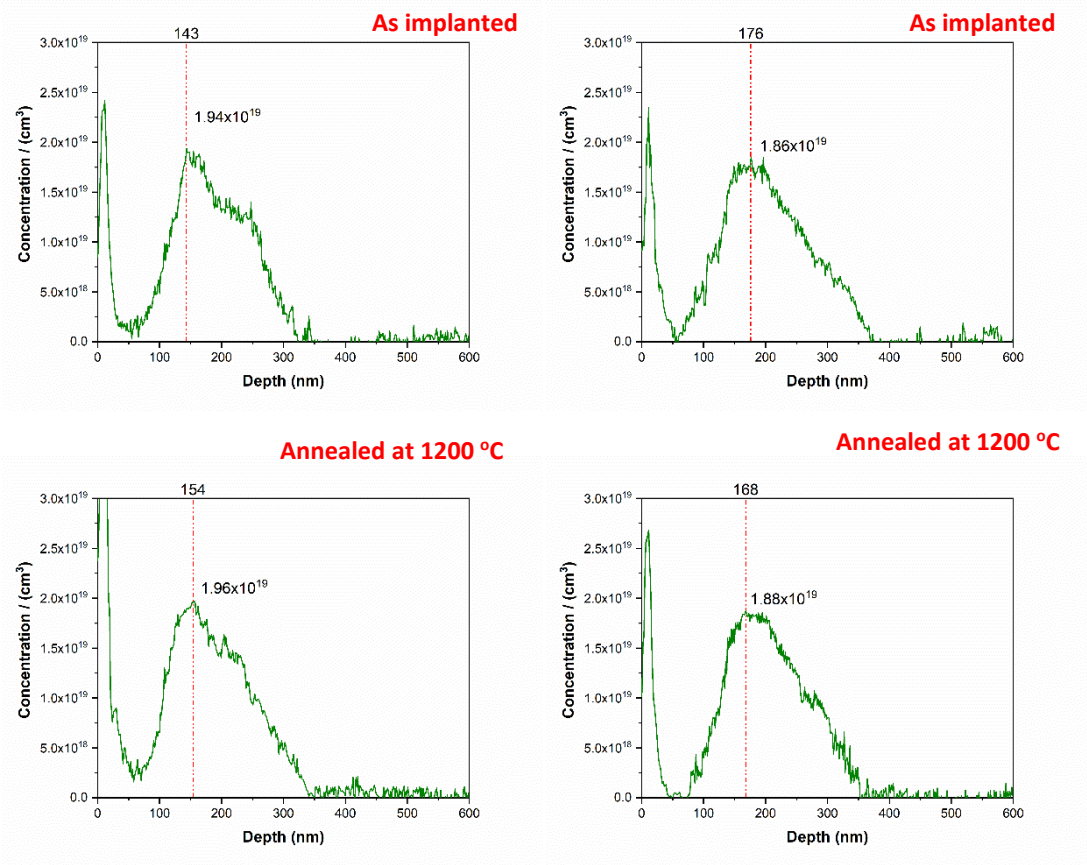

Figure 6-12 SIMS depth profiles to determine the calibrated magnesium concentration of the MgN12 (left panels) and MgN14 (right panels) samples before and after being annealed in a vacuum to 1200 °C of over 2 h.

The annealing of damage in diamond is complicated due to the dangling bonds being able to rearrange in either the sp^3 or sp^2 hybridization. The transformation barrier to graphite or back to diamond depends on the density of defects in the broken bond zone, which, in turn, depends on the implantation conditions (i.e., ion types, doses and energy, as well as implantation temperature). The critical dose of defects that initiated the graphitization upon annealing was determined experimentally using different techniques[47,48] and predicted using TRansport of Ions in Matter (TRIM)[49] as described by Uzan-Saguy et al.[44] In the present study, no TRIM simulation was performed and we chose the minimum level of dose based on the

previous critical doses estimated for Ar (second row element) 5×10^{15} cm^{-2} [50,44] and for C 2.5×10^{15} cm^{-2}.[44] However, such estimation is subject to ion types and implantation temperature.[51]

The Raman spectra of as-implanted diamond and diamond following annealing at temperatures of 400, 800 and 1200 ^{o}C for MgN12 and MgN14, and 1200 ^{o}C for Mg, are shown in Figure 6.13 to probe the annealing kinetics and damage. Due to the transparency of diamond, a Raman spectrum in Figure 6.9, taken from the implanted surface, showed an average of various damage levels up to the end of implantation layers. All three as-implanted samples displayed a single first-order Raman line at about 1332 cm^{-1}, and no other peaks were observed. However, the relaxation to graphite upon increased temperature dominated, exhibiting linearity with annealing.[48,52] Mg samples showed less damage as the relative intensity of the broad G band to diamond band [I (Diamond) / I (G)] ~ 5 at 1200 ^{o}C. The maximum damage was observed with increase in the implanted doses on MgN14 sample with the lowest of [I (Diamond) / I (G)], ~ 1 at 1200 ^{o}C.

Despite the rapid increase in G-band intensity with annealing, there was a noticeable narrowing in the "Full width half maximum" (FWHM) of the diamond peak from ~ 9-10 cm^{-1} in as-implanted samples to ~ 6 cm^{-1} after annealing, which indicated that some damage, such as sp^3 broken bonds, was removed with annealing. The FWHM of the G band showed contrasting behaviour compared with the diamond peak, as almost all widths increased with annealing, indicating spontaneous graphitization behaviour up to 1200 ^{o}C.

From SIMS measurements, the implanted layers were situated in a region close to the surface, starting from ~ 50 nm and reaching a maximum at ~ 200 nm, which probably enhanced the graphitization upon annealing. From previous cross-sectional Raman microscopy,[53,54] the damage level formed along each ion path reached a maximum at the end of the implantation range, which was close to the surface in the present study. As the damage layer formed deep, the relaxation to graphitization upon annealing is inhibited by the high internal pressure of the diamond matrix. Such pressure helps to restore the diamond structure even with doses beyond the critical dose.[53]

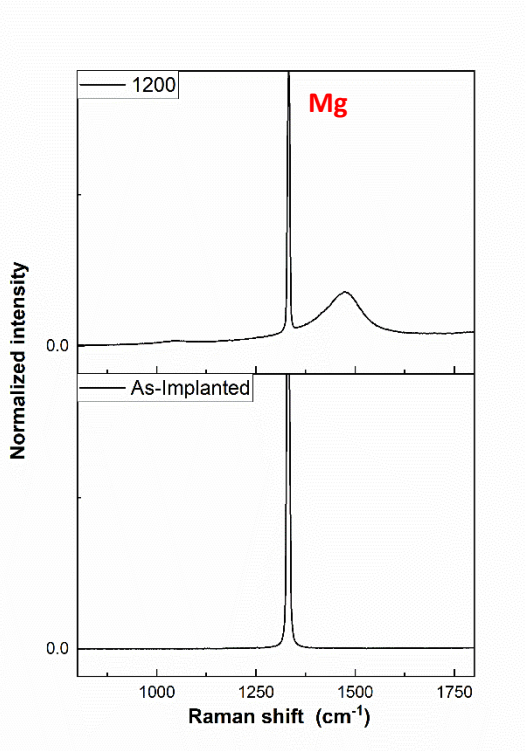

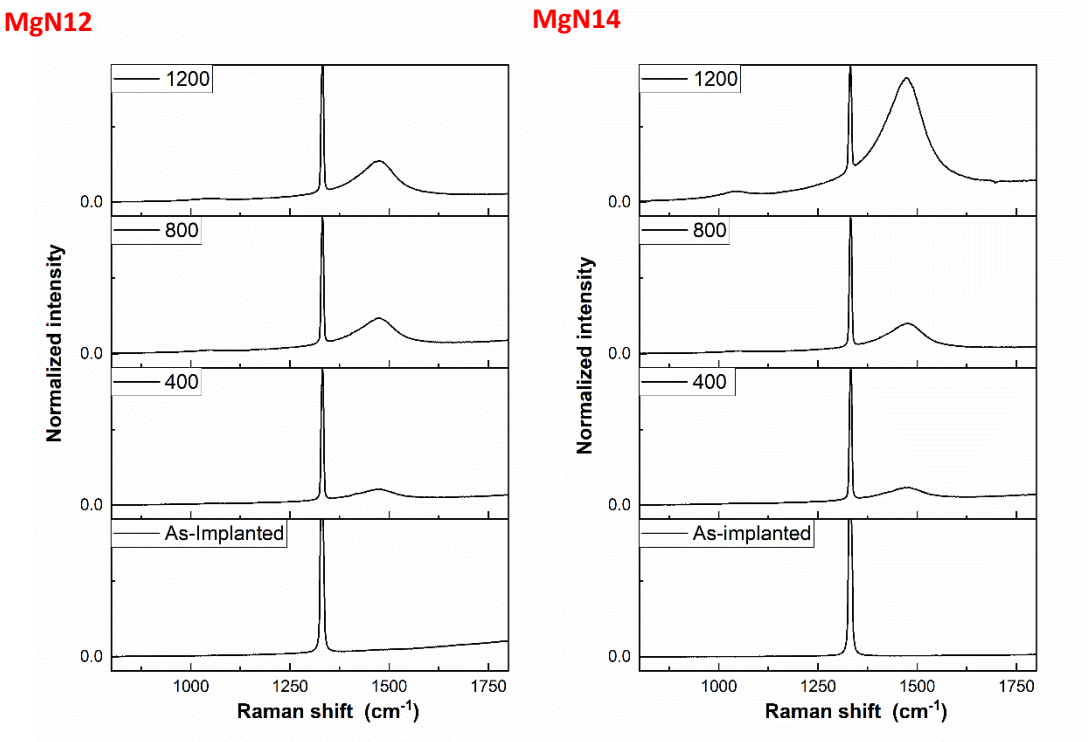

Figure 6-13 Raman spectra of the implanted samples by doses shown in Table 6.2 and following annealing at the indicated temperatures in °C using 514 nm excitation wavelength.

The sheet resistance measured at room temperature for Mg, MgN12, and MgN14 samples annealed at 400 °C showed high values: 3.36×10^{8}, 5.61×10^{8} and 5.62×10^{8} Ω/□, respectively. Increasing the annealing temperature to 800 °C caused the sheet resistance to rise in value, such that the conductivity of the samples became unmeasurable by our van der Pauw system. Repeat measurements after annealing at 1200 °C indicated that the samples permanently preserved this unmeasurably high sheet resistance. The conductivity loss probably indicated that the damaged surface, with broken sp^3 bonds or mobile defects, was reconstructed to the most stable configuration that causes a large reduction in the carrier concentration and increases in the resistance. The enhanced G band at 1200 °C (Figure 6.9) did not affect the conductivity, indicating non-overlap graphite zones. Such overlap forms a continuous conductive region which usually occurs in the sample implanted with doses beyond the critical dose.[51]

6.5 Conclusion

Co-doped diamond was investigated using magnesium and nitrogen as dopants. The magnesium was introduced into the diamond using two different methods: a CVD growth of an encapsulated layer sandwiched between two diamond layers and ion implantation. SEM and Raman spectroscopy studied the morphology and quality of the films while SIMS studied the dopant concentration and diffusion upon annealing. The magnesium layer encapsulated in CVD films affected the nitrogen near-surface diffusion in diamond, which caused a high accumulation of N on both sides of the Mg layer. Such accumulation was observed after depositing the top NDD film on Mg layer by hot filament CVD, occurring during the nucleation and growth step of the second NDD film and showed a large increase following annealing at 1200 ºC. This method could be useful in fabricating a thin layer ~ 500 nm of n-type diamond with proper heat treatment. The magnesium implanted into a CVD single-crystal diamond sample was unaffected by annealing, which can be attributed to binding with other defects, i.e., self-interstitials, vacancies created during implantation or nitrogen atoms implanted with magnesium. Thus, we conclude that Mg in diamond is effectively immobile at temperatures up to 1200 °C.

6.6 References

1. Mainwood, A. Theoretical modelling of dopants in diamond. *J. Mater. Sci. Mater. Electron.* **17**, 453–458 (2006).
2. Yan, B. *et al.* The effect of phosphorus and nitrogen co-doped on the synthesis of diamond at high pressure and high temperature. *Int. J. Refract. Met. Hard Mater.* **54**, 309–314 (2016).
3. Cao, G. Z., Giling, L. J. & Alkemade, P. F. A. Growth of phosphorus and nitrogen co-doped diamond films. *Diam. Relat. Mater.* **4**, 775–779 (1995).
4. Cao, G. Z., Driessen, F. A. J. M., Bauhuis, G. J., Giling, L. J. & Alkemade, P. F. A. Homoepitaxial diamond films codoped with phosphorus and nitrogen by chemical-vapor deposition. *J. Appl. Phys.* **78**, 3125–3131 (1995).
5. Hu, M. *et al.* Synthesis and characterization of boron and nitrogen co-doped diamond crystals under high pressure and high temperature conditions. *CrystEngComm* **19**, 4571–4575 (2017).
6. Othman, M. Z., May, P. W., Fox, N. A. & Heard, P. J. Incorporation of lithium and nitrogen into CVD diamond thin films. *Diam. Relat. Mater.* **44**, 1–7 (2014).
7. Halliwell, S. C., May, P. W., Fox, N. A. & Othman, M. Z. Investigations of the co-doping of boron and lithium into CVD diamond thin films. *Diam. Relat. Mater.* **76**, 115–122 (2017).
8. Sato, Y., Kamo, M. & Field, J. *The properties of natural and synthetic diamond*. (Academic Press, 1992).
9. Pinto, H. *et al.* On the diffusion of NV defects in diamond. *Phys. Status Solidi Appl. Mater. Sci.* **209**, 1765–1768 (2012).
10. Jones, R., Goss, J. P., Pinto, H. & Palmer, D. W. Diffusion of nitrogen in diamond and the formation of A-centres. *Diam. Relat. Mater.* **53**, 35–39 (2015).
11. Prawer, S., Uzan-Saguy, C., Braunstein, G. & Kalish, R. Can n-type doping of diamond be achieved by Li or Na ion implantation? *Appl. Phys. Lett.* **63**, 2502–2504 (1993).
12. Fontaine, F., Uzan-Saguy, C., Philosoph, B. & Kalish, R. Boron implantation / in situ annealing procedure for optimal p -type properties of diamond. *Appl. Phys. Lett.* **68**, 2264–2266 (1996).
13. Dresselhaus, M. S. & Kalish, R. *Ion implantation in diamond, graphite and related materials*. (Springer Science & Business Media, 2013).

14. Prins, J. F. Doping of diamond by the diffusion of interstitial atoms into layers containing a low density of vacancies. *Diam. Relat. Mater.* **7**, 545–549 (1998).
15. Neves, A. & Nazar, M. *Properties, Growth and Applications of Diamond*. (IET, 2001).
16. Lühmann, T. *et al.* Screening and engineering of colour centres in diamond. *J. Phys. D. Appl. Phys.* **51**, 483002 (2018).
17. Barjon, J., Jomard, F. & Morata, S. Arsenic-bound excitons in diamond. *Phys. Rev. B - Condens. Matter Mater. Phys.* **89**, 1–5 (2014).
18. Knight, D. S. & White, W. B. Characterization of diamond films by Raman spectroscopy. *J. Mater. Res.* **4**, 385–393 (1989).
19. Viljoen, P. E. Reaction between diamond and titanium for ohmic contact and metallization adhesion layers. *J. Vac. Sci. Technol. B Microelectron. Nanom. Struct.* **12**, 2997 (1994).
20. Moazed, K. L., Zeidler, J. R. & Taylor, M. J. A thermally activated solid state reaction process for fabricating ohmic contacts to semiconducting diamond. *J. Appl. Phys.* **68**, 2246–2254 (1990).
21. Koizumi, S., Kamo, M., Sato, Y., Ozaki, H. & Inuzuka, T. Growth and characterization of phosphorous doped {111} homoepitaxial diamond thin films. *Appl. Phys. Lett.* **71**, 1065–1067 (1997).
22. Kato, H., Yamasaki, S. & Okushi, H. N -type doping of (001)-oriented single-crystalline diamond by phosphorus. *Appl. Phys. Lett.* **86**, 1–3 (2005).
23. Katagiri, M., Isoya, J., Koizumi, S. & Kanda, H. Lightly phosphorus-doped homoepitaxial diamond films grown by chemical vapor deposition. *Appl. Phys. Lett.* **85**, 6365–6367 (2004).
24. Jin Looi, H. *et al.* Mechanisms of surface conductivity in thin film diamond: Application to high performance devices. *Carbon N. Y.* **37**, 801–805 (1999).
25. Hayashi, K. *et al.* Hydrogen-related gap states in the near surface of chemical vapor deposited homoepitaxial diamond films. *Diam. Relat. Mater.* **6**, 303–307 (1997).
26. Crawford, K. G. *et al.* Thermally Stable, High Performance Transfer Doping of Diamond using Transition Metal Oxides. *Sci. Rep.* **8**, 1–9 (2018).
27. Maier, F., Riedel, M., Mantel, B., Ristein, J. & Ley, L. Origin of surface conductivity in diamond. *Phys. Rev. Lett.* **85**, 3472–3475 (2000).
28. Jin, S. & Moustakas, T. D. Effect of nitrogen on the growth of diamond films. *Appl. Phys. Lett.* **65**, 403–405 (1994).
29. Yang, J. X. *et al.* Effects of nitrogen addition on morphology and mechanical property

of DC arc plasma jet CVD diamond films. *Diam. Relat. Mater.* **13**, 139–144 (2004).

30. Yan, C. S., Vohra, Y. K., Mao, H. K. & Hemley, R. J. Very high growth rate chemical vapor deposition of single-crystal diamond. *Proc. Natl. Acad. Sci. U. S. A.* **99**, 12523–12525 (2002).
31. Locher, R., Wild, C., Herres, N., Behr, D. & Koidl, P. Nitrogen stabilized 100 texture in chemical vapor deposited diamond films. *Appl. Phys. Lett.* **65**, 34–36 (1994).
32. Vandevelde, T. *et al.* On nitrogen incorporation during PE-CVD of diamond films. *Diam. Relat. Mater.* **7**, 152–157 (1998).
33. Prawer, S. & Nemanich, R. J. Raman spectroscopy of diamond and doped diamond. *Philos. Trans. R. Soc. A Math. Phys. Eng. Sci.* **362**, 2537–2565 (2004).
34. Ferrari, A. C. & Robertson, J. Origin of the 1150 − cm−1 Raman mode in nanocrystalline diamond. *Phys. Rev. B - Condens. Matter Mater. Phys.* **63**, 2–5 (2001).
35. Müller-Sebert, W., Wörner, E., Fuchs, F., Wild, C. & Koidl, P. Nitrogen induced increase of growth rate in chemical vapor deposition of diamond. *Appl. Phys. Lett.* **759**, 759 (1995).
36. Mokuno, Y. *et al.* High rate homoepitaxial growth of diamond by microwave plasma CVD with nitrogen addition. *Diam. Relat. Mater.* **15**, 455–459 (2006).
37. Chayahara, A. *et al.* The effect of nitrogen addition during high-rate homoepitaxial growth of diamond by microwave plasma CVD. *Diam. Relat. Mater.* **13**, 1954–1958 (2004).
38. Yamada, H., Chayahara, A. & Mokuno, Y. Effects of intentionally introduced nitrogen and substrate temperature on growth of diamond bulk single crystals. *Jpn. J. Appl. Phys.* **55**, 01AC07 (2016).
39. Achard, J., Silva, F., Brinza, O., Tallaire, A. & Gicquel, A. Coupled effect of nitrogen addition and surface temperature on the morphology and the kinetics of thick CVD diamond single crystals. *Diam. Relat. Mater.* **16**, 685–689 (2007).
40. Uzan-Saguy, C. *et al.* Diffusion of lithium in diamond. *Phys. Status Solidi Appl. Res.* **193**, 508–516 (2002).
41. Shaanan, M. & Kalish, R. Simulation of SIMS measurements of light element profiles in diamond. *Nucl. Instruments Methods Phys. Res. Sect. B Beam Interact. with Mater. Atoms* **171**, 332–341 (2000).
42. Deák, P., Aradi, B., Kaviani, M., Frauenheim, T. & Gali, A. Formation of NV centers in diamond: A theoretical study based on calculated transitions and migration of nitrogen and vacancy related defects. *Phys. Rev. B - Condens. Matter Mater. Phys.* **89**, 1–12

(2014).

43. Fizgeer, B. *et al.* Inhibition of Light Element Diffusion in Diamond Due to Ion Implantation Related Defects. *Phys. Status Solidi Appl. Res.* **186**, 281–289 (2001).
44. Uzan-Saguy, C. *et al.* Damage threshold for ion-beam induced graphitization of diamond. *Appl. Phys. Lett.* **67**, 1194 (1995).
45. Cytermann, C., Brener, R. & Kalish, R. Search for diffusion of Li implants in natural and polycrystalline CVD diamond. *Diam. Relat. Mater.* **3**, 677–680 (1994).
46. Kalish, R. *et al.* Nitrogen doping of diamond by ion implantation. *Diam. Relat. Mater.* **6**, 516–520 (1997).
47. Reznik, A., Richter, V. & Kalish, R. Kinetics of the conversion of broken diamond bonds to graphitic bonds. *Phys. Rev. B - Condens. Matter Mater. Phys.* **56**, 7930–7934 (1997).
48. Kalish, R., Reznik, A., Prawer, S., Saada, D. & Adler, J. Ion-implantation-induced defects in diamond and their annealing: Experiment and simulation. *Phys. Status Solidi Appl. Res.* **174**, 83–99 (1999).
49. Ziegler, J. F. & Biersack, J. P. *The stopping and range of ions in matter*. (Springer. Boston. MA, 1985).
50. Vavilov, V. S., Krasnopevtsev, V. V., Miljutin, Y. V., Gorodetsky, A. E. & Zakharov, A. P. on Structural Transitions in Ion-Implanted Diamond. *Radiat. Eff.* **22**, 141–143 (1974).
51. Prawer, S. & Kalish, R. Ion-beam-induced transformation of diamond. *Phys. Rev. B* **51**, 15711–15722 (1995).
52. Kalish, R., Reznik, A., Nugent, K. W. & Prawer, S. The nature of damage in ion-implanted and annealed diamond. *Nucl. Instruments Methods Phys. Res. B* **148**, 626–633 (1999).
53. Orwa, J. O., Nugent, K. W., Jamieson, D. N. & Prawer, S. Raman investigation of damage caused by deep ion implantation in diamond. *Phys. Rev. B - Condens. Matter Mater. Phys.* **62**, 5461–5472 (2000).
54. Jamieson, D. N., Prawer, S., Nugent, K. W. & Dooley, S. P. Cross-sectional Raman microscopy of MeV implanted diamond. *Nucl. Instruments Methods Phys. Res. B* **106**, 641–645 (1995).

CHAPTER 7

THEORETICAL STUDY OF SUBSTITUTIONAL PHOSPHORUS AND NITROGEN PAIRS IN DIAMOND

CHAPTER 7 – THEORETICAL STUDY OF SUBSTITUTIONAL PHOSPHORUS AND NITROGEN PAIRS IN DIAMOND

7.1 Introduction

Most of diamond defects have not yet been completely characterized in terms of electronic configuration or spectroscopic features. An exhaustive interpretation and understanding of the physical properties of the different point defects in diamond are of primary importance for diamond technology. The dominant defect present in diamond and extensively studied in the literature is N in an isolated substitutional lattice site (C-centre), classifying the diamond as type Ib[1–9]. Most commercial synthetic diamonds prepared by chemical vapor deposition (CVD) processes usually include unintentionally a small concentration of nitrogen (from 40 to 100 ppm)[10,11], originating from air-leaks in the gas-lines or as N_2 impurities in the process gases.

The main characteristics of the C-centre defect shown in IR absorption spectra is a principal peak at 1130 cm^{-1} and a very sharp absorption at 1344 cm^{-1} [12,13]. The first peak has been predicted theoretically [14] whereas the latter peak was absent in the simulated spectra and did not show an isotopic shift with N^{15} substitution [15] (chapter 3). This led to the 1344 cm^{-1} peak being attributed to other defects. A pair of two N atoms at substitutional sites (A-Centre) is one of common defects that attracted a special interest. The simulated IR spectra of A-Centre was studied using the B3LYP hybrid functional and a supercell size of 216-atom[16,17]. It shows a sharp peak at 1,276 cm^{-1}, two other peaks at 1,202 and 1,087 cm^{-1} with moderate intensities, and other small peaks at 451 and 571 cm^{-1} which were in line with that found experimentally by Davies[6] at 1,285, 1,210, 1,087 and 472 cm^{-1}, respectively. In the same study, the frequencies of NB pair, where one N atom in A-Centre was substituted by B, were also reported at 890, 945, 1,018, 1,078 and 1,281 cm^{-1} with medium intensities compared with A-centre.

Another defect in diamond which is considered important for electronic applications is P in a substitutional site.[18] The n-type behaviour of this defect is confirmed theoretically[19–22] and experimentally.[18,23]The calculated vibrational frequencies of single substitutional P identified modes at low energy frequency, 380 cm^{-1} [24] and 354, 586 cm^{-1}. [22] However, it has proven difficult to conduct experimental studies on P-doped diamond with reliable, consistent results, and this may be attributed in most cases to the P also incorporating into the diamond in inactive forms, such as PV, PH, or PN.[5,25–30] Previous studies investigated the IR spectra of P

complexes[31–33] without clearly assigning any absorption peaks to P due to the similarity of the obtained spectra with that of the most known defects in diamond, such as the A-centre and B-centre.[31]

In recent years, computational spectroscopy – using computational methods to simulate IR, Raman and other spectra - has become an efficient method in the interpretation of experimental data of isolated point defects.[8,14,16,34–41]In the present study, we performed simulations to study the geometric, electronic, and IR features of a pair of N and P atoms in adjacent substitutional sites in a diamond. A range of hybrid functional incorporated into the CRYSTAL code and a periodic supercell approach were used to explicitly study the defect. The aim is to determine the most significant IR features (fingerprints) of this defect which might be helpful to characterize related experimental IR spectra in the future.

7.2 Computational parameters

For details on the CRYSTAL code, and discussion of the parameters used, please see Chapter 3.

7.3. Results and discussion

7.3.1. Structural and charge distribution

In the P-N pair, we performed different full relaxation methods to explore the ground structure of the system. At the beginning of the calculation, the P and N dopant atoms were left on adjacent substitutional C sites as in pure diamond. As with the C-centre, the calculations were then performed by first moving the P, N, or both atoms, by only ~ 0.08 Å in two different directions along [111], keeping the C_{3v} symmetry. This resulted on converged the system with an elongated P-N bond. In a further relaxation, one of C atoms bonded to N was displaced from their original site by only ~ 0.08 Å at the beginning along [111], which broke the symmetry to C_s. The converged C_s geometry with its closed shell singlet, ($S_z = 0$) is the ground-state structure (lower than that of C_{3v} by ~ 1 eV) and is consistent with previous calculations of the same system.[5,4] A further reduction from two to one symmetry operations by release the symmetry did not result in a further change in the geometry indicated that the system reached the minimum ground energy.

Figure 7.1 shows the local optimized structure of the P-N pair as well as the distribution of the Mulliken charges obtained with B3LYP and a 128-atom supercell after full structural relaxation, with the data shown up to the second shell of nearest neighbours around the defect. The corresponding data related to other functionals are shown in Table 7.1. In the final C_s structure, the P-N bond length increase by ~ 0.05 Å to be 1.61 Å, compared with the C-C bond in pure diamond, 1.556 Å. The greatest separation distance is between the N and one of its C neighbours (C_C) with a bond length of 2.21 Å. Similar to the previous findings on the C-centre (Chapter 3), the high localization of the lone pair on nitrogen atom prevents covalent-bond formation with C_C leading to a repulsive interaction between them due to Pauli exclusion principle. This hindrance by the N lone pair results in the C_C atom moving closer to the P, with a separation distance of P-C_C ~ 2.21 Å (a decrease by 0.3 Å compared with pure diamond). This reconstruction was also associated with a closing of the C_C-N-P angle to ~ 68.65°, almost half that of the diamond (109.47°), indicating the strong interaction between P and C_C. The P- N interaction increases the P-C_E and P-C_F bonds by ~ 0.09 and 0.04 Å compared with the corresponding bonds in the isolated P_{sub} defect, which are 1.78 and 1.71 Å, respectively. Conversely, the N-C_D decreases by ~ 0.08 Å and N-C_C increases by 0.15 Å compared with equivalent interatomic distances in C-centre, which are 1.48 and 2.06 Å, respectively.

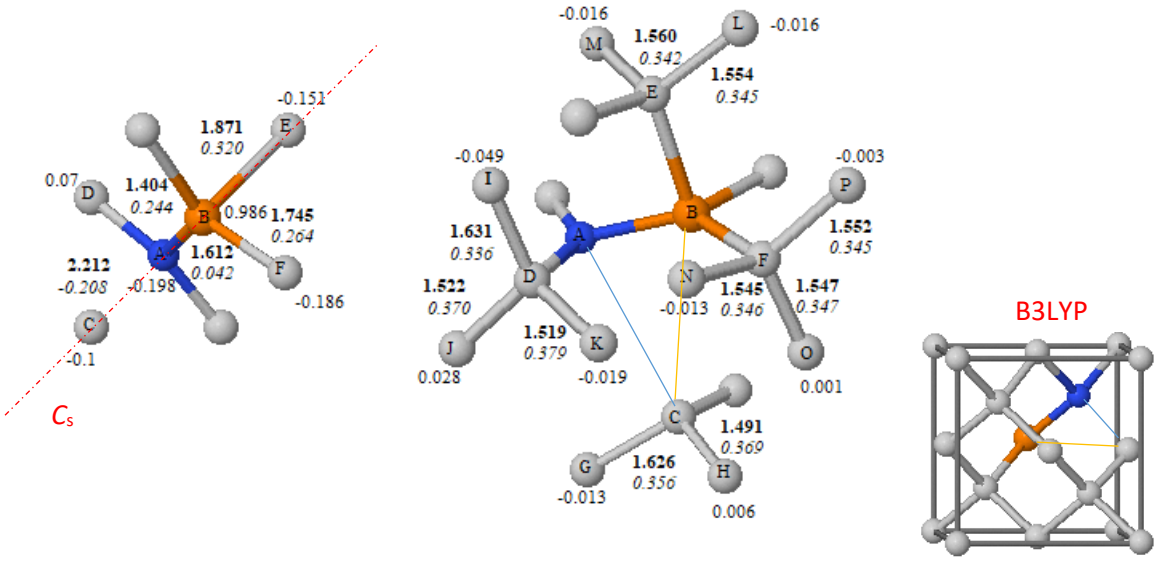

Figure 7-1 Show interatomic distances (**bold**) (in Å); bond overlap population (*italic*); Mulliken atomic charges (all in *e*) for irreducible C atoms in the first and the second shell of the PN point defect. Grey, orange, and blue indicated to C, P, and N atoms, respectively. All data were obtained with C/6-21G* and P, N/TZVP basis sets and 128-atom supercell.

Table 7.1 The geometry information of the defect pair and their first-nearest neighbours. For the indicated bonds; the equilibrium bond distances (*R*) (in Å); the overlap bond population (*b*) (in *e*); Mulliken atomic charges (*q*) (in *e*). SC refers to supercell size. Refer to Fig.7.1 for the carbon atom labels.

Functionals	SC	N-P		N-C_D		N-C_C		P-C_C		P-C_F		P-C_E	
		R	***b***	***R***	***b***	***R***	***b***	***R***	***b***	***R***	***b***	***R***	***b***
B3LYP	**64**	1.615	0.049	1.410	0.244	2.231	-0.201	2.233	0.342	1.751	0.265	1.878	0.319
	128	1.612	0.042	1.404	0.244	2.212	-0.208	2.212	0.350	1.745	0.264	1.871	0.320
	216	1.611	0.044	1.406	0.243	2.220	-0.207	2.238	0.345	1.745	0.263	1.863	0.321
HSE06	**64**	1.609	0.041	1.401	0.255	2.208	-0.215	2.192	0.364	1.744	0.276	1.874	0.332
	128	1.607	0.033	1.396	0.256	2.190	-0.223	2.174	0.371	1.738	0.275	1.866	0.334
PBE0	**64**	1.609	0.024	1.401	0.251	2.207	-0.216	2.186	0.366	1.744	0.273	1.874	0.330
	128	1.606	0.019	1.396	0.252	2.189	-0.224	2.169	0.373	1.738	0.272	1.867	0.332
PBE0-13	**64**	1.603	0.003	1.398	0.246	2.203	-0.224	2.172	0.376	1.740	0.275	1.872	0.334
	128	1.600	-0.009	1.393	0.245	2.186	-0.231	2.156	0.382	1.734	0.273	1.864	0.335
PBEsol0	**64**	1.606	0.021	1.397	0.263	2.199	-0.218	2.175	0.369	1.740	0.279	1.870	0.336
	128	1.603	0.014	1.392	0.263	2.181	-0.226	2.159	0.375	1.734	0.277	1.862	0.338

		N	C_D	C_C	P	C_F	C_E
		q	***q***	***q***	***q***	***q***	***q***
B3LYP	**64**	-0.205	0.071	-0.101	0.977	-0.185	-0.149
	128	-0.198	0.070	-0.100	0.986	-0.186	-0.151
	216	-0.195	0.069	-0.100	0.983	-0.187	-0.151
HSE06	**64**	-0.243	0.087	-0.086	0.922	-0.173	-0.137
	128	-0.240	0.087	-0.085	0.929	-0.174	-0.138
PBE0	**64**	-0.241	0.087	-0.087	0.916	-0.172	-0.136
	128	-0.238	0.087	-0.085	0.922	-0.173	-0.137
PBE0-13	**64**	-0.246	0.089	-0.095	0.948	-0.178	-0.141
	128	-0.244	0.090	-0.094	0.955	-0.179	-0.143
PBEsol0	**64**	-0.302	0.104	-0.072	0.856	-0.159	-0.122
	128	-0.301	0.105	-0.070	0.861	-0.159	-0.122

The local perturbation in the lattice around the PN defect is slightly extended to the second shell, from P side all the bonds show small change ~ < 0.01 Å. From N side, there were variation in the bond lengths, e.g. C_D-C_I and C_C-C_G show increase by about 0.07 and 0.08 Å, respectively, whereas the C_C-C_H show reduction by 0.07 Å and C_D-C_J and C_D-C_K reduce by 0.04 Å. Using the Mulliken charge analysis, it can be seen that the electrostatic interaction between P and C_C due to the opposite net charge, -0.1 *e* on C_C and 0.98 *e* on P. Interestingly, the net charge on N decreases by ~ 0.1 *e* compared to the isolated defect, while the P charge increases by ~ 0.1 *e* and consequently the nearest C neighbours effected by this change.

Among all the geometric features, the appearance of positive bond populations (*b*) between the C_C and P turns out to be a specific feature for this defect, proving the strong interaction in P-C_C with *b* (0.350 *e*) higher than the corresponding value in a perfect cell (0.348 *e*). There is a weak interaction in the N-P bond with *b* ~ 0.04 *e*. In contrast, the antibonding

interaction in N-C_C is confirmed by the negative value of *b*, which is almost double that in the isolated defect due to C_C also bonding with the P atom. The *b* values for the nearest C neighbours shows no significant changes. Due to the P has less electronegativity than C, the unpair electron donated by the valence electrons of P involved in the covalent bond with the dangling orbital on C_C give rise this unique close shell reconstruction.

7.3.2. Electronic structure

The band structures of the P-N pair are shown in figure 7.2. These were obtained with B3LYP, and three supercell sizes 64, 128, and 216, together with pure diamond for comparison. In these bands, there is only one band that is non-degenerate at all *k*-points, that appears in the gap, and which is fully occupied by the two-electrons provided by the defect. No shift appears between α and β states, as seen (in Chapter 3) with isolated defects, to stabilize the electronic structure. This leads to a fall in the resulting band to just above the top of the valence band, giving a wide bandgap between the defect level and the bottom of the conduction band of about 3.7 eV with B3LYP, consistent with the value of 3.9 eV obtained in previous calculations with clusters.[5] Table 7.2 provides a comparison between the bandgap of the P-N pair and that of isolated defects calculated with the same theoretical levels. The results explain clearly the absence of conductivity previously observed with this defect[23]; the shallow level of the P defect state occupied by α electron drops deeper into the bandgap, resulting in an insulating state.

The effect of supercell size can be measured by looking at the band dispersion, which almost disappears with size 216 atoms as the band becomes flat and nearly matches with the Fermi level. The contributions to the defective level are shared between the three atoms P, N, and C_C, as calculated by the projected density of states (PDOS) in Figure 7.3. For more quantitative analysis, only ~11% contribution comes from P, and almost equal contributions come from N and C_C by about ~27% and ~27-30%, respectively. These values are not affected by the type of functional or crystal size used.

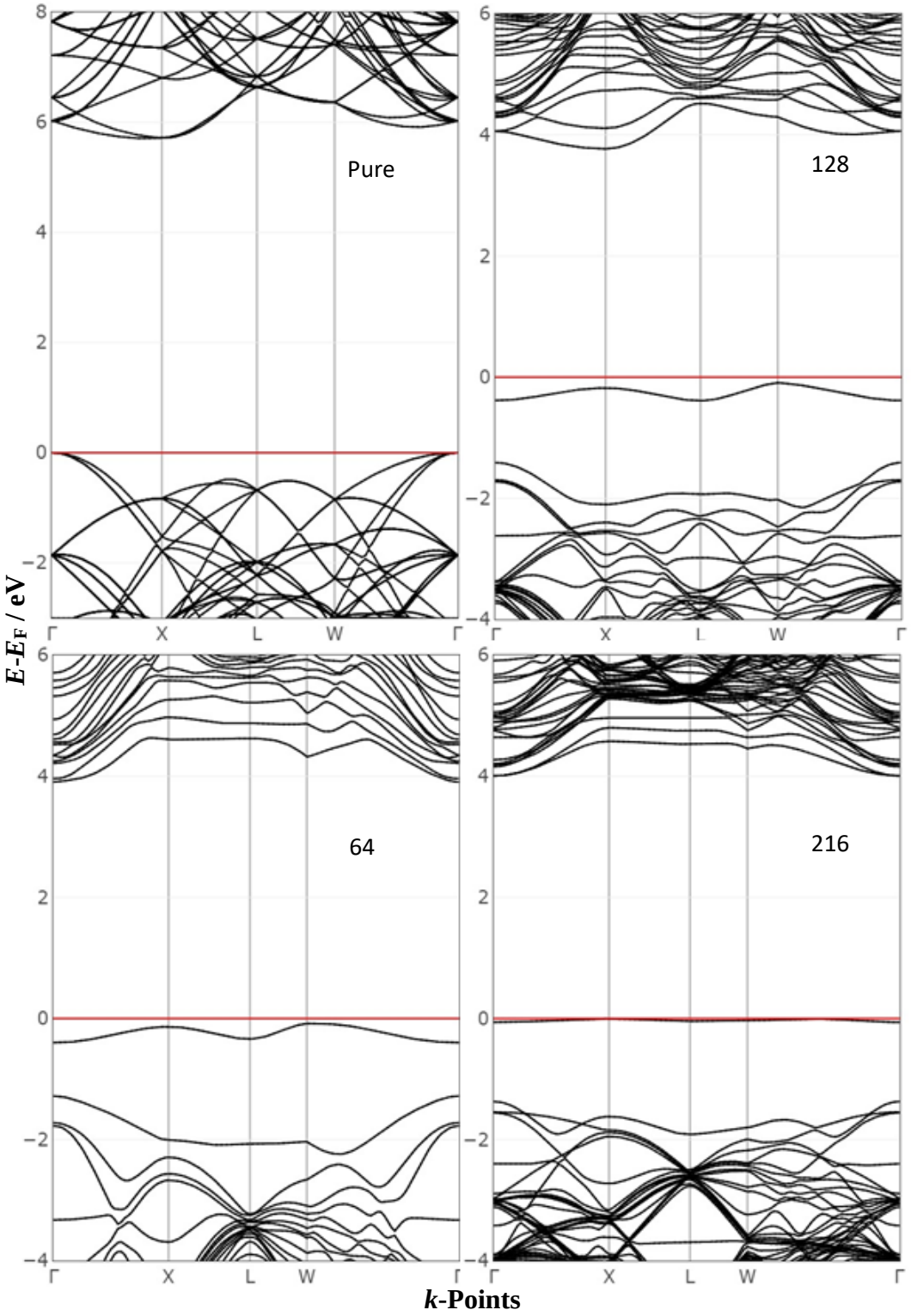

Figure 7-2 Band structure comparing pure diamond with a crystal containing a PN pair in a substitutional site with three supercell sizes: 128, 64, and 216-atom supercells, respectively. All calculations are computed with C/6-21G* and P, N/TZVP basis sets, respectively, and the B3LYP. All energy is presented relative to Fermi energies, indicated by a red line.

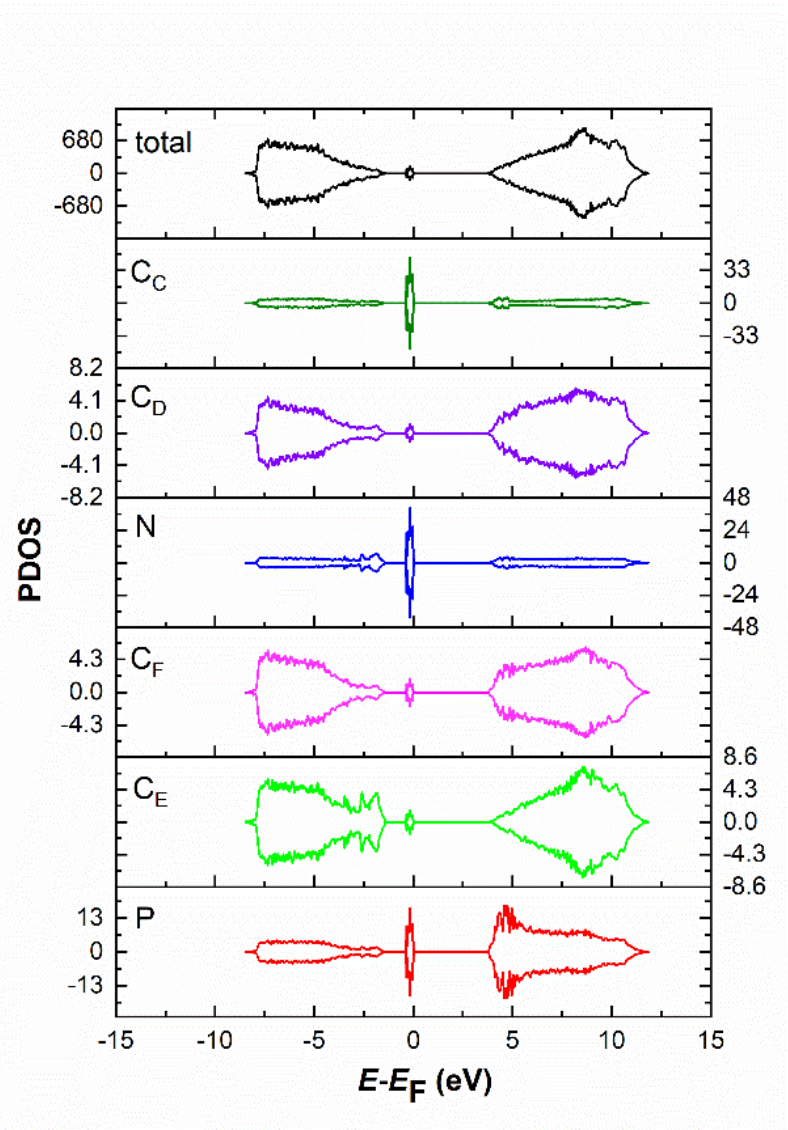

Figure 7-3 Projected DOS of the PN defect performed with128-atoms supercell, B3LYP, and C/6-21G* and N, P/TZVP basis sets. The density is plotted only for a range of 300-500 bands.

7.3.3 Defect stability

To characterize the defect further, we explored the stability of the PN pair in a diamond. The binding energies E_b were calculated according to the following equation[42],

$$\Delta E_b = E_{f(N)}^{Def} + E_{f(P)}^{Def} - E_{f(PN)}^{Def} \qquad 7\text{-}1$$

where $E_{f(N)}^{Def}$, $E_{f(P)}^{Def}$ and $E_{f(PN)}^{Def}$ are the formation energies calculated for the isolated defects N, P and the PN pair, respectively, from the following equation

$$\Delta E_f = E_{tot}^{Def} - E_{tot}^{Perf} - \sum n_i \, \mu_i \qquad 7\text{-}2$$

The chemical potential μ_i of the n_i atom was obtained by surrounding the atom with three shells of "ghost" atoms placed in a diamond crystal structure. As shown in Chapter 4, different choices of the atoms' chemical potentials do not affect the binding energy; therefore, one option was used in this section. Table 7.2 shows the energies of the single-atom, isolated defects (N, P) and the PN pair computed with different functionals and supercell sizes that were used in the binding energy calculations of PN pair (Table 7.3). The value of E_b is positive in the range 2.4-2.6 eV indicating that this defect is stable, and the formation of the PN pair in its relaxed position is energetically favoured if N is incorporated in the lattice during the growth of P-doped diamond.

Table 7.2 The computed energies of single atoms surrounded by three shells of 'ghost' atoms, the isolated defect, pure diamond, and the PN pair, computed with different functionals. All energies are in hartree. SC refers to supercell size. All calculations are computed with (6-21G*) and TZVP basis sets for C and P, N, respectively.

Functionals	**SC**	***E* (C)**	***E* (P)**	***E* (N)**	***E* (P_{sub})**	***E* (N_{sub})**	***E* (Pure)**	***E* (PN_{sub})**
B3LYP	**64**				-2739.2745	-2452.8319	-2436.3006	-2755.9043
	128	-37.7764	-341.2228	-54.5790	-5175.5712	-4889.1307	-4872.6013	-5192.1963
	216				-8525.4849	-8239.0450	-8222.5148	-8542.1099
HSE06	**64**	-37.7474	-341.1322	-54.5430	-2738.3946	-2451.9906	-2435.4767	-2755.0044
	128				-5173.8690	-4887.4658	-4870.9535	-5190.4728
PBE0	**64**	-37.7381	-341.1333	-54.5437	-2738.43417	-2452.0322	-2435.5191	-2755.0464
	128				-5173.9496	-4887.5498	-4871.0382	-5190.5572
PBE0-13	**64**	-37.7288	-341.1438	-54.5477	-2738.5895	-2452.1821	-2755.2010	-2755.2010
	128				-5174.2563	-4887.8543	-5190.8663	-5190.8663
PBEsol0	**64**	-37.6177	-340.7156	-54.3963	-2731.2766	-2445.1447	-2747.8633	-2747.8633
	128				-5159.9320	-4873.8020	-5176.5138	-5176.5138

Table 7.3 Defect binding energies (E_b) of PN. The band gaps (E_g) of the PN defect compared with the corresponding isolated defects in diamond. All energies are in eV; SC refers to supercell size. All calculations are performed with (6-21G*) and TZVP basis sets for C and P, N, respectively.

Functionals	SC	E_b^{PN}	$E_{g(PN)}^{C}$	$E_{g(N)}^{\alpha C}$	$E_{g(N)}^{\beta v}$	$E_{g(p)}^{\alpha C}$	$E_{g(p)}^{\beta v}$
B3LYP	**64**	2.679	3.624	3.153	4.476	0.245	5.333
	128	2.604	3.771	3.157	4.813	0.472	5.489
	216	2.580	4.005	3.338	4.919	0.553	5.579
HSE06	**64**	2.610	3.205	2.603	4.092	-	4.772
	128	2.489	3.332	2.603	4.429	-	4.907
PBE0	**64**	2.698	3.926	3.327	4.726	0.470	5.422
	128	2.613	4.056	3.325	5.069	0.678	5.577
PBE0-13	**64**	2.802	4.624	4.056	5.383	1.013	6.049
	128	2.804	4.757	4.054	5.738	1.193	6.212
PBEsol0	**64**	2.740	3.882	3.198	4.645	0.356	5.346
	128	2.560	4.009	3.198	4.990	0.581	5.499

7.3.3 IR spectroscopy

The interpretation of the IR spectra obtained experimentally remains ambiguous due to the uncontrolled dopants concentration and the unknown interactions with another defect during growth or annealing. This makes assigning a peak to a specific defect difficult. These complications can be helped using a simulation with a clearly defined defect environment.

In the present study, the calculated Raman peak of a primitive cell is found at 1331 cm^{-1}, as seen in Chapter 3, close to the experimental value of 1332 cm^{-1}, which confirms the efficient combination of the B3LYP and the (C/6-21G*) basis sets in defining the spectroscopic features of a diamond accurately. With these computational conditions, we calculated the frequencies of the C-centre spectrum according to previous theoretical and experimental studies (see Chapter 3). There are no peaks in the IR spectra of pure diamond due to the absence of dipole. The PN defect reduces the symmetry of pure diamond to C_s, which produces frequencies in the range 200-1400 cm^{-1}. Due to the variety of frequencies existing in the simulated spectra, the focus is placed on the highest significant peaks, which represent the frequencies of atoms in the defect region.

The effect of the concentration on the spectrum was investigated by changing the supercell sizes (64, 128, and 216 atoms), as seen in Figure 7.4. The distinctive features of all the calculated spectra are two intense peaks at ~200 cm^{-1} and ~1400 cm^{-1}, with several smaller peaks appearing in the wavenumber region between them.

Starting the analysis using supercell size 64, two unique peaks were found at 1359 cm^{-1} (above the Raman peak of 1331 cm^{-1}) and one at an exceptionally low frequency, 262 cm^{-1}. Taking the peaks in order: the normal mode at 1359 cm^{-1} is directly related to the defect and relates to the asymmetric stretching of the two N-C bonds (equivalent to N-C_D in Figure 7.1). The peak at 1062 cm^{-1} has a weak localization due to involve the stretching mode of C-C_G together with P-C_E-C and has a small relative intensity about 1:10 to the highest peak. The small twin peaks at 470 and 450 cm^{-1} relate to three bending modes centred on the N atom: N-P-C_E and two of the N-C_D-C fragments. The second highest-intensity peak at 294 cm^{-1}, with relative intensity about 47% of that of the highest peak, is related to a P atom vibrating against its C neighbours, as seen by animations. This peak is a very characteristic feature for NP-doped diamond because of its location in a unique area at the low-energy end of the spectrum, where usually there are no features for most common impurity defects in diamond such as N, B, V, and H, and in a lower region compared to the previously computed frequencies of P_{sub} defect at 380[24] and 354 cm^{-1}.[22]

The highest-wavenumber peak appears to be the least affected by concentration, compared to 1359, 1386 and 1379 cm^{-1} peaks. Using 64, 128, and 216-atom supercells, respectively, the 1359 cm^{-1} peak exhibits only a 27 cm^{-1} shift to a higher frequency when going from 64 to 128 atoms and only a 20 cm^{-1} shift to lower frequency when comparing the two cubic supercells (64, 216). The 1359 cm^{-1}peak exhibits a shoulder at 1369 cm^{-1} using 128 atoms and at 1365 cm^{-1} using 216 atoms, which is related to the bending modes of the two fragments of C_D-N-P. These shoulders were invisible using the 64-atom spectrum due to its overlapping with the main peak.

The second noteworthy feature in the low-concentration spectra is the small peak shift corresponding to the bending modes of N-P-C_E at 470 cm^{-1} using 64 atoms: this shifts by 25 cm^{-1} to 495 cm^{-1} using 128 atoms and it shifts by 13 cm^{-1} to 457 cm^{-1} using 216 atoms. The last intense peak (294 cm^{-1}) appears at almost the same position with a low concentration (238 cm^{-1} using 128 atoms and 234 cm^{-1} using 216 atoms). It is shifted to a lower frequency by 56 and

60 cm^{-1}, respectively, compared with the 64-atom spectrum, together with an obvious increase in the intensity relative to the highest peak (67% using 128 atoms, 85.5% using 216 atoms).

Table 7.4 shows the simulated frequencies for PN spectra calculated with different supercell sizes, together with the predicted isotopic shift that would be obtained by isotopic substitution of N^{14} with N^{15}. As there is only the one stable isotope for the P atom, analysis is limited to the isotopic shift of N. Replacing N^{14} with N^{15}, the highest peak with the three supercell sizes exhibits a large shift to lower frequency by ~16-17 cm^{-1} and the corresponding shoulders by ~ 9 cm^{-1}, indicating a high degree of localization in the defect. The small intense peaks at 470 (64 atoms), 495 (128 atoms), and 457 cm^{-1} (216 atoms) were also affected by N^{15} substitution, as they shifted by 9, 5, and 4 cm^{-1}, respectively, with a noticeable decrease in the shift with dilution.

Table 7.4 IR peak positions (in cm^{-1}) for the PN defect calculated using B3LYP (6-21G*/C and TZVP for P and N) using 64-, 128-, and 216-atom supercells, plus the peak positions and shifts when substituting N^{14} for N^{15}.

64 atoms			**128 atoms**			**216 atoms**		
$\bar{\nu}$ **(cm^{-1})**	Isotopic N^{15} $\bar{\nu}$	Shift of N^{15}	$\bar{\nu}$ (cm^{-1})	Isotopic N^{15} $\bar{\nu}$	Shift of N^{15}	$\bar{\nu}$ (cm^{-1})	Isotopic N^{15} $\bar{\nu}$	Shift of N^{15}
1359	1343	16	**1386**	1369	17	**1379**	1362	17
1357	1348	9	**1369**	1360	9	**1365**	1354	9
1062	1061	1				**546**	545	1
470	461	9	**495**	490	5	**457**	453	4
450	448	2	**445**	445	0			
294	294	0	**238**	237	1	**234**	233	1

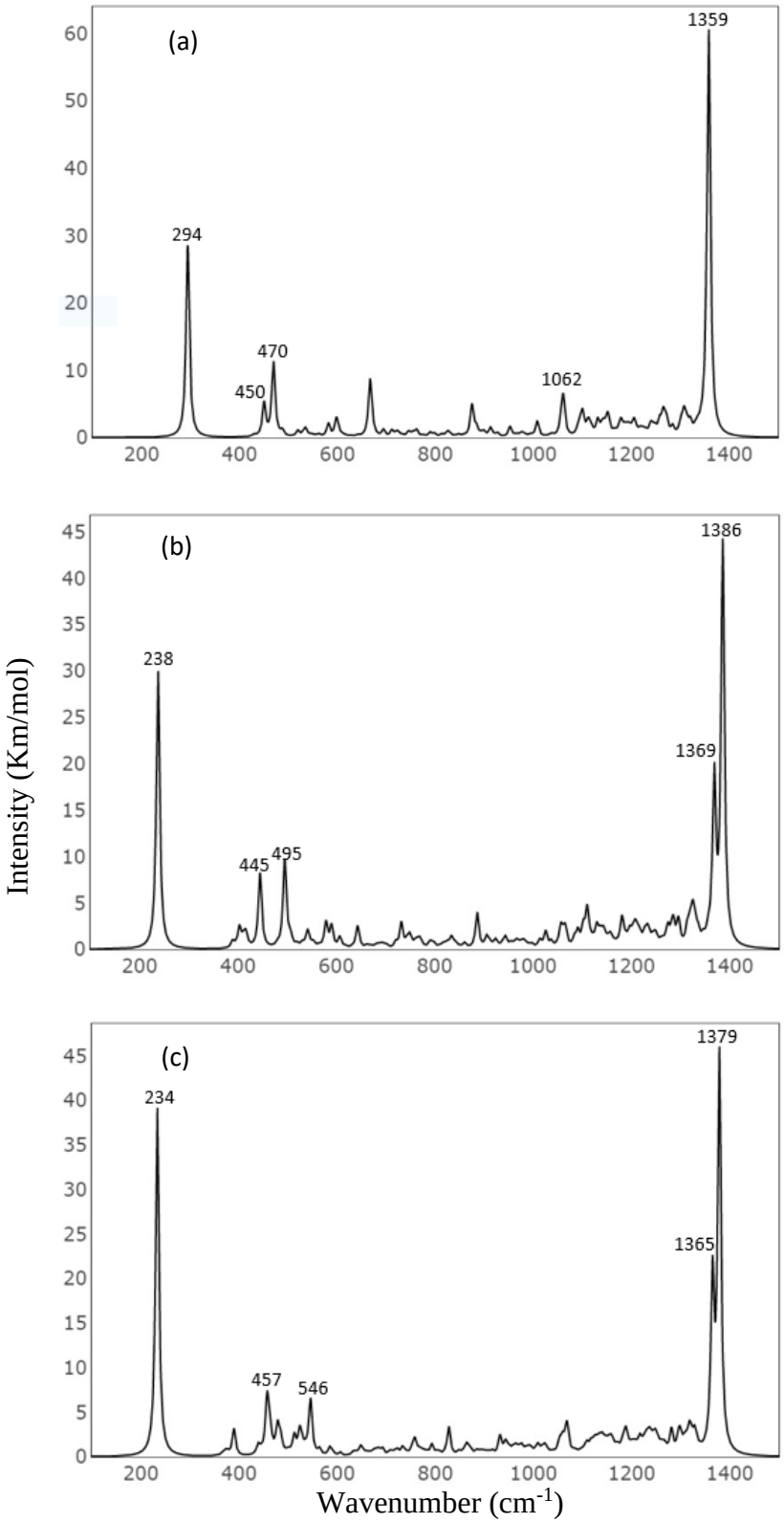

Figure 7-4 A comparison between the calculated IR spectra of the PN defect with three supercell sizes: (a) 64, (b) 128 and (c) 216 atoms. The calculations spectra were performed with B3YLP, and C/6-21G* and N, P/TZVP basis sets. A full width at half-maximum (FWHM) value of 8 cm^{-1} was used together with a Lorentzian function to plot the spectra.

7.4 Conclusion

The structural geometry, charge distribution, electronic structure, binding energy, and IR spectrums of the PN pair defect in diamond have been studied via the supercell approach with a range of hybrid functional and three supercell sizes consisting of 64, 128, and 216 atoms. The defect introduces a unique distortion in the lattice causing elongation of one of the N-C bonds due to the localization of the N lone pair, as to that previously observed in the C-centre. The relaxed defect structure gives rise to a new bond between the P atom and a unique carbon involving the elongation of an N-C bond, but with the bond population the same as pure diamond. The charge distribution on the defect and first-nearest neighbours were discussed in detail. The defect introduces a deep band which decreases the bandgap by ~ 2 eV, giving an insulating state. The PN pair is stable in diamond with a binding energy ~ 2.6 eV, close to that predicted for the PH complex 2.56 [43], 2.45 [19], 3.1[42] and 2.6 eV [28] with H being in an anti-bonding site behind P.

The most significant peaks in the simulated IR spectrum are the two most intense bands appearing at either end of the spectrum. The highest intensity peak occurs at 1359, 1386 and 1379 cm^{-1}, depending upon the size of supercell used in the calculation (64, 128 and 216 atoms, respectively). This peak is assigned to the highly localized asymmetric stretching mode of the two N-C_D bonds. The second highest-intensity peak occurs at 294, 238 and 234 cm^{-1} (using 64, 128, or 216-atom supercells, respectively). This peak is related to the atomic motion of P in the opposite direction of the three surrounding C atoms. The localization of the several other peaks around ~ 450 cm^{-1} was confirmed by isotopic N^{15} substitutions which were assigned to the bending modes centred at the N atom with an intensity very low compared with the two highest peaks.

7.5 References

1. Messmer, R. P. & Watkins, G. D. Molecular-orbital treatment for deep levels in semiconductors: Substitutional nitrogen and the lattice vacancy in diamond. *Phys. Rev. B* **7**, 2568–2590 (1973).

2. Lombardi, E. B., Mainwood, A., Osuch, K. & Reynhardt, E. C. Computational models of the single substitutional nitrogen atom in diamond. *J. Phys. Condens. Matter* **15**, 3135–3149 (2003).

3. Kajihara, S. A., Antonelli, A., Bernholc, J. & Car, R. Nitrogen and potential n-type dopants in diamond. *Phys. Rev. Lett.* **66**, 2010–2013 (1991).

4. Hang, D. B. Electronic Band Structure of N and P Dopants in Diamond. *Bull. Korean Chem. Soc.* **19**, 628–634 (1998).

5. Anderson, A. B. & Kostadinov, L. N. P and N compensation in diamond molecular orbital theory. *J. Appl. Phys.* **81**, 264–267 (1997).

6. Davies, G. The A nitrogen aggregate in diamond-its symmetry and possible structure. *J. Phys. C Solid State Phys.* **9**, L537 (1976).

7. Sutherland, G.B.B.M., Blackwell, D.E. and Simeral, W. G. The problem of the two types of diamond. *Nature* **174**, 901–904 (1954).

8. Salustro, S. *et al.* Characterization of the B-Center Defect in Diamond through the Vibrational Spectrum: A Quantum-Mechanical Approach. *J. Phys. Chem. A* **122**, 594–600 (2018).

9. Breuer, S. J. & Briddon, P. R. Ab initio investigation of the native defects in diamond and self-diffusion. *Phys. Rev. B* **51**, 6984–6994 (1995).

10. Yan, C. S., Vohra, Y. K., Mao, H. K. & Hemley, R. J. Very high growth rate chemical vapor deposition of single-crystal diamond. *Proc. Natl. Acad. Sci. U. S. A.* **99**, 12523–12525 (2002).

11. Yan, C. S. & Vohra, Y. K. Multiple twinning and nitrogen defect center in chemical vapor deposited homoepitaxial diamond. *Diam. Relat. Mater.* **8**, 2022–2031 (1999).

12. Collins, A. T., Stanley, M. & Woods, G. S. Nitrogen isotope effects in synthetic diamonds. *J. Phys. D. Appl. Phys.* **20**, 969–974 (1987).

13. Hu, M. *et al.* Synthesis and characterization of boron and nitrogen co-doped diamond crystals under high pressure and high temperature conditions. *CrystEngComm* **19**, 4571–4575 (2017).

14. Ferrari, A. M., Salustro, S., Gentile, F. S., Mackrodt, W. C. & Dovesi, R. Substitutional nitrogen atom in diamond. A quantum mechanical investigation of the electronic and spectroscopic properties. *Carbon N. Y.* **134**, 354–365 (2018).

15. Collins, A. T. & Woods, G. S. An anomaly in the infrared absorption spectrum of

synthetic diamond. *Philos. Mag. B Phys. Condens. Matter; Stat. Mech. Electron. Opt. Magn. Prop.* **46**, 77–83 (1982).

16. Salustro, S. *et al*. The A-center defect in diamond: Quantum mechanical characterization through the infrared spectrum. *Phys. Chem. Chem. Phys.* **19**, 14478–14485 (2017).

17. Salustro, S. *et al.* Substitutional boron and nitrogen pairs in diamond. A quantum mechanical vibrational analysis. *Carbon N. Y.* **146**, 709–716 (2019).

18. Koizumi, S. Growth and characterization of phosphorus doped n-type diamond thin films. *Phys. Status Solidi Appl. Res.* **172**, 71–78 (1999).

19. Wang, L. G. & Zunger, A. Phosphorus and sulphur doping of diamond. *Phys. Rev. B - Condens. Matter Mater. Phys.* **66**, 1–4 (2002).

20. Eyre, R. J., Goss, J. P., Briddon, P. R. & Hagon, J. P. Theory of Jahn-Teller distortions of the P donor in diamond. *J. Phys. Condens. Matter* **17**, 5831–5837 (2005).

21. He, Y., Chen, H., Poon, S. J. & Shiflet, G. The effect of temperature on stability of the al-cu-co decagonal phase. *Philos. Mag. Lett.* **64**, 307–315 (1991).

22. Butorac, B. & Mainwood, A. Symmetry of the phosphorus donor in diamond from first principles. *Phys. Rev. B - Condens. Matter Mater. Phys.* **78**, 1–8 (2008).

23. Koizumi, S., Teraji, T. & Kanda, H. Phosphorus-doped chemical vapor deposition of diamond. *Diam. Relat. Mater.* **9**, 935–940 (2000).

24. R. Jones and S.Öberg. Structure and dynamics of substitutional phosphorus in diamond. *Philos. Mag. Lett.* **65**, 317–319 (1991).

25. Jones, R., Lowther, J. E. & Goss, J. Limitations to n-type doping in diamond: The phosphorus-vacancy complex. *Appl. Phys. Lett.* **69**, 2489–2491 (1996).

26. Goss, J. P., Briddon, P. R., Jones, R. & Sque, S. Donor and acceptor states in diamond. *Diam. Relat. Mater.* **13**, 684–690 (2004).

27. Nishimatsu, T., Katayama-Yoshida, H. & Orita, N. Theoretical study of hydrogen-related complexes in diamond for low-resistive n-type diamond semiconductor. *Phys. B Condens. Matter* **302**–**303**, 149–154 (2001).

28. Miyazaki, T. & Yamasaki, S. Ab initio energetics of phosphorus related complex defects in synthetic diamond. *Phys. B Condens. Matter* **376**–**377**, 304–306 (2006).

29. Flatae, A. M. *et al.* Silicon-vacancy color centers in phosphorus-doped diamond. *Diam. Relat. Mater.* **105**, 107797 (2020).

30. Lombardi, E. B., Mainwood, A. & Osuch, K. Ab initio study of the passivation and interaction of substitutional impurities with hydrogen in diamond. *Diam. Relat. Mater.* **12**, 490–494 (2003).

31. Cao, G. Z., Driessen, F. A. J. M., Bauhuis, G. J., Giling, L. J. & Alkemade, P. F. A. Homoepitaxial diamond films codoped with phosphorus and nitrogen by chemical-vapor deposition. *J. Appl. Phys.* **78**, 3125–3131 (1995).

32. Yan, B. *et al.* The effect of phosphorus and nitrogen co-doped on the synthesis of diamond at high pressure and high temperature. *Int. J. Refract. Met. Hard Mater.* **54**, 309–314 (2016).

33. Cao, G. Z., Giling, L. J. & Alkemade, P. F. A. Growth of phosphorus and nitrogen co-doped diamond films. *Diam. Relat. Mater.* **4**, 775–779 (1995).

34. Salustro, S. *et al.* The characterization of the VNxHy defects in diamond through the infrared vibrational spectrum. A quantum mechanical investigation. *Carbon N. Y.* **132**, 210–219 (2018).

35. Salustro, S. *et al.* Infrared and Raman spectroscopic features of the self-interstitial defect in diamond from exact-exchange hybrid DFT calculations. *Phys. Chem. Chem. Phys.* **18**, 21288–21295 (2016).

36. Zelferino, A. *et al.* The electronic states of the neutral vacancy in diamond: a quantum mechanical approach. *Theor. Chem. Acc.* **135**, 1–11 (2016).

37. Salustro, S., Nöel, Y., Zicovich-Wilson, C. M., Olivero, P. & Dovesi, R. The v + i defects in diamond: An ab initio investigation of the electronic structure, of the Raman and IR spectra, and of their possible recombination. *J. Chem. Phys.* **145**, (2016).

38. Gentile, F. S. *et al.* Hydrogen, boron and nitrogen atoms in diamond: a quantum mechanical vibrational analysis. *Theor. Chem. Acc.* **137**, 1–10 (2018).

39. Sansone, G. *et al.* Looking for sp2 carbon atoms in diamond: a quantum mechanical study of interacting vacancies. *Theor. Chem. Acc.* **137**, 1–9 (2018).

40. Gentile, F. S. *et al.* The VN3H defect in diamond: A quantum-mechanical

characterization. *Phys. Chem. Chem. Phys.* **19**, 22221–22229 (2017).

41. Salustro, S. *et al.* Hydrogen atoms in the diamond vacancy defect. A quantum mechanical vibrational analysis. *Carbon N. Y.* **129**, 349–356 (2018).

42. Goss, J. P. *et al.* Theory of hydrogen in diamond. *Phys. Rev. B - Condens. Matter Mater. Phys.* **65**, 1–13 (2002).

43. Katayama-Yoshida, H., Nishimatsu, T., Yamamoto, T. & Orita, N. Codoping method for the fabrication of low-resistivity wide band-gap semiconductors in p-type GaN, p-type AlN and n-type diamond: Prediction versus experiment. *J. Phys. Condens. Matter* **13**, 8901–8914 (2001).

CHAPTER 8 –THESIS SUMMARY AND FUTURE WORK

8.1 Summary

This thesis covers a variety of theoretical and experimental aspects of n-type doped diamond semiconductors. A range of point defects in diamonds were explored, initially described in chapter 3, with simulations of three defects: a vacancy (in its three-spin states — singlet, triplet and quintuplet), the C-centre (in its C_{3v} symmetry) and substitutional phosphorus (in its C_{3v} and D_{2d} symmetries). Hybrid functionals that included a different percentage of Hartree-Fock in the approximations were used in the study. The results from the first two defects showed good agreement with previous studies in terms of geometry, energy and electronic structure. The main IR frequency of the C-centre was computed to be 1,132 cm^{-1}, in good agreement with previous theoretical and experimental values of 1,130 and 1,135 cm^{-1}, respectively. We presented, for the first time, hybrid calculations for P defects in diamond. The relative stabilities of P in its C_{3v} and D_{2d} symmetries were explored with all the adopted functionals, and C_{3v} was found to be lower in energy by less than 0.1 eV. The P donor level was marginally affected by the band gap of pure diamond, as seen with the vacancy and C-centre defects. In B3LYP and 512 supercell calculations, the impurity levels of C-centre and P appeared at $E_g^{c\alpha}$, 3.376 and 0.680 eV, associated with empty bands at $E_g^{v\beta}$, 5.080 and 5.635 eV, respectively.

In the subsequent two chapters—4 and 5—we proposed a complex consisting of one Mg coordinated by three N atoms to produce n-type diamond. The geometry, energy and electronic structure of the individual Mg point defect and its complex with N, MgN_2 and MgN_3, in addition to 2NV, were studied and presented in detail. The relative stabilities of Mg in its two spin states—singlet and triplet—were found to be independent of the supercell size and the basis sets used but varied with the choice of hybrid functional. Using HSE06, the triplet was lower in energy by 0.1 eV, but with PBE0 and PBEsol0, the situation was reversed, with a difference of ~ 0.03 eV, and with B3LYP the difference became of the order of 10^{-3} eV. The trend of the charge and spin distribution over the first and second neighbours in both spin states, as evaluated from Mulliken atomic charges and spin moments, was found to be the same for

all the functionals. The localisations of spin density on the first four carbon neighbours was ~ 0.4 *e* per atom; in the triplet (the four carbon atoms carry α), while in the singlet (2 carbon atoms carry α, and the other two carry β), associated with the equal charge distribution, ~ - 0.30 *e* for each atom.

For a diamond lattice occupied by a MgN_3 complex, the perturbation to substitutional sites was found to be mainly on the first and second shells. The donor level of the MgN_3 complex was calculated from the electronic structure computed with the HSE06, B3LYP, PBE0 and EMM methods. In all the calculations, the MgN_3 donor level was shallower than P by ~ 1–3 eV. The P level computed using a 512-atom supercell and B3LYP (0.68 eV from the CBM) was in good agreement with most experimental study values (~0.6 eV), and the corresponding level for MgN_3 was found to be 0.26 eV. The EMM donor level prediction, using B3LYP/512, was in line with that obtained with the electronic structure analysis, as the donor level of MgN_3 was at 0.37 eV relative to the P level.

The formation energy (E_f), of MgN_3 was evaluated using different approaches in order to explore the possibility of synthesising this defect in diamond. In the first method (A), with the chemical potentials of the C, N and Mg atoms taken from diamond, nitrogen molecules and hexagonal closest packed (hcp) solid Mg, respectively, it was found that the E_f of MgN_2 from the pre-existing 2NV defect was lower than the E_f of Mg calculated assuming the direct substitutional of a C atom by about three orders of magnitude, at ≤ 3.75 eV. In the second method (B), the chemical potentials were taken to be those of the isolated atoms, the E_f of Mg from 2NV defect is lowered further to become ≤ 2.3 eV. Consequently, a two-step formation mechanism was proposed to synthesise the MgN_3 defect, that depended mainly on N-related defects diffusing to an immobile Mg defect. In the last method (C), the chemical potential of N was taken such that the E_f of the C-centre is zero, consistent with the standard observation of the high solubility of N in diamond. The E_f of MgN_3 was then calculated via direct substitution of C atoms in pure diamond by Mg and N, and was exothermic, raising the possibility for synthesising this defect by a CVD technique.

The main features of the IR spectra of MgN_2 (close shell) and 2NV (in its singlet state, which is lower in energy than the triplet by 0.2 eV) were computed using B3LYP and analysed in detail. In the 2NV defect, the most intense peak appeared at a high frequency 1,095 cm^{-1}, close to the most significant IR peaks for MgN_2 defects at 1,071 cm^{-1}, with a shoulder at 1,060 cm^{-1}, making distinguishing them in a complex spectrum impractical. The low intensity peak

of MgN_2 at 324 cm^{-1} is potentially measurable due to its strong localisation on the Mg atom and its appearance in a region that usually has no features in the IR spectra from the best-known defects in diamond, such as N-related defects. Therefore, detection of this peak in a complex spectrum for a sample containing only Mg and N is most likely to be related to Mg.

In chapter 6, two experimental approaches were explored to introduce a complex defect, consisting of Mg and N atoms, into diamond. In the first method, the Mg metal was encapsulated between two NDD films and annealed at 1,200°C to promote the diffusion of the dopants. Two types of substrate were used in the study for comparison: Si wafers abraded by diamond grit and polycrystalline diamond purchased from Element Six. The morphology and quality of the NDD films grown with different ratios of N/H, studied using SEM and Raman spectroscopy, were in line with previously reported results. From the SIMS profile, it was observed that the nitrogen concentration significantly increased in the near-surface regions between the two NDD films, showing a tendency to diffuse to the metal layer. This caused variations in the N concentrations between the two NDD films and the intermediate layer. In the second method, the Mg and N ions were implanted into CVD single-crystal diamond samples at different doses then subjected to annealing in a vacuum at different temperatures of up to 1,200°C. The SIMS signal from the Mg ions was unaffected by the annealing, with a maximum concentration detected at ~ 2×10^{19} cm^{-3}. The binding with N ions or other defects formed during implantation may cause immobility of the Mg at 1,200°C.

In chapter 7, the calculations of isolated defects—the C-centre and substitutional phosphorus—in chapter 3, were extended to include a PN pair in adjacent substitutional sites in diamond. The defect geometry, charge distribution, electronic structure, stability, and spectroscopic features of this defect in diamond were explored with a range of hybrid functionals using different supercell sizes—64, 128 and 216. The most significant finding with this defect was the positive bond population (as in pure diamond) arising between the C on the elongated N-C bond and the P atom, giving a new unique chemical reconstruction. The electronic structure analysis showed that the defect introduces a deep, fully occupied band, giving an insulating state with a gap of ~ 4.0–4.8 eV. The stability of this defect in diamond is similar to that of a PH pair, with H being in an anti-bonding site, with a binding energy of ~ 2.6 eV. In the simulated IR spectrum, there are two unique bands that appear at the edges of the spectrum, having higher intensity than the other peaks. The first peak appears at high frequencies of 1,359, 1,386 and 1,379 cm^{-1}, obtained with supercell sizes of 64, 128 and 216 atoms, respectively, and the corresponding peak in the end-range of the spectrum appears at

294, 238 and 234 cm^{-1}. The latter peak is related to the P and shows a shift to a lower frequency than that of a single P defect previously reported at 354 cm^{-1}.

8.2 Future work

From a theoretical perspective, there are a few interesting points related to Mg-doped diamond that were beyond the scope of the present study, such as calculating the activation energy for Mg diffusion in diamond. Some ab initio DFT studies have previously conducted such calculations for Li and Na in interstitial sites and found that the activation energy for the diffusion of Na is three orders of magnitude larger than that of Li. It is important to evaluate the diffusion activation energy of Mg as a dopant in diamond primarily to control any annealing process required to activate the dopant, especially in co-doping systems. Another point related to Mg is that the simulation of the spectroscopic features of this defect at substitutional sites with the different spin states indicated in this study needs to be effectively correlated with experimental data.

Experimentally, introducing the Mg from the gas phase during CVD diamond growth with N would be a very interesting study. According to our knowledge, most co-doping systems with CVD growth that explored in the literature used B-N, B-H, B-S and P-N combinations, probably due to most CVD diamond-growth setups already being set up to use these gases. Such combinations are known from DFT calculations to produce a deep level, with no preference over P. Biscyclopentadienemagnesium (Cp2Mg) gas, which is used to dope GaN with Mg, could be studied with diamond. However, it is produced by AkzoNobel (Amsterdam, Netherlands) at a cost of around €4,000 per 50 ml cylinder making experiments very expensive. In the ion implantation technique, some previously reported successful implantation schemes with B and N can be examined using an Mg-N system, such as cold implantation rapid annealing (CIRA) and low-damage drive-in (LODDI) schemes. The limitations of a CIRA implantation scheme that have been found with P might be overcome by presenting the N together with Mg in the system. Other potential work that could be carried out with an Mg-N system include preparing high-quality single-crystal diamond grown with an MW reactor, heavily doped by N, then performing the implant with only Mg ions to minimise the damage induced by the high doses of implanted ions, followed by annealing at different temperatures to study the diffusion of the dopants.

Appendix

CHAPTER 3

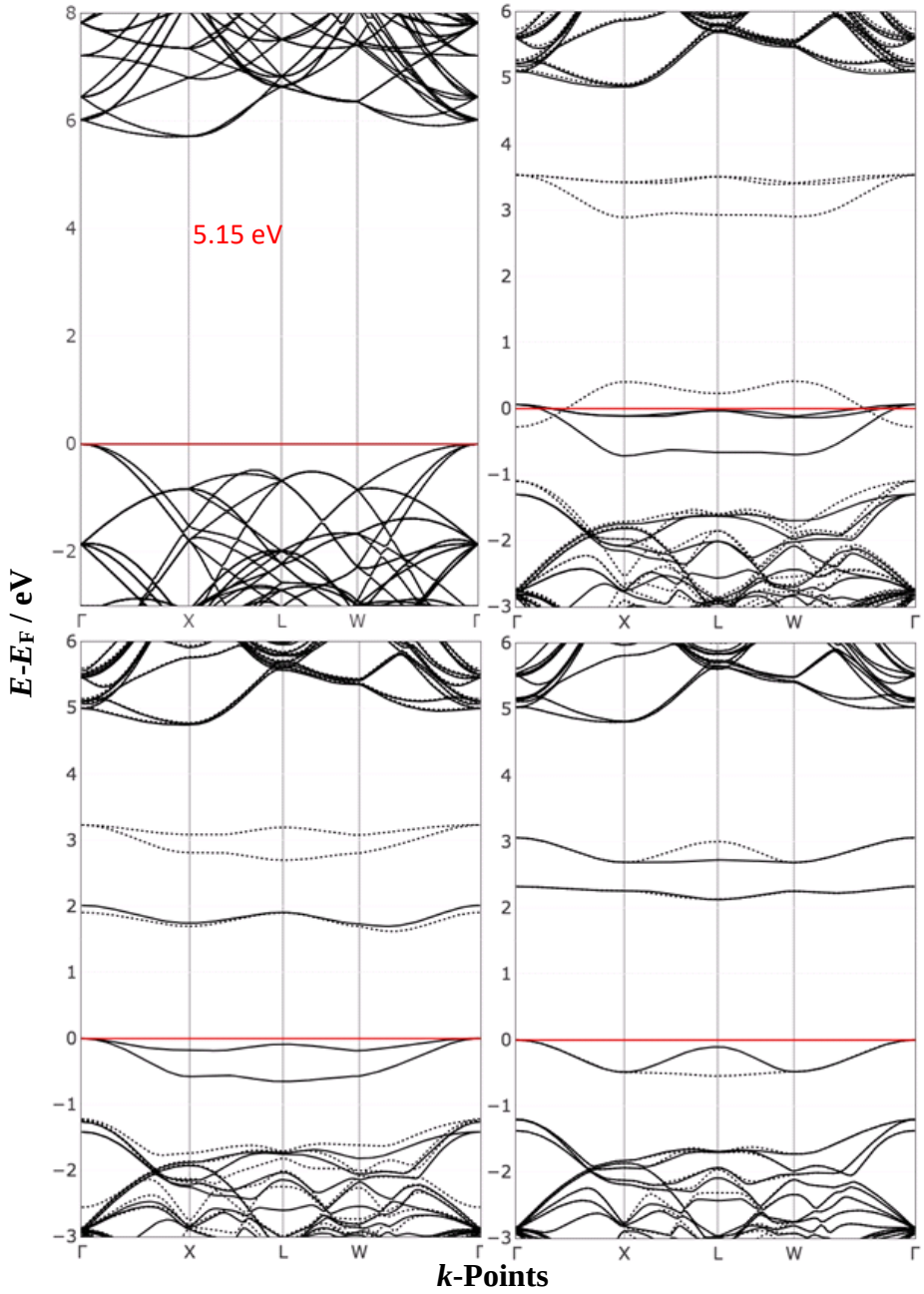

Figure A1.3: Band structure of perfect diamond compared with V defects with different symmetries. All calculations were computed with the HSE06 functional, C / 6-21G* basis sets and 128-atom supercells.

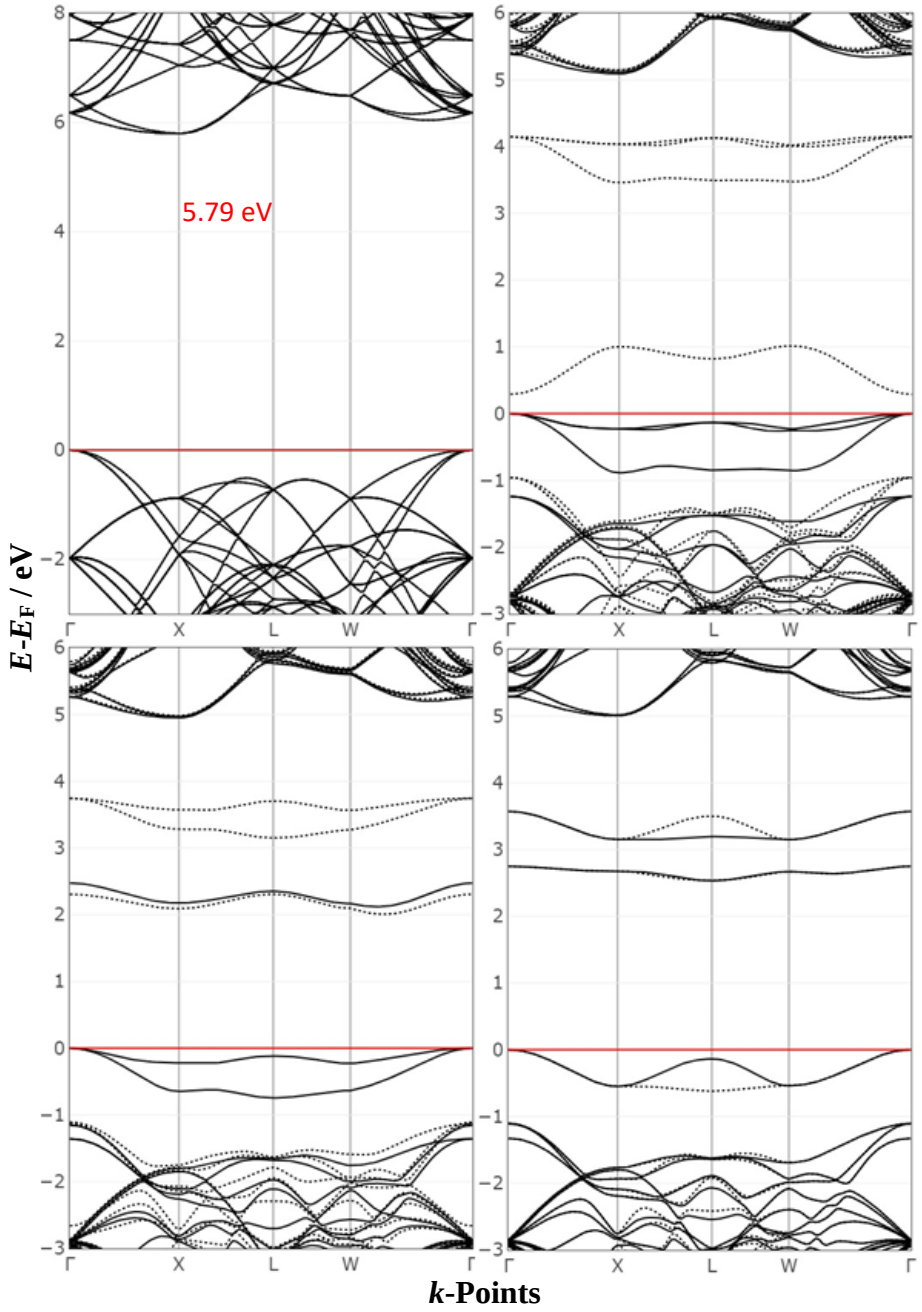

Figure A2.3: Band structure of perfect diamond compared with V defects with different symmetries. All calculations were computed with the PBE0 functional, C / 6-21G* basis sets and 128-atom supercells.

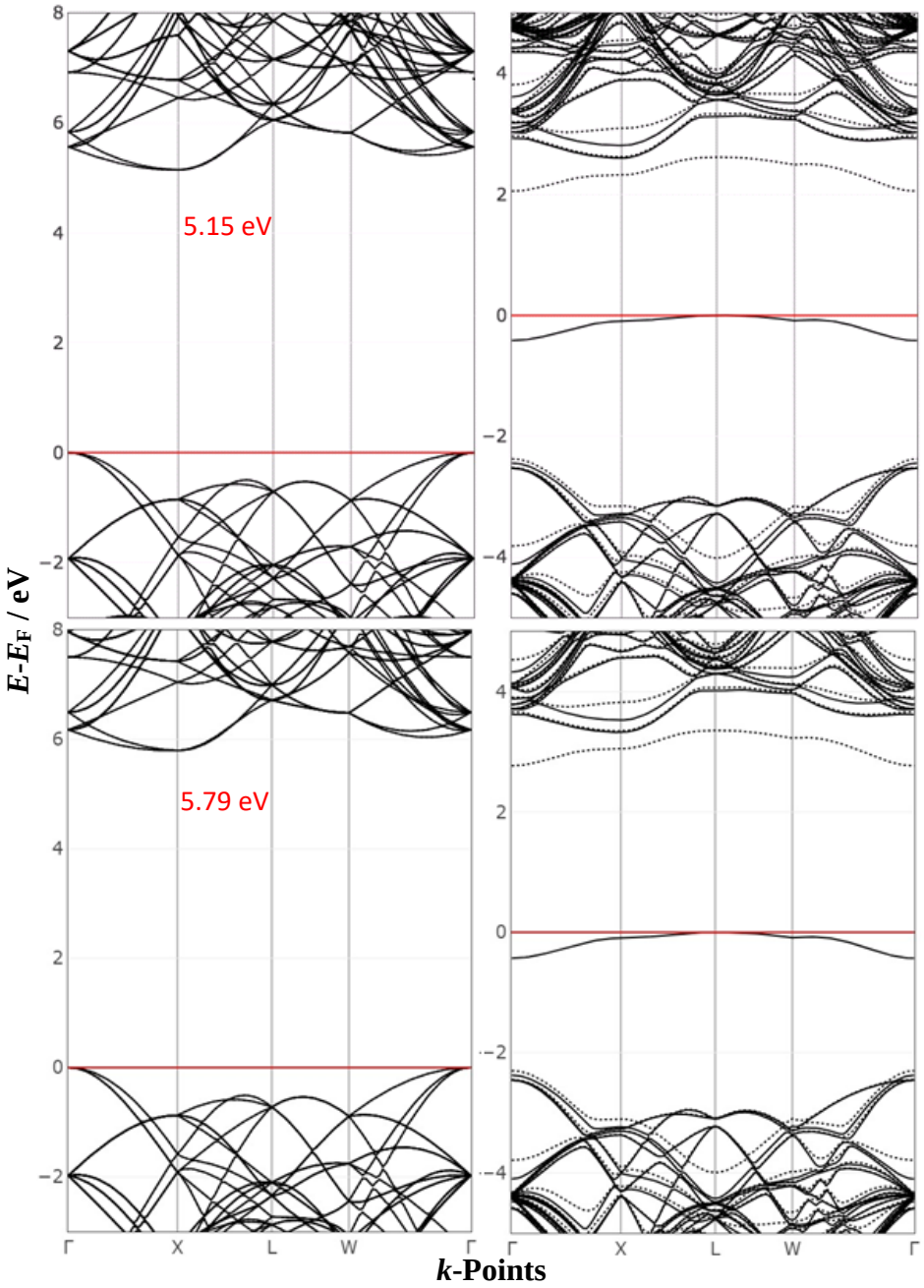

Figure A3.3: Band structure of perfect diamond compared with the N defect in a substitutional site with S_z = ½ and C_{3v} symmetry. Top panel refers to HSE06 and the bottom PBE0. All calculations were computed with the C / 6-21G* and N / TZVP basis sets. 128-atom supercells.

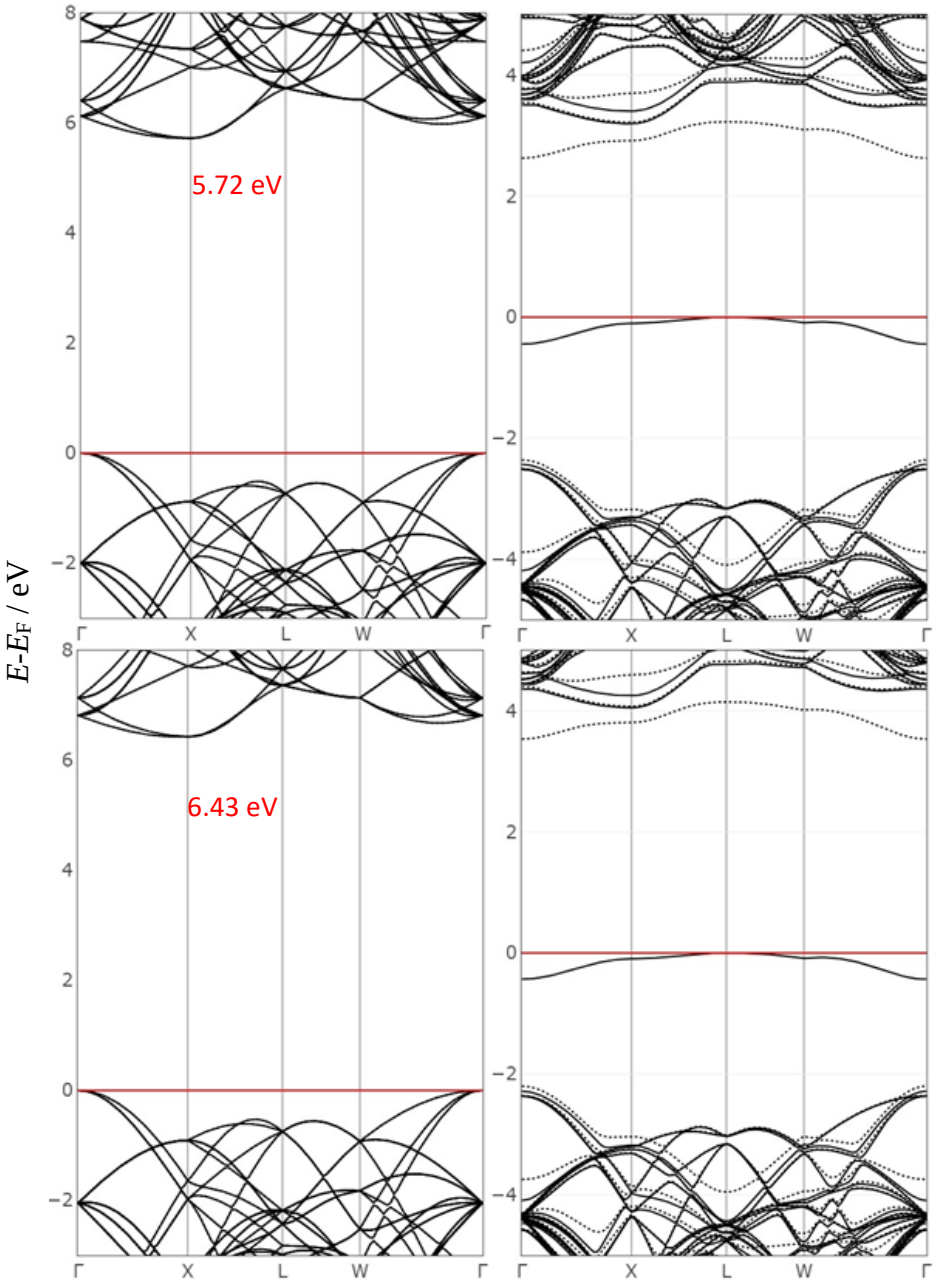

Figure A4.3: Band structure of perfect diamond compared with the N defect in a substitutional site with S_z = ½ and C_{3v} symmetry. Top panel refers to PBEsol0 and the bottom PBE0-13. All calculations were computed with the C / 6-21G* and N / TZVP basis sets and 128-atom supercells.

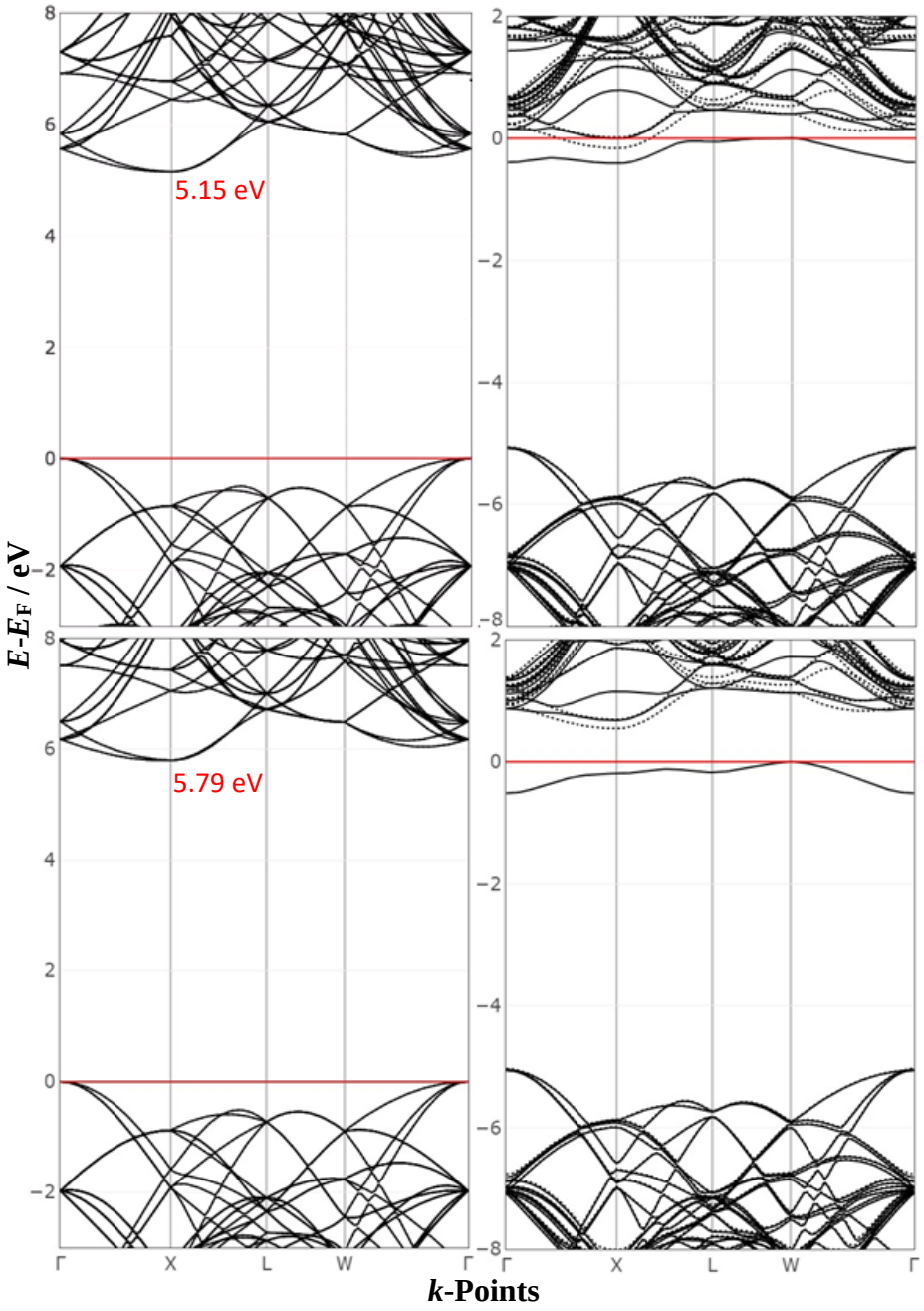

Figure A5.3: Band structure of perfect diamond compared with the P defect in a substitutional site with C_{3v} symmetry. Top panel refers to HSE06 and the bottom PBE0. All calculations were computed with the C / 6-21G* and P / TZVP basis sets and 128-atom supercells.

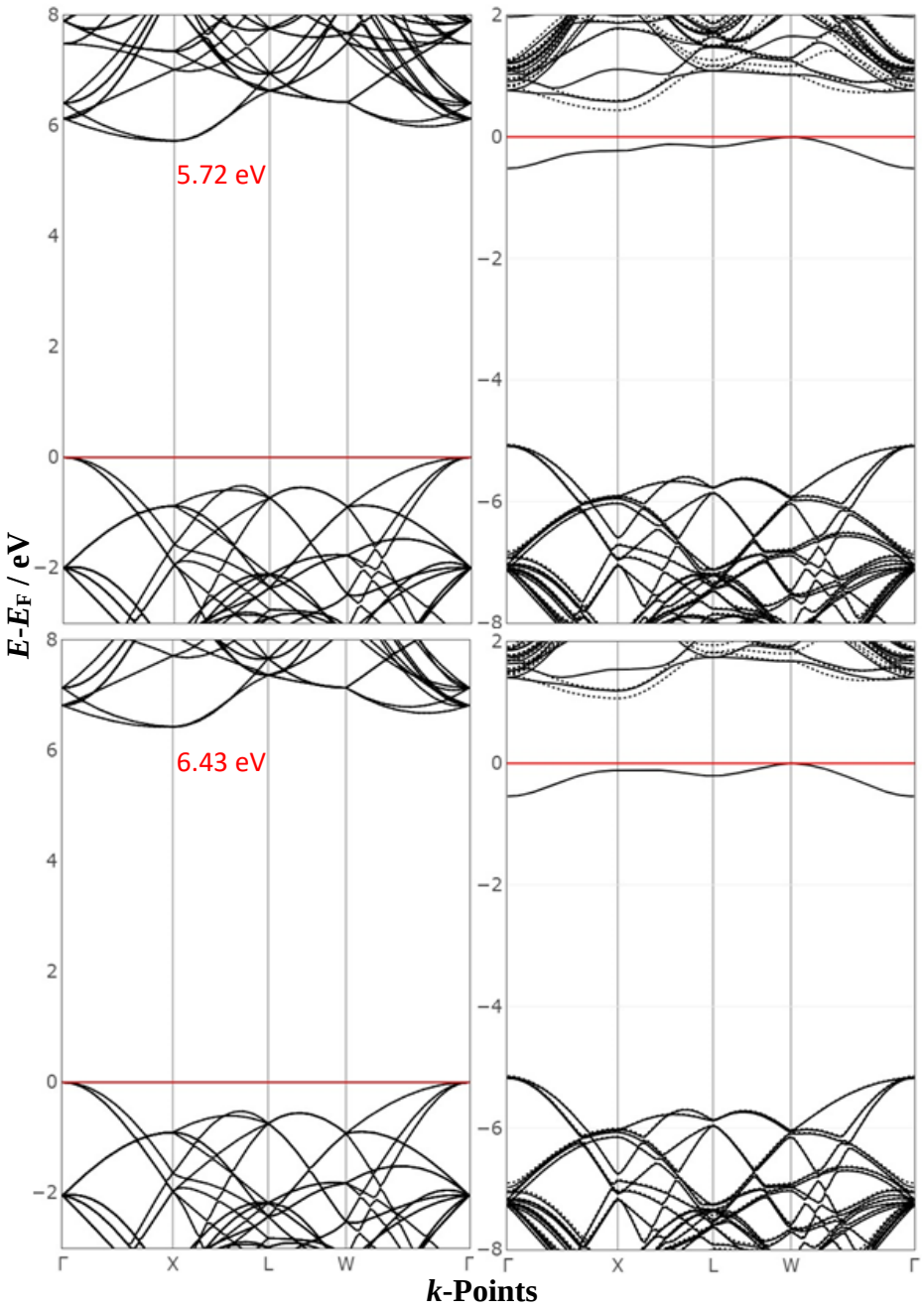

Figure A6.3: Band structure of perfect diamond compared with the P defect in a substitutional site with C_{3v} symmetry. Top panel refers to PBEsol0 and the bottom PBE0-13. All calculations were computed with the C / 6-21G* and P / TZVP basis sets and 128-atom supercells.

In CRYSTAL code, the frequencies (wavenumber) obtained from the following expression.

$$W^{\Gamma}_{ai,bj} = \frac{H^{0}_{ai,bj}}{\sqrt{M_a M_b}} \text{ where } \qquad H^{0}_{ai,bj} = \frac{\partial^2 E}{\partial u^{0}_{ai}\, \partial u^{0}_{bi}}$$

Where *u* atomic displacements and *M* refers to the atomic mass of atom a, and b in the system. The *i*-th and *j*-th are the Cartesian directions in which the atoms move. The integrated intensity for IR absorption I_p for each *P* mode is computed as follows:

$$I_p = \frac{\pi N_A}{3\, c^2} \,.\, d_p \,.\, \left|\vec{\mathbf{z}}_p\right|^2$$

Where *c* is the speed of light, N_A is the Avogadro's number, d_p is the degeneracy of the mode, and last term $\vec{\mathbf{z}}_p$ is the mass-weighted effective mode Born charge vector.

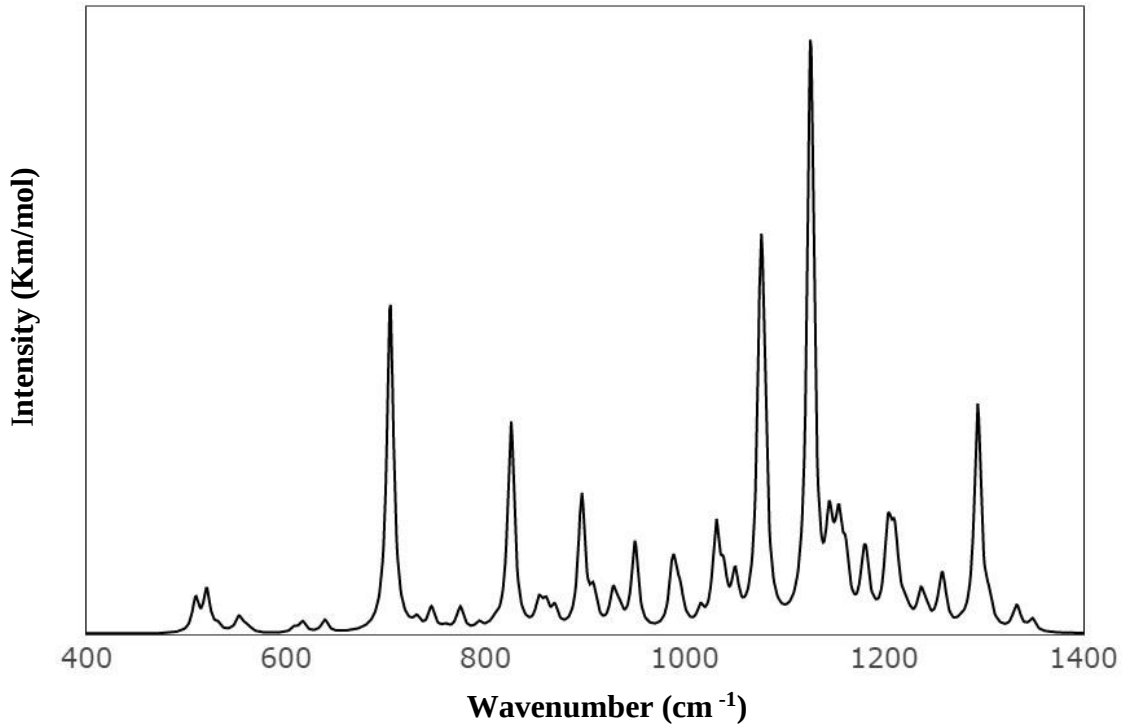

Figure A7.3: The simulated IR spectra computed with B3LYP/ 6-21G* for the N^{15} isotope C- centre defect obtained with 64-atom supercell.

CHAPTER 4

Table A 1.4 Shows the converged energies of a pure diamond at different of the dimensions of the *k*-point mesh. All the calculations performed with 64 supercell size C / 6-21G* basis sets. The energies are in hartree.

***k*-point mesh**	**HSE06**	**B3LYP**	**PBE0**	**PBEsol0**	**PBE0-13**
222	-2.435474595265E+03	-2.436298861627E+03	-2.435517071418E+03	-2.428656647749E+03	-2.435671704843E+03
444	-2.435476764761E+03	-2.436300685777E+03	-2.435519134233E+03	-2.428658816637E+03	-2.435673674500E+03
666	-2.435476773798E+03	-2.436300692108E+03	-2.435519135686E+03	-2.428658817985E+03	-2.435673675695E+03
888	-2.435476773876E+03	-2.436300692063E+03	-2.435519135622E+03	-2.428658817993E+03	-2.435673675698E+03

Table A 2.4 Shows the converged energies of a pure diamond at different dimensions of the *k*-point mesh. All the calculations performed with 128-atom supercells C / 6-21G* basis sets. The energies are in hartree.

***k*-point mesh**	**HSE06**	**B3LYP**	**PBE0**	**PBEsol0**	**PBE0-13**
222	-4.870951656758E+03	-4.872599823019E+03	-4.871036462095E+03	-4.857315752443E+03	-4.871345635562E+03
444	-4.870953531637E+03	-4.872601372648E+03	-4.871038269955E+03	-4.857317634217E+03	-4.871347349964E+03
666	-4.870953546533E+03	-4.872601385966E+03	-4.871038270157E+03	-4.857317634416E+03	-4.871347350089E+03
888	-4.870953546530E+03	-4.872601385967E+03	-4.871038270157E+03	-4.857317634414E+03	-4.871347350093E+03

Table A 3.4 Shows the converged energies of C-centre at different dimensions of the *k*-point mesh. All the calculations performed with 128-atom supercells and C / 6-21G* and N / TZVP basis sets. The energies are in hartree.

***k*-point mesh**	**HSE06**	**B3LYP**	**PBE0**	**PBEsol0**	**PBE0-13**
222	-4.887464052782E+03	-4.889129309798E+03	-4.887548166246E+03	-4.873800245470E+03	-4.887852682934E+03
444	-4.887465830235E+03	-4.889130788899E+03	-4.887549877431E+03	-4.873802022413E+03	-4.887854312407E+03
666	-4.887465830470E+03	-4.889130789058E+03	-4.887549877638E+03	-4.873802022630E+03	-4.887854312581E+03
888	-4.887465830469E+03	-4.889130789059E+03	-4.887549877636E+03	-4.873802022631E+03	-4.887854312581E+03

Table A 4.4 Shows the converged energies of P_{sub} defect in diamond with C_{3v} at different dimensions of the *k*-points mesh. All the calculations performed with 128-atom supercell and C / 6-21G* and P / TZVP basis sets. The energies are in hartree.

***k*-points mesh**	**HSE06**	**B3LYP**	**PBE0**	**PBEsol0**	**PBE0-13**
444	-5.173869045551E+03	-5.175571252098E+03	-5.173949650624E+03	-5.159932033593E+03	-5.174259062044E+03
666	-5.173869032481E+03	-5.175571259338E+03	-5.173949657637E+03	-5.159932041711E+03	-5.174259064784E+03
888	-5.173869036018E+03	-5.175571259435E+03	-5.173949657639E+03	-5.159932041868E+03	-5.174259064774E+03

Table A 5.4 shows converged energies at different dimensions of the *k*-point mesh for Mg_{sub} in its singlet spin states. All calculations performed with 128-atom supercells and (C / 6-21G*) basis sets. The energies are in Hartree.

***k*-points mesh**	**B3LYP**	
	Basis set of Mg/ TZVP	Basis set of Mg/ 6-311G(d)
4 4 4	-5.034188758240E+03	-5.034196301630E+03
6 6 6	5.034188760854E+03	-5.034196304029E+03
8 8 8	-5.034188760875E+03	-5.034196304065E+03
	HSE06	
4 4 4	-5.032468154800E+03	-5.032475380626E+03
6 6 6	-5.032468158859E+03	-5.032475384283E+03
8 8 8	-5.032468158820E+03	-5.032475384344E+03
	PBE0	
4 4 4	-5.032548803549E+03	-5.032556233671E+03
6 6 6	-5.032548806165E+03	-5.032556236110E+03
8 8 8	-5.032548806192E+03	-5.032556236142E+03
	PBEsol0	
4 4 4	-5.018627640092E+03	-5.018635505460E+03
6 6 6	-5.018627642842E+03	-5.018635507930E+03
8 8 8	-5.018627642833E+03	-5.018635507964E+03

Table 4.6 (*q*) Refer to Mulliken atomic charges; (μ) spin moments (both in *e*) at defect sites and on the four carbon atoms around the defect (C_α and C_β); (*R*) equilibrium bond distances of the first neighbours from the Mg (in Å); (*b*) overlap bond populations of the bond between Mg atoms and the first neighbours (in *e*); *E* the energy (in hartree); and E_R energies relative to that of compared to $S_z = 0$ in eV. SC refers to supercell size.

Functional	SC	Basis set		$S_z = 1$ (T_d)		$S_z = 0$ (C_{2v})		
				Mg	$4C_\alpha$	Mg	$2C_\alpha$	$2C_\beta$
B3LYP	64	(Mg / TZVP) (C / 6-21G*)	*q*	1.248	-0.320	1.241	-0.318	-0.318
			μ	0.093	0.383	-0.00	0.391	-0.391
			R		1.865		1.864	1.863
			b		0.100		0.101	0.101
			E	-2597.8956			-2597.8956	
			E	0.00			0.00	
B3LYP	128	(Mg / TZVP) (C / 6-21G*)	*q*	1.252	-0.321	1.245	-0.319	-0.319
			μ	0.095	0.382	0.00	0.390	-0.390
			R		1.857		1.855	1.855
			b		0.098		0.100	0.100
				-5034.1888			-5034.1887	
			E	0.00			0.00	
B3LYP	128	(C / 6-21G*) (Mg / 311G(d))	*q*	1.094	-0.264	1.087	0.262	0.262
			μ	0.039	0.390	0.00	0.398	0.398
			R		1.861		1.859	1.859
			b		0.134		0.134	0.134
				-5034.1963			-5034.1963	
			E	0.00			0.00	
PBE0	64	(Mg / TZVP) (C / 6-21G*)	*q*	-1.242	-0.313	1.232	-0.310	-0.310
			μ	0.096	0.391	-0.00	0.402	-0.402
			R		1.860		1.857	1.857
			b		0.100		0.102	0.102
			E	-2597.0356			-2597.0367	
			E	0.03			0	
PBE0	128	(Mg / TZVP) (C / 6-21G*)	*q*	1.247	-0.314	1.237	-0.312	-0.312
			μ	0.096	0.389	0.00	0.401	-0.401
			R		1.851		1.849	1.849
			b		0.098		0.100	0.100
				-5032.5477			-5032.5488	
			E	0.03			0	
PBE0	128	(Mg / 311G(d)) (C / 6-21G*)	***q***	1.016	-0.248	1.008	-0.246	-0.246
			μ	0.026	0.400	-0.000	0.412	-0.412
			R		1.855		1.853	1.852
			b		0.144		0.145	0.145
				-5032.5551			-5032.5562	
			E	0.03			0	
PBEsol0	64	(Mg / TZVP) (C / 6-21G*)	***q***	1.208	-0.303	1.199		-0.301
			μ	0.101	0.383	0.000		0.394
			R		1.855			1.852
			b		0.103			0.105
			E	-2589.9749			-2589.9760	
			E	0.03			0	

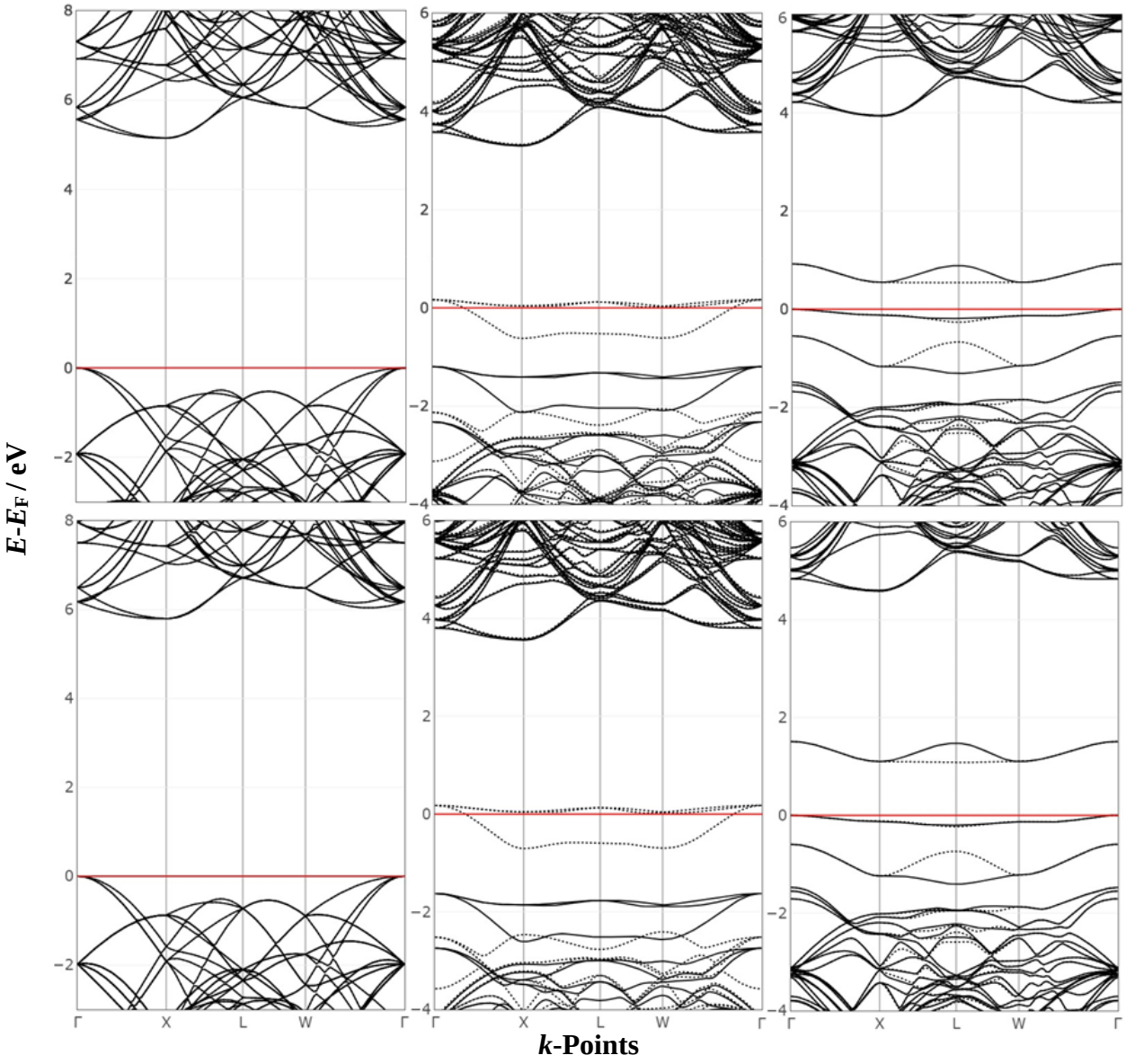

Figure A1.4. Band structure of pure diamond (left) compared with an Mg defect in a substitutional site with $S_z = 1$ (middle) and $S_z = 0$ (right). The top three panels refer to HSE06 and the lower one refers to PBE0. All calculations are computed with C / 6-21G* and Mg / TZVP basis sets and 128-atom supercells.

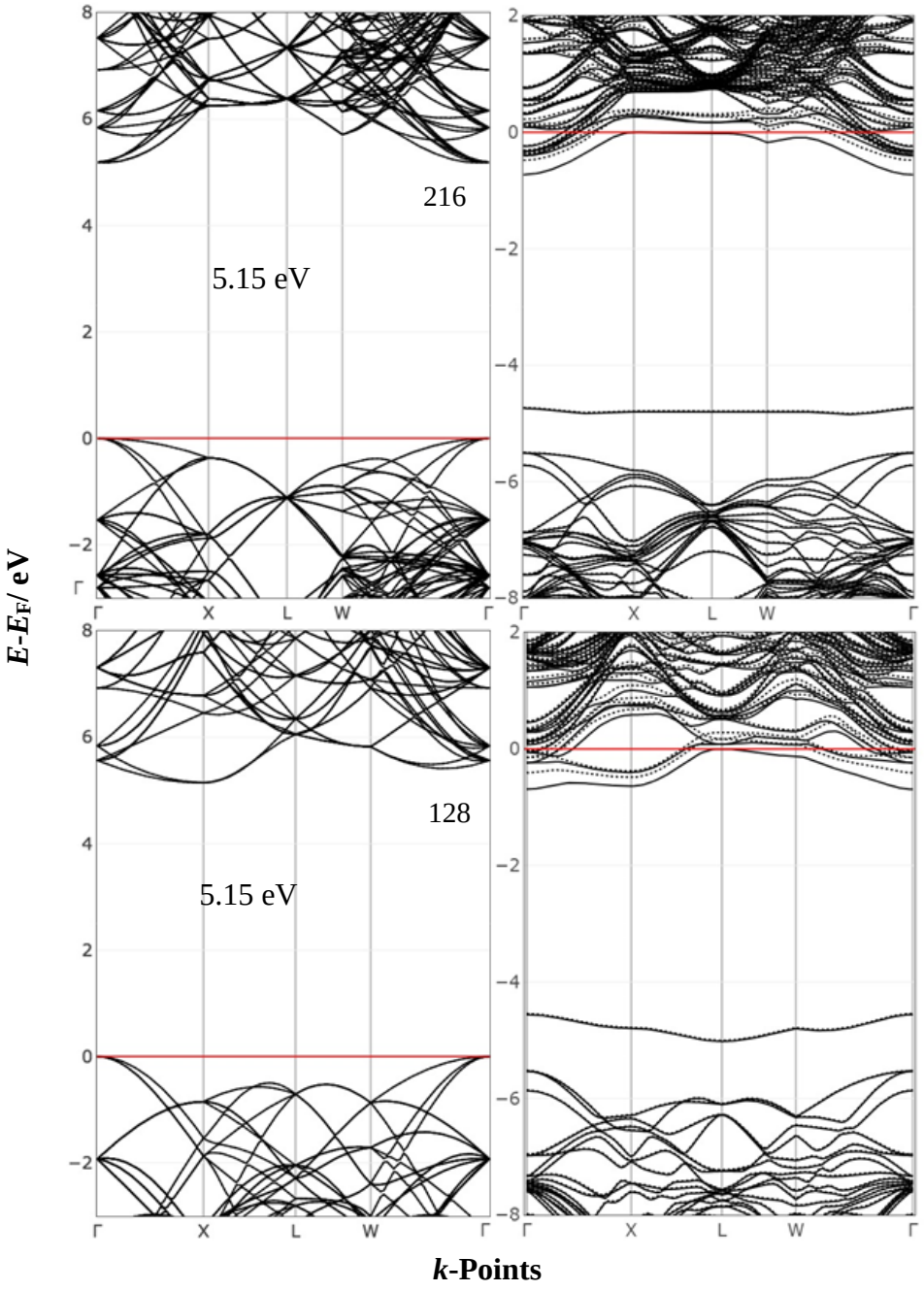

Figure A4.2. Band structure of perfect diamond compared with a corresponding MgN_3 defect in a substitutional site with C_{3v} symmetry. The top panel refers to 216-atom supercells and the lower refers to 128-atom supercells. All calculations were computed with HSE06 and C / 6- 21G* and Mg, N / TZVP basis sets.

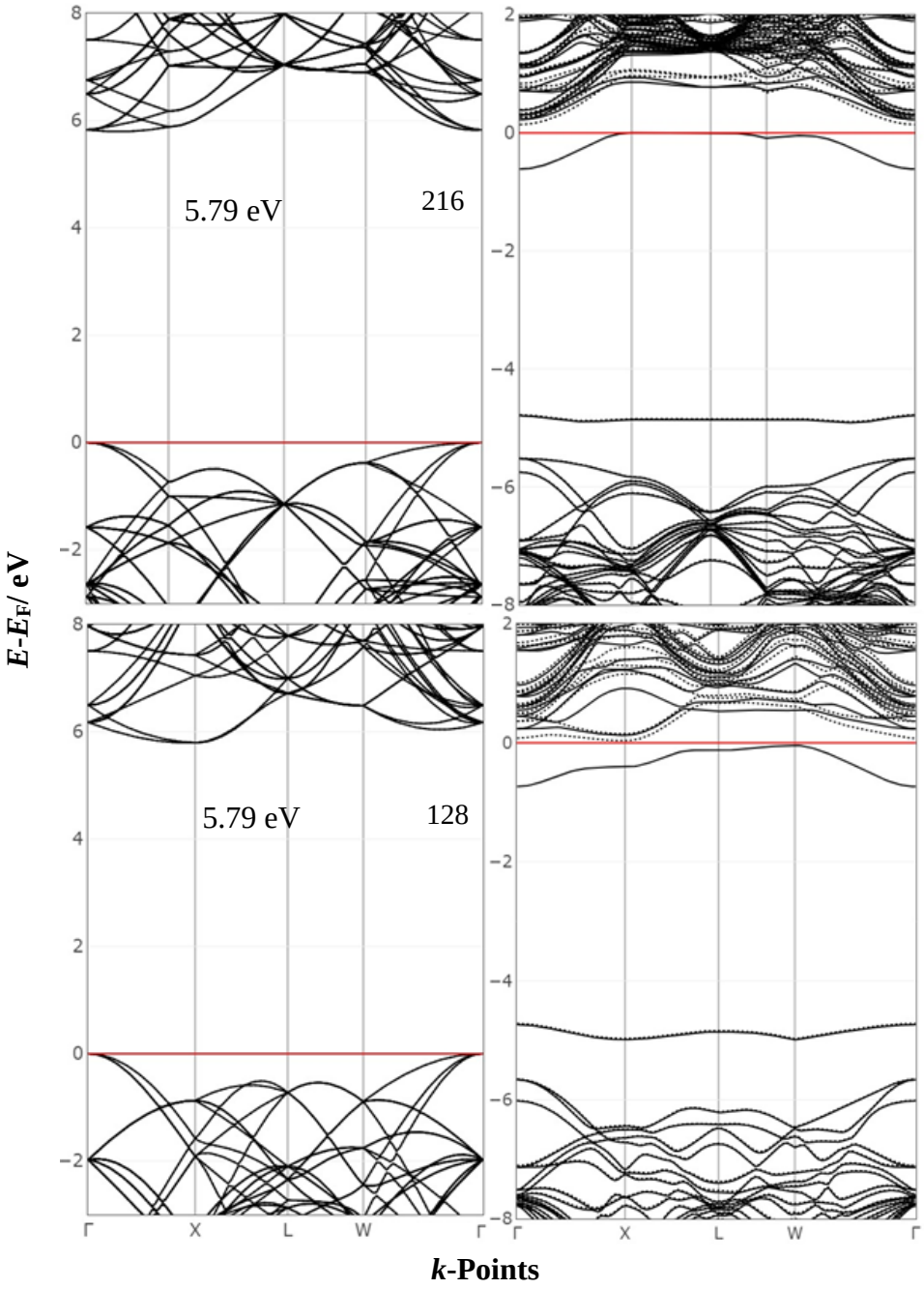

Figure A3.4. Band structure of perfect diamond compared with a corresponding MgN_3 defect in a substitutional site with C_{3v} symmetry. The top panel refers to 216 and the lower refers to 128-atom supercells. All calculations were computed with PBE0 and C / 6-21G* and Mg, N / TZVP basis sets.

Table A 7.4: Ionization energy for different substitutional defects in diamond, calculated with EMM and GGA functionals All energies are in eV.

Defect	Ionization energy/ eV			
	PBE		PW91	
	Fixed Volume	Relaxed volume	Fixed Volume	Relaxed volume
N	- 1.600	-1.560	-1.624	- 1.589
P	- 0.699	-0.639	-0.675	- 0.711
S	-1.258	-1.264	-1.264	-1.271
O	-2.494	-2.458	-2.486	-2.454

Table A 8.4: C-C bond length, lattice parameter (in Å) and energy per atom (in eV) of undefective supercell calculated with GGA.

Functionals	Supercell size	C-C bond lengths (Å)	Lattice parameter (Å)	Energy / cell (eV)	energy / atom (eV)
PW91	64	1.5475	3.5738	-10102.7212	157.8550
	512	1.5475	3.5737	-80821.6789	157.8548
PBE	64	1.5464	3.5714	-10089.3083	157.6454
	512	1.5464	3.5714	-80714.3738	157.6452

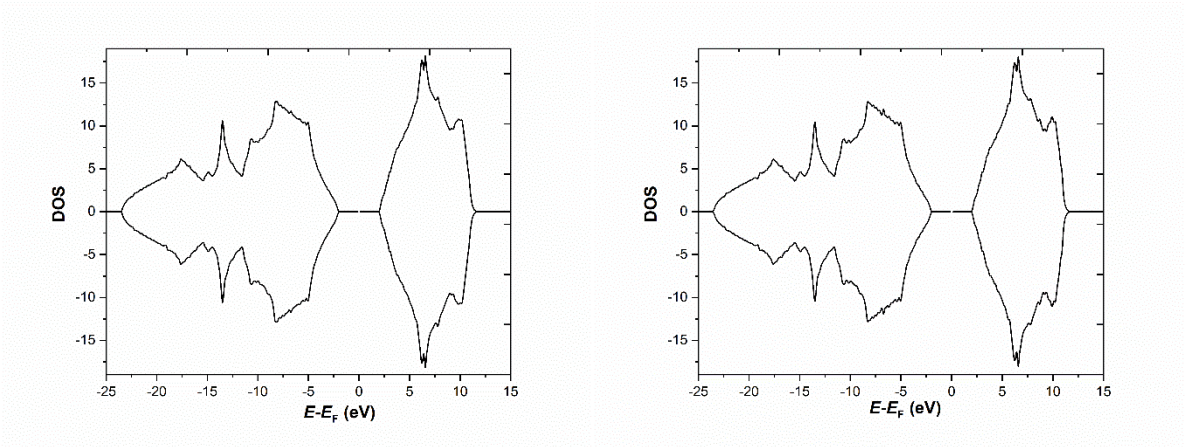

Figure A 4.4: DOS of pure diamond calculated with 64 supercell and two GGA functionals, the panels from right to left refers to PW91 and PBE, respectively. The band gap is 4.2 eV.

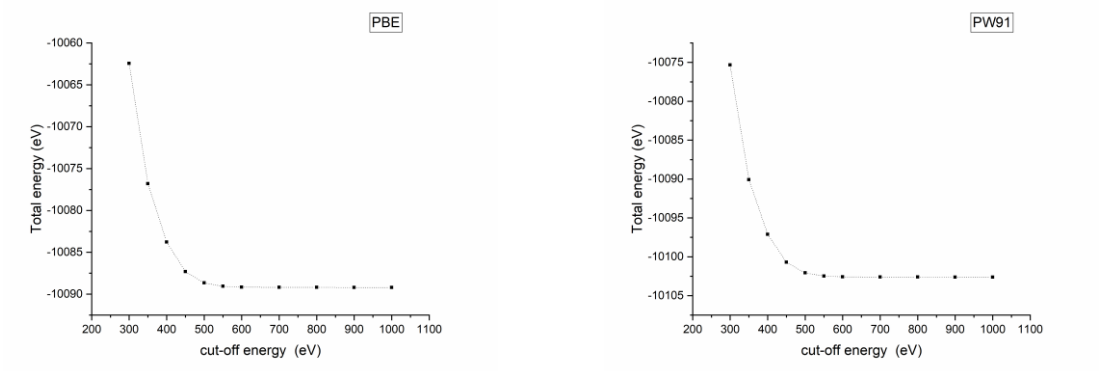

Figure A 4.5 Convergence test with respect to cut-off energy performed with 64 supercell size.

CHAPTER 5

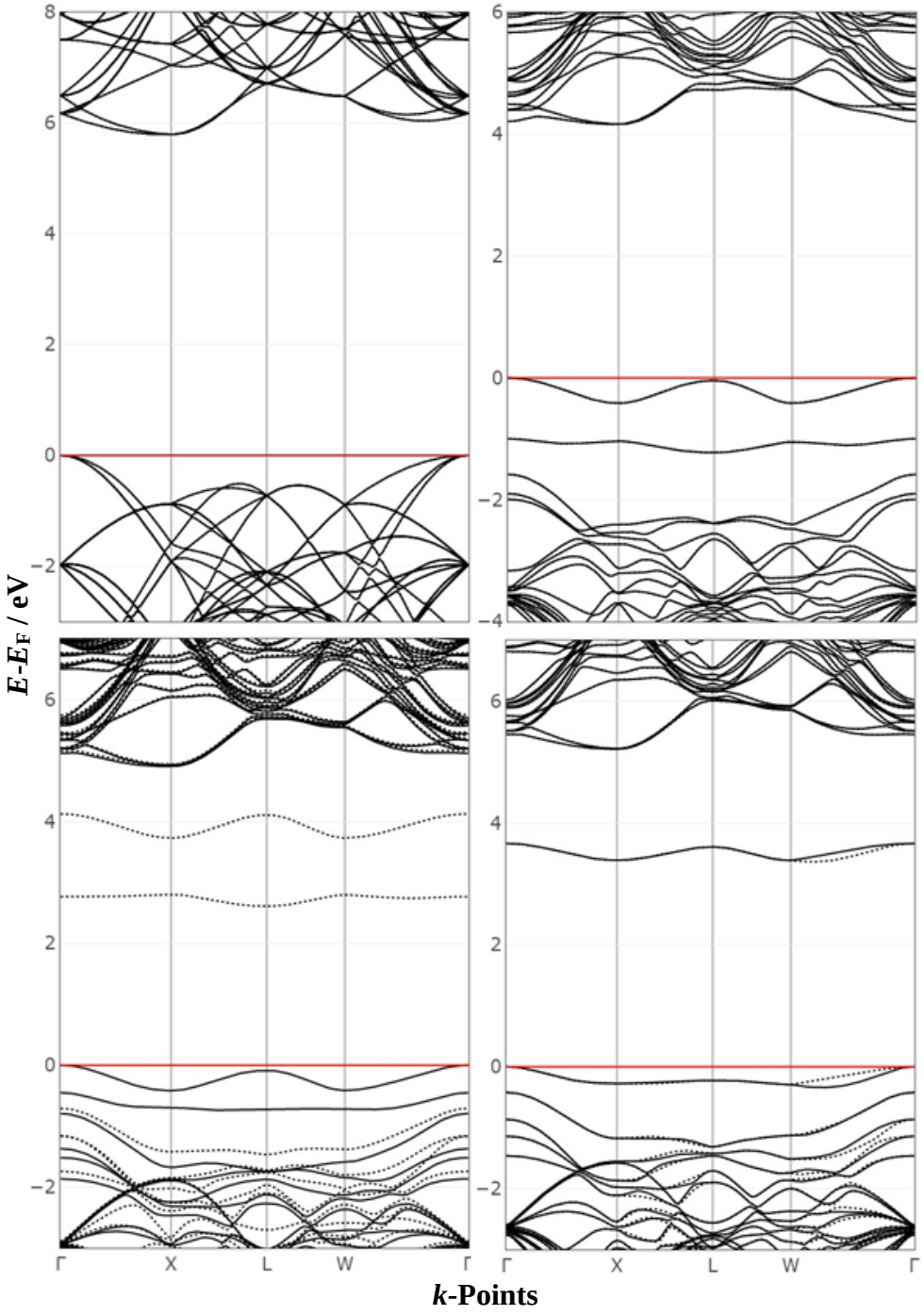

Figure A 1.5: Electronic band structure of pure diamond and a closed-shell system of MgN_2 (top panel, left and right, respectively) unsaturated open-shell 2NV system (bottom panel) with it is two spin states, triplet (right) and singlet left. respectively. All panels refer to the 128- atom supercells, the PBE0 functional and C / 6-21G* and N, Mg / TZVP basis sets.

CHAPTER 6

The Gas Correction Factor for any pure gas is calculated from the following equation:

$$GCFx = \frac{d_t Cp_t \times s}{d_x Cp_x}$$

where:

d_t and d_X , is the standard density (in g/l) at 0 °C and 1013,25 mbar, of the test gas and the X gas, respectively, and Cp_t and Cp_x the specific heat (in cal/g° C).

S is the molecular structure correction factor which determined by the gas type

Gas type	S
monoatomic gases	1.030
diatomic gases	1.000
triatomic gases	0.941
polyatomic gases	0.880

The Gas Correction Factor for mixture gases is calculated from the following equation:

$$GCFx = \frac{d_t Cp_t * (a_1 s_1 + a_2 s_2 + \cdots . a_n s_n)}{(a_1 d_1 Cp_1 + a_2 d_2 cp_2 + \cdots a_n d_n cp_n)}$$

a_1, a_2 ,…,a_n are the fractional flow of gases 1 through n

Table 1.6 shows the specific heat and density of some gasses used in the study.

GAS	SPECIFIC HEAT, Cp cal / g ºC	DENSITY g/l at 0 ºC
Nitrogen (N_2)	0.2485	1.250
Hydrogen (H_2)	3.419	0.0899
Ammonia (NH_3)	0.492	0.760
Methane (CH_3)	0.5328	0.715

Gases	MFCs offset	Gas correction factor	Gas volume (on MFCs controller)
H_2	-6.00	1.00	200.00
CH_4	-0.32	0.72	2.00
NH_3	~ -0.01	1.17	0.7-1.0 0.7-2.0

CHAPTER 7

Table A 7.1 Shows the total energies (in hartree) obtained by different relaxation methods with different functionals and supercell sizes.

Functionals	SC	On-site	Elongated P-N bond (C_{3v})	Elongated one of N-C bond (C_s)
B3LYP	64	-2755.8253	-2755.8664	-2755.9043
	128	-5192.1177	-5192.1572	-5192.1963
HSE06	64	-2754.9260	-2754.9655	-2755.0044
	128	-5190.3959	-5190.4333	-5190.4728
PBE0	64	-2754.9640	-2755.0075	-2755.0464
	128	-5190.4758	-5190.5176	-5190.5572
PBE0-13	64	-2755.1090	-2755.16038	-2755.2010
	128	-5190.7751	-5190.8248	-5190.8663
PBEsol0	64	-2747.7806	-2747.8249	-2747.8633
	128	-5176.4325	-5176.4747	-5176.5138

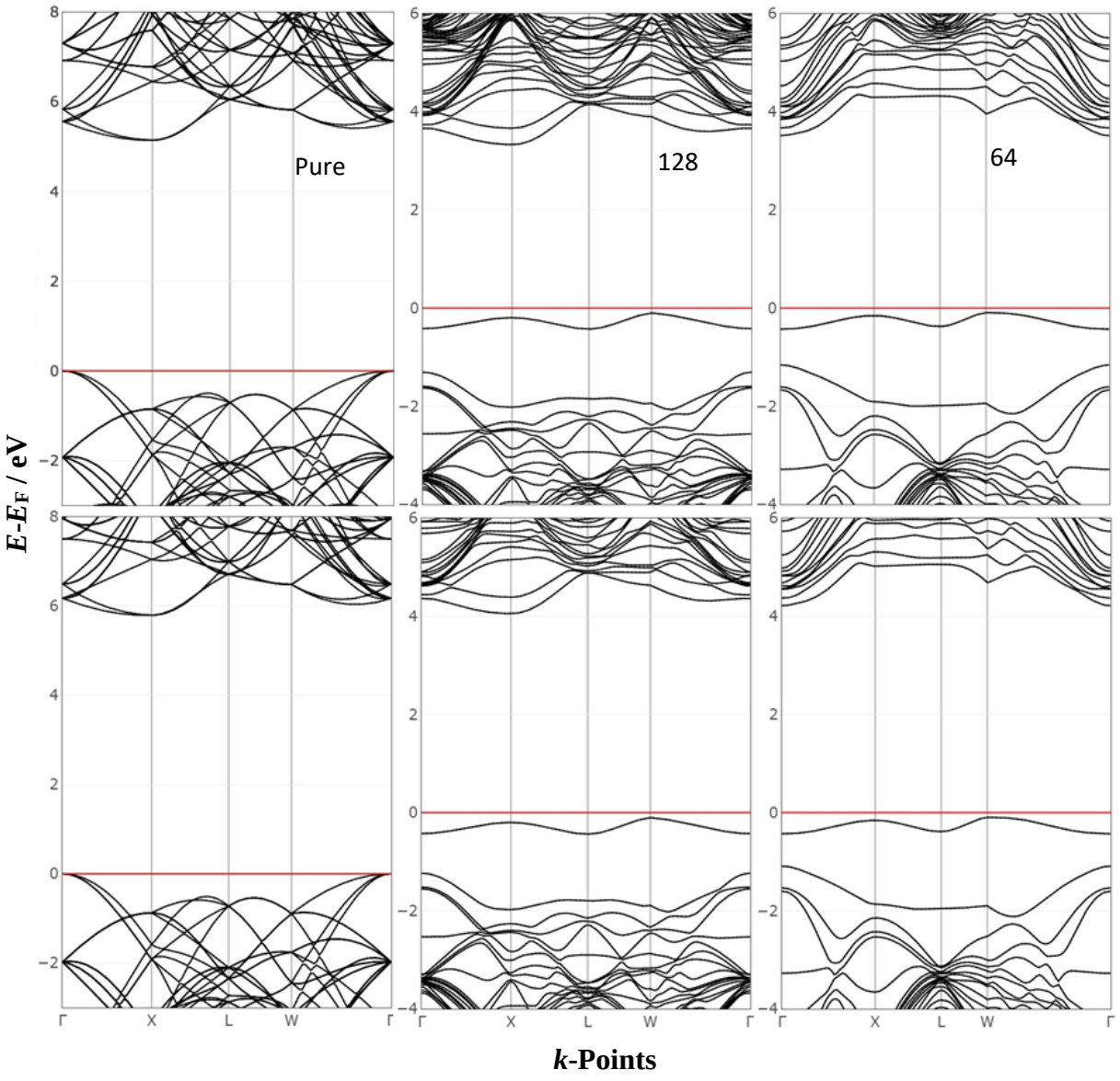

Figure A 7.1. Band structure comparing pure diamond with a diamond containing a PN defect in substitutional sites with two supercell sizes of 128 and 64, respectively. The top three panels refer to HSE06 and the lower three refer to PBE0. All calculations were computed with C / 6- 21G* and P, N / TZVP basis sets.

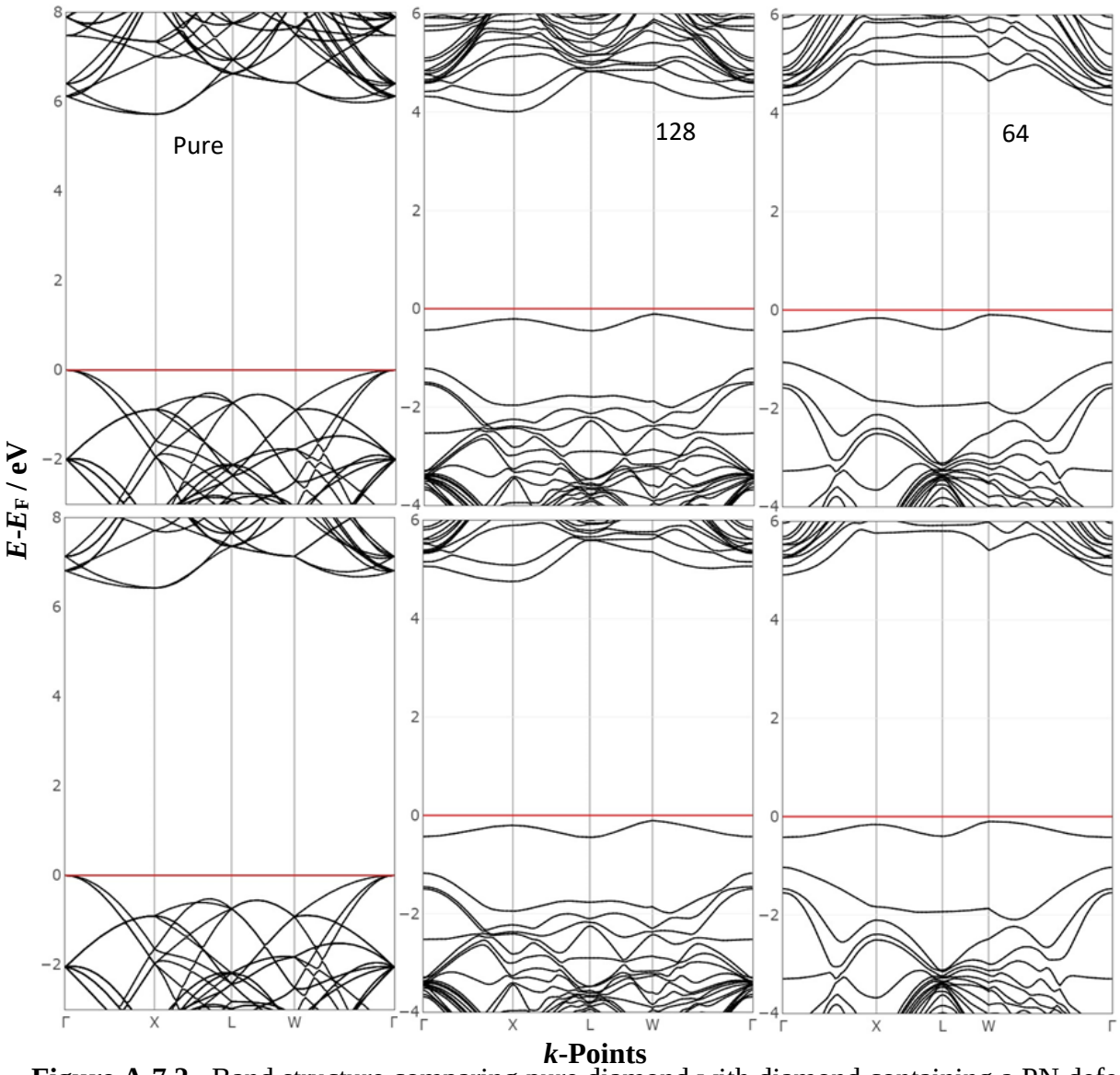

Figure A 7.2. Band structure comparing pure diamond with diamond containing a PN defect in substitutional sites with two supercell sizes of 128 and 64, respectively. The top three panels refer to PBE0sol and the lower three refer to PBE0-13. All calculations are computed with C / 6- 21G* and P,N / TZVP basis sets.